



**Micromechanical study of the role of precipitates on the
plastic deformation of AZ91 magnesium alloy**

by

Shanshan Si

A thesis submitted to University of Birmingham for the degree of
DOCTOR OF PHILOSOPHY

School of Metallurgy and Materials
College of Engineering and Physical Sciences
University of Birmingham
September 2019

UNIVERSITY OF
BIRMINGHAM

University of Birmingham Research Archive

e-theses repository

This unpublished thesis/dissertation is copyright of the author and/or third parties. The intellectual property rights of the author or third parties in respect of this work are as defined by The Copyright Designs and Patents Act 1988 or as modified by any successor legislation.

Any use made of information contained in this thesis/dissertation must be in accordance with that legislation and must be properly acknowledged. Further distribution or reproduction in any format is prohibited without the permission of the copyright holder.

Preface

This research was carried out by Shanshan Si in School of Metallurgy and Materials, University of Birmingham (from September 2015 to September 2019), under the supervision of Dr Yu-Lung Chiu and Prof Ian P. Jones.

The present work is original and no part of the work has been submitted for another degree at any other university. Wherever other researchers' work has been drawn on or cited, it is acknowledged in the text and the references are listed.

Acknowledgements

I would like to express my sincere gratitude to my supervisors Dr Yu-Lung Chiu and Professor Ian P. Jones for their support and guidance of my PhD study. I appreciate all Dr Yu-Lung Chiu's contributions of time and idea to make my PhD study innovative and productive. I would like to say a big thank you to Prof Ian P. Jones for his support with his immense knowledge and continued inspiration during my PhD study.

I sincerely appreciate the academic advice and facilities support from Dr Rengen Ding, Dr Jing Wu and Dr Jinsen Tian.

Many thanks to Mr Paul Stanley, Mrs Theresa Morris and Mr David Price for technical support of facilities in the department.

I would like to thank Prof Michael Loretto, Prof Yoji Mine, Prof Joseph Robson, Dr Jayant Jain and Dr Daniel Reed for the valuable discussions.

Many thanks to Dr David Healy for provision of Eshelby code.

I would like give thanks to my colleagues and friends: Minshi Wang, Xinyu Lu, Yu Lu, Gareth Douglas, Daniel Higgins, Rayan Ameen, Subash Rai, Siben Jiang, Yukiko Ikebe, Wanqi Chen, Gnanavel Thirunavukkarasu, Bo Pang, Yang Lyu, Zhaozhuan Wu, Mark Elliot, Ubaid Ur Rehman Ghori, Jianbing Zhang, Peng Lin, Yulin Ju and Qi Wei.

I gratefully acknowledge the funding received towards my PhD from China Scholarship Council (CSC) and School of Metallurgy and Materials of University of Birmingham.

Lastly, my eternal debt of gratitude goes to my family for their love, understanding and encouragement that have brought me to where I am today.

Abstract

AZ91 magnesium alloy micro-pillars have been studied in order to study the role of precipitates on plastic deformation.

Micro-pillars with a loading direction of $[55\bar{1}0\ 9]$ were prepared in both the solution treated and peak-aged AZ91 conditions to study the influence of precipitates on basal $\langle a \rangle$ dislocation slip. Precipitation has been found to have a very limited strengthening effect with the critical resolved shear stress (CRSS) of the basal $\langle a \rangle$ slip increased by only 4 MPa. No precipitate shearing or Orowan looping has been observed in post-mortem TEM study.

Micro-pillars with a loading direction of $[01\bar{1}0]$ were prepared in both the solution treated and peak-aged AZ91 conditions to study the influence of precipitates on tension twinning. The 0.2% proof stress was increased by about 60 MPa by the precipitates. In the peak-aged sample, more and smaller twins were observed than in the solution treated sample. The precipitates were engulfed by the tension twins during deformation. The back stress generated due to the presence of the precipitates is expected to provide a considerable contribution to strengthening which potentially slows the twin growth. The working hardening rate is slightly higher in the aged sample than in the solution treated sample. A higher density of stacking faults was observed in the aged sample than in the solution treated sample, which may influence the dislocation transmission upon further deformation resulting higher work hardening rate.

Submicron-pillars with a loading direction of $[01\bar{1}0]$ were prepared in the solution treated and under-aged AZ91 conditions and subjected to in-situ TEM compression, in

order to study the influence of precipitates on the tension twin nucleation and growth. In-situ TEM shows that the high stress concentration locations were preferential sites for tension twin nucleation while the precipitates had no obvious influence on twin nucleation. Twin growth, however, was obviously inhibited by the presence of precipitates, which would require an increased applied stress to overcome.

Table of Contents

Preface	i
Acknowledgements	ii
Abstract	iv
Table of Contents	vi
1 Introduction	1
2 Literature Review	4
2.1 Crystallography of Mg	4
2.2 Deformation in Mg	4
2.2.1 Dislocations in Mg	4
2.2.2 Slip systems in Mg	6
2.2.3 Deformation twinning in Mg	9
2.3 Introduction to the Mg alloy used in the current work - AZ91	14
2.4 Strengthening mechanisms in Mg alloys.....	17
2.4.1 Grain boundary strengthening.....	17
2.4.2 Solution strengthening	18
2.4.3 Precipitation strengthening.....	19
2.4.4 Work hardening.....	24
2.5 Mechanical behaviour of Mg and its alloys	24

2.5.1	Determining critical resolved shear stress (CRSS)	24
2.5.2	Anisotropy of deformation	25
2.5.3	Effect of temperature	27
2.5.4	Effect of strain rate	29
2.5.5	Effect of alloying	30
2.5.6	Effect of precipitation	34
2.5.7	Specimen size effect	37
2.6	In-situ tests	38
2.7	Aims and objectives	41
3	Experimental	43
3.1	Raw material	43
3.2	Heat treatment	43
3.3	Hardness testing	44
3.4	Precipitate number density	44
3.4.1	Foil thickness measurement	45
3.4.2	Precipitate dimension measurement	46
3.5	EBSD mapping and Schmid factor calculation	47
3.6	Micro-mechanical testing	50
3.6.1	Micro-pillar fabrication	50
3.6.2	Micro-pillar compression in SEM	51

3.7	Submicron-sized mechanical testing	53
3.7.1	Pillar fabrication.....	53
3.7.2	In-situ TEM compression.....	55
3.8	TEM specimen preparation from deformed micro-pillars.....	57
3.9	Microscopy characterization	59
3.9.1	Optical microscopy (OM)	59
3.9.2	Scanning Electron Microscopy (SEM)	60
3.9.3	Transmission Electron Microscopy (TEM)	60
3.9.4	Electron Back-Scattered Diffraction (EBSD) and Transmission Kikuchi Diffraction (TKD)	61
3.9.5	Focused Ion Beam and Dual-beam Systems.....	62
4	Results	64
4.1	Microstructure of AZ91.....	64
4.1.1	As-cast AZ91	64
4.1.2	Solution treated AZ91	66
4.1.3	Aged AZ91.....	69
4.1.4	TEM foil thickness.....	74
4.2	Compression of micro-pillars oriented for basal slip	75
4.2.1	Mechanical behaviour	75
4.2.2	Surface morphology of deformed micro-pillars.....	78

4.2.3	Transmission electron microscopy results	81
4.2.4	Summary	85
4.3	Compression of micro-pillars oriented for 0112 twinning	85
4.3.1	Mechanical behaviour	85
4.3.2	Surface morphology of deformed micro-pillars.....	88
4.3.3	Transmission electron microscopy results	91
4.3.4	Summary	106
4.4	In-situ TEM Compression of submicron-pillars oriented for 0112 twinning	108
4.4.1	Mechanical behaviour	108
4.4.2	Solution treated submicron-pillars	111
4.4.3	Aged submicron-pillars	130
4.4.4	Summary	150
5	Discussion.....	151
5.1	Age hardening behaviour of bulk AZ91.....	151
5.2	Micro-compression tests.....	152
5.3	Effects of precipitates on basal slip.....	153
5.4	Effect of precipitates on 0112 twinning at the micro-scale	155
5.4.1	Precipitate rotation w.r.t. the matrix upon twinning	155
5.4.2	Back stress caused by the non-shearable precipitates	156
5.4.3	Strain bursts in the stress-strain curves	161

5.4.4	Apparent CRSS determined from mean yield strengths (0.2% strain offset rule)	164
5.4.5	Stacking faults in the twin.....	165
5.5	Effect of precipitates on 0112 twinning at the submicron-scale	167
5.5.1	Twin nucleation.....	167
5.5.2	Twin growth.....	168
5.6	General discussion of the effect of precipitates on twinning	169
6	Conclusions and future work	176
6.1	Conclusions	176
6.2	Suggestions for future work	178
	Appendix: Publish list.....	180
	References	181

1 Introduction

Magnesium is the lightest practical engineering metal with a density of 1.738 g/cm^3 . It is widely distributed in the earth. Beside its low density and easy availability, Mg also has excellent specific strength, good castability, high damping capacity, biocompatibility and recyclability. Because of these attractive features, Mg and its alloys have increasing applications in automotive, aerospace, electronics, bioengineering and sports.

For the hexagonal close-packed (HCP) Mg, the mechanical properties, including strength and ductility, are more complex than those of the body centred cubic (BCC) and face centred cubic (FCC) structures, such as are possessed by steel and Al. For BCC and FCC structures, there are more than five individual slip systems which can operate to accommodate an arbitrary plastic deformation. However, there are four independent easy slip systems (i.e., $\langle a \rangle$ slip) [1, 2] for the HCP structure. This leads to an inherently low ductility of Mg alloys. Also, the highly anisotropic crystalline structure of HCP Mg shows correspondingly mechanically anisotropic behaviour (different critical resolved shear stresses for individual deformation modes) and restricts the plasticity. So, although Mg and its alloys have many attractive features, their relatively low strength and low ductility restricts their applications as engineering materials. It is therefore important to study Mg deformation and strengthening.

Precipitation strengthening is one of the most important strengthening methods in Mg alloys. It can change the deformation mechanisms, and thus influence the overall mechanical behaviour. The precipitation strengthening response in Mg alloys is determined by precipitate orientation, shape, size, volume fraction and interparticle

spacing. A quantitative understanding of precipitate microstructures and their interaction with plastic deformation is of importance for improving the mechanical behaviour of existing alloys and developing new precipitation hardenable alloys.

Extensive studies have been carried out on the deformation and strengthening of pure Mg and its alloys. However, the majority of the work mainly concerns the overall mechanical behaviour and mechanism of individual slip or twinning systems. The precipitation strengthening of individual deformation modes in Mg alloys is far less well researched. Most pioneering work for this purpose has been carried out using polycrystals and the considerable scatter between the reported measurements could be caused by texture, loading condition, grain size and the models involved in the fitting procedure. The recent development of in-situ SEM/TEM mechanical testing offers the opportunity to examine specific small volumes of single crystals. The precipitation strengthening effect can thereby be studied in single crystals. Without the influence of grain boundaries and texture, the factors that influence deformation behaviour are simplified, and thus the effect of precipitates is more directly obtained. The aim of this research was to investigate the effect of the precipitates on slip and tension twinning in AZ91 single crystals by employing micro-mechanical testing and microstructure analysis.

This thesis is structured as follows:

Chapter 2 contains a review of relevant literature. It begins with a general overview of the crystallography of HCP Mg followed by the introduction to deformation mechanisms in HCP Mg. The Mg alloy used in the present work is introduced and its strengthening mechanisms and mechanical behaviour are also reviewed.

Chapter 3 describes the experimental procedures.

Chapter 4 presents all the experimental results, including the microstructure of AZ91, the mechanical behaviour, surface morphology and detailed defect analysis of the micro-pillars deformed for basal slip and tension twinning. The mechanical behaviour and the in-situ TEM observations of the submicron-pillars oriented for tension twinning are also presented.

Chapter 5 discusses the effect of the precipitation on basal slip and tension twinning.

Chapter 6 draws the main conclusions from the current work and makes suggestions for the future work.

2 Literature Review

2.1 Crystallography of Mg

Mg has an HCP structure with an ABAB..... stacking sequence. The lattice parameters are $a=0.32092$ nm and $c=0.52105$ nm at room temperature. The c/a ratio is 1.6236, which is very close to the 'perfect' ratio of 1.633. The atomic positions and stacking sequence in HCP alloys are shown in Figure 2.1.

In order to index the crystallographic directions and planes in the HCP structure, Miller-Bravais indices are usually used. It is based on the vectors a_1 , a_2 , a_3 and c . a_3 is redundant since $a_3 = -(a_1 + a_2)$. A direction can be expressed as $d = ua_1 + va_2 + ta_3 + wc$, where $u + v + t = 0$ with respect to the four index basis.

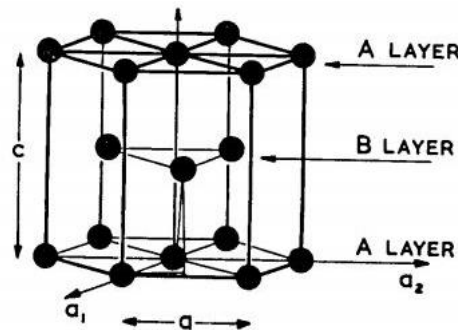


Figure 2.1 HCP structure and axes. The stacking sequence is ABAB...[3].

2.2 Deformation in Mg

2.2.1 Dislocations in Mg

The dislocations in HCP structure are described by a bi-pyramidal structure illustrated in Figure 2.2. The dislocations in HCP structure are listed in Table 2.1.

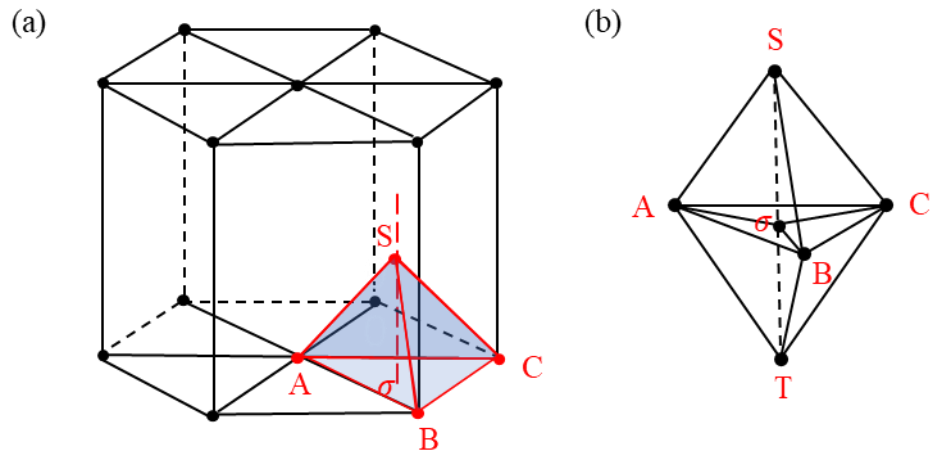


Figure 2.2 Bi-pyramidal construction showing the dislocation Burgers vectors in HCP.

Table 2.1 Dislocations in HCP [3, 4].

Type	AB (perfect)	TS (perfect)	ST+AB (perfect)	$A\sigma$ (partial)	σS (partial)	AS (partial)
Miller-Bravais indices	$\frac{1}{3}\langle 11\bar{2}0 \rangle$	$[0001]$	$\frac{1}{3}\langle 11\bar{2}3 \rangle$	$\frac{1}{3}\langle 1\bar{1}00 \rangle$	$\frac{1}{2}[0001]$	$\frac{1}{6}\langle 2\bar{2}03 \rangle$
b	a	c	$(c^2 + a^2)^{\frac{1}{2}}$	$\frac{a}{\sqrt{3}}$	$\frac{c}{2}$	$\left(\frac{a^2}{3} + \frac{c^2}{4}\right)^{\frac{1}{2}}$
b^2	a^2	c^2	$c^2 + a^2$	$\frac{1}{3}a^2$	$\frac{c^2}{4}$	$\frac{a^2}{3} + \frac{c^2}{4}$
Total No. of dislocations (including negative)	6	2	12	6	4	12

A perfect $\langle a \rangle$ type dislocation may decompose into two Shockley partial dislocations bounding an intrinsic stacking fault on the basal plane. The Burgers vector reaction is:

$$AB \rightarrow A\sigma + \sigma B$$

Equation 2.1

or

$$\frac{1}{3}[11\bar{2}0] \rightarrow \frac{1}{3}[10\bar{1}0] + \frac{1}{3}[01\bar{1}0] \quad \text{Equation 2.2}$$

The stacking fault energy for the above dissociation is 30~40 mJm⁻² [4]. The dislocation on the basal plane is in a low energy configuration. Nevertheless, cross-slip of $\langle a \rangle$ dislocations between the basal plane and the prismatic plane has been reported in Mg [5-7]. A jog-pair mechanism was proposed for cross-slip in Mg [8]. The configuration of cross-slip of basal dislocation onto prismatic plane is shown in Figure 2.3.

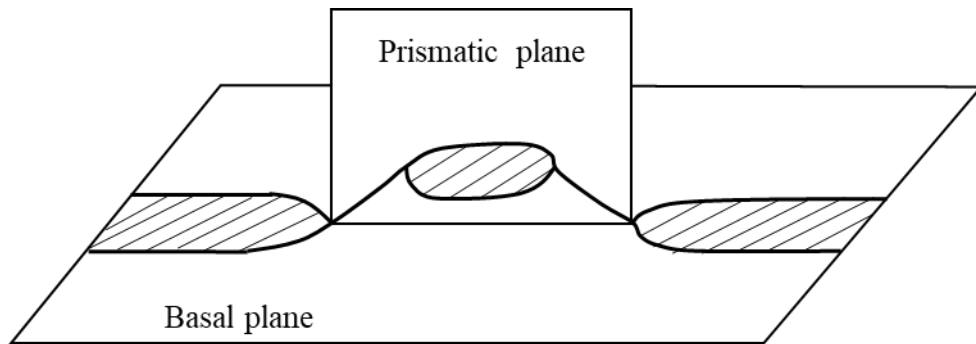


Figure 2.3 Configuration of cross-slip of basal dislocations onto prismatic planes. The basal dislocation has cross-slipped and re-dissociated in the next parallel basal plane [9].

2.2.2 Slip systems in Mg

The important slip systems in HCP Mg are shown in Figure 2.4. The numbers of independent slip systems for each type are listed in Table 2.2. According to the Von Mises criterion [3, 10], a minimum of five independent slip systems is required to generate an arbitrary shape change. Basal $\langle a \rangle$ slip occurs preferentially at room temperature. The $\langle a \rangle$ dislocations on the basal plane offer only two independent slip systems, thus not satisfying

the Von Mises criterion. To achieve an arbitrary shape change, non-basal dislocation slip is needed.

There are two types of non-basal slip. One is $\langle a \rangle$ slip on prismatic planes. Another type is pyramidal slip, including dislocations moving on a first order pyramidal plane or a second order pyramidal plane. $\langle a \rangle$ dislocations can only slip on first order pyramidal planes while $\langle c + a \rangle$ dislocations can slip on both types of pyramidal plane [3]. Beside the two independent slip systems provided by $\langle a \rangle$ slip on basal planes, two additional independent slip systems are provided by $\langle a \rangle$ slip on prismatic planes. $\langle a \rangle$ slip on first order pyramidal planes provides four independent slip systems, which is equivalent to the combined four independent slip systems in basal and prismatic slip systems when cross-slip occurs [2]. In other words, all possible $\langle a \rangle$ slip systems can provide four independent slip systems in total when cross-slip is included. No matter which slip plane the $\langle a \rangle$ dislocations locate on, they cannot produce strain along the c -axis. $\langle c + a \rangle$ dislocations are needed for strain accommodation along the c -axis and to achieve an arbitrary shape change. These non-basal slip systems thus help the ductility of Mg.

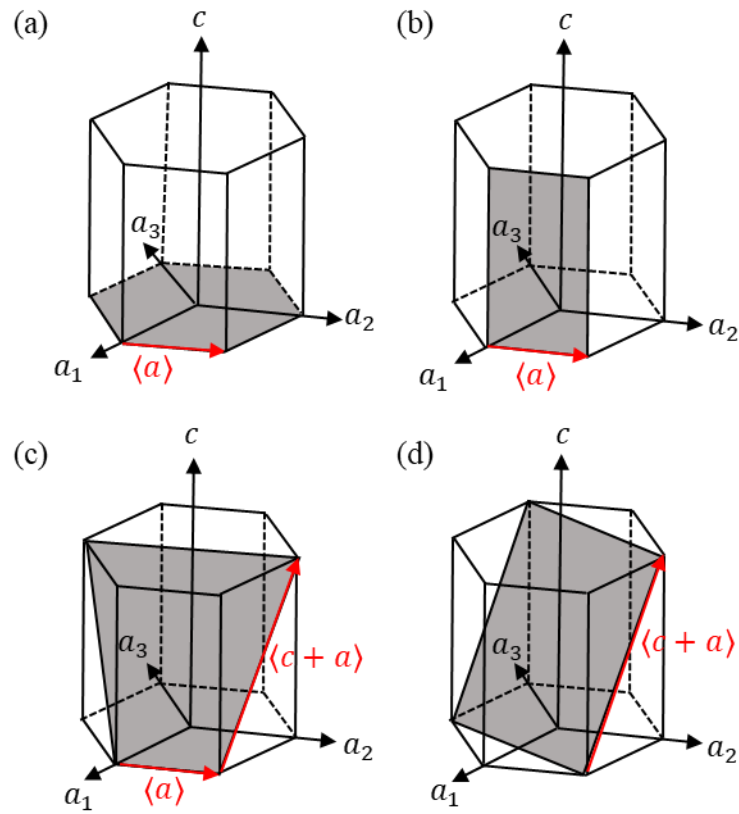


Figure 2.4 The slip systems in HCP. (a) $\frac{1}{3}\langle 11\bar{2}0 \rangle \{0001\}$, (b) $\frac{1}{3}\langle 11\bar{2}0 \rangle \{1\bar{1}00\}$, (c) $\frac{1}{3}\langle 11\bar{2}0 \rangle \{1\bar{1}01\}$ and $\frac{1}{3}\langle 11\bar{2}3 \rangle \{1\bar{1}01\}$, and (d) $\frac{1}{3}\langle 11\bar{2}3 \rangle \{11\bar{2}2\}$.

Table 2.2 The slip systems in Mg [1, 3].

Slip direction	Slip plane	No. of independent slip systems
$\langle 11\bar{2}0 \rangle$	Basal plane (0001)	2
$\langle 11\bar{2}0 \rangle$	Prismatic plane $\{1\bar{1}00\}$	2
$\langle 11\bar{2}0 \rangle$	1 st order pyramidal plane $\{1\bar{1}01\}$	4
$\langle 11\bar{2}3 \rangle$	2 nd order pyramidal plane $\{11\bar{2}2\}$	5

2.2.3 Deformation twinning in Mg

As discussed above, sole basal slip in Mg cannot provide the five independent slip systems necessary for an arbitrary shape change. Apart from the non-basal $\langle c + a \rangle$ slip which can operate to accommodate the deformation, twinning can operate to accommodate the deformation and is one of the important deformation modes in Mg. A deformation twin is a crystal region that has undergone a displacive transformation (simple shear), resulting in the new structure identical to that of the matrix, but oriented differently [11, 12].

A notation describing twinning shear is shown in Figure 2.5. The twinning plane which is the invariant and unrotated plane of the shear is denoted by K_1 and the direction of the shear is η_1 . The conjugate twinning plane which is the second undistorted but rotated plane is denoted by K_2 and the conjugate twinning direction is η_2 . The plane perpendicular to K_1 and K_2 is called the plane of shear and is denoted by P . The plane of shear contains η_1 and η_2 [11]. The magnitude of the twinning shear is denoted by γ .

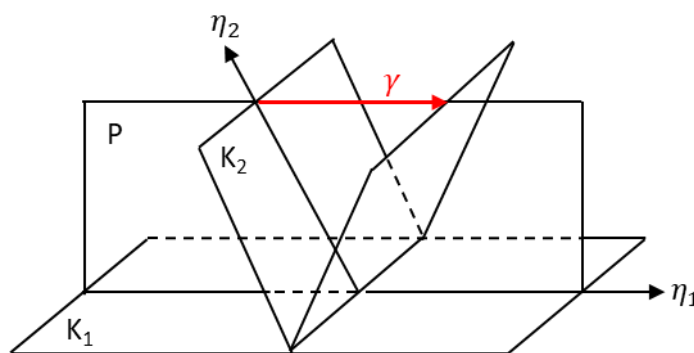


Figure 2.5 A Schematic diagram of twinning parameters: K_1 , η_1 , K_2 , η_2 and P [11].

The most common twinning system in HCP metals is $\{10\bar{1}2\}\langle\bar{1}011\rangle$. The associated twinning shear direction depends on the c/a ratio, as shown in Figure 2.6 [2, 13]. If the c/a ratio is greater than $\sqrt{3}$ (e.g. Zn, Cd), a $\{10\bar{1}2\}\langle\bar{1}011\rangle$ system produces shortening parallel to the c -axis, which is called compression/contraction twinning. If the c/a ratio is lower than $\sqrt{3}$ (e.g. Be, Ti, Zr, Re, Mg), $\{10\bar{1}2\}\langle\bar{1}011\rangle$ twinning produces an elongation parallel to the c -axis, which is called tension/extension twinning. Apart from $\{10\bar{1}2\}\langle\bar{1}011\rangle$, $\{10\bar{1}\bar{1}\}\langle10\bar{1}2\rangle$ twinning occurs in Mg as well. The twinning systems in Mg and their related parameters are shown in Figure 2.7 and Table 2.3 [2].

The twin lattice reorientation in the HCP structure cannot be achieved completely by pure shear. It also requires additional atomic shuffling to re-establish the lattice, quite different from FCC metals [11, 12, 14]. For $\{10\bar{1}2\}\langle\bar{1}011\rangle$ twinning in Mg, a minor shuffle (~ 0.02 nm) is required to reach the correct lattice re-orientation in the twin lattice, which is much smaller than any well-defined dislocation [14, 15]. This minor shuffle is a hypothesized elementary twinning dislocation, which is used in twinning simulations but has not been identified by experiment. The precise geometric view of twinning is still less well understood than that for slip. But the resulting orientation relationship is clearly established and observed, as shown in Figure 2.7(b) [16]. The angle between the (0001) in the matrix and the (0001) in the twin is 86.3° around $\langle\bar{2}110\rangle$ axis.

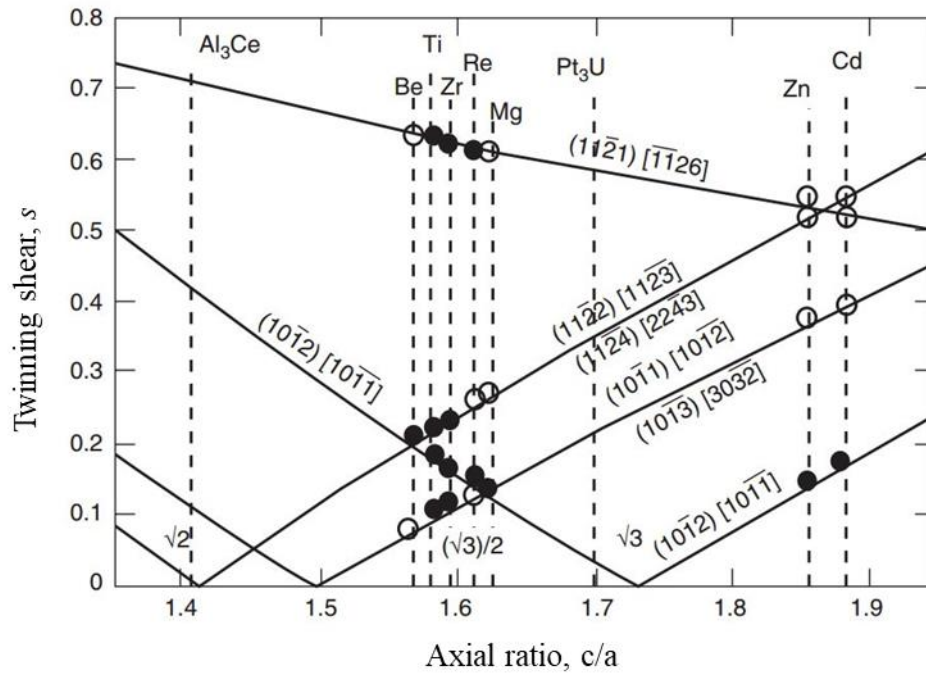


Figure 2.6 Twinning shear variation with c/a ratio in HCP [2].

Table 2.3 Twinning elements and parameters of twinning in Mg [2].

K_1	K_2	η_1	η_2	S	Twinning shear γ
$\{10\bar{1}2\}$	$\{10\bar{1}\bar{2}\}$	$\pm\langle 10\bar{1}\bar{1}\rangle$	$\pm\langle 10\bar{1}1\rangle$	$\pm\frac{1}{3}\langle 1\bar{2}10\rangle$	0.129
$\{10\bar{1}1\}$	$\{10\bar{1}3\}$	$\langle 10\bar{1}\bar{2}\rangle$	$\langle 30\bar{3}2\rangle$	$\frac{1}{3}\langle 1\bar{2}10\rangle$	0.138

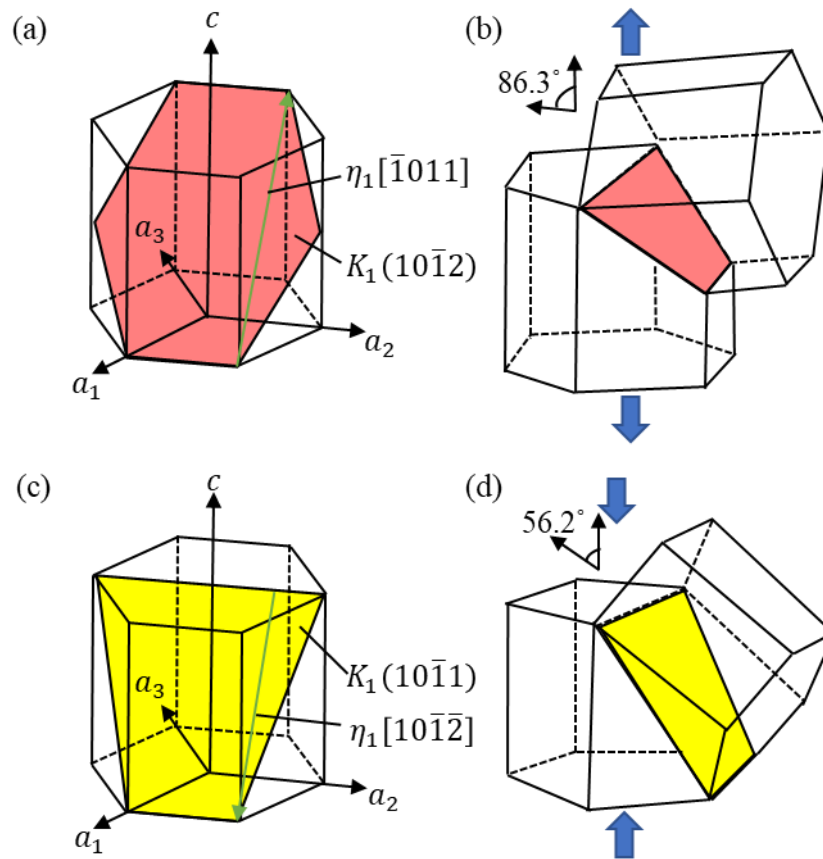


Figure 2.7 Twinning systems in Mg. (a) and (b) tension twin $\{10\bar{1}2\}\{\bar{1}011\}$, (c) and (d) compression twin $\{10\bar{1}\bar{1}\}\{10\bar{1}2\}$.

It is generally accepted that twinning involves three steps: nucleation, propagation and thickening [12]. Twinning nucleation is classified into homogeneous and heterogeneous mechanisms [12]. Homogeneous nucleation refers to homogeneous lattice shear induced twin embryo formation under an abnormally high stress [14, 17]. Bell et al. [18, 19] found that a much higher stress was needed to activate twinning in a carefully prepared and handled zinc single crystal than in less ideal crystals. Furthermore, Price [17] activated twinning in a nearly perfect Zn single crystal inside a TEM, and found that the stress needed was much higher than that measured in large crystals. The possible reason was that homogeneous nucleation for twinning is needed in nearly perfect crystals while

twinning is initiated by some existing internal imperfections in less perfect crystals. Twinning nucleation from the existing imperfections is the key point of heterogeneous nucleation [20-23]. Cottrell et al. [22] and Thompson et al. [23] proposed that a prismatic dislocation dissociated into a glissile twinning and a sessile pole dislocation. The former dislocation was regarded as a twin nucleus. Mendelson [24] proposed that the dissociation of basal and non-basal dislocations was able to produce various twinning partial dislocations on twin planes. Although heterogeneous twin nucleation theories agree on the necessity for dislocation dissociation, the mechanisms and pathways for dislocation dissociation are still in doubt and remain an area of intense research. Compared with homogeneous nucleation, heterogeneous nucleation requires significantly less stress. The twin may expand both laterally and transversely after a stable twin nucleus is formed. Lateral expansion (propagation) means that the twin advances rapidly along the twinning shear direction. Transverse expansion (thickening) means that the twin grows perpendicularly to the twin plane to form a lenticular ellipsoid.

Apart from the twinning process, detwinning occurs in Mg alloys under reverse loading or unloading for tension twinning. Detwinning is a process of twin shrink. The existing twins can disappear or become narrower when the external stress is relaxed. There are recent studies [25-27] of detwinning process which imply instability of twins in Mg alloys.

2.3 Introduction to the Mg alloy used in the current work - AZ91

A commercial AZ91 Mg alloy (the letter describes the elements: A refers to Al, Z refers to Zn; the number refines the chemical composition: 9 is 9 wt.% Al; 1 is 1 wt.% Zn) has been used in the present work.

According to the binary Mg-Al phase diagram at the Mg-rich end illustrated in Figure 2.8, the solubility of Al in Mg reaches maximum of 12.9 wt.% at the eutectic temperature 437°C but falls to 3.3 wt.% at 200°C. This leads to the β -Mg₁₇Al₁₂ precipitates formation when the specimen is aged at 200°C. The age hardening response of Mg₁₇Al₁₂ precipitates plays an important role in determining the mechanical properties. Mg₁₇Al₁₂ has a BCC crystal structure ($a=1.056$ nm) and a space group $I\bar{4}3m$. The precipitation reaction occurs both continuously (CP) and discontinuously (DP). DP starts from high angle grain boundaries and forms a lamellar structure with grain boundary migration while CP initiates and grows everywhere across the grains. The two types of precipitation reaction occur simultaneously and competitively during aging. Duly et al. [28] reported that CP dominated at high aging temperatures and low aging temperatures while DP dominated at intermediate temperatures. At high aging temperatures, the high volume diffusion rate of solute is not favourable for the nucleation and propagation of the DP, which starts from the grain boundaries, leading to the absence of DP; at low aging temperatures, CP initiates at an early stage of aging which eliminates most of the supersaturation and leads to an absence of DP. Braszczyńska-Malik [29] reported that only DP was observed after aging at 150°C whereas only CP formed after aging at 350°C in Mg-9 wt.% Al. Both DP and CP occurred simultaneously after aging at 200°C and 250°C. Braszczyńska-Malik [29]

pointed out that besides the aging temperature, the precipitation process in Mg-Al alloys was also influenced by the concentration of structural defects.

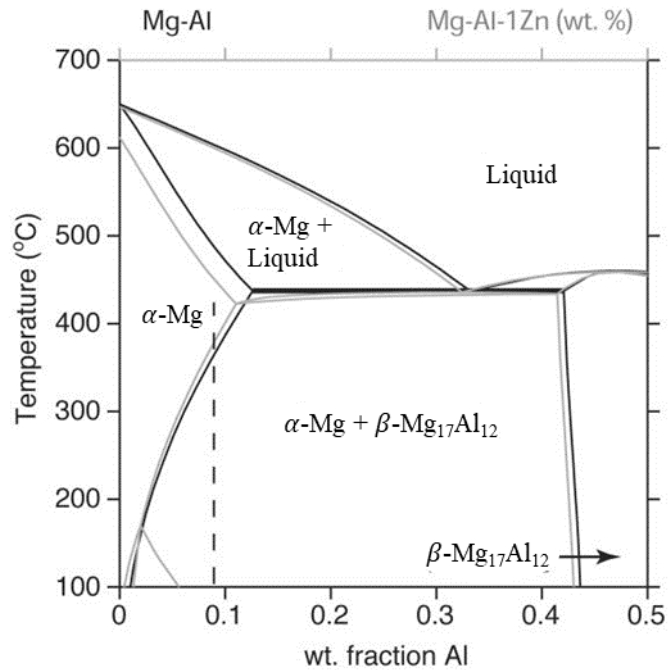


Figure 2.8 Binary Mg-Al phase diagram at the Mg-rich end (black lines). The light grey lines are the ternary isopleth at 1 wt.% Zn corresponding to the AZ series [30].

Most CP and DP were initially reported to exhibit an exact Burgers orientation relationship (OR) with the matrix phase, namely $(0001)_m // (011)_p$, $[1\bar{2}10]_m // [1\bar{1}1]_p$ [31, 32] (Figure 2.9). CPs with this OR appear as thin plates lying on the basal plane, i.e., the habit plane is $(0001)_m$. Subsequently, a slight deviation between the directions $[1\bar{1}1]_p$ and $[1\bar{2}10]_m$ has been observed for some continuous precipitates, indicating that the OR is not an exact Burgers OR [33, 34]. A small proportion of CPs are rod-shaped with their long axis along the $[0001]$ direction. They adopt Crawley OR $(0001)_m // (1\bar{1}1)_p$, $[1\bar{2}10]_m // [\bar{1}12]_p$ [32, 35]. A third and even smaller proportion of CPs is

inclined to the basal plane [31, 32, 35] with Porter OR described by $(0001)_m // (11\bar{5})_p$, $[1\bar{1}00]_m // [0\bar{1}1]_p$, the $(011)_p$ is parallel to the $(11\bar{2}1)_m$. The precipitates perpendicular to the basal plane or inclined to the basal plane are more effective in impeding basal dislocations than precipitates lying on the basal plane, but they contribute to only a small fraction of the microstructure. All ORs in Mg-Al based alloys are summarized in Table 2.4.

Zn addition does not introduce a new phase to AZ91 alloy as compared with binary Mg-Al alloys. The presence of a small amount of Mn leads to the formation of various Al-Mn intermetallic precipitates [36-38]. Al-Mn intermetallic precipitates show different sizes, morphologies and chemical compositions [38, 39]. They are undissolved by solution heat treatment.

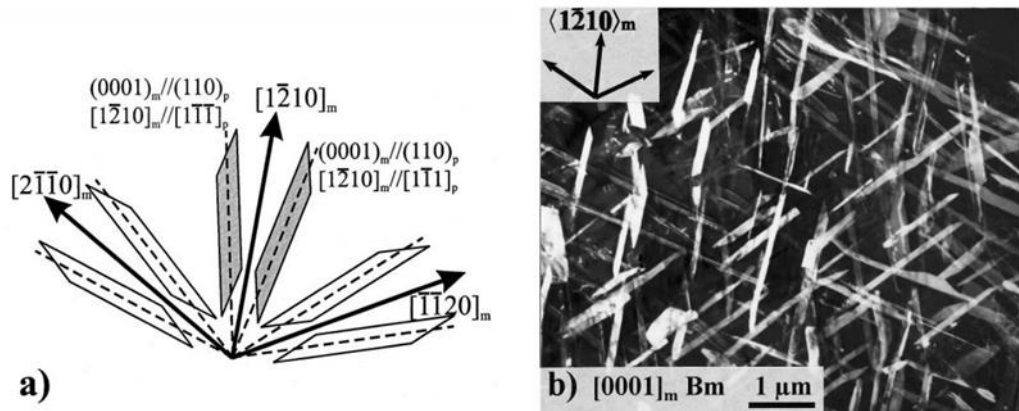


Figure 2.9 (a) A schematic diagram of the continuous precipitates' morphology with the Burgers orientation relationship. (b) A dark field TEM image showing the plate-shaped continuous precipitates in an AZ91 aged at 200°C for 8.3h. The beam direction is $[0001]$ with relation to the matrix [32].

Table 2.4 The reported orientation relationships and precipitate morphologies in Mg-Al alloys (adopted from [40]).

Name	Morphology	Orientation relationship	Ref.
Burgers OR	Plate-shaped	$(0001)_m // (011)_p$ $[1\bar{2}10]_m // [1\bar{1}1]_p$	[31-34, 41, 42]
Crawley OR	Rod shaped	$(0001)_m // (1\bar{1}1)_p$ $[1\bar{2}10]_m // [\bar{1}12]_p$	[32, 35, 43]
Porter OR	Short rod-shaped	$(11\bar{2}1)_m // (011)_p$ $[1\bar{1}00]_m // [0\bar{1}1]_p$	[32, 35, 43]
Gjønnes-Östmoe OR	Plate-shaped	$(0001)_m // (011)_p$ $[2\bar{1}\bar{1}0]_m // [12\bar{1}]_p$	[43]
Potter OR	Plate/rod shaped	$(0001)_m$ 2° from $(011)_p$ $[2\bar{1}\bar{1}0]_m // [1\bar{1}1]_p$	[44]

2.4 Strengthening mechanisms in Mg alloys

2.4.1 Grain boundary strengthening

Grain boundaries strengthen the metal because grain boundaries act as strong impediments to dislocation movement and lead to dislocation pile-up at the grain boundaries. The relationship between yield stress (σ_{gb}) and grain size (d) is expressed via the Hall-Petch relation:

$$\sigma_{gb} = \sigma_0 + kd^{-1/2} \quad \text{Equation 2.3}$$

where σ_0 is the intrinsic yield strength. The Hall-Petch relationship tells us that high strength can be achieved by grain refinement.

2.4.2 Solution strengthening

Solute atoms strengthen the metals because of the size misfit and differences in elastic modulus between the solute and matrix atoms [45]. The relationship between yield stress (σ_{ss}) and the concentration of atoms (c) was described by Fleischer [45] as

$$\sigma_{ss} = \sigma_{y0} + Z_F G \varepsilon_F^{3/2} c^{1/2} \quad \text{Equation 2.4}$$

where $\varepsilon_F = |\delta| + \beta|\eta|$

or by Labusch [46] as

$$\sigma_{ss} = \sigma_{y0} + Z_L G \varepsilon_L^{4/3} c^{2/3} \quad \text{Equation 2.5}$$

where $\varepsilon_L = \delta^2 + \beta^2 \eta^2$

where σ_{y0} is the yield strength of pure Mg, Z_F and Z_L are constants equal to 1/760 and 1/550, respectively, G is the shear modulus, β is a constant between 1/20 and 1/16, ε_F and ε_L are parameters including the atomic size and shear modulus misfits, δ is the size misfit parameter and η is the modulus misfit parameter. Equations 2.4 and 2.5 both suggest that the yield stress is positively proportional to the solute concentration c^n ($n = 1/2$ or $2/3$). Caceres et al. [47] studied solid solution strengthening by Al in polycrystalline Mg-Al alloys. The yield strength increased linearly with c^n ($n =$

1/2 or 2/3), showing good agreement with the results obtained from single crystal Mg-Al alloys [48, 49].

Gao et al. [50] studied the misfit parameters and the corresponding solution strengthening rates of Y, Gd, Zn and Al in Mg alloys. The misfits show the following sequence: Zn > Al > Y > Gd, but the solid solution strengthening rate shows the sequence: Y > Gd > Zn > Al. Zn has a better solid solution strengthening effect than Al, which can be explained by combining the size misfit and elastic modulus misfit. However, Y and Gd strengthen the Mg better than Zn and Al, which cannot be completely explained by the above equations. It was suggested that valence electron structure differences between the solute and solvent atoms may be an important factor determining the solid solution strengthening rate. Guo et al. [50] studied the valence structure of Mg-Y and Mg-Al, suggesting that Mg and Y have higher bond energy than that between Mg and Al. Thus, Y shows more efficient solid solution strengthening than Al.

Also, the solid solution strengthening effect is anisotropic because of the HCP structure. Mechanical behaviour will be discussed in section 2.5.5.

2.4.3 Precipitation strengthening

Many cast and wrought Mg alloys show a reasonable precipitation strengthening effect. The precipitation procedure involves: (1) solution treatment within the α -Mg phase region to dissolve the solute atoms, (2) rapid cooling to obtain a super-saturated solid solution (SSSS) and (3) subsequent aging to form small, intra-granular precipitates with different chemical composition from that of the supersaturated solid solution. The precipitation strengthening response in Mg alloys is determined by precipitate orientation, size, shape, volume fraction and thus interparticle spacing.

Dispersed shear resistant particles strengthen the metals because of the dislocations bowing around the particles. The Orowan stress used in the current thesis is:

$$\sigma_{Orowan} = \left(\frac{Gb}{2\pi\sqrt{1-\nu}} \right) \left(\frac{1}{\lambda} \right) \ln \left(\frac{d_p}{r_0} \right) \quad \text{Equation 2.6}$$

where σ_{Orowan} is the particle induced yield stress increment, G is the shear modulus of the matrix, ν is Poisson's ratio, d_p is outer cut-off radius and r_0 is inner cut-off radius. d_p is taken as the mean planar diameter of the particles on the slip plane. r_0 is taken equal to the dislocation core radius. λ and d_p vary with the shape and orientation of the particles with respect to the slip plane.

For the shear resistant precipitates in Mg alloys, the Orowan equation is even more complicated due to the different precipitates' orientation, morphology and the numerous slip planes. As such, the modification of Orowan equation for precipitates in Mg alloys has attracted some attention. Three common kinds of precipitate morphology [42, 51-54] are considered in the Orowan strengthening calculation: (1) basal plate-shaped precipitates (e.g. Mg-Al system) [29, 32, 35, 43], (2) rod-shaped precipitates along the c -axis (e.g. Mg-Zn system) [55-58] and (3) plate-shaped precipitates on prismatic planes (e.g. Mg-RE system) [59-61].

To derive interparticle spacing of plate-shaped precipitates on (0001), the precipitates in Mg have a uniform diameter d_t and thickness t_t at volume fraction f and form a triangular array on the slip plane [51]. The arrangement of basal plate precipitates and projection of intersected precipitation by the (0001) slip plane of α -Mg are shown in Figure 2.10(a) and (c).

According to Fullman [62], the number density of precipitates per unit area on the slip plane (N_A) is equal to the number density of precipitates per unit volume (N_V) times the probability (p) that a plane intersects a precipitate. p is equal to the thickness t_t and the d_p is equal to d_t through the thesis.

$$N_A = N_V p \quad \text{Equation 2.7}$$

$$f = N_V V = N_V \frac{\pi}{4} d_t^2 t_t \quad \text{Equation 2.8}$$

The interparticle spacing on the basal plane is given by:

$$\lambda = L_p - d_p = \frac{1}{\sqrt{N_A}} - d_p = \sqrt{\frac{2}{\sqrt{3}}} \frac{1}{\sqrt{\frac{f t_t}{\frac{\pi}{4} d_t^2 t_t}}} - d_t = \left(\frac{0.953}{\sqrt{f}} - 1 \right) d_t \quad \text{Equation 2.9}$$

where L_p is the mean planar centre-to centre interparticle spacing.

Thus, Equation 2.6 can be rewritten as in the form:

$$\sigma_{Orowan} = \frac{Gb}{2\pi\sqrt{1-\nu}\left(\frac{0.953}{\sqrt{f}}-1\right)d_t} \ln \frac{d_t}{b} \quad \text{Equation 2.10}$$

Apart from the Orowan equation for basal precipitates, the Orowan equations for prismatic plates and rod-shaped precipitates along the c -axis have also been derived as shown in Table 2.5. Comparisons of identical volume fractions indicate that basal plate-shaped precipitates are not effective in Orowan hardening basal slip due to the large interparticle spacing. Plate-shaped precipitates on prismatic planes and rod-shaped precipitates along the c -axis would be expected to be more effective because of the increased probability of interaction between dislocations and precipitates [53].

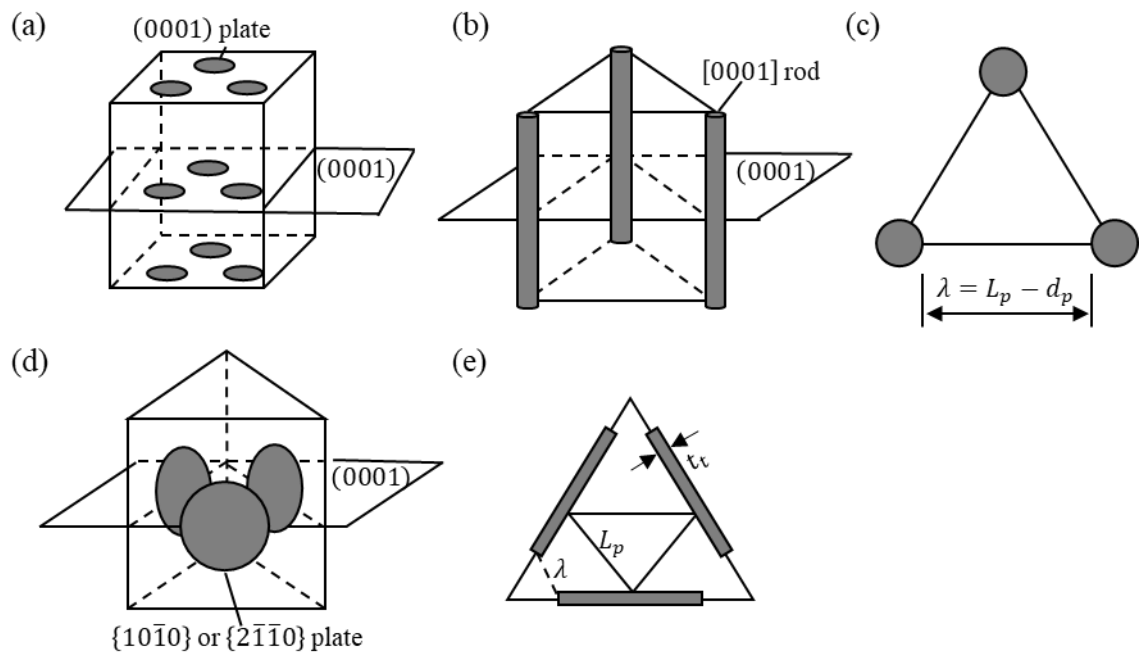


Figure 2.10 Arrangement of precipitates and projection of precipitates on (0001) when precipitates are intersected by (0001). (a) Basal plate-shaped precipitates, (b) rod-shaped precipitates along the c -axis, (c) projection of intersected basal plates or c -axis rods on (0001) plane of α -Mg, (d) $\{10\bar{1}0\}$ or $\{2\bar{1}\bar{1}0\}$ plate-shaped precipitates, and (e) projection of intersected prismatic plates on (0001) of α -Mg [51].

Table 2.5 Different formulas for the effect of interparticle spacing on the Orowan equations for basal slip.

Precipitate morphology	Effective interparticle spacing on (0001) slip plane	Orowan stress σ_{Orowan}	Ref.
Spherical precipitates	$\lambda = \left(\frac{0.779}{\sqrt{f}} - 0.785 \right) d_t$	$\sigma_{Orowan} = \frac{Gb}{2\pi\sqrt{1-\nu} \left(\frac{0.779}{\sqrt{f}} - 0.785 \right) d_t} \ln \frac{0.785d_t}{b}$	Nie et al. [51] assumes a triangular array of precipitates.
Basal plate-shaped precipitates	$\lambda = \left(\frac{0.953}{\sqrt{f}} - 1 \right) d_t$	$\sigma_{Orowan} = \frac{Gb}{2\pi\sqrt{1-\nu} \left(\frac{0.953}{\sqrt{f}} - 1 \right) d_t} \ln \frac{d_t}{b}$	
Prismatic plates	$\lambda = 0.825 \sqrt{\frac{d_t t_t}{f}} - 0.393d_t - 0.886t_t$	$\sigma_{Orowan} = \frac{Gb}{2\pi\sqrt{1-\nu} \left(0.825 \sqrt{\frac{d_t t_t}{f}} - 0.393d_t - 0.886t_t \right)} \ln \frac{0.886\sqrt{d_t t_t}}{b}$	
Rod-shaped precipitates along the c-axis	$\lambda = \left(\frac{0.953}{\sqrt{f}} - 1 \right) d_t$	$\sigma_{Orowan} = \frac{Gb}{2\pi\sqrt{1-\nu} \left(\frac{0.953}{\sqrt{f}} - 1 \right) d_t} \ln \frac{d_t}{b}$	
Basal plate-shaped precipitates	$\lambda = \left(\frac{0.886}{\sqrt{f}} - 1 \right) d_t$	$\sigma_{Orowan} = \frac{Gb}{2\pi\sqrt{1-\nu} \left(\frac{0.886}{\sqrt{f}} - 1 \right) d_t} \ln \frac{d_t}{b}$	

2.4.4 Work hardening

Work hardening describes the fact that the flow stress required for crystal deformation increases with plastic strain. The work hardening behaviour is strongly dependent on the orientation of a single crystal or the texture of polycrystals. The work hardening effect is greatest, for Mg single crystals, if the basal plane is parallel or perpendicular to the tensile axis [5, 63]. For polycrystalline Mg and its alloys, the texture can directly affect work hardening by affecting dislocation storage and dynamic recovery [64].

2.5 Mechanical behaviour of Mg and its alloys

Studies of mechanical behaviour are important for widening the application of Mg alloys as engineering materials. The factors influencing the mechanical behaviour of Mg and its alloys are reviewed in the following sections.

2.5.1 Determining critical resolved shear stress (CRSS)

CRSS is the resolved shear stress necessary to initiate the operation of a slip or twin system. CRSS directly reflects a material's mechanical properties and is not dependent on the applied load or grain orientation. It can be derived via the Schmid factor from the measured yield stress.

The CRSS measurement can be performed either on bulk or micro-specimens. It is difficult to obtain truly single crystalline bulk specimens. The recently developed tension and compression testing of nano-pillars or micro-pillars permits the measurement of the yield stress and analysis of the deformation mechanism for individual slip systems from single crystals from a very restricted material volume. The CRSS values can then be derived via the Schmid factor for each slip system. This method can help us to understand

the deformation mechanisms and mechanical properties at various scales (predominantly at micro- and nanoscales). Pillar testing can be achieved on specific areas or individual grains of a polycrystalline material. However, there is no agreed standard yet for pillar testing because it is a recently developed technology. Several experimental parameters may affect accurate measurement of the strain and stress, such as specimen taper angle and misalignment between the indenter and the pillar [65]. Whatever the disadvantages of micro-pillar testing, it has been permitted for the study of single crystal plasticity data and this method is adopted in the present work.

The CRSS can be influenced by a lot of factors, such as the anisotropy of the deformation systems, deformation temperature, strain rate, solid solution alloying, precipitation and specimen size.

2.5.2 Anisotropy of deformation

The CRSSs for different slip systems in pure Mg and its alloys at room temperature are summarized in Table 2.6 [66]. The data show that $CRSS_{basal} < CRSS_{prismatic} < CRSS_{pyramidal}$. Basal slip is the easiest slip system to activate; the CRSS for basal slip is about 0.50 MPa for single crystal Mg [48, 49]. Prismatic slip is significantly harder to activate with higher CRSS values in the range 7~ 110 MPa. Pyramidal $\langle c + a \rangle$ slip is another slip system hard to activate with CRSS values in the range 60~ 112.5 MPa [67, 68]. The big difference in CRSS values for different slip systems is a measurement of the anisotropy of the HCP structure.

Table 2.6 The CRSSs for different slip systems in Mg at room temperature.

Material/Method	CRSS (MPa)			Ref.
	Basal $\langle a \rangle$	Prismatic $\langle a \rangle$	Pyramidal $\langle c + a \rangle$	
Pure Mg single crystal/microscale tension	0.50	44		Akhtar et al. [48, 49, 69]
Pure Mg single crystal/microscale tensile	0.52			Conrad et al. [70]
Pure Mg single crystal/microscale tension		39		Reed-Hill et al. [71]
Pure Mg single crystal/microscale compression			112.5	Kim [68]
Pure Mg single crystal/in-plane compression	2.3	7.0		Chapuis et al. [72]
Mg-0.018 at.% Al single crystal/ macroscale tensile		40		Akhtar et al. [49, 69]
Mg-0.054 at.% Zn single crystal/microscale tension	0.78	47.6		Akhtar et al. [48, 69]
AZ31 polycrystal/in-plane tension and elastic plastic self-consistent model	10	55	60	Agnew et al. [73]
AZ31 polycrystal /in-plane tension and visco-plastic self-consistent model	45	110		Agnew [74]

2.5.3 Effect of temperature

The CRSSs for different slip systems in pure Mg at different temperatures are shown in Figure 2.11. The data show that basal slip is only slightly dependent on temperature while the prismatic slip and pyramidal slip are more sensitive to temperature change. There are consistent reports that basal slip is not sensitive to temperature change for both pure Mg single crystals and polycrystals [48, 72]. Tension [8] and compression [75] tests have been performed on single crystals to investigate the prismatic slip. Figure 2.11 shows that the CRSS for prismatic slip decreases rapidly with increasing deformation temperature. Figure 2.11 also shows that temperature has a similar effect on pyramidal slip [67]. Thus increasing temperature leads to enhancement of non-basal slip activity.

The CRSSs for $\{10\bar{1}2\}$ twinning in Mg and its alloys at different temperatures are summarized in Figure 2.12. Unlike slip, the twinning stress dependence on temperature is less well understood and there is no agreed conclusion. Christian et al. [12] considered that the twinning stress was slightly positively correlated with temperature for most HCP twinning systems except for $\{10\bar{1}1\}$ twinning. Jain et al. [76] reported that the $\{10\bar{1}2\}$ twinning stress of polycrystalline AZ31 increased slightly over the temperature range from 22°C to 250°C after in plane compression and visco-plastic self-consistent modelling. However, Chapuis et al. [72] reported that the $\{10\bar{1}2\}$ twinning stress of pure Mg single crystals was a little higher at 150 °C than the stress at other temperatures after in plane compression and crystal plasticity modelling, as shown in Figure 2.12.

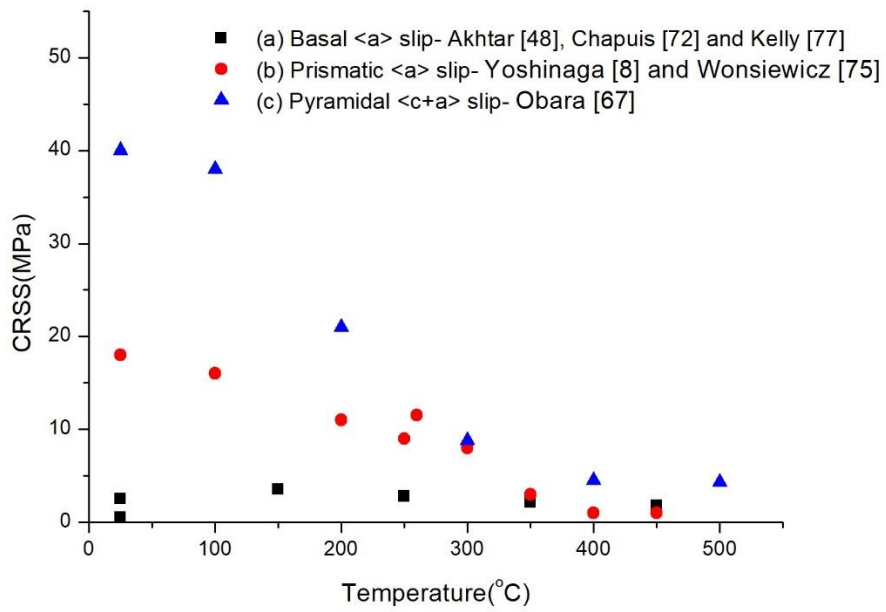


Figure 2.11 The reported CRSSs for different slip systems in pure Mg at different temperatures. (a) Basal $\langle a \rangle$ slip [48, 72, 77], (b) prismatic $\langle a \rangle$ slip [8, 75] and (c) second order pyramidal $\langle c + a \rangle$ slip [67].

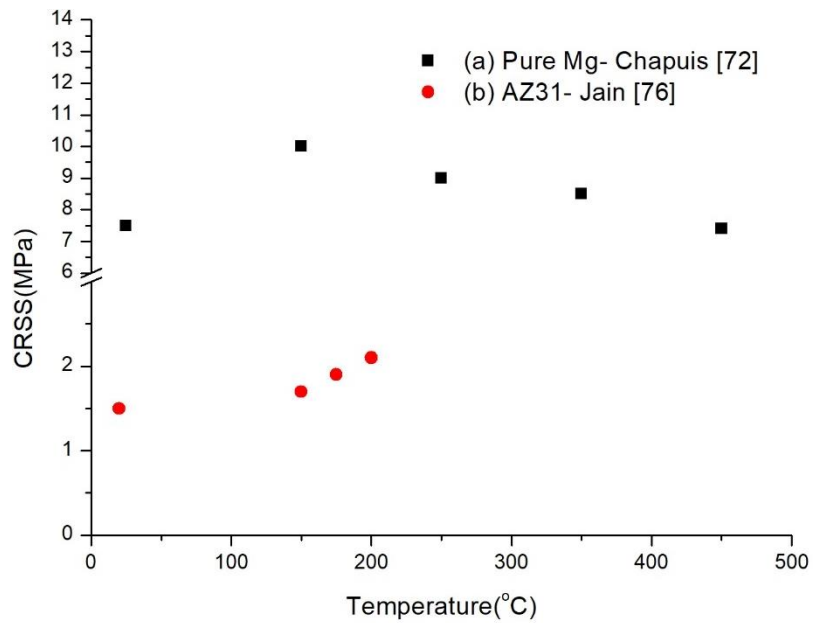


Figure 2.12 The reported CRSSs for $\{10\bar{1}2\}$ twinning in Mg and its alloys at different temperatures [72, 76].

2.5.4 Effect of strain rate

Extensive research has been conducted on the strain rate dependence of the plastic deformation of extruded or cast AZ series alloys. Kurukuri et al. [78] studied the strain rate sensitivity of rolled AZ31B under tensile and compressive loading at room temperature. The tensile stress-strain curves in Figure 2.13(a) show that yield stress is positively correlated with the strain rate. The compressive stress-strain curves in Figure 2.13(b) are initially insensitive to the strain rate, then the work hardening rate increases rapidly under higher strain rate deformation. The work hardening rate change is attributed to that slip dominates deformation after twinning is exhausted. More experiments [79-81] and simulation [81] studies on rolled AZ31 show consistently that the tensile yield stress, compressive yield stress and work hardening rate increase to different extents with increasing strain rate. Increasing the strain rate has the similar effect as reducing the temperature.

$\{10\bar{1}2\}$ twinning's relationship with strain rate at room temperature has also been studied. Yoo [2] believed that deformation twinning in HCP became prevalent only at high strain rates.

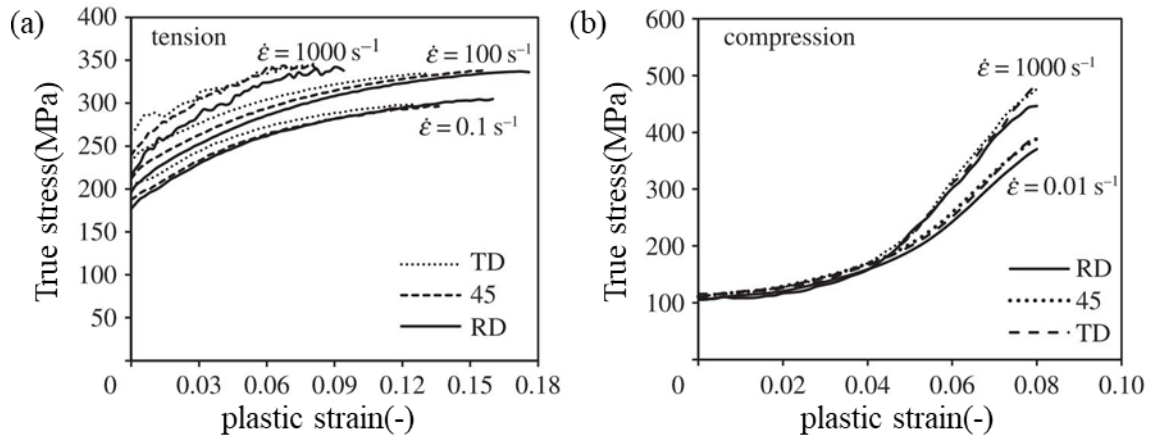


Figure 2.13 True stress-strain curves for rolled AZ31B at different strain rates and for different loading directions. (a) Tensile stress-strain curves and (b) compressive stress-strain curves. [78]

2.5.5 Effect of alloying

Alloying is an important way to tune a material's mechanical properties. The solid solution strengthening effect in HCP alloys is anisotropic.

Basal slip can be strengthened by many solute atoms, such as Zn, Al, In and Sn [48, 49, 82]. Akhtar et al. [48, 49] studied the solid solution strengthening of basal slip by tensile tests on binary Mg-X (X=Zn, Al and In) single crystals. Figure 2.14 shows that CRSSs for basal slip increase with increasing solute concentration. Furthermore, the solid solution strengthening effect is linearly proportional to the concentration (c) of a solute as $c^{2/3}$, as shown in Figure 2.15.

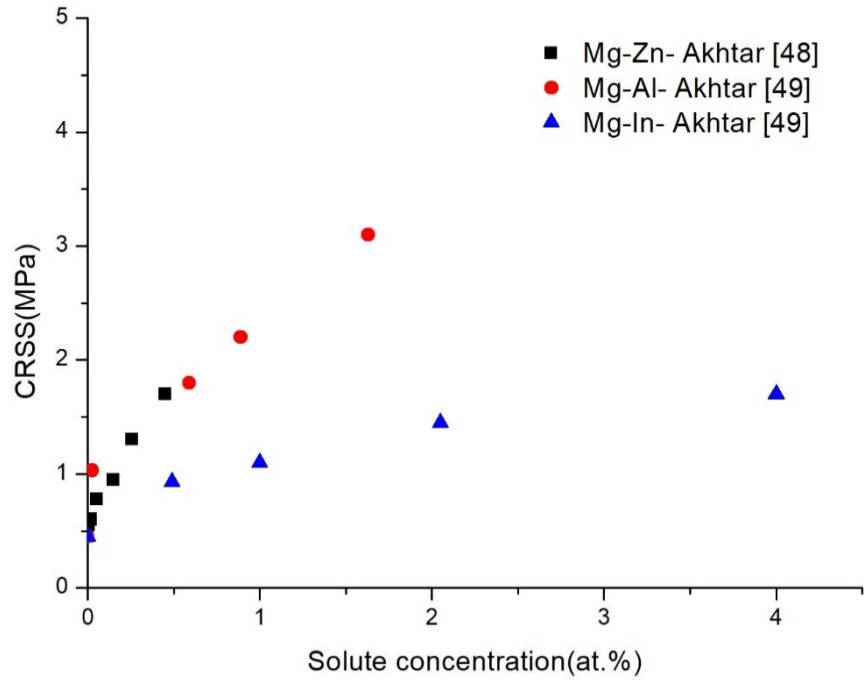


Figure 2.14 The reported CRSSs for basal slip of binary Mg-X (X=Zn, Al and In) at room temperature [48, 49].

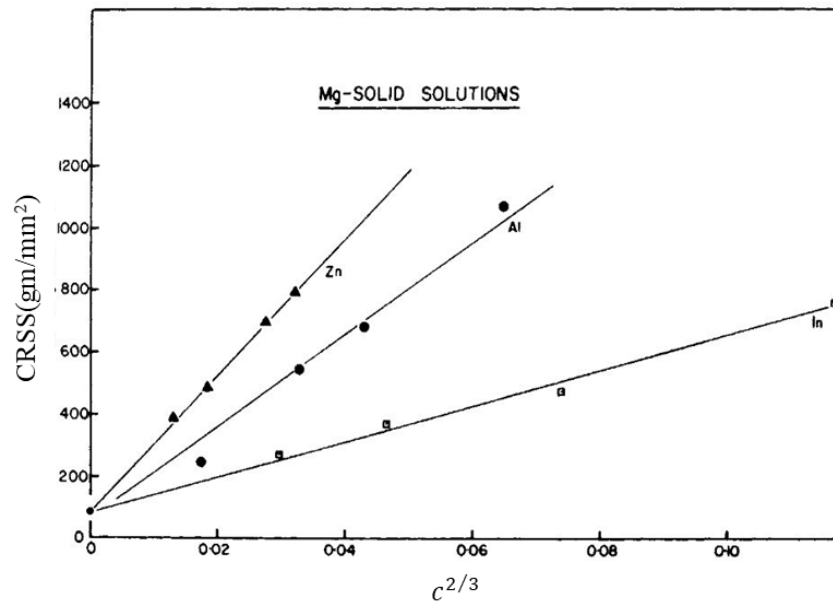


Figure 2.15 CRSS versus $c^{2/3}$ for Zn, Al and In solutes in Mg [49].

Akhtar et al. [69] also studied the solid solution strengthening of prismatic slip by tensile tests on binary Mg-Zn single crystals. Figure 2.16 shows that a small addition of Zn strengthens prismatic slip while a higher concentration then softens prismatic slip. Stanford et al. [83] re-visited Akhtar's work [69] in strongly textured polycrystalline Mg-Zn alloys. Figure 2.17 shows the effect of Zn concentration on the yield stress of prismatic slip for different grain sizes. It can be seen that Zn can soften prismatic slip for large grain sizes (larger than 50 μm) but harden prismatic slip for smaller grain sizes. It is explained that the presence of solute atoms can reduce the stress for cross-slip from prismatic plane to basal plane which is considered as the deformation controlling step in larger grain sizes and in single crystals, so specimens would soften [69]. However, the grain boundary hardening effect is stronger than the solute softening for small grain sizes, so specimens would exhibit hardening [83].

Besides the solid solution strengthening of slip systems, the solid solution strengthening of $\{10\bar{1}2\}$ twinning has also been studied by compression along the rolling direction in highly textured polycrystalline Mg-Zn alloy [83] and weakly textured Mg-Y alloy [84]. For Mg-Zn alloys, the $\{10\bar{1}2\}$ twinning yield stress was found to be insensitive to Zn concentration change from 0 to 2.8 wt.%. For Mg-Y alloys, $\{10\bar{1}2\}$ twinning showed a significant hardening effect as the Y concentration varied from 5 wt.% to 10 wt.%.

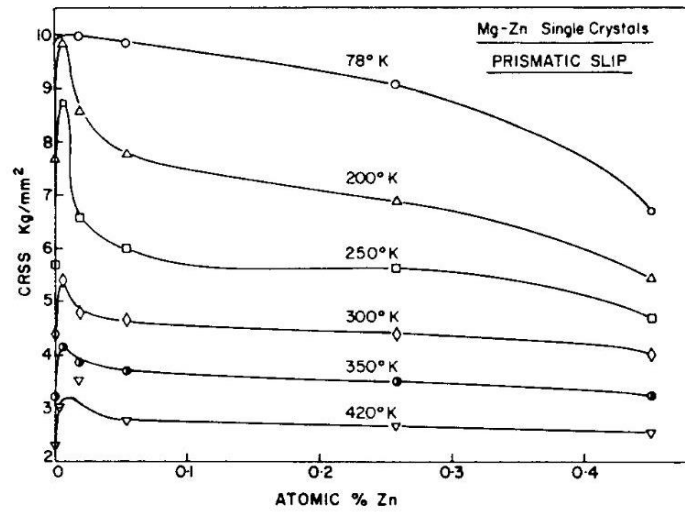


Figure 2.16 The reported CRSSs for prismatic slip of binary Mg-Zn single crystals [69].

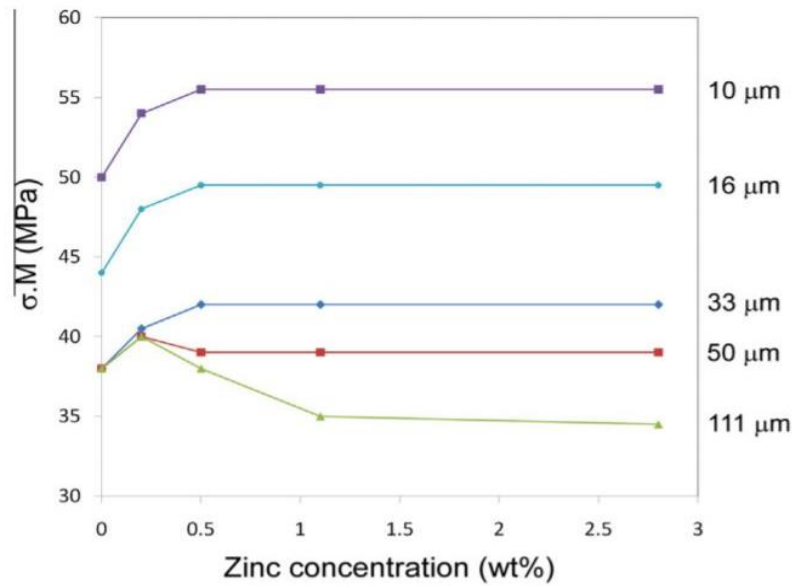


Figure 2.17 The yield stress of prismatic $\langle a \rangle$ slip as a function of Zn concentration for different grain sizes [83].

2.5.6 Effect of precipitation

The influence of precipitate size, distribution and morphology on deformation behaviour has been calculated, which provides useful estimates of the expected strengthening effects of precipitates, and many experimental measurements of the precipitation hardening in Mg alloys have been reported [55, 85-89]. A summary of the CRSS increments is listed in Table 2.7. Different aging times and temperatures are chosen to get a generally homogenous distribution of precipitates and relatively good hardness increment.

The effect of rod-shaped precipitates along the *c*-axis on twinning and slip has been studied in tension in strongly textured Mg-6 wt.% Zn [55] and via micro-pillar compression in Mg-5 wt.% Zn [85]. Precipitates in Mg-Zn cause moderate hardening of basal slip and prismatic slip, but have little effect on second order pyramidal slip. An explanation for this latter effect remains an open question. Also, precipitates in Mg-5 wt.% Zn were found to have little effect on $\{10\bar{1}2\}$ twinning during the micro-pillar compression along $[11\bar{2}0]$. The possible reason is that *c*-axis rod precipitates provide poor obstacles to basal dislocation slip in the twinned crystal. However, precipitates in strongly textured Mg-5 wt.% Zn can increase the twin number density, reduce the twin size and total volume fraction of twins in macroscale tensile tests [90]. It is proposed that basal slip is required to accommodate the twinning shear and that basal slip is hardened by the precipitates. Another study of polycrystalline Mg-5 wt.% Zn showed that the precipitates suppressed twin growth but increased twin nucleation [91]. It indicates that the precipitate effect on deformation is very different between single crystals and polycrystals. A Mg-Y-Nd-Zr alloy has been used to study the effects of plate-shaped precipitates on pyramidal planes on twinning and slip by in-situ neutron diffraction

compression [87]. The precipitates cause strong hardening of the basal slip systems, but do not necessarily increase the stress needed to initiate twinning [87]. For basal plate-shaped precipitates, an AZ91 alloy has been deformed to study the age hardening response of the basal slip and tension twins [88]. They have a poor strengthening effect on basal slip, but increase the hardening effect on twinning. The large basal plate-shaped precipitates can arrest twin growth or be engulfed and rotated by the twin. Also, basal plate-shaped precipitates are effective in hardening the basal slip systems in the twinned crystal where the precipitates become nearly perpendicular to the basal plane.

To sum up, there has been limited study of how precipitates and slip/twinning interact, and how this influence mechanical properties. An improved understanding of precipitate microstructure (such as precipitate size, morphology and orientation) and their effect on the mechanical properties is essential and critical for strengthening the existing Mg alloys and developing new age-hardenable alloys.

Table 2.7 The increment in CRSS for various deformation systems showing the precipitation strengthening effect.

Material/Method	Precipitate morphology	CRSS increment (MPa)				Ref.
		Basal $\langle a \rangle$	Prismatic $\langle a \rangle$	Pyramidal $\langle c + a \rangle$	$\{10\bar{1}2\}$ twinning	
Mg-6 wt.% Zn polycrystals/aging at 200°C for 8 hrs, macroscale tension	Rod-shaped precipitates along the c -axis	50	39			Jain et al. [55]
Mg-5 wt.% Zn single crystal /aging at 150°C for 8 days, micro-pillar compression along particular crystal direction	Rod-shaped precipitates along the c -axis	17		-43	1	Wang et al. [85]
Mg-1 wt.% Mn-1 wt.% Nd polycrystal/aging at 275°C for 5 hrs	Prismatic plate-shaped precipitates	37	23	42	3.5	Hidalgo-Manrique et al. [86]
Mg-Y-Nd-Zr alloy /aging at 250°C for 16 hrs, in-situ neutron diffraction compression	Prismatic plate-shaped precipitates	18	8	0	0	Agnew et al. [87]
AZ91/ aging at 200°C for 30 hrs, macroscale tension and compression	Basal plate-shaped precipitates	5	29		22	Stanford et al. [88]
AZ91/aging at 200°C for 30 hrs, macroscale tension and compression	Basal plate-shaped precipitates	5~8			36	Kada et al. [89]

2.5.7 Specimen size effect

Size effects at the sub-micron scale are receiving more attention as micro- and nano-testing develops. This phenomenon was firstly reported by Uchic et al. [92] for pure Ni and Ni-based alloys. In the experiment, micro-pillars of diameters from 0.5 to 40 μm were machined by Focused Ion Beam (FIB) and compressed by a flat-punch indentation tip. The micro-pillar compression indicates that the plastic deformation was strongly affected by the specimen dimensions. Subsequently, the method has been exploited to study the size effect in different crystallographic structured metals [93-95] and amorphous [96-99] materials.

The size effect in Mg has also been studied by the micro-pillar compression. Lilleodden [100] activated pyramidal $\langle c + a \rangle$ slip by pillar compression along [0001] of pure Mg single crystals, and found that yield stresses increased with decreasing pillar diameter from 10.0 μm to 2.1 μm . Ye et al. [101] activated basal slip and $\{10\bar{1}2\}$ twinning by in-situ TEM nano-pillar compression of Mg and Mg-0.2 wt.% Ce, and found that that a higher yield stress was required for smaller nano-pillars for both deformation modes. Kim [68] studied the size effect of basal and pyramidal slip and of $\{10\bar{1}2\}$ twinning by in-situ SEM micro-pillar compression of pure Mg. A size effect existed in all deformation modes, but the magnitude is different for different deformation modes.

The specimen size effect can be summarized as ‘smaller is stronger’. It can be rationalized by the dislocation starvation theory [94]. For smaller specimens, mobile dislocations have a higher chance to escape from the specimen free surface, leaving a lower density of dislocations in the specimen. The specimen reaches a dislocation-starved state when the existing dislocation sources are exhausted. Then, a higher applied stress is required to

activate new dislocations to achieve further deformation. The size effect can also be rationalized by the dislocation source truncation theory [102], the geometrically necessary dislocations (GND) [103] and changes in the dislocation forest [104].

2.6 In-situ tests

Conventional mechanical tests, such as tensile tests, compression tests and bending tests, are generally carried out outside the scanning electron microscope (SEM) or transmission electron microscope (TEM) chamber because of the size of the testing instruments and control systems. SEM and TEM are only performed before or after the deformation to image the microstructure evolution. This post-mortem SEM/TEM method lacks the time resolution to investigate the dynamic process which may contain abundant interesting phenomena.

Some commercial in-situ SEM/TEM mechanical test systems have been developed by companies such as Hysitron, Alemnis, Deben and MTI Instruments. With the help of these in-situ test systems, researchers have the opportunity to observe the real-time response of materials, especially in-situ TEM. In-situ TEM mechanical tests can video the defects' evolution and crystallographic change during the deformation process and record the mechanical response from the specimen. This contributes to a deeper understanding of mechanical behaviour and the corresponding deformation mechanisms.

Minor et al. [105] studied the onset of plasticity in a Al single grain by in-situ TEM nanoindentation. They showed direct evidence that plastic deformation can initiate at very small forces in a dislocation-free grain, as shown in Figure 2.18; the corresponding transient is arrowed '1' in Figure 2.19. The shear stresses associated with these very small

applied forces is close to the theoretical shear strength of Al. This study provided direct evidence for the earlier molecular dynamics simulation results, implying that a shear stress close to the theoretical shear strength of a perfect defect-free lattice could be achieved at the onset of plasticity. Shan et al. [106] reported the mechanical annealing phenomenon by in-situ TEM nano-pillar compression of single crystal Ni. Figure 2.20 shows dark-field TEM images of a nano-pillar. It can be seen that the nano-pillar contains a high density of pre-existing dislocations and FIB-induced damage, but becomes dislocation-free after compression. This provides direct evidence for the dislocation starvation hypothesis, which was used to explain the size effect in small specimens. Yu et al. [107] studied the nucleation and growth of deformation twinning by in-situ TEM tests on single crystal Mg. They showed real-time observations of twinning embryos which included an array of twin-related laths on the scale of several nanometres. All these breakthroughs made using in-situ tests can improve the fundamental understanding of deformation and provide useful information for simulation.

However, there are still limitations to in-situ testing. The dimensions of the specimens in this technique is more limited than specimens in conventional methods. For example, the specimens for in-situ TEM tests should be transparent to electrons. The micro- or nano-scale specimen is usually prepared using FIB milling. FIB preparation has a great influence on the specimen quality, such as surface damage, taper angle and roughness. These can influence the mechanical response of the specimen. Whatever the disadvantage of in-situ testing, it has been exploited for availability of single crystal plasticity data and this method is adopted in the present work.

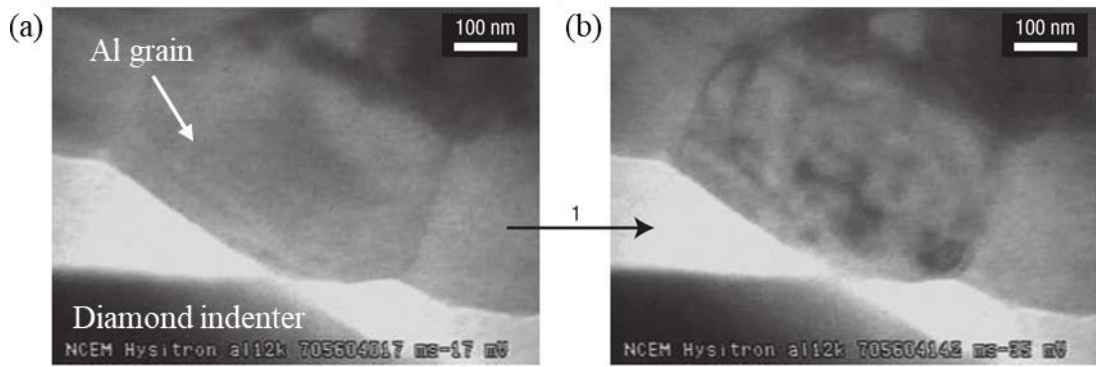


Figure 2.18 Bright-field TEM images of the generation of dislocations in an Al grain by in-situ TEM nanoindentation. (a) Image taken prior to the deformation, showing the dislocation-free region and (b) image extracted from the video corresponding to the transient arrowed '1' in Figure 2.19 [105].

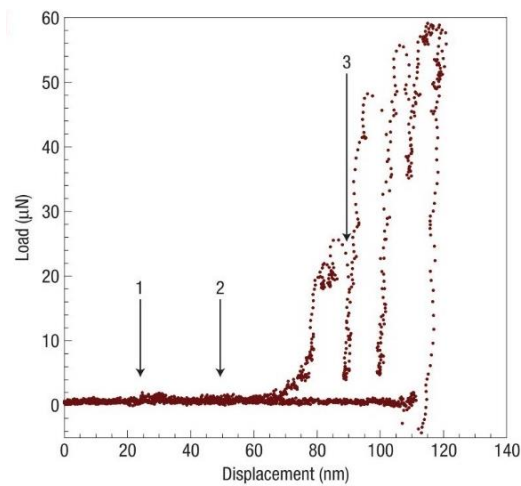


Figure 2.19 The load-displacement curve obtained from the in-situ TEM nanoindentation shown in Figure 2.18 [105].

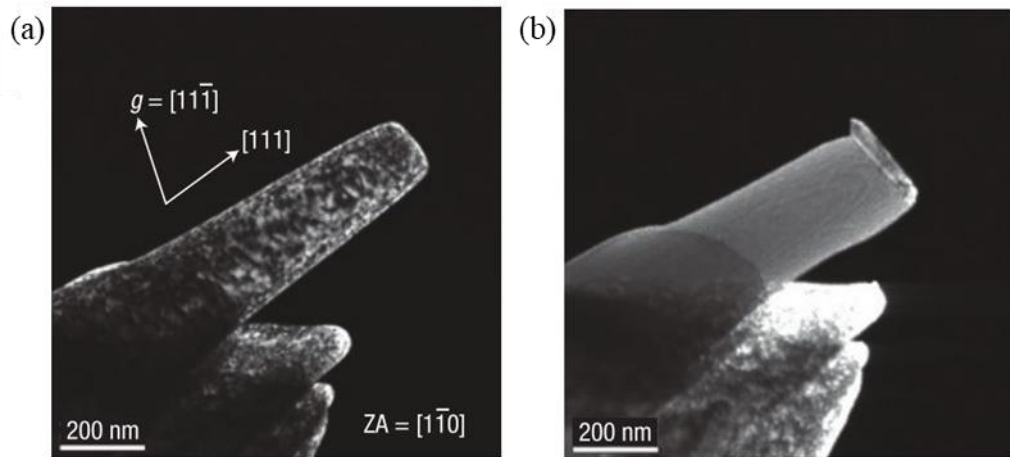


Figure 2.20 Dark field TEM images of single crystal Ni nano-pillar. Loading direction is $[111]$. Beam direction is $[1\bar{1}0]$. (a) Image taken before the compression, showing a large density of dislocations in the specimen. (b) Image taken after first compression, showing the dislocation-free state [106].

2.7 Aims and objectives

The aim of this project is to investigate how the precipitates interact with basal slip and tension twinning, and how this influences mechanical properties.

- (i) Micro-pillars from the solution treated and peak-aged AZ91 will be compressed along the $[55\bar{1}09]$ direction. The CRSS values, surface morphology and post-mortem TEM observations will provide an understanding of the effect of the precipitates on basal slip.
- (ii) Micro-pillars from the solution treated and peak-aged AZ91 will be compressed along the $[01\bar{1}0]$ direction. The apparent CRSS values, first twin nucleation stress, surface morphology, Transmission Kikuchi Diffraction (TKD) and post-mortem

TEM observations will help understand the influence of precipitates on tension twinning and deformation systems inside the twin.

- (iii) Submicron-pillars from the solution treated and under-aged AZ91 will be compressed in the TEM along the $[01\bar{1}0]$ direction. The in-situ videos recording the twinning and the correlated mechanical data will give a deeper understanding of the nucleation and growth of tension twins in the presence and otherwise of precipitates.

3 Experimental

In order to study the precipitate interaction with slip and twinning, a suitable heat treatment has been devised. This provides a precipitate-free specimen and a specimen in the presence of precipitates. Subsequently, micro-pillars and submicron-pillars from selected grains have been machined, deformed and characterised by different techniques.

3.1 Raw material

A commercially supplied as-cast AZ91 alloy ingot with dimensions of 550 mm × 50 mm × 50 mm has been used in this work. The actual chemical composition was analyzed by energy-dispersive X-ray (EDX) on a Tescan SEM.

Table 3.1 The chemical composition of as-cast AZ91 used in the present work.

	Al	Zn	Mn	Mg
wt. %	8.9	0.7	0.2	Balance

3.2 Heat treatment

Specimens with dimensions of 10 mm × 10 mm × 10 mm were cut from the ingot. The specimen was sealed into a glass tube filled with argon to minimize oxidation during solution treatment. The specimen was then solution treated at 415°C for 96 hours and subsequently quenched into water. The solution treated specimen was aged at 200°C for various times.

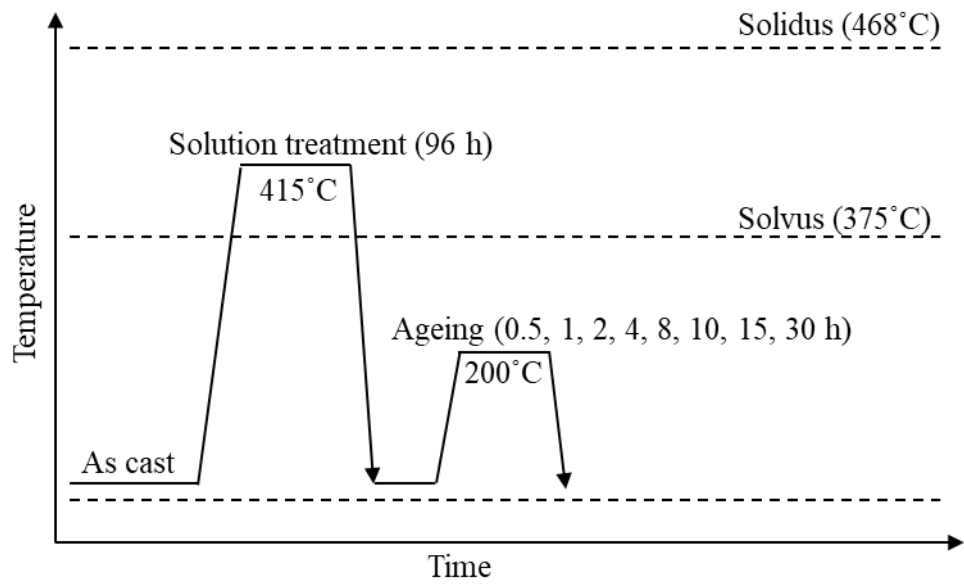


Figure 3.1 A schematic illustration showing the heat treatment procedure.

3.3 Hardness testing

Vickers hardness test was performed on the well-polished surface using a Mitutoyo MVK-H1 micro-hardness testing machine. The hardness of the aged AZ91 (aging from 0.5 h to 30 h) was measured under a load of 100 g.

3.4 Precipitate number density

The number density per unit volume (N_V) can be calculated as:

$$N_V = \frac{N_S}{t} \quad \text{Equation 3.1}$$

N_S is the number of the precipitates per unit area in projection, and t is the thickness of the specimen. N_S can be obtained by counting the number of precipitates over a given area and thickness of the specimen. Specimen thickness can be measured by several techniques, such as thickness fringes, electron energy loss spectroscopy (EELS) and

convergent electron beam diffraction (CBED) [108, 109]. CBDE is the most popular and accurate technique for the determination of crystalline specimen thickness.

3.4.1 Foil thickness measurement

The equation for thickness determination by CBED is [108]:

$$\left(\frac{s_i}{n_i}\right)^2 + \left(\frac{1}{n_i}\right)^2 \left(\frac{1}{\xi_g}\right)^2 = \frac{1}{t^2} \quad \text{Equation 3.2}$$

where s_i is the deviation from the Ewald sphere at the i^{th} fringes, n_i is an integer, ξ_g is the extinction distance and t is the thickness. s_i can be determined by direct measurement of the spacing of the fringes in the convergent beam pattern and it can then be calculated via:

$$s_i = \frac{\lambda}{d^2} \left(\frac{\Delta\theta_i}{2\theta_B}\right) \quad \text{Equation 3.3}$$

where λ is the wavelength of the incident electrons, d is the plane spacing of the operating reflection, $\Delta\theta_i$ is the angle from the Bragg position of the i^{th} fringe, θ_B is the Bragg angle for the diffracting planes. Plotting $\left(\frac{s_i}{n_i}\right)^2$ versus $\left(\frac{1}{n_i}\right)^2$ where i is chosen to obtain a straight line, the slope of the line represents $\frac{1}{\xi_g^2}$ and the intercept with the $\left(\frac{s_i}{n_i}\right)^2$ axis corresponds to $\frac{1}{t^2}$. Thus the thickness t is obtained. Figure 3.2 shows the thickness determination using CBED.

In the present work, thickness measurements were carried out near the $[2\bar{1}\bar{1}0]$ zone axis using $g = 02\bar{2}1$.

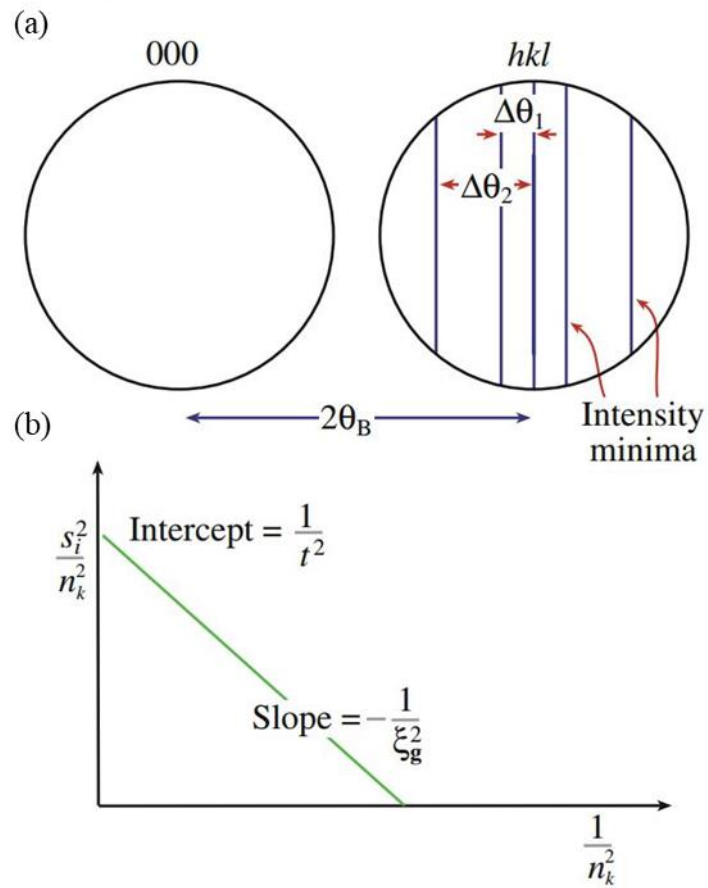


Figure 3.2 Schematic illustrations showing the foil thickness determination using CBED centred at the Bragg position. (a) The parameter measurements from Kossel-Möllenstedt (K-M) fringes. The deviations s_i is determined by measured $\Delta\theta_i$. (b) Plot of $(s_i/n_i)^2$ versus $(1/n_i)^2$.

3.4.2 Precipitate dimension measurement

In the present study, TEM bright field images have been used to count the number of precipitates and measure the precipitate dimensions. All the images were taken close to zone axes $\langle 1\bar{2}10 \rangle$ or $[0001]$. The normal directions of the foils of all the specimens used in the present work are within 10° from $\langle 1\bar{2}10 \rangle$ or $[0001]$.

3.5 EBSD mapping and Schmid factor calculation

The identification of crystal orientation was carried out by electron back-scattered diffraction (EBSD) system in a TESCAN Mira-3 microscope. Grains of selected directions were chosen to activate basal $\langle a \rangle$ slip or $\{01\bar{1}2\}$ twinning.

In the four-axis HCP notation, the Schmid factor m is calculated as:

$$m = \cos \varphi \cos \lambda$$

$$= \frac{h_1 u_1 + k_1 v_1 + i_1 t_1 + \frac{3c^2}{2a^2} l_1 w_1}{\sqrt{\left(h_1^2 + k_1^2 + i_1^2 + \frac{3c^2}{2a^2} l_1^2\right) \left(u_1^2 + v_1^2 + t_1^2 + \frac{3c^2}{2a^2} w_1^2\right)}} \frac{u_1 u_2 + v_1 v_2 + t_1 t_2 + \frac{2c^2}{3a^2} w_1 w_2}{\sqrt{\left(u_1^2 + v_1^2 + t_1^2 + \frac{2c^2}{3a^2} w_1^2\right) \left(u_2^2 + v_2^2 + t_2^2 + \frac{2c^2}{3a^2} w_2^2\right)}} \quad \text{Equation 3.4}$$

where φ is the angle between the loading direction $[u_1 v_1 t_1 w_1]$ and the slip plane normal $[h_1 k_1 i_1 l_1]$ and λ is the angle between the loading direction $[u_1 v_1 t_1 w_1]$ and the slip direction $[u_2 v_2 t_2 w_2]$. $c/a = 1.6236$ for Mg [110].

The normal directions of the selected grains (i.e. loading directions during the compression), the expected slip systems and the associated Schmid factors are shown in Table 3.2. $1/3[11\bar{2}0](0001)$ slip is expected to be activated when a specimen is loaded along $[55\bar{1}0\ 9]$. $[01\bar{1}1](0\bar{1}12)$ and $[0\bar{1}11](01\bar{1}2)$ twinning are both expected when the specimen is loaded along $[01\bar{1}0]$.

Table 3.2 Schmid factors for possible deformation systems in HCP Mg with loading directions along $[55\bar{1}0\ 9]$ and $[01\bar{1}0]$. The highest Schmid factors are in red.

Slip system	Slip direction	Slip plane	Loading direction	
			$[55\bar{1}0\ 9]$	$[01\bar{1}0]$
Basal $\langle a \rangle$ slip	$[11\bar{2}0]$	(0001)	0.499	0.000
	$[1\bar{2}10]$	(0001)	0.250	0.000
	$[\bar{2}110]$	(0001)	0.250	0.000
Prismatic $\langle a \rangle$ slip	$[11\bar{2}0]$	($1\bar{1}00$)	0.000	0.433
	$[1\bar{2}10]$	($10\bar{1}0$)	0.233	0.433
	$[\bar{2}110]$	($01\bar{1}0$)	0.233	0.000
Pyramidal $\langle a \rangle$ slip	$[11\bar{2}0]$	($1\bar{1}01$)	0.236	0.382
	$[11\bar{2}0]$	($\bar{1}101$)	0.236	0.382
	$[1\bar{2}10]$	($10\bar{1}1$)	0.314	0.382
	$[1\bar{2}10]$	($\bar{1}011$)	0.079	0.382
	$[\bar{2}110]$	($01\bar{1}1$)	0.314	0.000
	$[\bar{2}110]$	($0\bar{1}11$)	0.079	0.000
First pyramidal $\langle c + a \rangle$ slip	$[\bar{1}\bar{1}23]$	($10\bar{1}1$)	0.190	0.201
	$[\bar{1}\bar{1}23]$	($01\bar{1}1$)	0.190	0.401
	$[11\bar{2}3]$	($\bar{1}011$)	0.212	0.201
	$[11\bar{2}3]$	($0\bar{1}11$)	0.212	0.401

	$[\bar{1}\bar{2}\bar{1}3]$	$(0\bar{1}11)$	0.171	0.401
	$[\bar{1}\bar{2}\bar{1}3]$	$(1\bar{1}01)$	0.257	0.201
	$[1\bar{2}\bar{1}3]$	$(\bar{1}101)$	0.133	0.201
	$[1\bar{2}\bar{1}3]$	$(01\bar{1}1)$	0.355	0.401
	$[\bar{2}\bar{1}13]$	$(1\bar{1}01)$	0.133	0.000
	$[\bar{2}\bar{1}13]$	$(10\bar{1}1)$	0.355	0.000
	$[2\bar{1}\bar{1}3]$	$(\bar{1}101)$	0.257	0.000
	$[2\bar{1}\bar{1}3]$	$(\bar{1}011)$	0.171	0.000
	$[11\bar{2}3]$	$(\bar{1}\bar{1}22)$	0.237	0.335
	$[\bar{1}\bar{1}\bar{2}3]$	$(11\bar{2}2)$	0.211	0.335
Second pyramidal	$[1\bar{2}\bar{1}3]$	$(\bar{1}\bar{2}\bar{1}2)$	0.272	0.335
$\langle c + a \rangle$ slip	$[\bar{1}\bar{2}\bar{1}3]$	$(1\bar{2}\bar{1}2)$	0.048	0.335
	$[\bar{2}\bar{1}13]$	$(2\bar{1}\bar{1}2)$	0.272	0.000
	$[2\bar{1}\bar{1}3]$	$(\bar{2}112)$	0.048	0.000
	$[10\bar{1}1]$	$(\bar{1}012)$	0.079	0.125
	$[\bar{1}011]$	$(10\bar{1}2)$	0.021	0.125
Tension twinning	$[0\bar{1}\bar{1}1]$	$(01\bar{1}2)$	0.021	0.499
	$[01\bar{1}1]$	$(0\bar{1}12)$	0.079	0.499
	$[\bar{1}\bar{1}01]$	$(1\bar{1}02)$	0.242	0.125
	$[1\bar{1}01]$	$(\bar{1}102)$	0.242	0.125

3.6 Micro-mechanical testing

3.6.1 Micro-pillar fabrication

Square micro-pillars were fabricated using a focused ion beam (FIB) microscope (FEI Quanta 3D FEG) from grains of selected orientations. The nominal dimensions of the micro-pillars are $4.5\ \mu\text{m} \times 4.5\ \mu\text{m} \times 9\ \mu\text{m}$, as illustrated in Figure 3.3. Annular cutting was employed for rough milling at 30 kV voltage and 5~ 30 nA current, and rectangular cutting was employed for the fine milling at 30 kV voltage and 30 pA~ 1 nA current. The specimen was tilted $\pm 2^\circ$ from 52° to minimize the taper angle during the rectangular cutting. This is an easy way to minimize the taper angle and thus reduce the influence on the deformation behaviour.

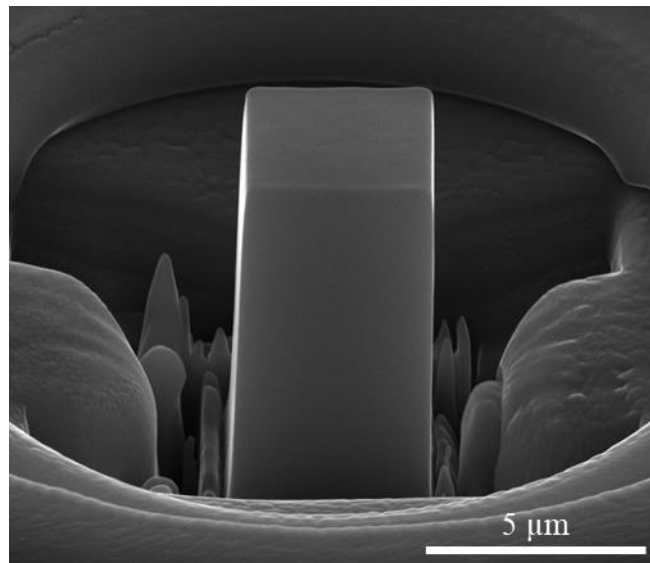


Figure 3.3 A SEM image of a micro-pillar prepared by FIB milling. The image was taken at a tilt of 52° .

3.6.2 Micro-pillar compression in SEM

Compression tests were carried out using a Hysitron PI85 Picoindenter with a flat punch under displacement-control mode in a TESCAN Mira-3 microscope. The micro-pillars were compressed to varying maximum strains at an initial strain rate of $2 \times 10^{-3} \text{ s}^{-1}$.

Misalignment between the compression direction and the micro-pillar axis is an outstanding issue for micro-pillar compression and can result in a non-uniaxial stress state. The misalignment is likely because of the misalignment of the diamond tip axis and micro-pillar axis. In order to have a view of the micro-pillar during compression, the whole stage shown in Figure 3.4 is tilted 20° before compression; the relative positions of diamond tip and micro-pillar are shown in Figure 3.5. The diamond tip bottom surface cannot be seen which makes it difficult to align the diamond tip axis and micro-pillar axis. Figure 3.6 shows the alignment of the diamond tip and micro-pillar at 20° . The diamond tip was moved to touch the lower edge of the micro-pillar. Then the diamond tip was moved a distance equal to the radius of the diamond tip surface along the black arrow direction.

Apart from the above reason, misalignment may be due to the specimen surface not being parallel to the mount when it is mounted into the FIB before micro-pillar fabrication. Some amount of misalignment is unavoidable. What can be done is to minimize it.

In order to guarantee the repeatability of the experiments, at least 8 micro-pillars from each specimen were compressed.

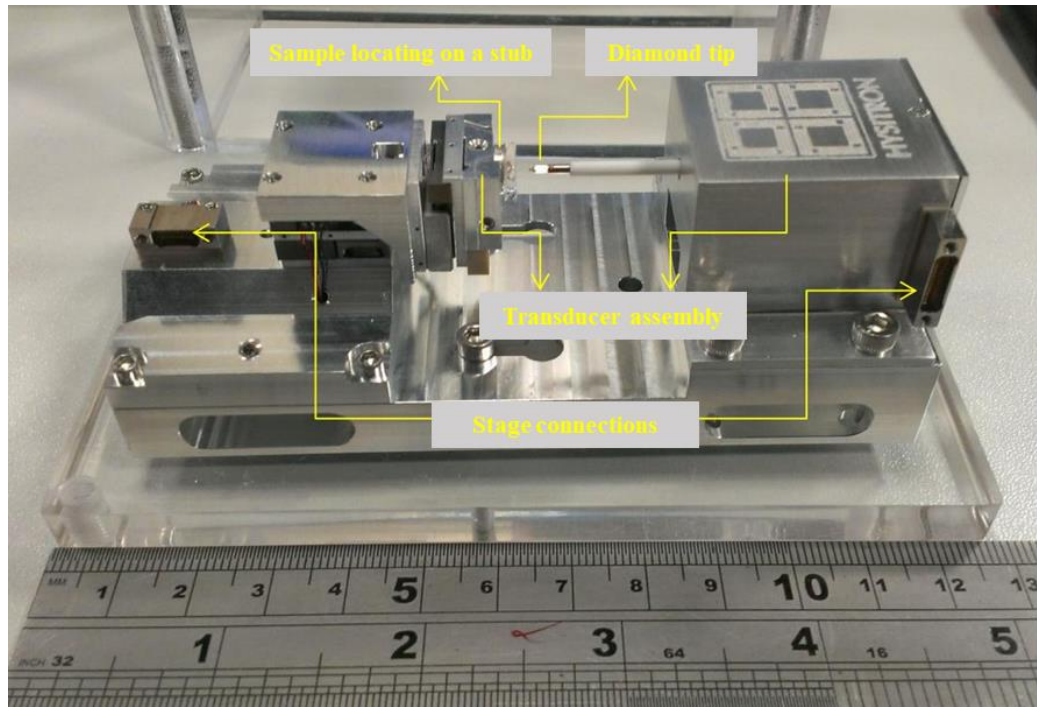


Figure 3.4 Hysitron PI85 Picoindenter system.

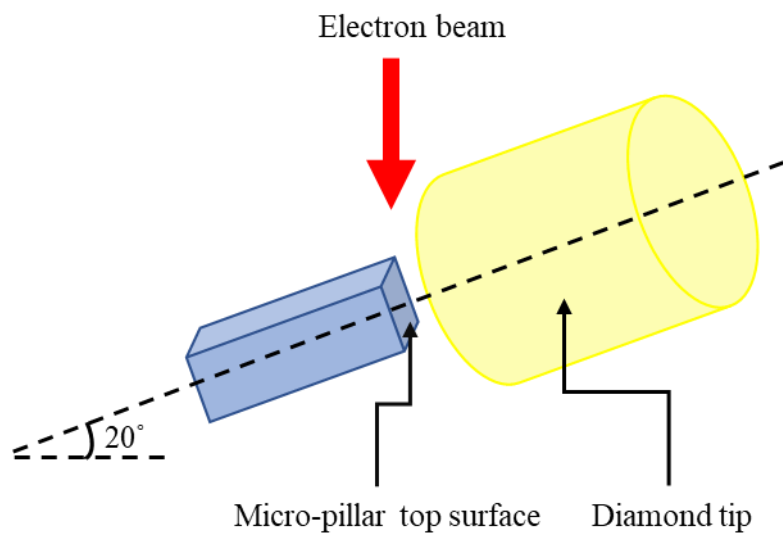


Figure 3.5 The positions of the micro-pillar and diamond tip after the whole stage is tilted by 20° . The micro-pillar top surface can be seen by the electron beam. However, the centre of the diamond tip cannot be seen.

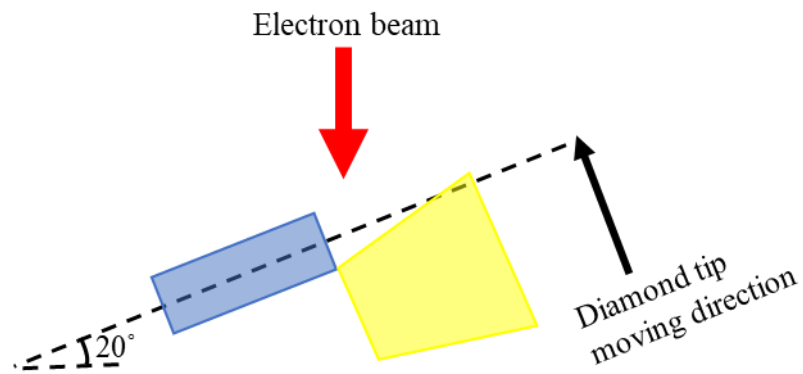


Figure 3.6 Two dimensional schematic diagram showing the alignment of the diamond (yellow trapezium) and the micro-pillar (blue rectangle) at 20° tilt. The diamond tip just touched the lower edge of the micro-pillar.

3.7 Submicron-sized mechanical testing

3.7.1 Pillar fabrication

Submicron-sized pillars of selected orientations were fabricated using a FIB microscope (Helios G4 PFIB CXe) from a large foil with dimensions of $60\ \mu\text{m} \times 60\ \mu\text{m} \times 8\ \mu\text{m}$. The large foil was lifted out from grains of selected orientations in bulk samples and welded to a copper grid. The detailed lifting out and welding procedures are described in section 3.8.

The copper grid was glued to a copper mount for in-situ TEM using silver paint and colloidal graphite. Then the copper mount was glued to a 38° SEM pre-tilted holder. The whole was installed into an FIB chamber for pillar fabrication. Since the angle between the ion beam and electron beam is 52°, the large foil was parallel to the ion beam. The foil was thinned from both sides with ion beam current from 1 nA to 0.3 nA until the foil was thinner than 1 μm . The stage was rotated by 180° and tilted by 14°, so that the foil

was perpendicular to the ion beam. The rough shape of the compression bar was machined using 0.1 nA ion beam current. The foil was further thinned with 30 pA and 10 pA current when the foil was parallel to the ion beam and machined to the designed size of the pillar with 10 pA current when the foil was perpendicular to the ion beam. The relative positions of the foil and the ion beam are shown in Figure 3.7.

The dimension of the freestanding pillar is 1400 ~ 1800 nm in height, 700 ~ 900 nm in width and about 300 nm in thickness, as shown in Figure 3.8.

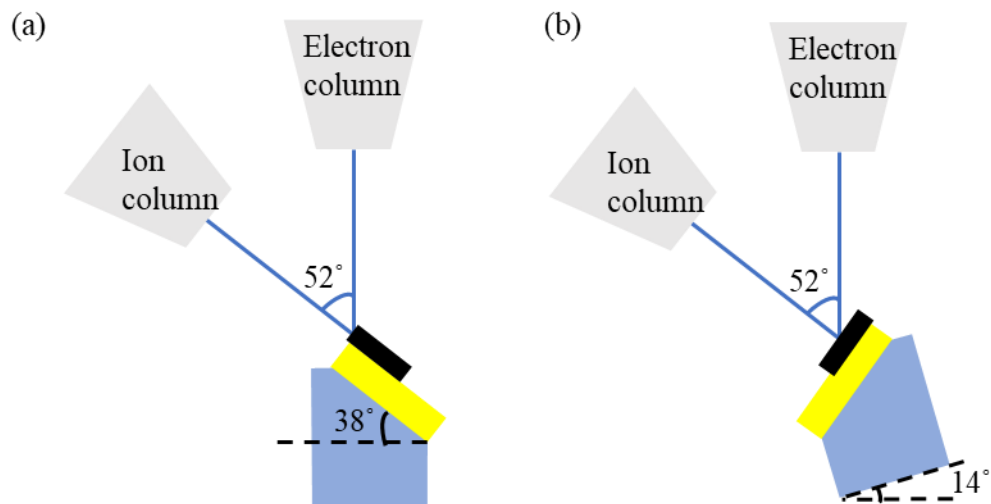


Figure 3.7 (a) The foil is parallel to the ion beam in order to thin the foil. (b) The foil is perpendicular to the ion beam in order to shape the compression bar. The specimen is indicated by the black rectangle, the specimen mount is indicated by the yellow rectangle and the pre-tilted holder is indicated by the blue near-trapezium.

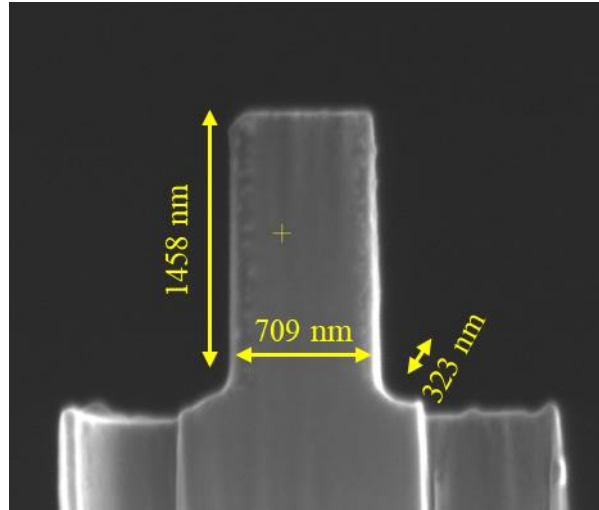


Figure 3.8 A SEM image of a submicron-pillar prepared by FIB milling. Image is taken at a tilt of 52°. The dimensions of this pillar are labelled.

3.7.2 In-situ TEM compression

Compression tests were performed using a Hysitron PI95 Picoindenter system (Figure 3.9) with a flat punch in a JEOL-2100 TEM operating at 200 kV. The pillars were compressed to different maximum strains with a displacement rate of 5 nm/s.

Figure 3.10 shows the TEM image of the pillar before testing. The orthogonal orientation of the pillar is confirmed by the inset diffraction pattern $[\bar{2}110]$. The loading direction is along $[01\bar{1}0]$.

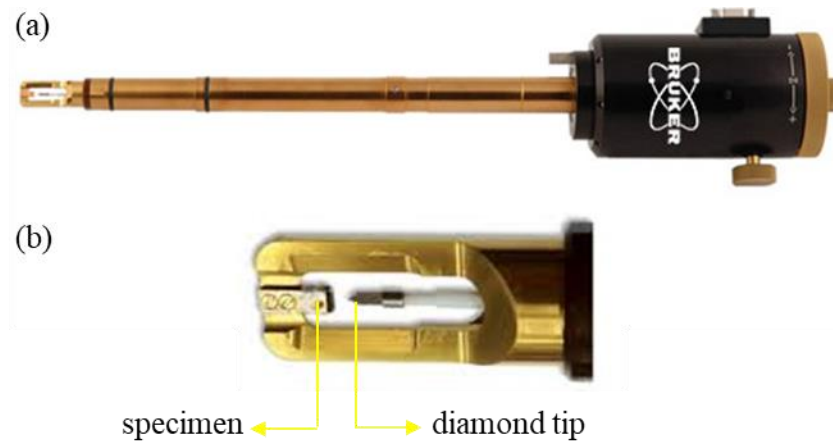


Figure 3.9 (a) Hysitron PI95 Picoindenter. (b) Holder of PI95.

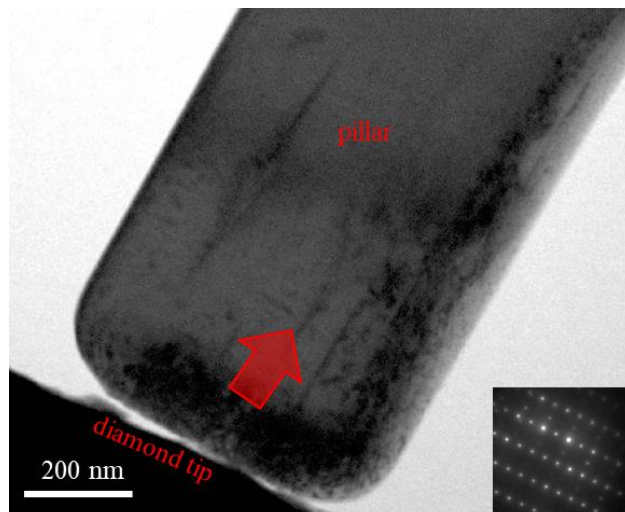


Figure 3.10 (a) A $01\bar{1}1$ reflection TEM bright field image showing the position of the diamond tip and the pillar. The red arrow indicates the loading direction. The inset diffraction pattern is taken along $[\bar{2}110]$ zone axis, and the extra spots are from diffraction by precipitates in this submicron-pillar.

3.8 TEM specimen preparation from deformed micro-pillars

After micro-pillar compression, TEM foils were extracted from the deformed micro-pillars to investigate the dislocation/twin activities and the interaction between precipitates and dislocations/twins. TKD was also performed on the TEM foil to investigate the deformation associated with the twinning.

TEM foils were extracted along the pillar axis by FIB cross-sectional cutting, and the foil preparation procedure was as follows:

- (1) Platinum was deposited on the top and side surfaces of the micro-pillar to form a protective layer. (Figure 3.11(b))
- (2) Rectangular cross-section cutting was performed on each side of the micro-pillar. The foil to be lifted out is about 2 μ m thick. (Figure 3.11(c))
- (3) The through-section cutting (U-cut pattern) was performed to free the lamella from the bulk, leaving one small attachment. (Figure 3.11(d))
- (4) The lamella was lifted out using the Omniprobe. The Omniprobe approaches the top of the lamella and they are attached together by platinum deposition. Then the lamella is cut off from the bulk and lifted out. (Figure 3.11(e))
- (5) The lamella was attached to a copper grid by platinum deposition. Then the probe is detached from the lamella and retracted. (Figure 3.11(f-h))
- (6) The lamella was thinned from both sides until the thickness was around 400 nm. Then final cleaning was performed using low voltage (5 kV) and low current (48 pA) FIB milling to reduce the Ga-induced damage layer. Alternatively, final cleaning was performed to with Xe source milling (Helios G4 PFIB) instead of Ga source milling (FEI Quanta 3D). (Figure 3.11(i))

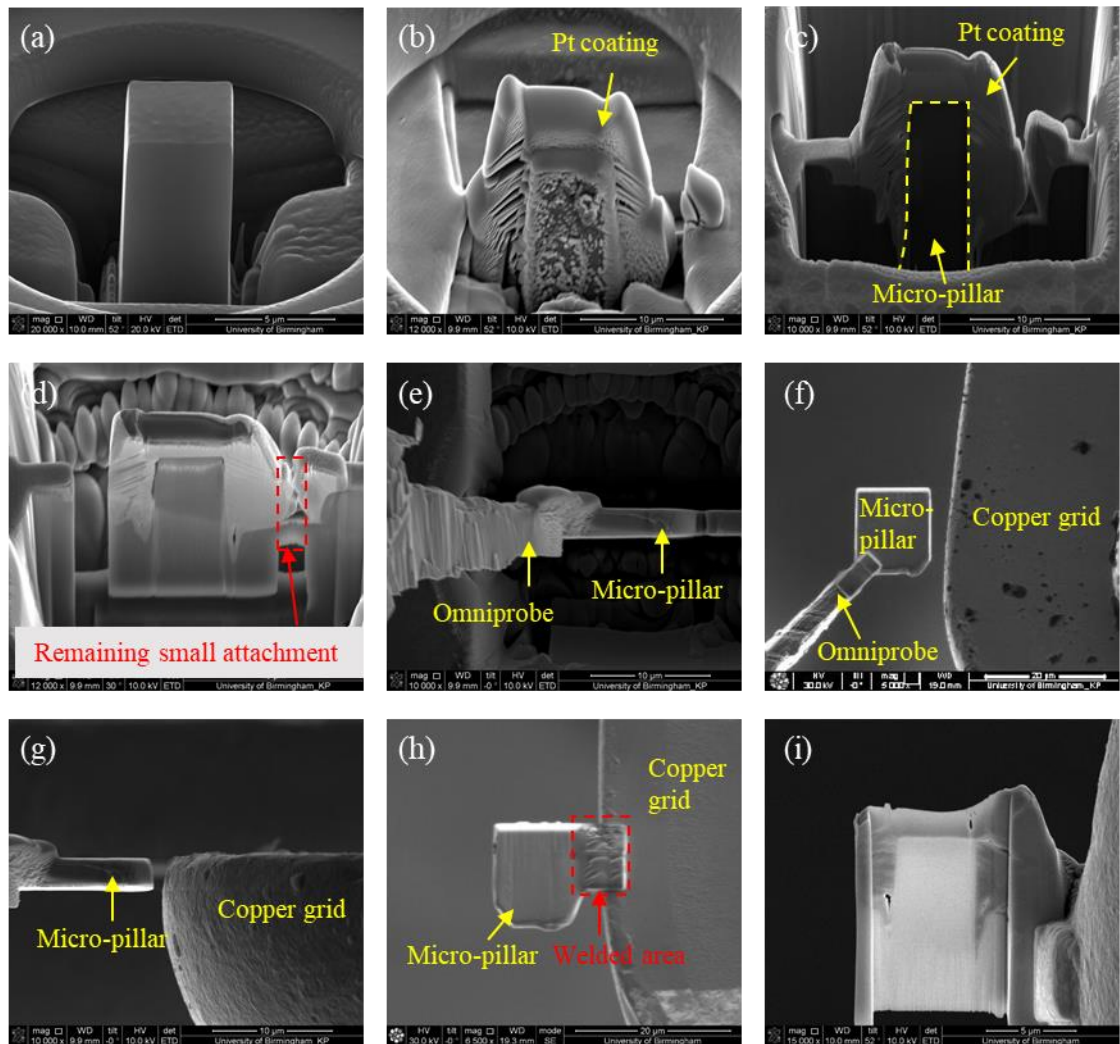


Figure 3.11 TEM specimen preparation procedure: (a) SEM image of a micro-pillar. (b) SEM image of the micro-pillar after Pt coating the top and side surfaces. (c) SEM image showing one side of the micro-pillar after cutting. (d) SEM image of the lamella after U-cut. (e) SEM image showing the lamella lift out using the Omniprobe. (f) Ion beam image showing the lamella approaching the copper grid. (g) SEM image showing the lamella's position before attachment to the copper grid. (h) Ion beam image showing the lamella welded to the copper grid. The Omniprobe has been disconnected. (i) SEM image of the foil thinned to electron transparency.

In order to investigate the interaction between the basal plate-shaped precipitates and basal slip, TEM foils parallel to the slip step required. The important difference in this foil preparation procedure is that the platinum is deposited on the slip trace. Figure 3.12 shows the TEM foil lifted out along the (0001) slip planes.

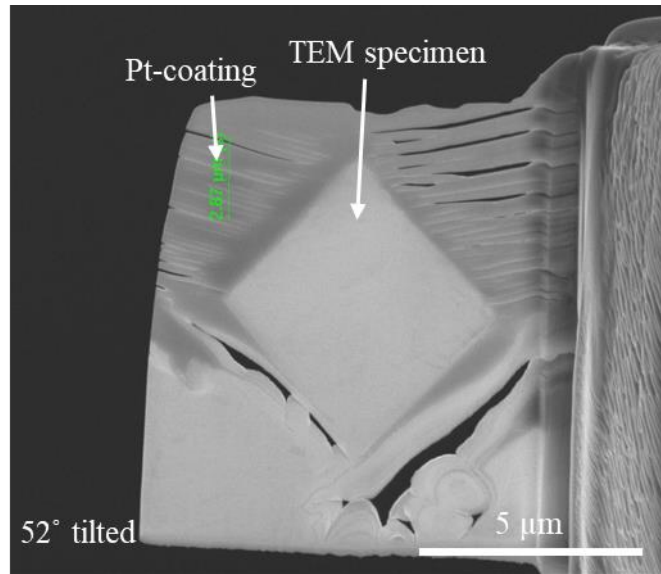


Figure 3.12 An SEM image of the TEM foil parallel to the slip planes.

3.9 Microscopy characterization

3.9.1 Optical microscopy (OM)

In the present work, a Zeiss Axioskop 2 optical microscope was employed for general microstructure overview.

The specimens for OM were gently grounded using SiC papers up to 4000 grit and polished down to 1 μm using diamond suspension. Ethanol was used to clean the specimen after final polishing to avoid surface oxidation. Then the specimen was rinsed in the ethanol ultrasonically.

In order to reveal the microstructures, subsequent etching was carried out on the well-polished specimens in different solutions. The as-cast specimen was etched in a solution containing 4 ml nitric acid and 96 ml ethanol for 40 seconds. The solution treated specimen was etched in a solution containing 1 ml acetic acid, 150 ml ethanol and 50 ml distilled water for 60 seconds. The aged specimen was also etched in a solution containing 4 ml nitric acid and 96 ml ethanol for various times depending on the specimen's aging time. After etching, the specimen was cleaned and rinsed in ethanol ultrasonically.

3.9.2 Scanning Electron Microscopy (SEM)

In the present work, a TESCAN Mira-3 SEM equipped with Energy Dispersive X-ray (EDX) and Electron Back-Scattered Diffraction (EBSD) was employed for microstructure observation, chemical composition analysis and grain orientation identification.

Generally, the preparation process for SEM specimens was the same as for OM imaging. The chemical composition of the as-cast specimen was determined by EDX spectroscopy. The solution treated and aged specimens which were chosen to investigate the influence of precipitation on the plastic deformation were polished mechanically down to 1 μm and electropolished in an electrolyte containing 10% perchloric acid and 90% ethanol. Then crystal orientations were identified by an EBSD system on the TESCAN Mira-3 microscope.

3.9.3 Transmission Electron Microscopy (TEM)

In the present work, an FEI Talos 200F TEM operating at 200 kV was employed for precipitate characterization and detailed dislocation analysis and a JEOL 2100 operating

at 200 kV was employed for in-situ TEM compression and specimen thickness determination by CBED.

3.9.4 Electron Back-Scattered Diffraction (EBSD) and Transmission Kikuchi Diffraction (TKD)

Electron Back-Scattered Diffraction (EBSD) is a conventional technique to obtain crystallographic information from bulk materials, providing a spatial resolution 150 nm. Based on SEM-EBSD, Transmission Kikuchi Diffraction (TKD) technique is recently developed recently. It shows significant improvements in spatial resolution (~ 10 nm) compared to conventional EBSD [111, 112]. TKD is applied to a thin foil transparent to electrons.

For EBSD, the specimen surface is steeply inclined by 70° from the horizontal and the working distance is about 14~ 15 mm (Figure 3.13(a)) [113]. For TKD, the specimen tilt is 20° from the horizontal and the working distance is approximately 4 mm (Figure 3.13(b)) [113].

In this study, the selected grain orientations of bulk specimens for micro-pillar and submicron-pillar machining were identified using the EBSD technique in the TESCAN Mira-3 SEM. TKD of the deformed TEM foil has also been carried out on the TESCAN Mira-3 SEM equipped with the same EBSD detector.

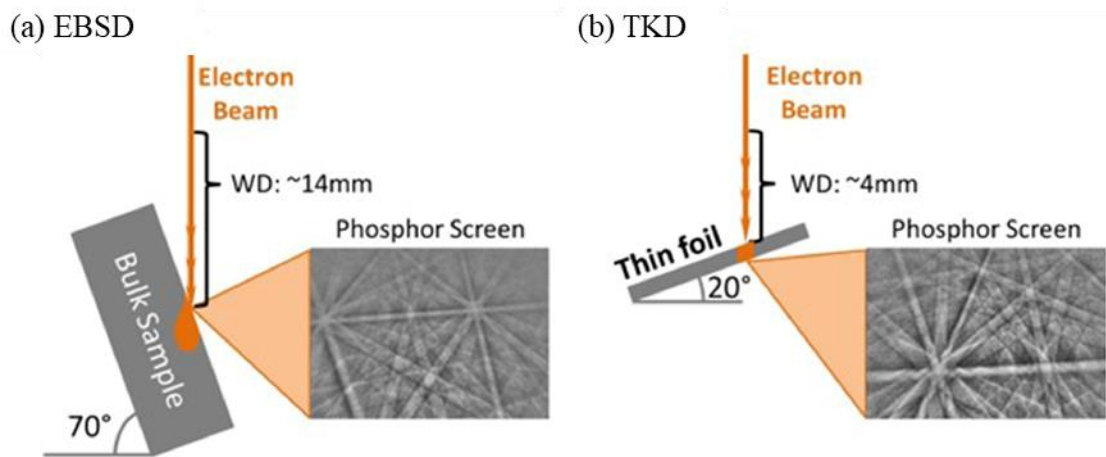


Figure 3.13 Set-up of EBSD and TKD. (a) EBSD specimen-detector configuration, and (b) TKD specimen-detector configuration [113].

3.9.5 Focused Ion Beam and Dual-beam Systems

Focused ion beam (FIB) is a technique preferentially used for preparation of TEM specimens. Commercial dual-beam system combines both electron beam (SEM) and ion beam (FIB) in one system, allowing the same feature to be investigated using either of the beams, as shown in Figure 3.14. Micron-sized and site-specific TEM foils were cut from the bulk material using a highly focused ion beam from a liquid gallium ion source. The energetic gallium beam creates artifacts in the specimen, such as gallium implantation, an amorphous layer on the specimen surface, lattice defects and the redeposition of milled material on the surface of the thinned material [114-116]. Recently, dual-beam FIB-SEMs with Xe plasma ion sources have been developed. Such plasma FIB (PFIB) have a higher milling rate, and the Xe ions may have the advantage of reduced implantation, which makes PFIB instruments more suitable for certain types of specimen.

In this study, micro-pillars, submicron-pillars and TEM specimens were prepared on a FEI Quanta 3D FEG Dual Beam (SEM/FIB) or a Helios G4 PFIB CXe Dual Beam (SEM/FIB).

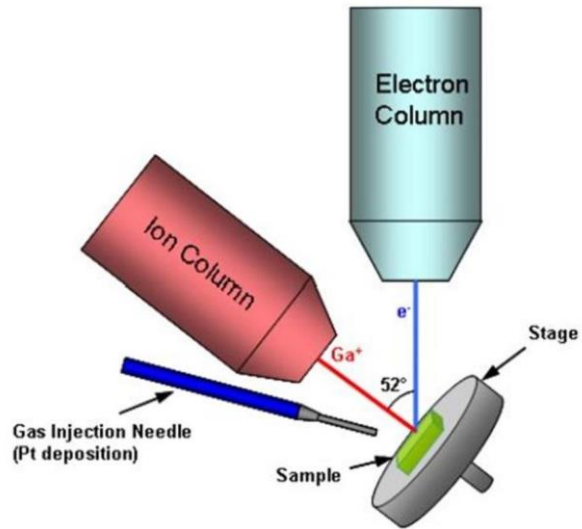


Figure 3.14 A schematic illustration of the FIB/SEM dual beam system.

4 Results

4.1 Microstructure of AZ91

4.1.1 As-cast AZ91

Figure 4.1 is an optical image of the as-cast AZ91 alloy showing a dendrite microstructure but not revealing the grain boundaries. According to the binary Mg-Al phase diagram (Figure 2.8), the dendrites consist of α -Mg solid solution and β -Mg₁₇Al₁₂ phase.

The precipitates distribution in the as-cast AZ91 is shown in Figure 4.2. Figure 4.2(a) presents the dendrite structure forming networks surrounding the matrix. Figure 4.2(b) shows the continuous precipitates (CP) which are generally less than 5 μm in size. Figure 4.2(c) shows the lamellar discontinuous precipitates (DP) which have a larger size distribution of 1-20 μm .

Apart from the continuous precipitates and discontinuous precipitates, micron-scale Al-Mn precipitates have been observed in as-cast AZ91, as shown in Figure 4.2(d). The EDX spectrum is shown in Figure 4.3(b), indicating that the precipitate contains 38.8 at.% Mn, 60.2 at.% Al and less than 1 at.% Mg according to the measured weight percentage. This is probably an Al₈Mn₅ particle, which has been previously reported in AZ91 [36, 117, 118]. The small amount of Mg is probably due to the spatial resolution limitation of EDS on the SEM.

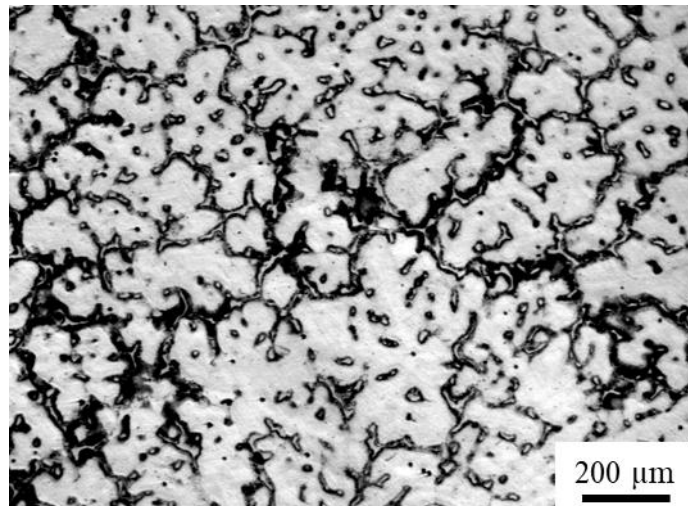


Figure 4.1 An optical image of the as-cast AZ91 alloy.

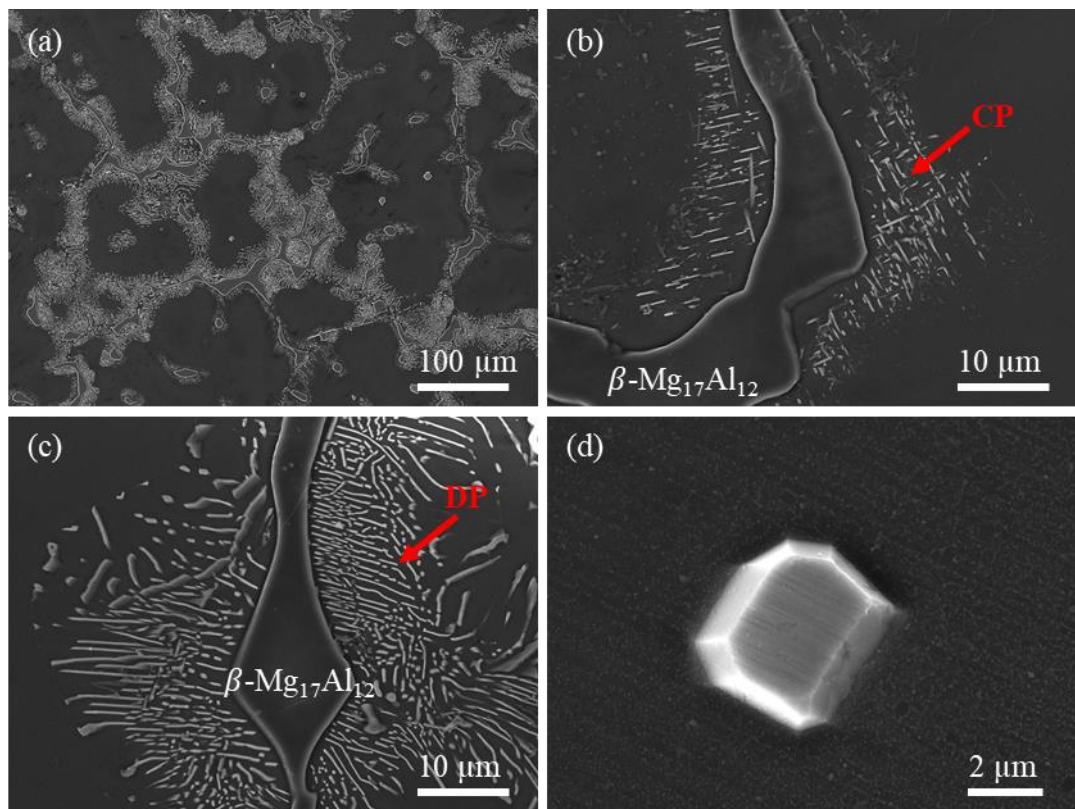


Figure 4.2 SEM images showing the precipitates in as-cast AZ91 alloy: (a) dendrites distribution, (b) continuous precipitates (CP), (c) discontinuous precipitates (DP) and (d) Al-Mn precipitate.

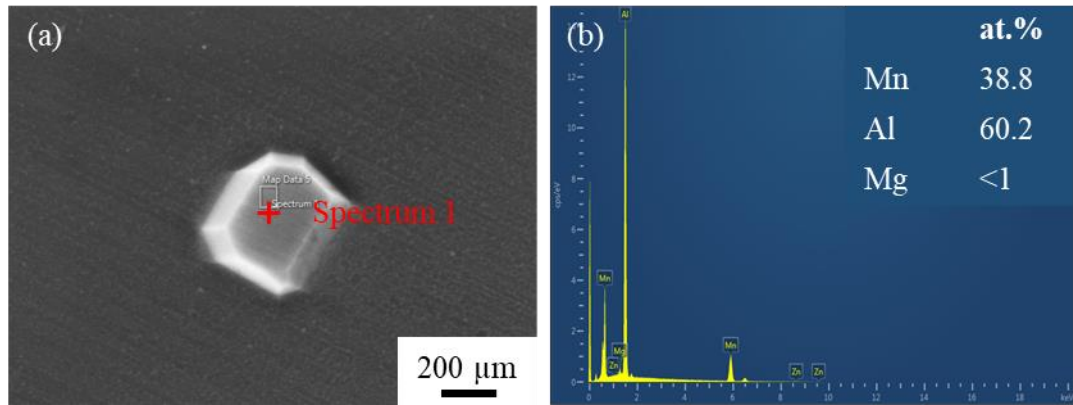


Figure 4.3. (a) An SEM image showing Al-Mn particles in as-cast AZ91. (b) is the EDX spectrum 1 from Figure 4.3(a). The atomic percentage of each element is shown in the top right corner in Figure 4.3(b).

4.1.2 Solution treated AZ91

The as-cast specimen was solution treated at 415°C for 96 hours and water quenched. This temperature was chosen based on the Mg-Al phase diagram and other Ref.[29, 30, 32]. The long-time heat treatment was chosen to in order to produce large grains and thus allow fabrication of at least 10 micro-pillars from one grain.

Figure 4.4 shows an optical image of the AZ91 after solution treatment and water quenching. No dendrite structure or $Mg_{17}Al_{12}$ precipitates have been observed in the solution treated specimen, indicating the formation of a super-saturated solid solution. The grain size is $284 \pm 61 \mu\text{m}$.

To assess the evolution of the dislocation structure after micro-pillar compression, it is essential to analyse the initial dislocations in the undeformed specimen. Figure 4.5 shows the existence of dislocations in the solution treated specimen; the dislocations are indicated by yellow arrows. The dislocation analysis in the TEM sample was carried out

using the $g \cdot b = 0$ extinction criterion. The dislocations in this area are out of contrast using the 0002 reflection, and in contrast using $\bar{2}112$, $10\bar{1}1$ and $10\bar{1}0$ reflections, indicating their Burgers vectors are $\langle a \rangle$ type. The dislocations could be introduced by the mechanical polishing during the sample preparation. The distribution of pre-existing dislocations in the solution treated specimen is not uniform. This non-uniform distribution may exist in different micro-pillars in the same grain and contributes to the scatter in their mechanical behaviour.

Apart from the dislocations, there are other defects (shown as black dots) and curtaining (shown as straight lines) in the TEM images in Figure 4.5. Both of them are induced by the FIB milling, and they are not the inherent features in solution treated AZ91.

Al-Mn particles exist in the solution treated specimen, and a particle is outlined by the red dashed circle in Figure 4.5. Al-Mn particles cannot be dissolved into the Mg matrix at 415°C solution treatment.

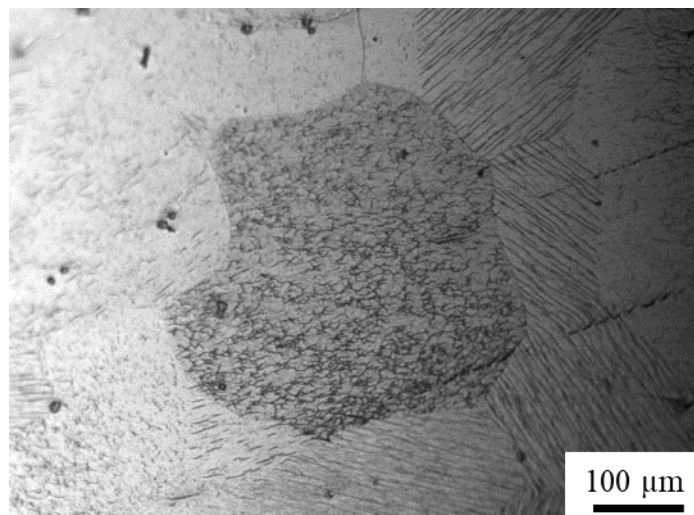


Figure 4.4 An optical image of solution treated AZ91(as etched).

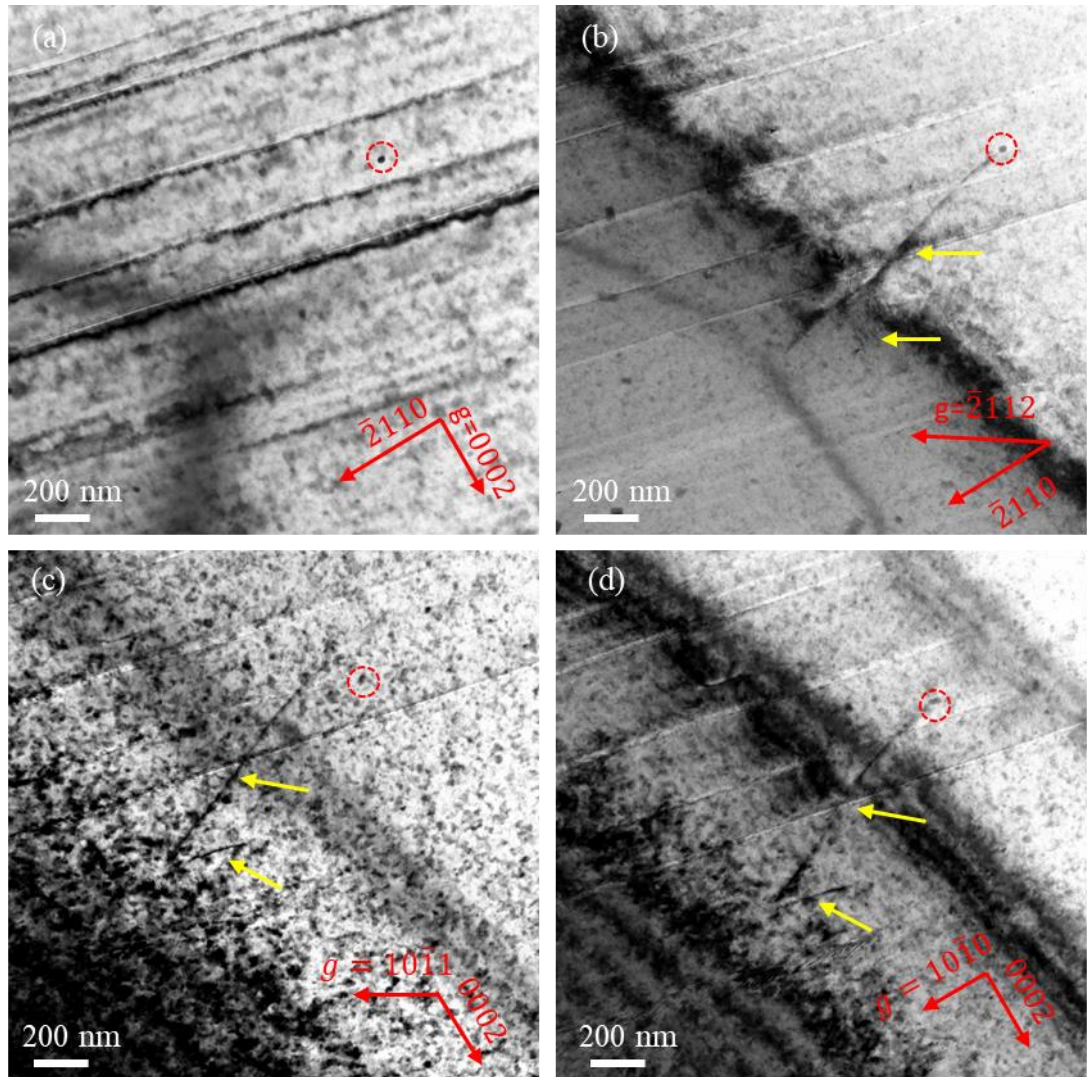


Figure 4.5 Bright field TEM images showing dislocations in the solution treated specimen. The dislocations are indicated by yellow arrows. An Al-Mn particle is outlined by a red dashed circle as a reference for the dislocation analysis. (a) $g = 0002$, $BD \sim [0\bar{1}10]$, (b) $g = \bar{2}112$, $BD \sim [0\bar{1}10]$, (c) $g = 10\bar{1}1$, $BD \sim [1\bar{2}10]$ and (d) $g = 10\bar{1}0$, $BD \sim [1\bar{2}10]$.

4.1.3 Aged AZ91

(1) Hardness

The hardness evolution on aging at 200°C is shown in Figure 4.6. The hardness of AZ91 increases at a steady pace before 10 hours reaching the peak hardness (95 ± 5 HV0.1) which it retains for some time, and then decreases slowly. The peak hardness increased by 33 HV0.1 as compared with the solution treated specimen (62 ± 5 HV0.1).

The peak hardness increments after aging at 200°C reported in the literature are around 30 HV10 [32] and 29 HRE [41]. The peak hardness increment in the present work is thus consistent with the results in the literature.

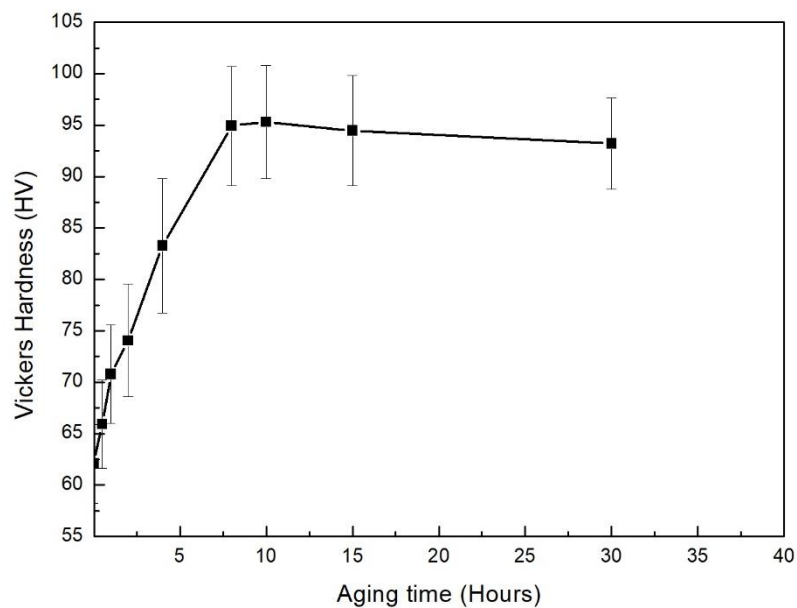


Figure 4.6 Hardness versus aging time for AZ91 aged at 200°C.

(2) Discontinuous precipitate and continuous precipitate

Figure 4.7 is an SEM image of the continuous precipitates and discontinuous precipitates in the AZ91 aged at 200°C for 10 h. The left region is taken up by continuous precipitates and the right region is occupied by discontinuous precipitates. The continuous precipitates are small and the distribution is generally homogenous. The discontinuous precipitates are lamellar with different sizes.

Figure 4.8 shows SEM images of the precipitate evolution when the specimen is aged at 200°C for different times. Figure 4.8 (b) shows that the discontinuous precipitates (bright areas) initiate on the grain boundaries. Figure 4.8(c-f) show that the discontinuous precipitation areas expanded with aging time. Discontinuous precipitates nucleate at the grain boundaries. These discontinuous precipitates grow and form lamellar structures on aging.

The continuous precipitates were characterised by TEM. Figure 4.9 shows TEM images of continuous precipitates after aging at 200°C for 2 hours and 10 hours when viewed along $[\bar{2}110]$ and $[0001]$. The $Mg_{17}Al_{12}$ precipitates are plates parallel to the basal plane of the matrix, consistent with earlier observations [29, 32, 41]. For a detailed calculation of the strengthening effect, a full understanding of the precipitate shape is necessary. The dimensions are indicated in Figure 4.9: the width (w) is measured when viewed along $[0001]$; length (l) and the thickness (t) are measured when viewed along $[\bar{2}110]$ [30]. For the samples after 10 hours aging, the plates are 550 ± 94 nm in length (l), 130 ± 35 nm in width (w) and the thickness (t) of the plates is 36 ± 5 nm. The number density and dimensions of the continuous precipitates after aging for 2 hours and 10 hours are both listed in Table 4.1. These dimensions are consistent with the data reported in [32, 88, 119].

The number density of continuous precipitates from the specimen aged at 200°C for 10 hours is $93 \mu\text{m}^{-3}$. Each micro-pillar (nominal dimensions $4.5 \mu\text{m} \times 4.5 \mu\text{m} \times 9 \mu\text{m}$) fabricated from this aged specimen therefore contains about 17000 precipitates. The precipitate distribution is generally homogeneous. Also the micro-pillars fabricated from this aged specimen show strong precipitation strengthening due to its peak hardness.

The submicron-pillars for in-situ TEM deformation were fabricated from a specimen which was aged at 200°C for 2 hours. This under-aging condition was chosen to provide a reasonable number of small precipitates in one submicron-pillar, considering the dimension of the freestanding submicron-pillar (1400~1800 nm in height, 700~ 900 nm in width and around 300 nm in thickness).

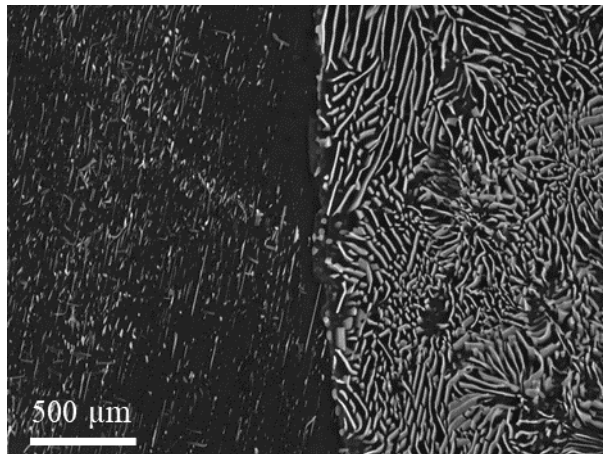


Figure 4.7 SEM image showing discontinuous and continuous precipitates after aging at 200°C for 10 hours. The left region is taken up by continuous precipitates and the right region by discontinuous precipitates.

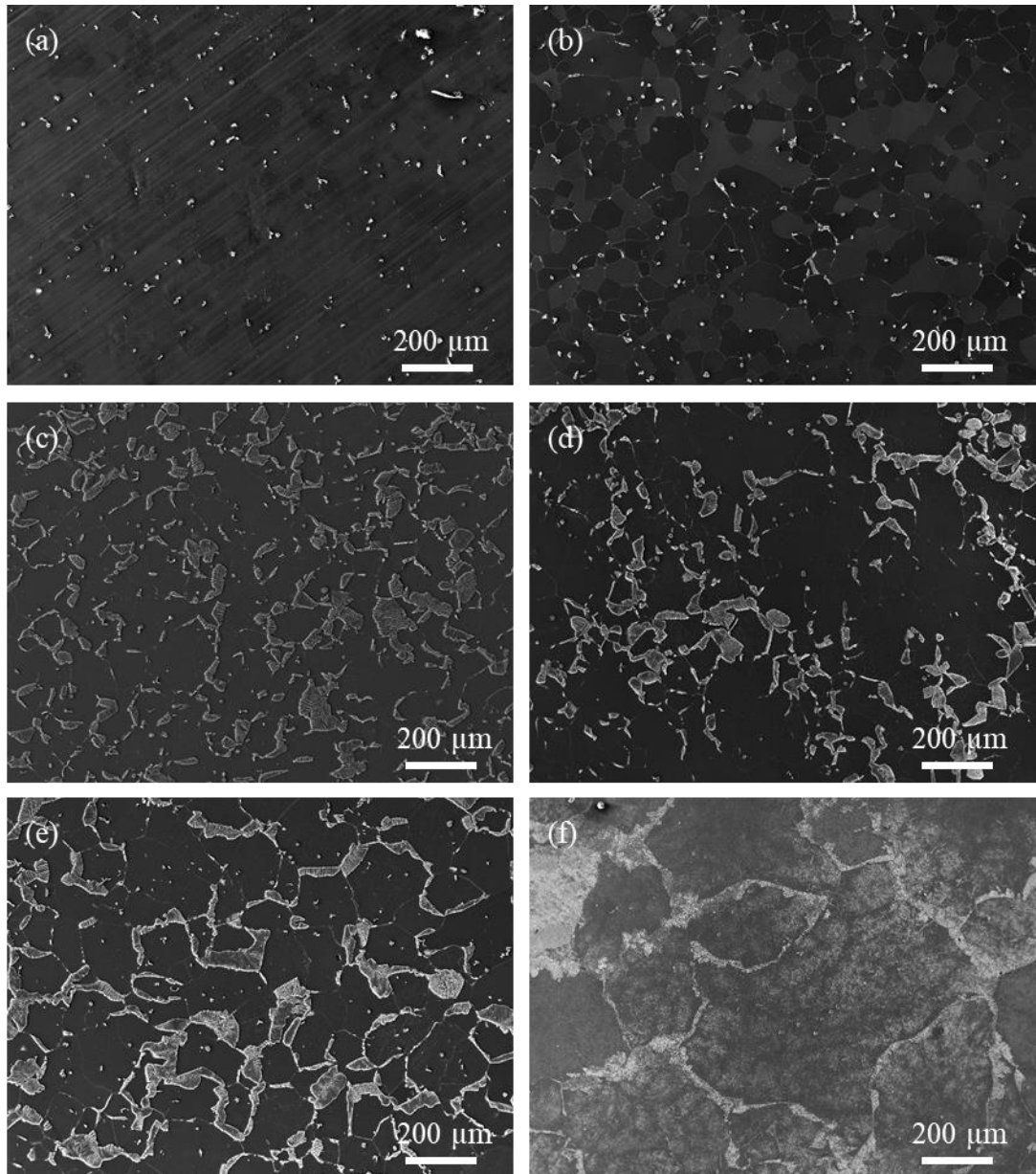


Figure 4.8 SEM images showing the evolution of the discontinuous precipitates when the bulk samples are aged at 200°C for different times. (a) 0.25 h, (b) 0.5 h, (c) 2 h, (d) 3 h, (e) 4 h and (f) 10 h. The discontinuous precipitates initiate on the grain boundaries and grow into the grains.

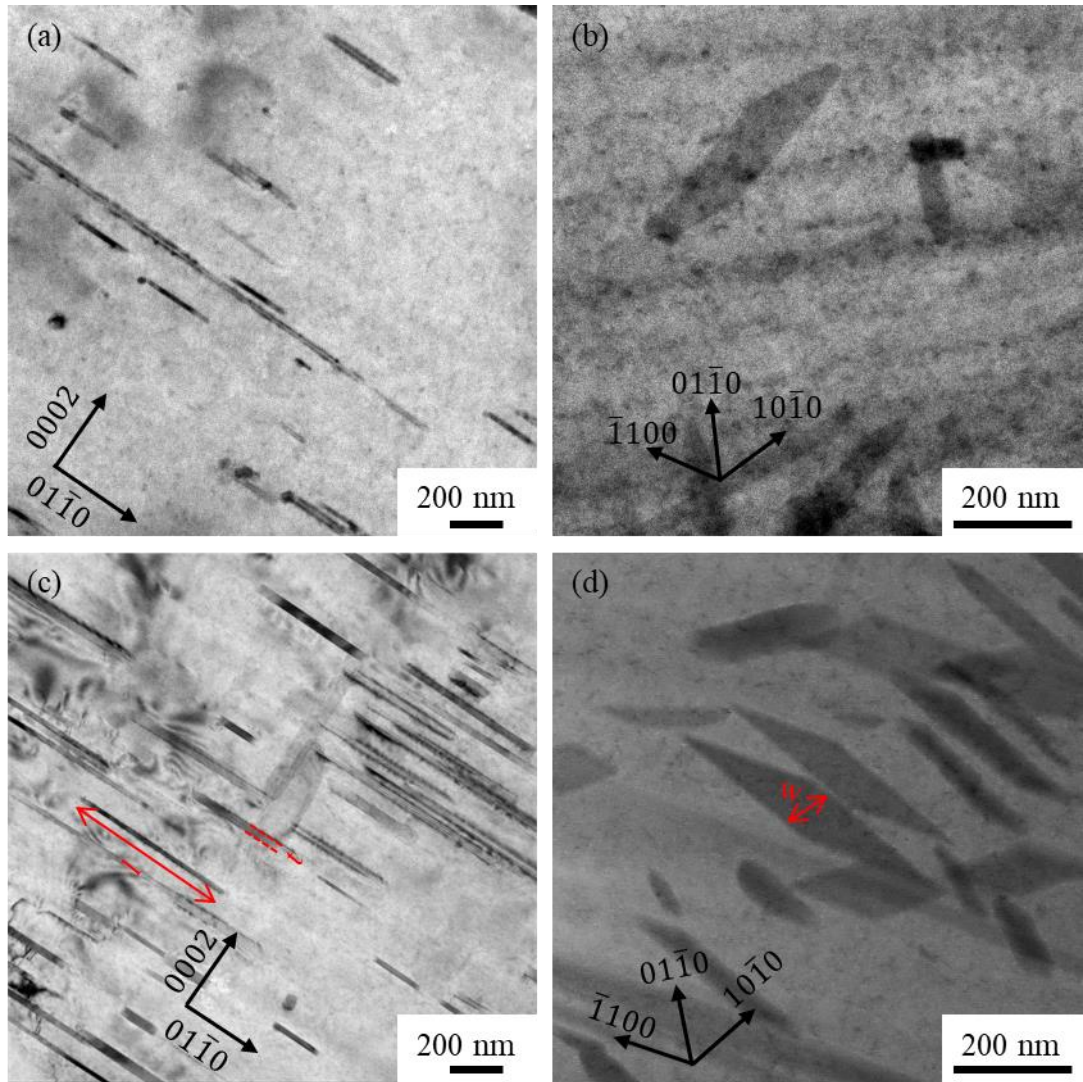


Figure 4.9 Bright field images obtained from AZ91 after aging for 2hour (a-b) and 10 hours (c-d) when viewed along (a, c) $[\bar{2}110]$ and (b, d) $[0001]$. The dimensions are indicated in the images.

Table 4.1 Precipitate dimensions and number density in the aged AZ91.

Aging time	$N_V(\mu\text{m}^{-3})$	l (nm)	w (nm)	t (nm)
2 h	12	359	61	14
10 h	93	550	130	36

4.1.4 TEM foil thickness

A knowledge of the TEM foil thickness is essential for the quantification of precipitate density N_V in the TEM specimens. Foil thickness measurement using CBED is shown in Figure 4.10. The CBED pattern in Figure 4.10 is taken close to $[\bar{2}110]$ using reflection $02\bar{2}1$ in a specimen after aging at 200°C for 10 h. The inter-planar spacing $d_{02\bar{2}1}$ is 0.134 nm, wavelength of the electron λ at 200 kV is 2.509 pm, s_i is calculated using Equation 3.3. The foil thickness of this sample is 172.5 nm.

The foil thicknesses were generally between 150 nm and 260 nm for the purpose of number density calculation. The submicron-pillar thicknesses were generally between 260 nm and 420 nm.

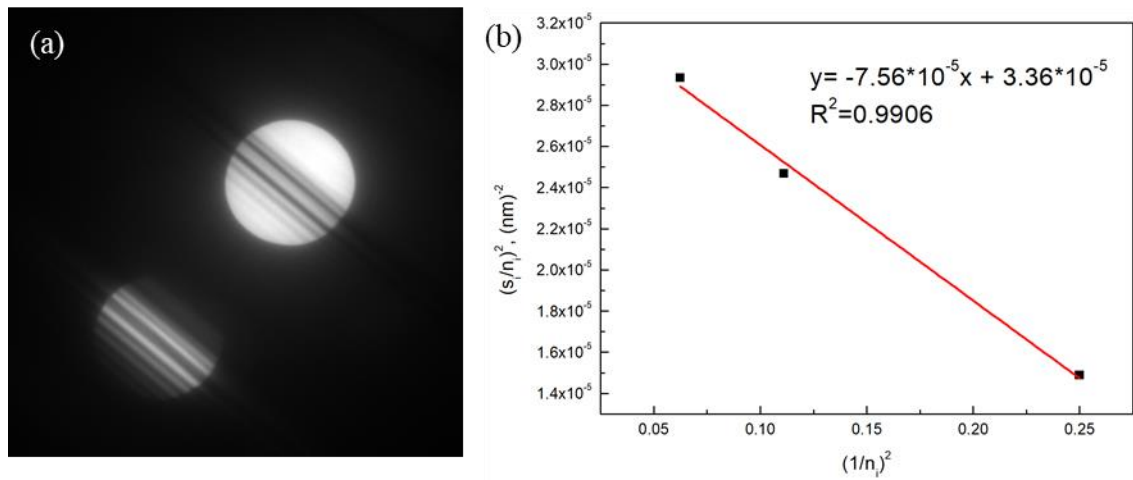


Figure 4.10 (a) A CBED pattern taken near $[\bar{2}110]$ zone axis using $g = 02\bar{2}1$ in AZ91 aged at 200°C for 10 h. (b) An example of measured thickness.

4.2 Compression of micro-pillars oriented for basal slip

The first group of square micro-pillars was deformed in order to study the precipitate interaction with $\langle a \rangle$ slip on the basal plane by the CRSS values, surface morphology and post-mortem TEM observations.

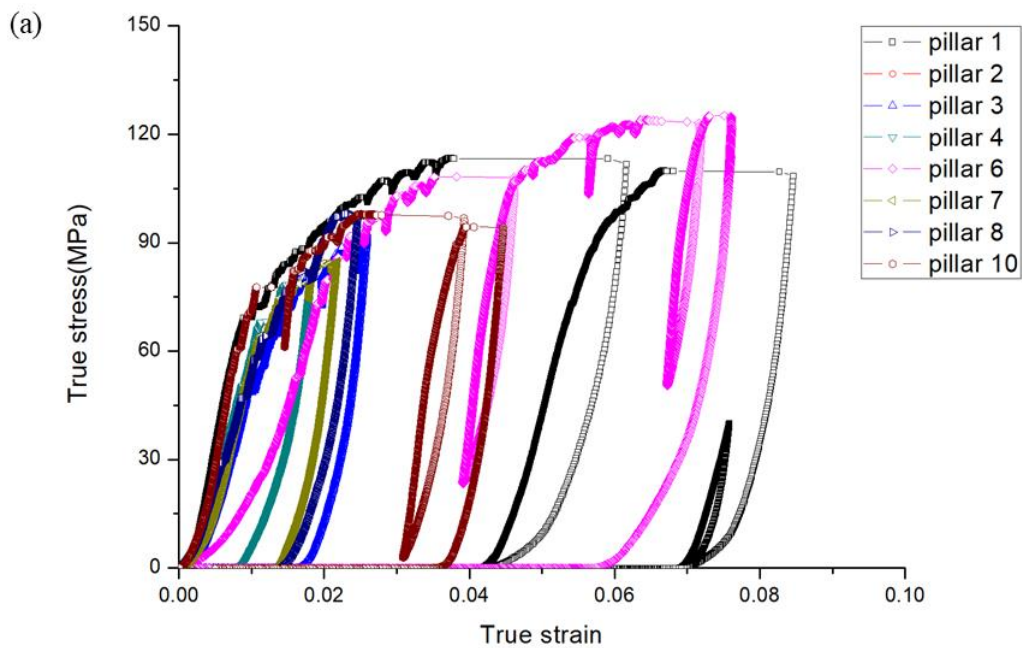
4.2.1 Mechanical behaviour

Compression of the solution treated and the peak-aged specimens along $[55 \bar{1}0 9]$ was performed to strains between 2% to 8%. 8 solution treated micro-pillars and 7 aged micro-pillars were compressed. The stress-strain curves in Figure 4.11(a) and Figure 4.11(b) show good repeatability. Two single stress-strain curves obtained from the compression of the solution treated and the peak-aged specimens along $[55 \bar{1}0 9]$ are shown in Figure 4.11(c).

Non-linear section was observed on the curve in the early stage of loading. This is frequently observed in micro-pillar compression experiments due to the factors such as misalignment between the flat diamond tip and the micro-pillar. In Figure 4.11(c) both the solution treated and the aged specimens show obvious strain bursts (indicated by green arrows) followed by stress drops (indicated by yellow arrows). Such strain bursts have been widely reported in associated with the avalanche of dislocations often in the form of slip bands. The stress drop following the strain burst, as shown for example in the blue box, is believed to be related with the instrumentation. The PI85 system currently used is an instrument with intrinsic load control mechanism with the displacement being controlled via a feedback loop from the loading signal detected. In the current setting it seems that the feedback loop response was not sufficient to match the strain rate incurred

during the strain burst and therefore the over-shoot of the displacement. To compensate the over-shoot, a displacement opposite to the loading direct would be needed to maintain the constant displacement rate. Due to the difficulty in evaluate the strain rate during the strain burst, no further analysis of the suitable displacement rate was attempted in this study.

The mean yield strengths (averaged 0.2% proof stresses) were found to be 73.4 ± 3.4 MPa and 81.6 ± 5.2 MPa for the solution treated and aged micro-pillars, respectively. Thus the CRSSs for basal slip were determined to be 36.7 MPa and 40.8 MPa for the solution treated and aged AZ91, respectively.



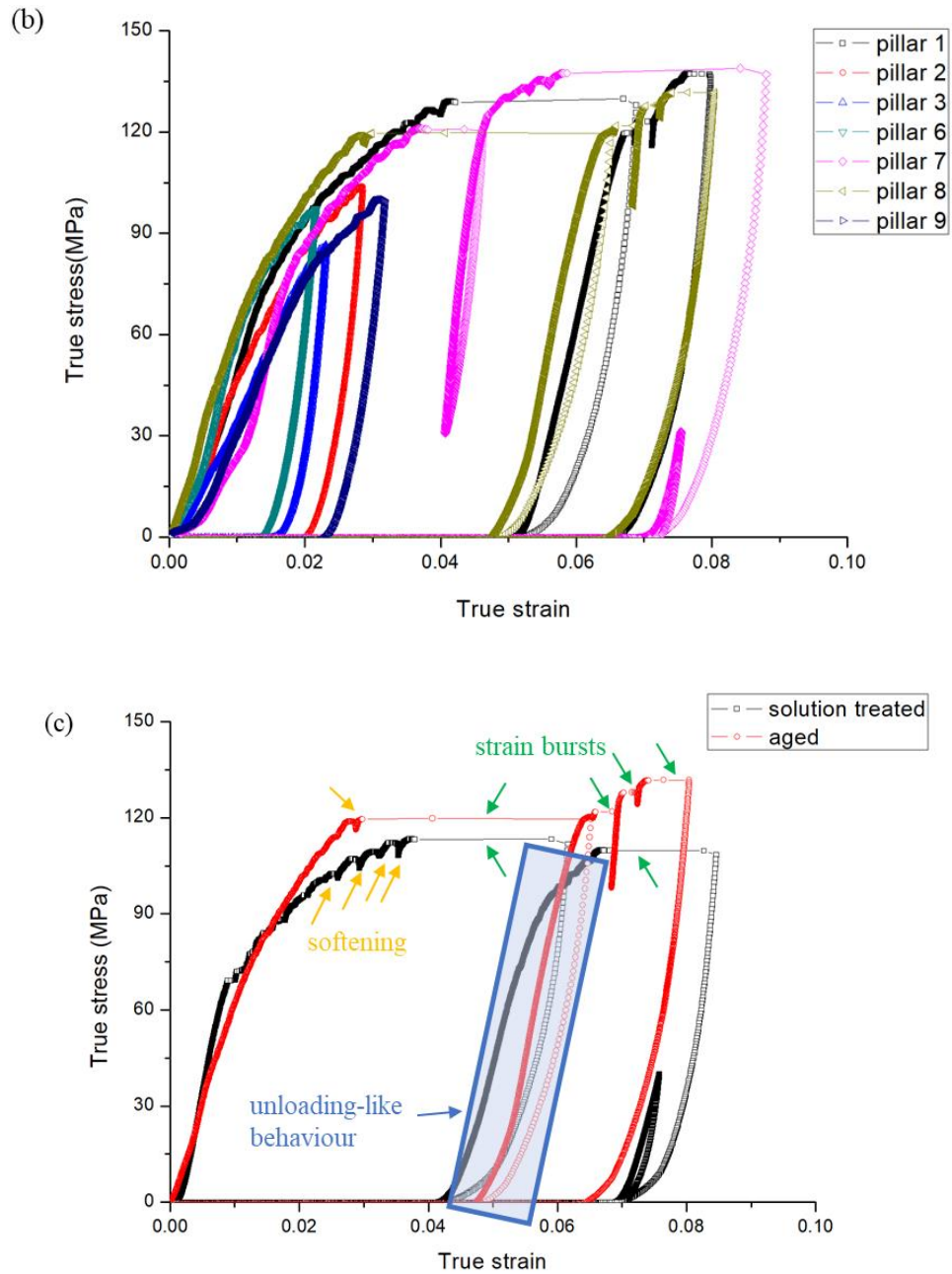


Figure 4.11 True stress-strain curves obtained from the compression of micro-pillars oriented for basal slip: (a) Solution treated; (b) aged; and (c) two stress-strain curves: one is solution treated, the other is aged. Softening is indicated by yellow arrows, the strain bursts are indicated by green arrows, and unloading-like behaviour (over-shoot of the displacement) is outlined by the blue box. Both solution treated and aged micro-pillars show obvious strain bursts with limited work hardening.

4.2.2 Surface morphology of deformed micro-pillars

Representative SEM images of the deformed micro-pillars are given in Figure 4.12 and Figure 4.13. The massive slip bands are marked in Figure 4.12(c) (d) and Figure 4.13(c) (d). All the slip bands form on (0001).

The position of the slip bands is random: they can occur at the top (Figure 4.13(d)) or in the middle (Figure 4.12(c) (d) and Figure 4.13(c)) of the micro-pillar. There is no obvious distinction in appearance between the solution treated and aged micro-pillars after deformation.

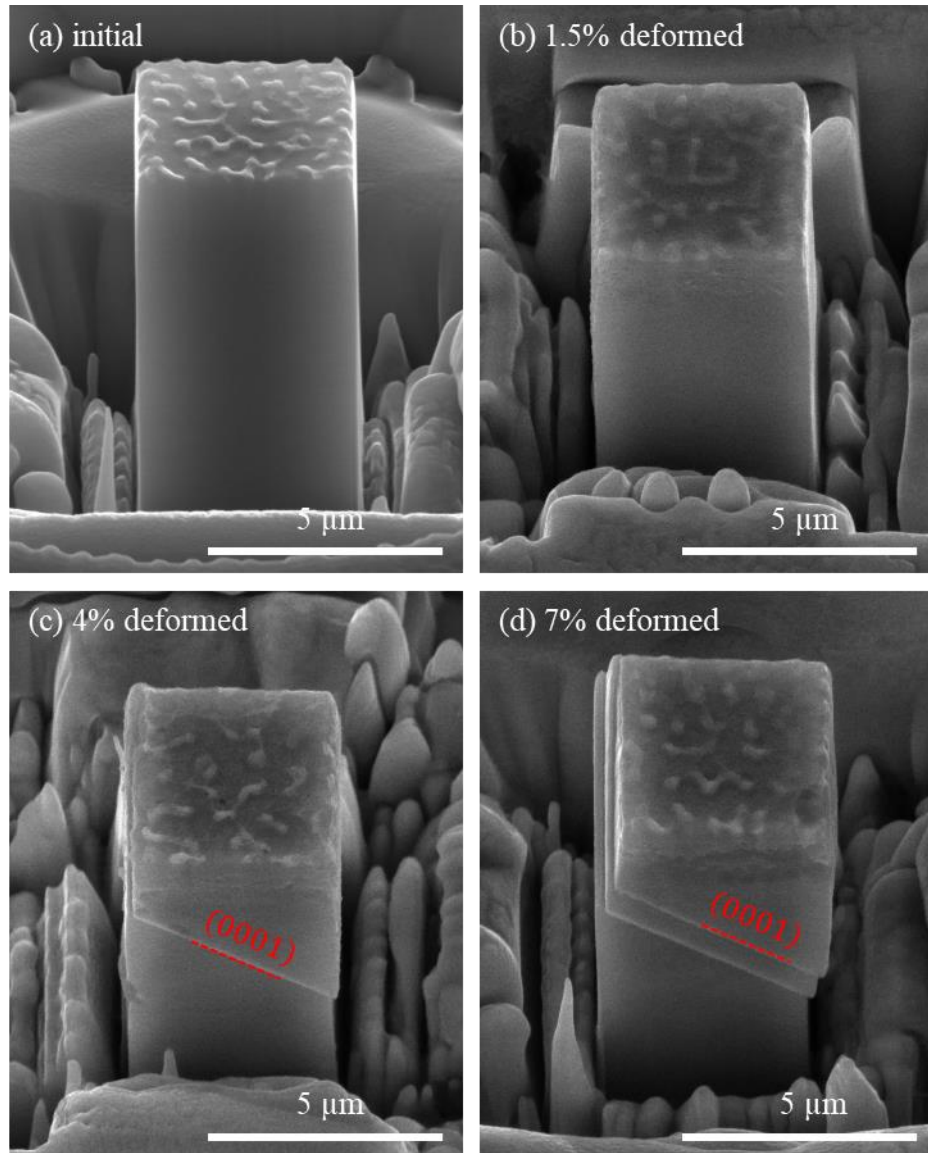


Figure 4.12 Representative SEM images of $[55\bar{10}9]$ oriented micro-pillars of solution treated AZ91 before compression and after compression to different strains, as noted. Image (a) was taken at a tilt angle of 52° and images of micro-pillars (b), (c) and (d) were taken at a tilt angle of 30° .

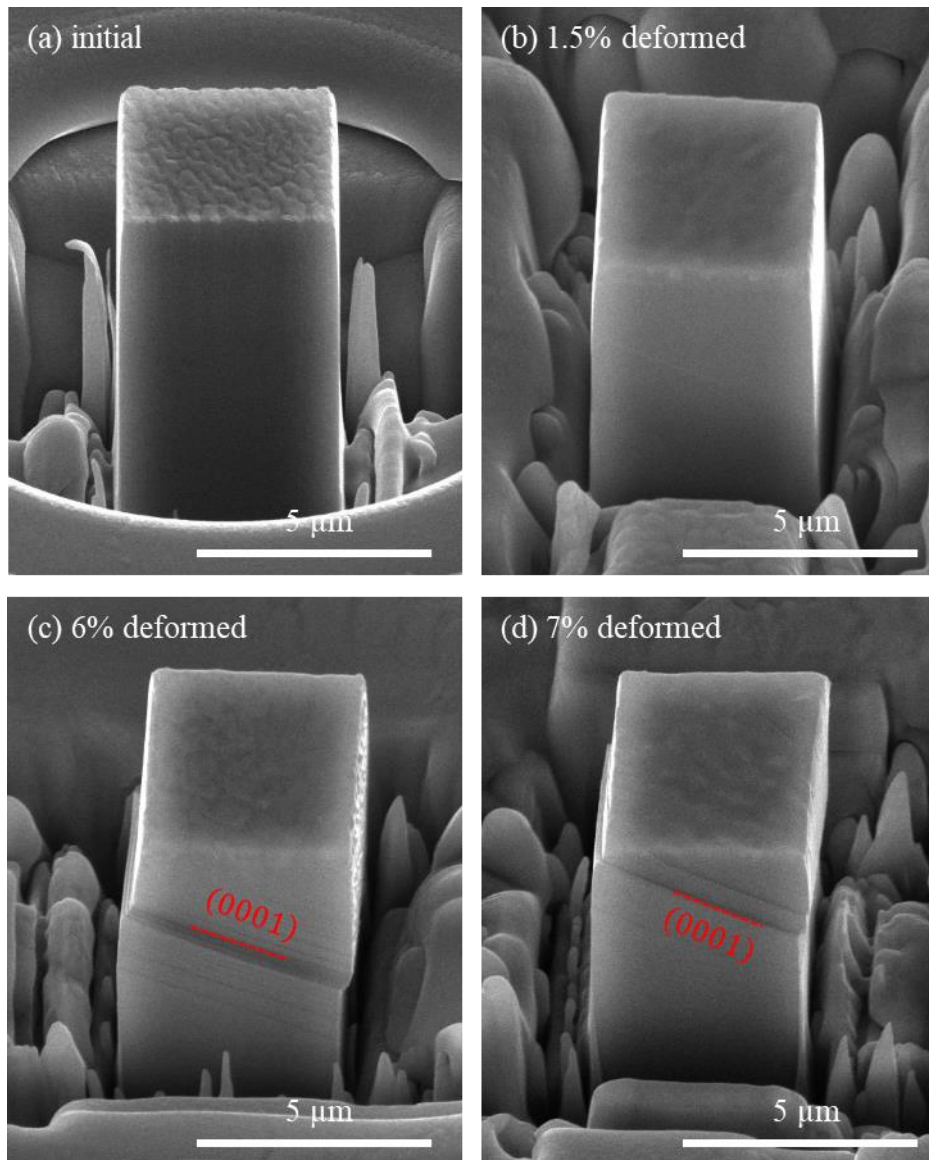


Figure 4.13 Representative SEM images of $[55\bar{1}09]$ oriented micro-pillars of aged AZ91 before compression and after compression to different strains, as noted. Image (a) was taken at a tilt angle of 52° and images of micro-pillars (b), (c) and (d) were taken at a tilt angle of 30° .

4.2.3 Transmission electron microscopy results

TEM was used to study the dislocation activities in precipitate-free micro-pillars (solution treated) and micro-pillars with precipitates (aged).

For the solution treated specimen, a TEM foil was extracted parallel to (0001) from the compressed micro-pillar in the way shown in Figure 4.14. Dislocation analysis from this TEM foil under different two-beam conditions is shown in Figure 4.15. The bright field images in Figure 4.15(a-c) show a group of long and curved dislocations in the solution treated micro-pillar (indicated by the blue lines in Figure 4.15(d)). They are visible for $g = 0\bar{1}10$ and $g = \bar{1}010$, but invisible when $g = \bar{1}100$, showing that they have Burgers vector $1/3[11\bar{2}0]$.

For the aged specimen, a TEM foil was extracted parallel to (0001) in the same way. The bright field images in Figure 4.16(a-d) show a large number of dislocations in the aged micro-pillar. They are visible when $g = 10\bar{1}0$ and $g = 0\bar{1}10$ and they are invisible when $g = 1\bar{1}00$, showing that they have Burgers vector $1/3[11\bar{2}0]$. The precipitates show little contrast when viewed near the foil normal because the precipitates and the large number of dislocations are both parallel to (0001). In order to show the interaction between precipitates and dislocations more clearly, a schematic diagram of Figure 4.16(d) is shown in Figure 4.16(e).

Two basal precipitates (named precipitate ① and precipitate ②) are indicated by yellow quadrangles, and basal dislocations are indicated by lines. For these two precipitates, no obvious shearing of precipitates is observed and no basal dislocation motion blocking by precipitates is observed.

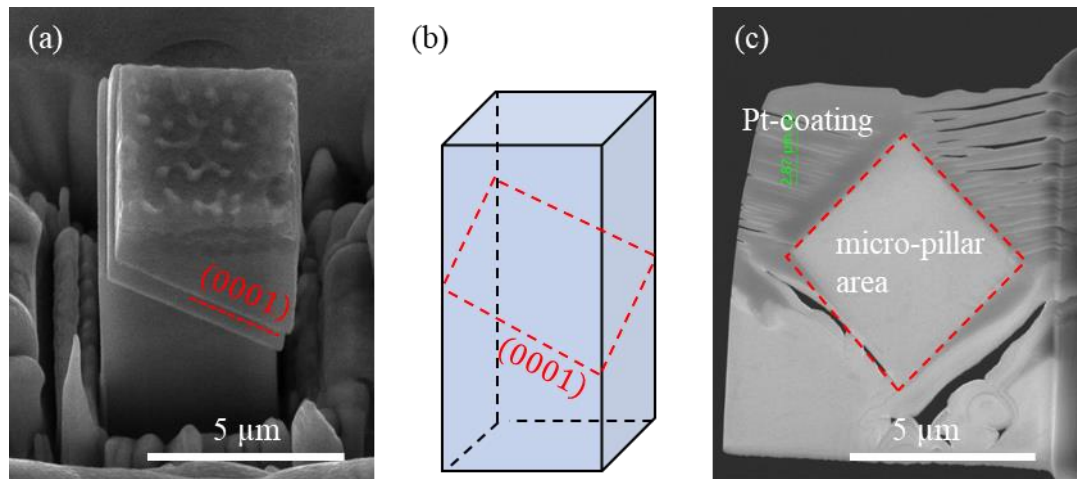


Figure 4.14 (a) An SEM image of a solution treated micro-pillar with 7% strain. The (0001) slip trace is highlighted by the red dashed line. (b) A schematic diagram showing the micro-pillar and (0001) slip trace. The micro-pillar is indicated by the blue box, and the (0001) slip trace is indicated by the red dashed quadrangle. (c) A TEM foil with (0001) foil normal. The micro-pillar area is indicated by the red dashed quadrangle. The dark area on the top of the micro-pillar is the Pt coating deposited during TEM specimen fabrication using FIB.

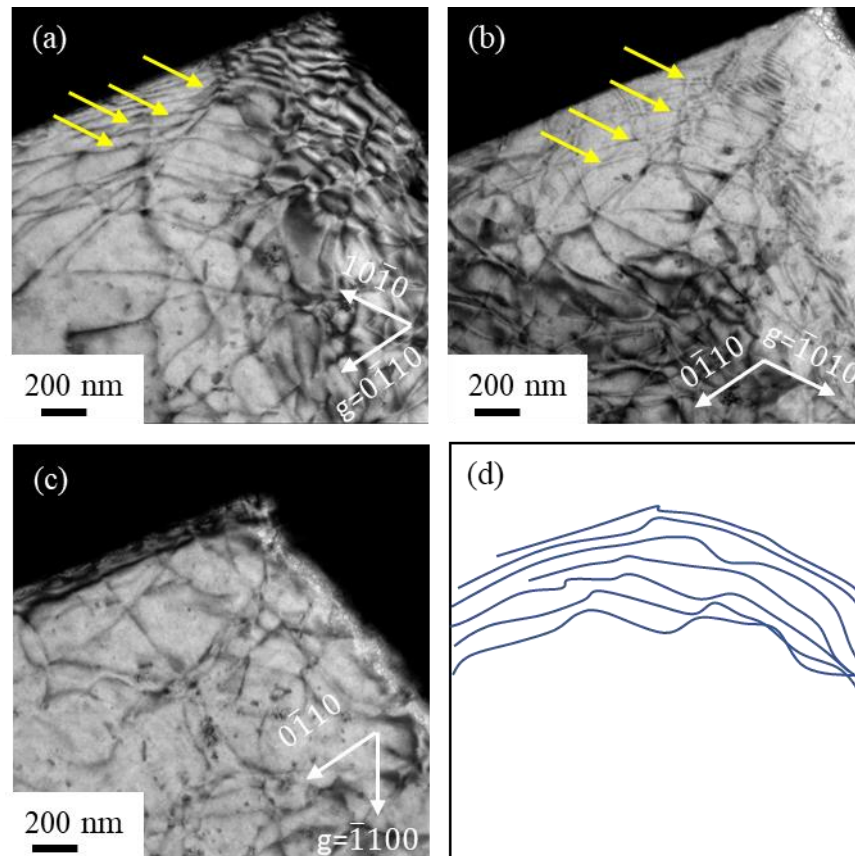


Figure 4.15 (a-c) TEM bright field images under different two-beam conditions after 2% strain of solution treated micro-pillar. The yellow arrows in Figure 4.15(a) and (b) indicate the long and curved dislocations. (a) $g = 01\bar{1}0, BD \sim [0001]$, (b) $g = 10\bar{1}0, BD \sim [0001]$ and (c) $g = \bar{1}100, BD \sim [0001]$. (d) A schematic diagram showing the basal dislocations which were activated by the compression. They are more numerous than the others and therefore they are deduced to be the dislocations which accomplished the strain.

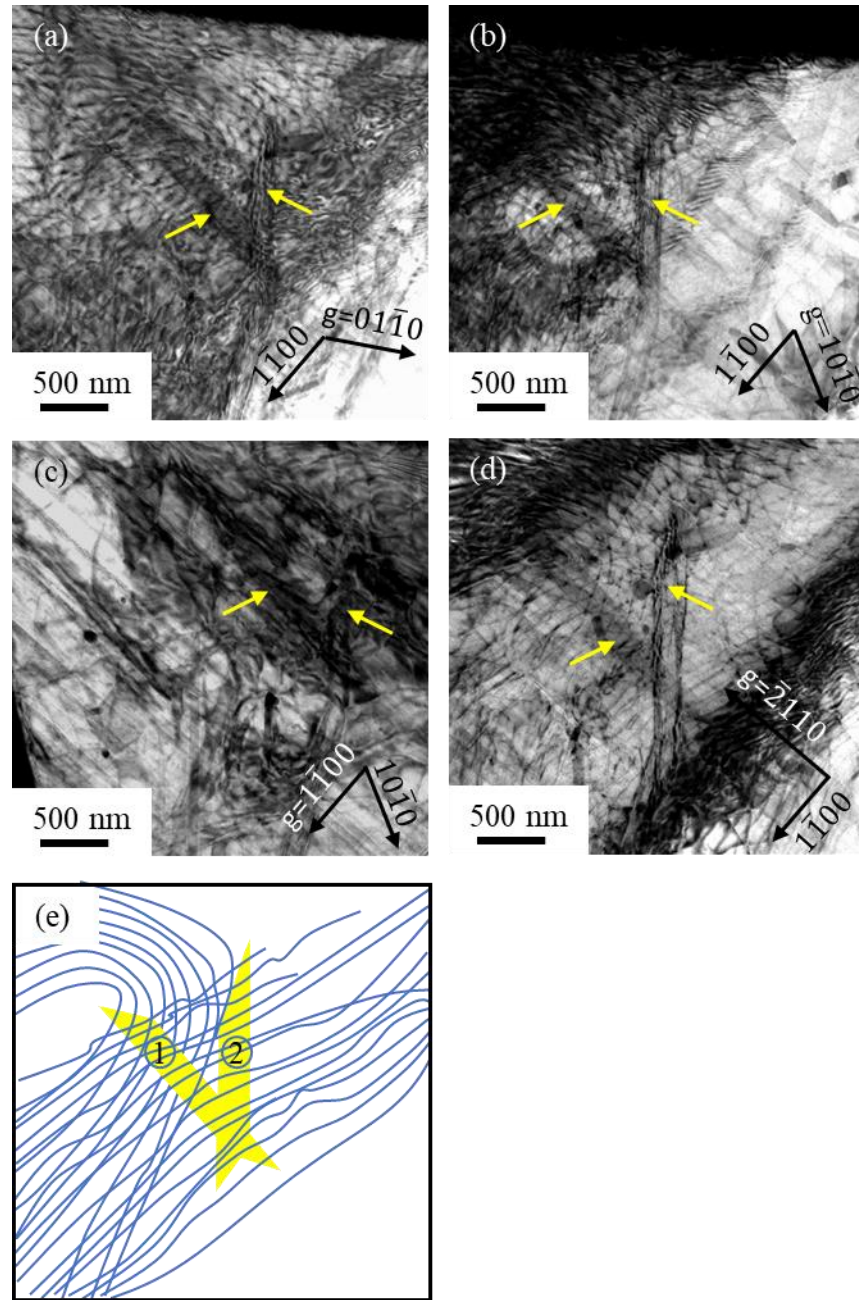


Figure 4.16 (a-d) TEM bright field images under different two-beam conditions after 7% strain deformation of aged micro-pillar. (a) $g = 01\bar{1}0, BD \sim [0001]$, (b) $g = 10\bar{1}0, BD \sim [0001]$, (c) $g = \bar{1}100, BD \sim [0001]$, (d) $g = \bar{2}110, BD \sim [0001]$. (e) A schematic diagram showing the dislocations and the precipitates. Two precipitates are indicated by yellow quadrangles, and dislocations are indicated by blue lines.

4.2.4 Summary

The precipitate interaction with $\langle a \rangle$ slip on the basal plane has been studied by micro-pillar compression along $[55\bar{1}0\ 9]$. The derived CRSSs for basal slip were determined to be 36.7 MPa and 40.8 MPa for the solution treated and aged AZ91, respectively. TEM observations show that the dislocations in both the solution treated and the aged specimens have Burgers vector $1/3[11\bar{2}0]$. Also no shearing of precipitates or dislocation motion blocked by precipitates is observed.

4.3 Compression of micro-pillars oriented for $\{01\bar{1}2\}$ twinning

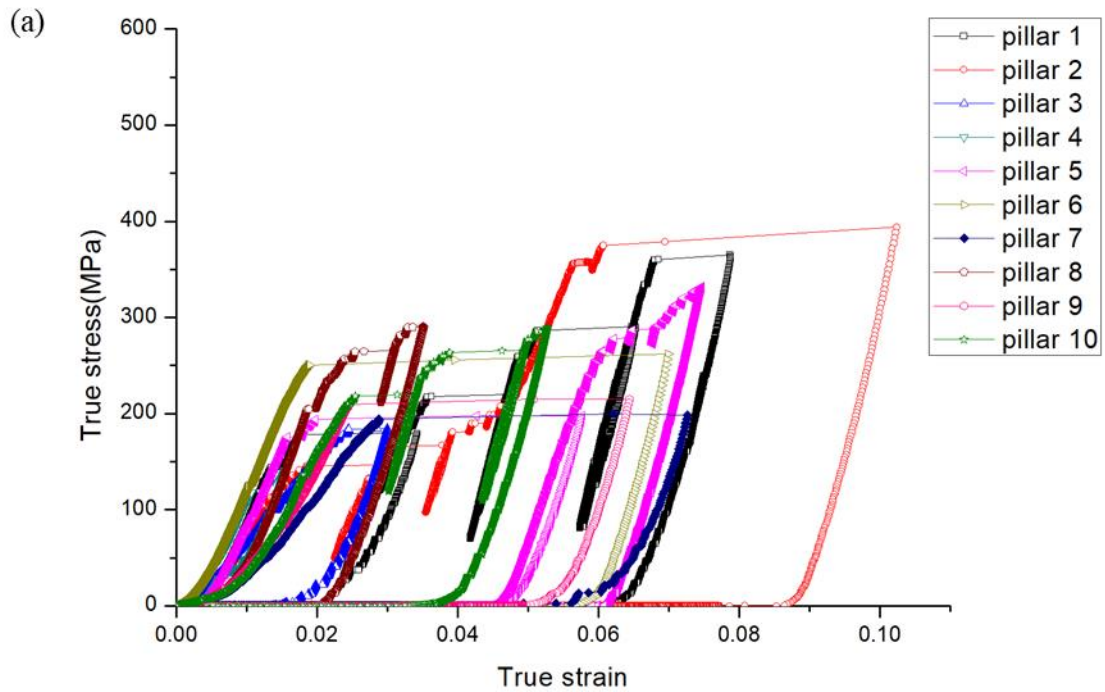
The second group of square micro-pillars was compressed in order to study the precipitate interaction with $\{01\bar{1}2\}$ twinning by the CRSS values, surface morphology, TKD and post-mortem TEM observations.

4.3.1 Mechanical behaviour

Compression of the solution treated and the aged specimens along $[01\bar{1}0]$ was performed to strains between 2% to 9%. This orientation was chosen in order to activate $\{01\bar{1}2\}$ extension twinning. 10 solution treated micro-pillars and 10 aged micro-pillars were compressed. Figure 4.17 shows the true stress-strain curves from (a) the solution treated and (b) the aged micro-pillars. Figure 4.17(c) are two stress-strain curves for detailed comparison of the solution treated and aged conditions. It is noted that there is a large variation in the stress-strain curves in Figure 4.17(a) and Figure 4.17(b). This is mainly attributed to the heterogeneous twinning nucleation. Both solution treated and aged micro-pillars show obvious strain bursts, and these strain bursts are attributed to twinning. As shown in Figure 4.17(c), the stress-strain curve obtained from the aged

micro-pillar shows more small strain bursts than that from the solution treated micro-pillar which is characterised by one large strain burst.

The mean yield strengths (0.2% proof stresses) were determined to be 176.8 ± 21.2 MPa and 237.1 ± 23.7 MPa for the solution treated specimen and the aged specimen, respectively. The 0.2% proof stress was increased by about 60 MPa after peak aging.



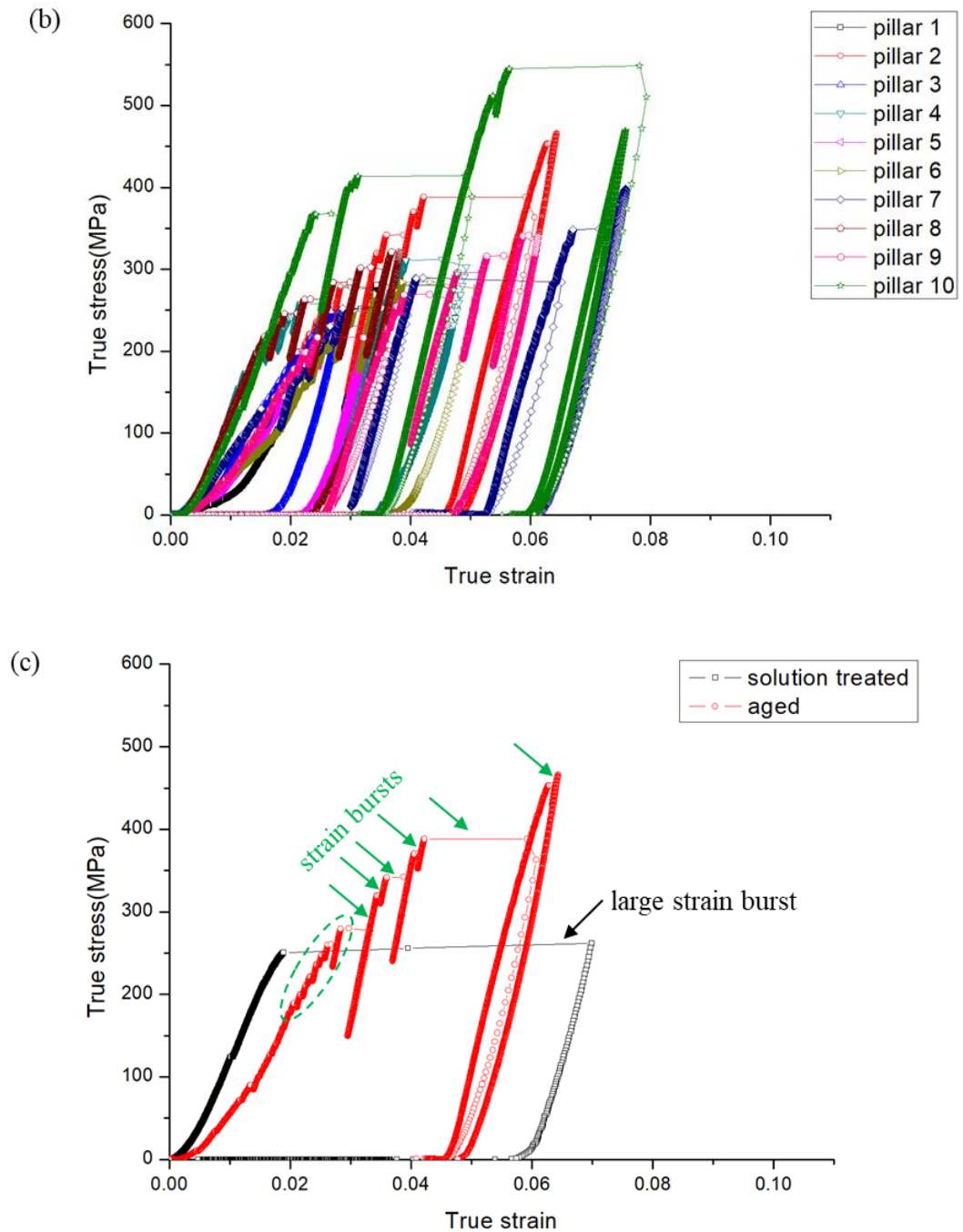


Figure 4.17 True stress-strain curves obtained from the compression of micro-pillars oriented for $\{01\bar{1}2\}$ twinning: (a) solution treated; (b) aged; and (c) solution treated and aged stress-strain curves. One large strain burst in the solution treated sample is indicated by a black arrow and more smaller strain bursts in the aged sample are indicated by green arrows and a green dashed ellipse.

4.3.2 Surface morphology of deformed micro-pillars

Representative SEM images of the deformed micro-pillars under $[01\bar{1}0]$ loading are given in Figure 4.18 and Figure 4.19. All the deformed micro-pillars show a slight buckling shape.

For the solution treated micro-pillars, some twins show weak contrast after compression, as shown in Figure 4.18. A solution treated micro-pillar shows one large strain burst in the stress-strain curve and one large twin band is in weak contrast in the corresponding SEM image (Figure 4.18(c)). For the micro-pillar with 7% strain, there are no twin bands in contrast as shown in Figure 4.18(d).

Figure 4.19 shows the SEM images of $[01\bar{1}0]$ oriented micro-pillars of aged AZ91 before compression and after compression to 2% strain (Figure 4.19(b)), 3.5% strain (Figure 4.19(c)), and 6% strain (Figure 4.19(d)). Figure 4.19(b-d) show many small twin bands after compression. It can be observed that the twinning bands start from the top part of the micro-pillar. They expand to the middle and bottom part of the micro-pillar as the plastic strain goes up to 3.5% and 6%. The twinning deformation starts from the top of the micro-pillar due to the high local stress during the compression tests.

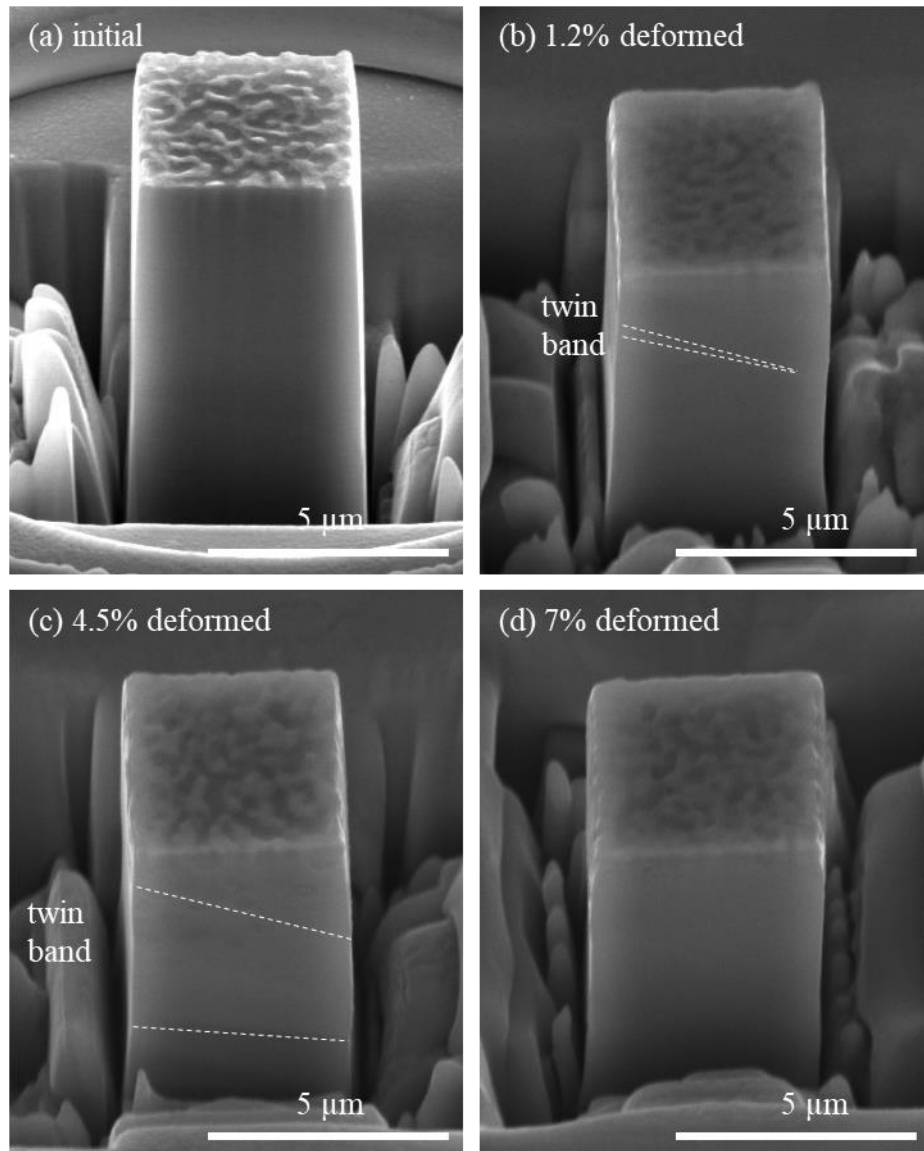


Figure 4.18 Representative SEM images of $[01\bar{1}0]$ oriented micro-pillars of solution treated AZ91 before compression and after compression to different strains, as noted. Image (a) was taken at a tilt angle of 52° and images of micro-pillars (b), (c) and (d) were taken at a tilt angle of 30° . The twin shows weak contrast and they are outlined by the white dashed lines.

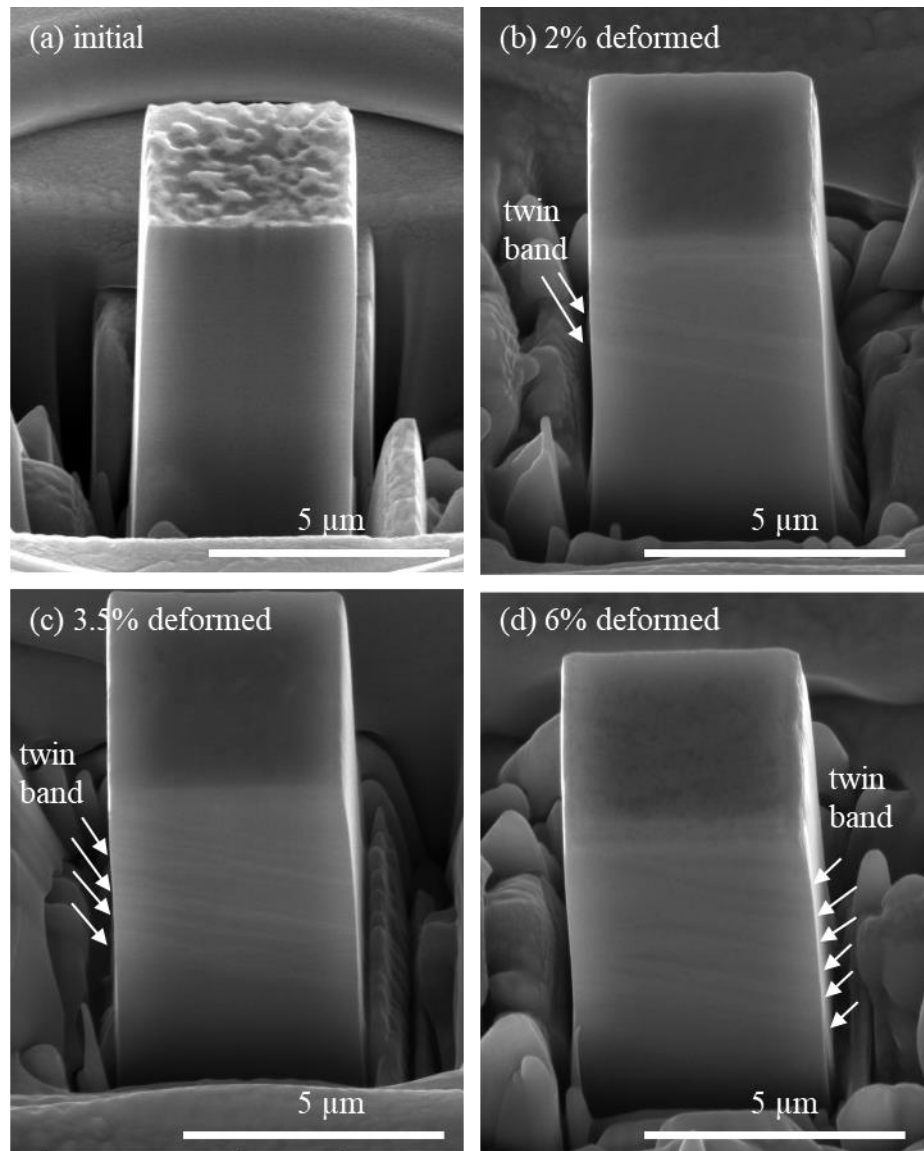


Figure 4.19 Representative SEM images of $[01\bar{1}0]$ oriented micro-pillars of aged AZ91 before compression and after compression to different strains, as noted in each image. Image (a) was taken at a tilt angle of 52° and images of micro-pillars (b), (c) and (d) were taken at a tilt angle of 30° .

4.3.3 Transmission electron microscopy results

For the solution treated specimen, a TEM foil extracted along the loading axis from a solution treated micro-pillar after 6% strain is shown in Figure 4.20(a) using the 0002 reflection and $BD \sim [2\bar{1}\bar{1}0]$ in the twin. The twin boundaries are outlined by yellow dashed lines. A large twin goes through the whole micro-pillar and a small twin locates at the top of the micro-pillar in the overview image Figure 4.20(a). $[2\bar{1}\bar{1}0]$ zone axis diffraction pattern taken from the twin (area ① in Figure 4.20(a)) and the matrix (area ② in Figure 4.20(a)) are shown in Figure 4.20(b) and Figure 4.20(c), respectively. The crystal axis is rotated about 86.3° (comparing the $[0001]$ axis of the twin and matrix). The large twin is identified as $[01\bar{1}1](0\bar{1}12)$ twin.

It is known that the solution treated micro-pillar is characterised by fewer and larger strain bursts. The strain bursts are attributed to extension twinning along the $[01\bar{1}0]$ loading direction. This can be confirmed by the TKD map of the solution treated micro-pillar after 5.5% strain which is shown in Figure 4.21, in which there is one large twin covering the majority of the micro-pillar. The orientation is changed with a rotation axis of $[2\bar{1}\bar{1}0]$ and a misorientation angle of about 87° as shown in Figure 4.21(c). The twin is identified as tension twin.

The TKD result shows that the compression direction is aligned along $[2\bar{1}\bar{1}\bar{1}\bar{8}]$ in the twin. The $[2\bar{1}\bar{1}\bar{1}\bar{8}]$ direction favours $\langle c + a \rangle$ slip with the highest Schmid factor 0.483. Basal $\langle a \rangle$ slip is also favourable within the twin because of the low CRSS.

$\langle c + a \rangle$ and $\langle c \rangle$ dislocations within the twin are shown in the TEM bright field images given in Figure 4.22. Two dislocations are outlined by the dashed ellipses in Figure

4.22(a-c). Using the diffraction vector $g = 0002$, dislocations ① and ② are visible in the twinned region, indicating that these are not $\langle a \rangle$ dislocations but $\langle c + a \rangle$ or $\langle c \rangle$ dislocations. Dislocation ① is still in contrast for $g = 1\bar{2}10$ and it is thus identified as a $\langle c + a \rangle$ dislocation. Dislocation ② is out of contrast for $g = 1\bar{2}10$ and it is thus identified as a $\langle c \rangle$ dislocation.

Basal $\langle a \rangle$ dislocations within the twin are shown in the TEM bright field images given in Figure 4.23. $\langle c + a \rangle$ or $\langle c \rangle$ dislocations are both visible for $g = 0002$ and $g = 01\bar{1}\bar{1}$, and they are indicated by the blue lines in Figure 4.23(c). Some basal dislocations are visible for $g = 01\bar{1}\bar{1}$ and invisible for $g = 0002$. The basal dislocations are indicated by the yellow lines in Figure 4.23(c).

Apart from the dislocations, there are stacking faults in the twinned region. Figure 4.24 shows a bright field image taken under $g = 01\bar{1}0$ and $BD \sim [2\bar{1}\bar{1}0]$ in the twinned region. Figure 4.24(a) and (b) show the stacking faults almost edge-on and looking like long straight lines parallel to (0001) . Figure 4.24(c) shows the stacking fault fringes when the sample is tilted along $01\bar{1}0$. The stacking faults are attached to either the twin boundaries or the micro-pillar surface in the solution treated specimen. The existence of stacking faults lying on basal planes in the twins has been widely reported for Mg alloys [120-123].

Basal $\langle a \rangle$ dislocations are also activated in the matrix region in the solution treated micro-pillar. TEM bright-field images in Figure 4.25 shows the existence of basal dislocations in the matrix. All dislocations are invisible for $g = 0002$ indicating they are basal dislocations. Some basal dislocations are visible for $g = 01\bar{1}\bar{1}$ and $g = 10\bar{1}1$.

For the aged micro-pillars, a TEM foil extracted along the loading axis is shown in Figure 4.26 using $g = 0002$ and $BD \sim [2\bar{1}\bar{1}0]$ within the twin. This micro-pillar was compressed by 5%. Some twins show clear contrast, and the twin boundaries are outlined by yellow dashed lines. Some tiny twins are not clear in this montage image due to the low magnification. This montage image shows more smaller twins are activated compared with the solution treated micro-pillar as shown in Figure 4.20. $[2\bar{1}\bar{1}0]$ diffraction patterns taken from the twin (area ① in Figure 4.26(a)) and the matrix (area ② in Figure 4.26(a)) are shown in Figure 4.26(b) and Figure 4.26(c), respectively. The crystal is rotated by 86.3° (comparing $[0001]$ of the twin and matrix), confirming the extension twinning activation. This twin is identified as $[0\bar{1}\bar{1}1](01\bar{1}2)$ twin.

Figure 4.27(a) is the band contrast map in TKD of the aged micro-pillar after 2% strain, showing 4 smaller twins activated by the compression. Figure 4.27(b) is the band contrast map image in TKD of the aged micro-pillar after 5% strain, showing more smaller twins activated by the compression. The TKD index rate for the aged specimens in Figure 4.27 is less than 50%, possibly due to the stress field introduced by the precipitates in the matrix and in the twin. The misorientation angle indexed by the TKD is not as reliable as for the solution treated specimen. The twin type confirmation is only achieved via TEM, as shown in Figure 4.26(b) and (c).

Figure 4.28(a) is a higher magnification TEM bright field image with $g = 01\bar{1}0$ of the aged micro-pillar after 5% strain, showing the twins, matrix and precipitates. Figure 4.28(b) is a schematic diagram corresponding to Figure 4.28(a). Many small twins are clearly shown in Figure 4.28(a) and (b). The selected diffraction pattern for the red-box

area in Figure 4.28(a) is shown in Figure 4.28(c) and the twin is identified as $[01\bar{1}1](0\bar{1}12)$.

The interaction of the $\{01\bar{1}2\}$ twin with precipitates in the aged specimen is illustrated in Figure 4.28(a). Three precipitates are labelled ①, ② and ③. Three stages of the interaction can be seen in this image. Stage 1 is when the tip of the twin just reaches the precipitate as exemplified by precipitate ①. Stage 2 is when half of the precipitate ② has been embedded while the precipitate ③ has been completely engulfed by the twin. The red dashed line in Figure 4.28(a) indicates a small rotation of about 4° for the precipitate ② which has been partly engulfed by the twin. This is consistent with the equivalent rotation angle of 86.3° expected between the matrix and the twin. The precipitates in Figure 4.28(d), which are highlighted by yellow arrows, led to the curved twin boundary when the twin boundary passes through the precipitate.

Many dislocations can be seen within the twinned region in the aged deformed micro-pillar as shown in Figure 4.29. Figure 4.29(a-c) show TEM bright field images taken under different two beam conditions. The schematic diagram and colour coding for the dislocations corresponding to Figure 4.29(a-c) are shown in Figure 4.29(d). In Figure 4.29(d), the twin boundaries are indicated by black dotted lines and the precipitates are indicated by grey rectangles. They are traced from Figure 4.29(a). Precipitates ① and ② are highlighted by yellow dashed quadrangles in Figure 4.29(a-c) to study whether there are interactions between precipitates and dislocations in the twin. Using the diffraction vector $g = 0002$, red dislocations and cyan dislocations are observable in the twinned region, indicating that these are not $\langle a \rangle$ dislocations and that the Burgers vectors of these dislocations are $\langle c + a \rangle$ or $\langle c \rangle$. Using the diffraction vector $g = \bar{1}210$, red dislocations

are in contrast while the cyan dislocations are out of contrast, indicating that the red dislocations are $\langle c + a \rangle$ and the cyan ones are $\langle c \rangle$. The purple dislocations in Figure 4.29(d) are out of contrast for $g = 0002$ and in contrast for $g = \bar{2}110$, and they are thus identified as basal $\langle a \rangle$ dislocations. For the aged micro-pillars, there are $\langle c + a \rangle$, $\langle c \rangle$ and basal dislocations which is the same as for solution treated micro-pillars. No interactions between precipitates and $\langle c + a \rangle$, $\langle c \rangle$ and basal dislocations have been observed.

Figure 4.30 shows the stacking faults formed in the twinned region in the aged micro-pillar. The stacking faults are almost edge-on and look like straight lines parallel to (0001). Therefore the stacking faults are on (0001). The stacking faults in the aged specimen were located between precipitates (Figure 4.30) apart from those attached to the twin boundaries and the specimen surface. Furthermore, the stacking faults in the aged sample are shorter than those in the solution treated sample due to their location between precipitates.

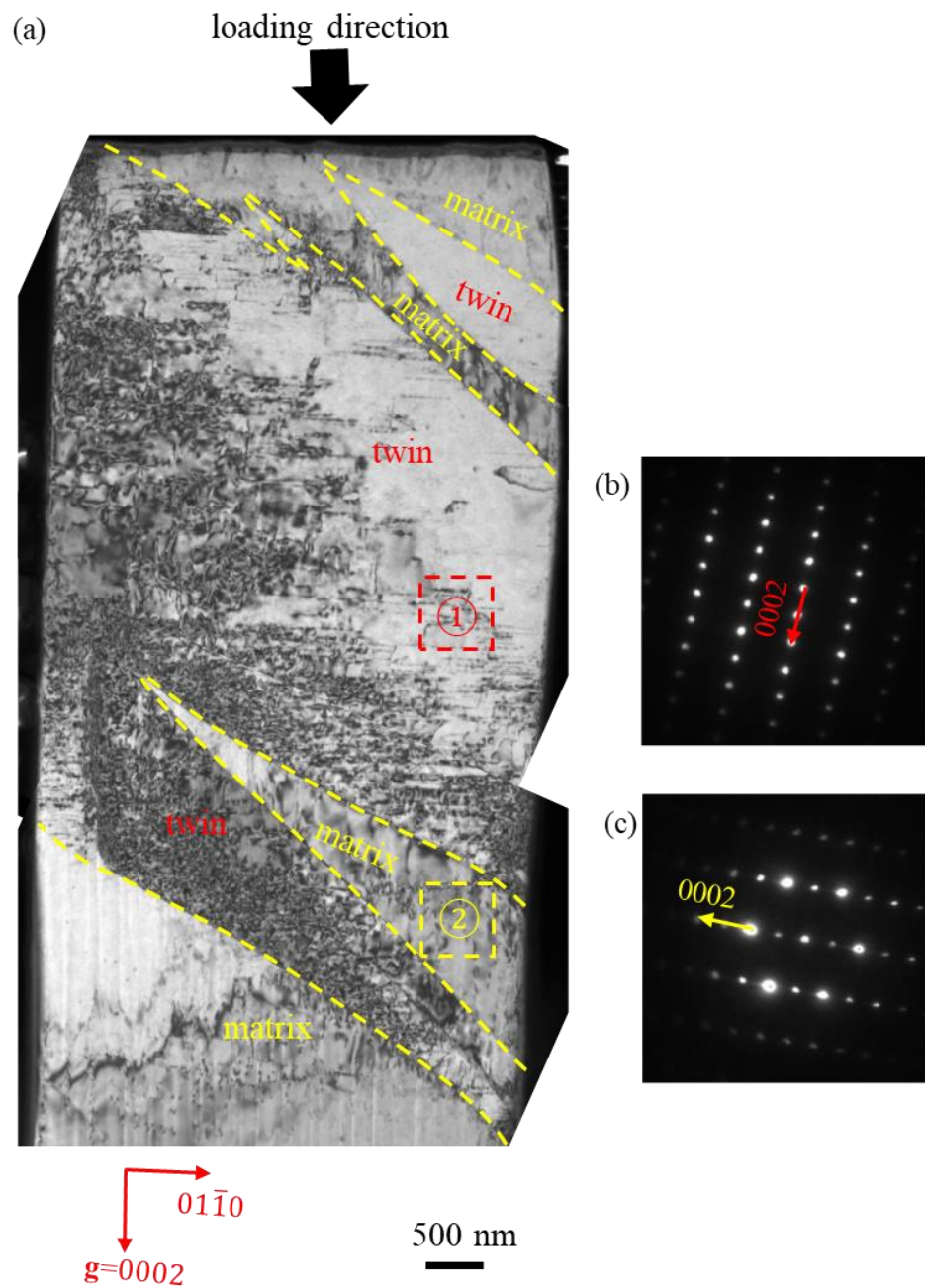


Figure 4.20 (a) A bright field image showing the TEM foil extracted along the loading axis from a 6% strained solution treated micro-pillar. $g = 0002$, $BD \sim [\bar{2}110]$ in the twin. The twin boundaries are outlined by yellow dashed lines. (b) $[\bar{2}110]$ diffraction pattern in the twin taken from area ① of Figure 4.20(a). (c) $[\bar{2}110]$ diffraction pattern in the matrix taken from area ② of Figure 4.20(a).

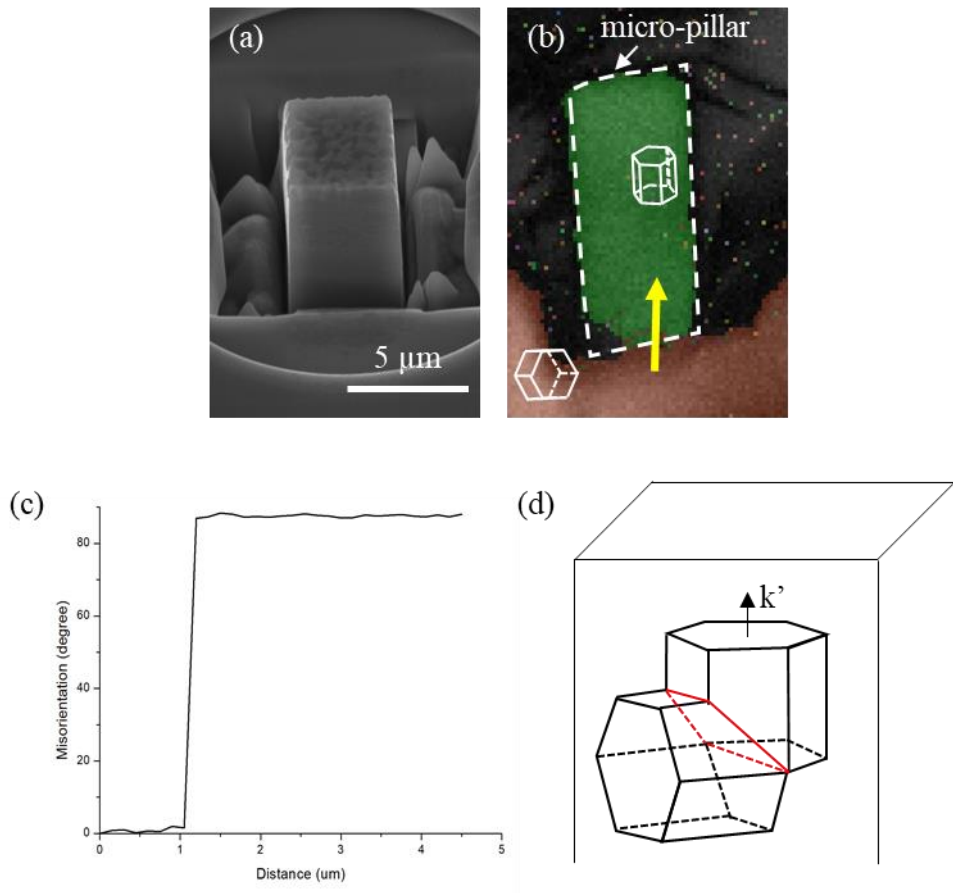


Figure 4.21 (a) SEM image of a 5.5% deformed solution treated micro-pillar initially oriented with $[01\bar{1}0]$ loading axis showing no obvious deformation band. (b) is the associated TKD map. (c) is the misorientation profile measured along the yellow arrow direction in (b). (d) orientation relationship of the twin and matrix.

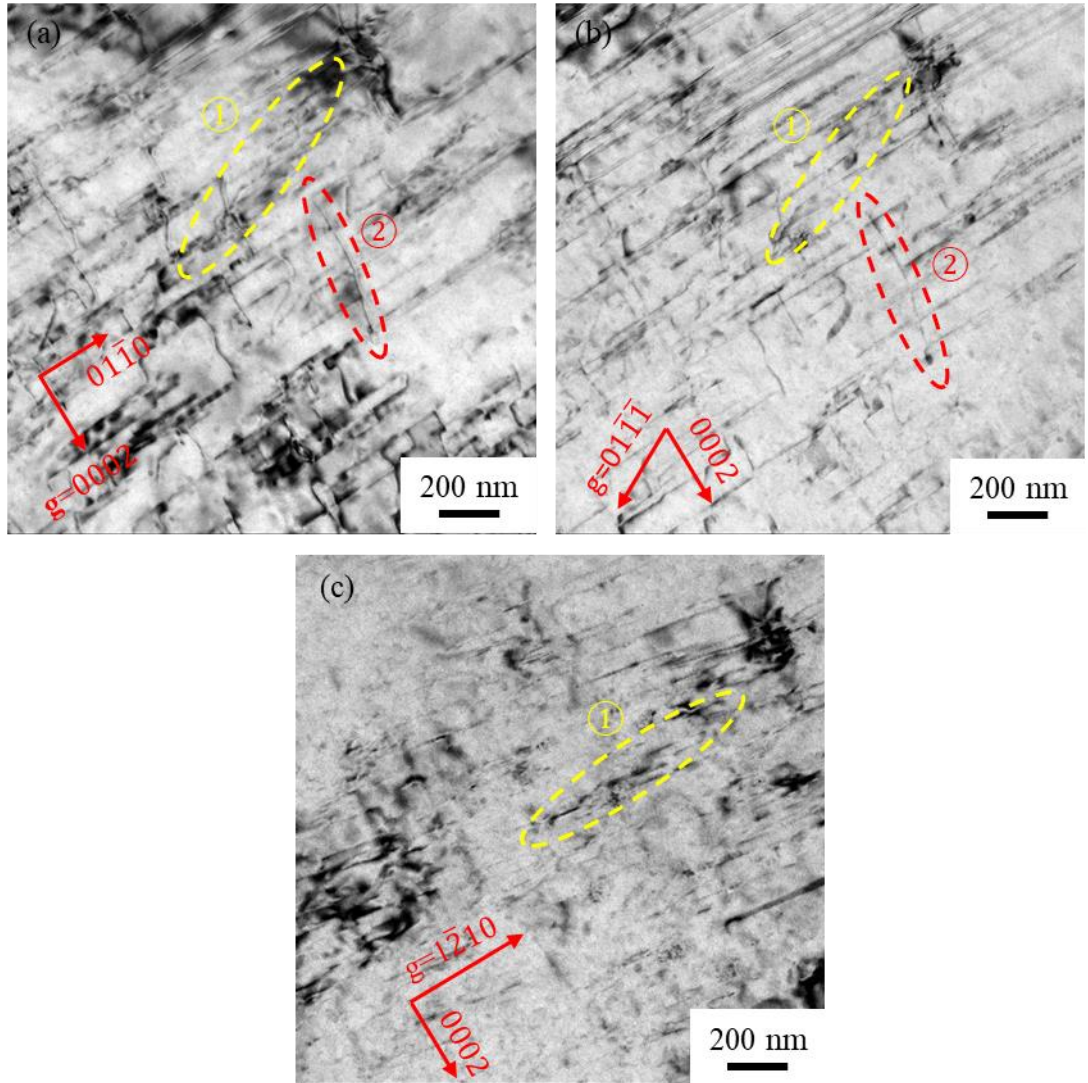


Figure 4.22 TEM bright-field images taken under different two-beam conditions showing the existence of dislocations in the twinned regions in the solution treated micro-pillar. Two dislocations (named as dislocations ① and ②) are highlighted by the dashed ellipses in Figure 4.22(a-c) (a) $g = 0002$, $BD \sim [\bar{2}110]$, (b) $g = 01\bar{1}\bar{1}$, $BD \sim [\bar{2}110]$ and (c) $g = 1\bar{2}10$, $BD \sim [10\bar{1}0]$.

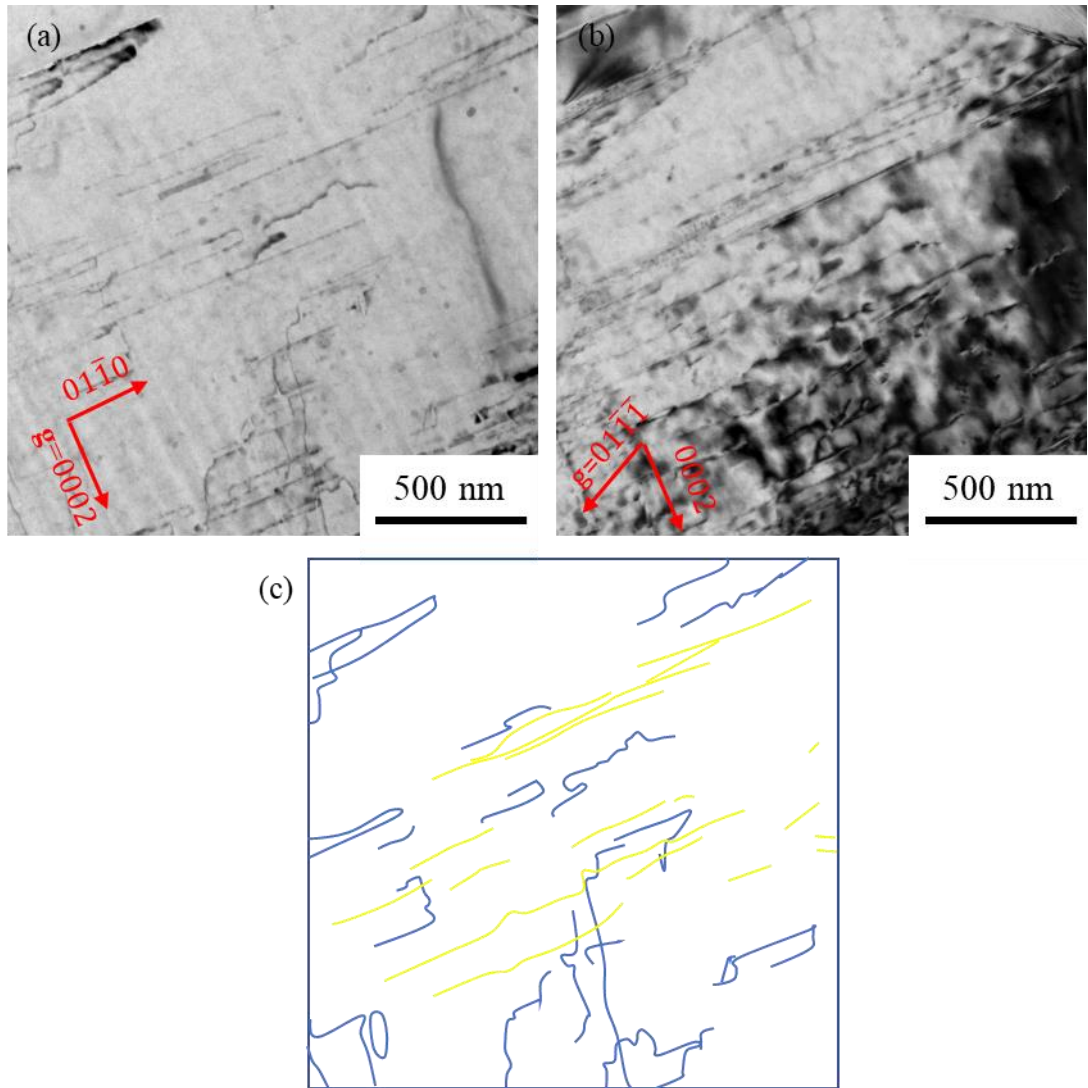


Figure 4.23 TEM bright-field images taken under different two-beam conditions showing the existence of dislocations in the twinned regions in the solution treated micro-pillar. (a) $g = 0002$, $BD \sim [2\bar{1}\bar{1}0]$, (b) $g = 01\bar{1}\bar{1}$, $BD \sim [2\bar{1}\bar{1}0]$. (c) Colour coding of the dislocations. The blue ones are traced from Figure 4.23(a) and the yellow ones are traced from Figure 4.23(b). Blue ones are visible for $g = 0002$, and they are identified as $\langle c + a \rangle$ or $\langle c \rangle$ dislocations. Yellow ones are invisible for $g = 0002$ and visible for $g = 01\bar{1}\bar{1}$, and they are identified as $\langle a \rangle$ dislocations.

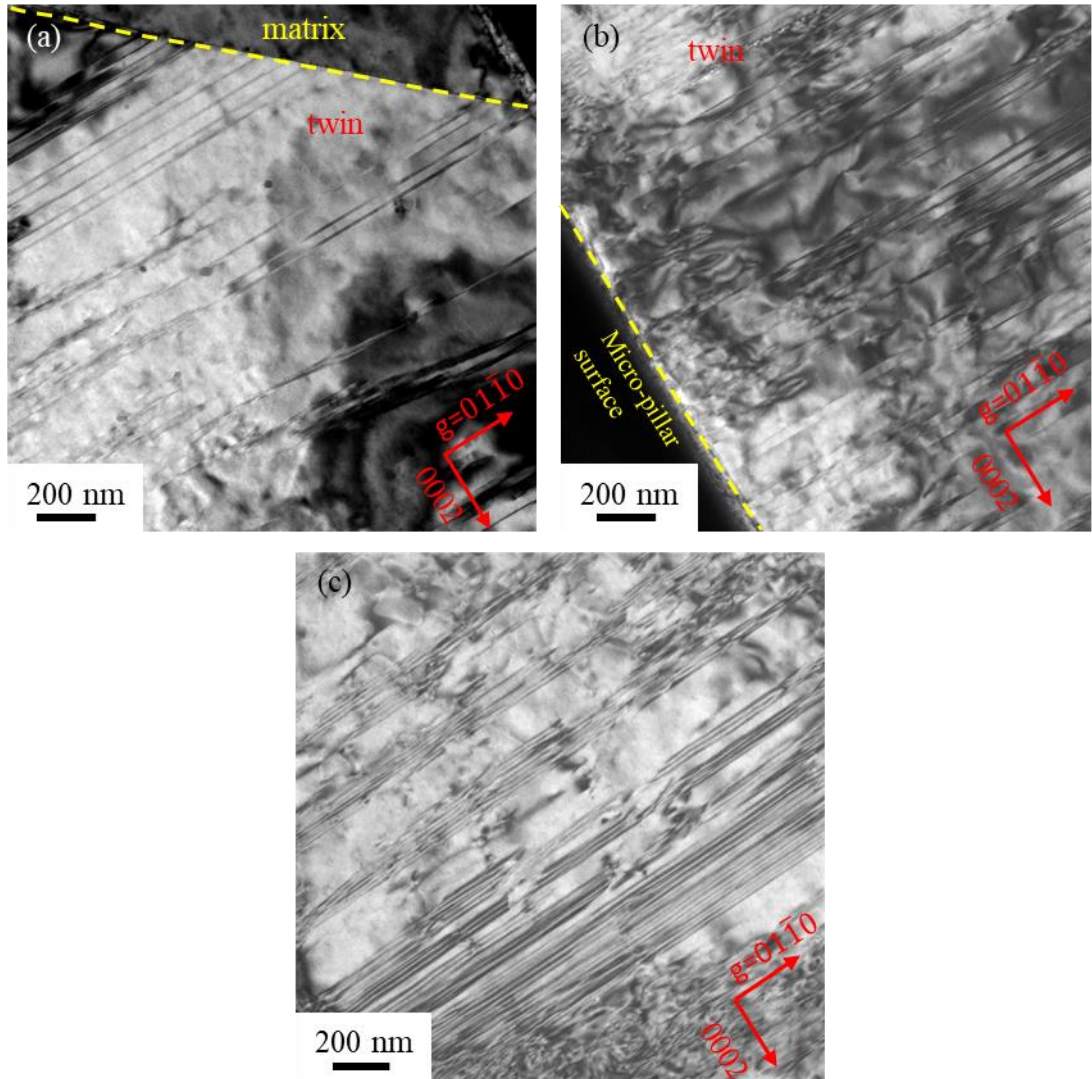


Figure 4.24 TEM bright-field images taken under two-beam conditions showing stacking faults in the twinned regions in the solution treated micro-pillar. $g = 01\bar{1}0$, $BD \sim [2\bar{1}\bar{1}0]$. Figure 4.24(a) and (b) show that the stacking faults are almost edge-on and looking like long straight lines parallel to (0001). Figure 4.24(c) shows the stacking fault fringes when the sample is tilted along $01\bar{1}0$, making the basal plane as wide as possible.

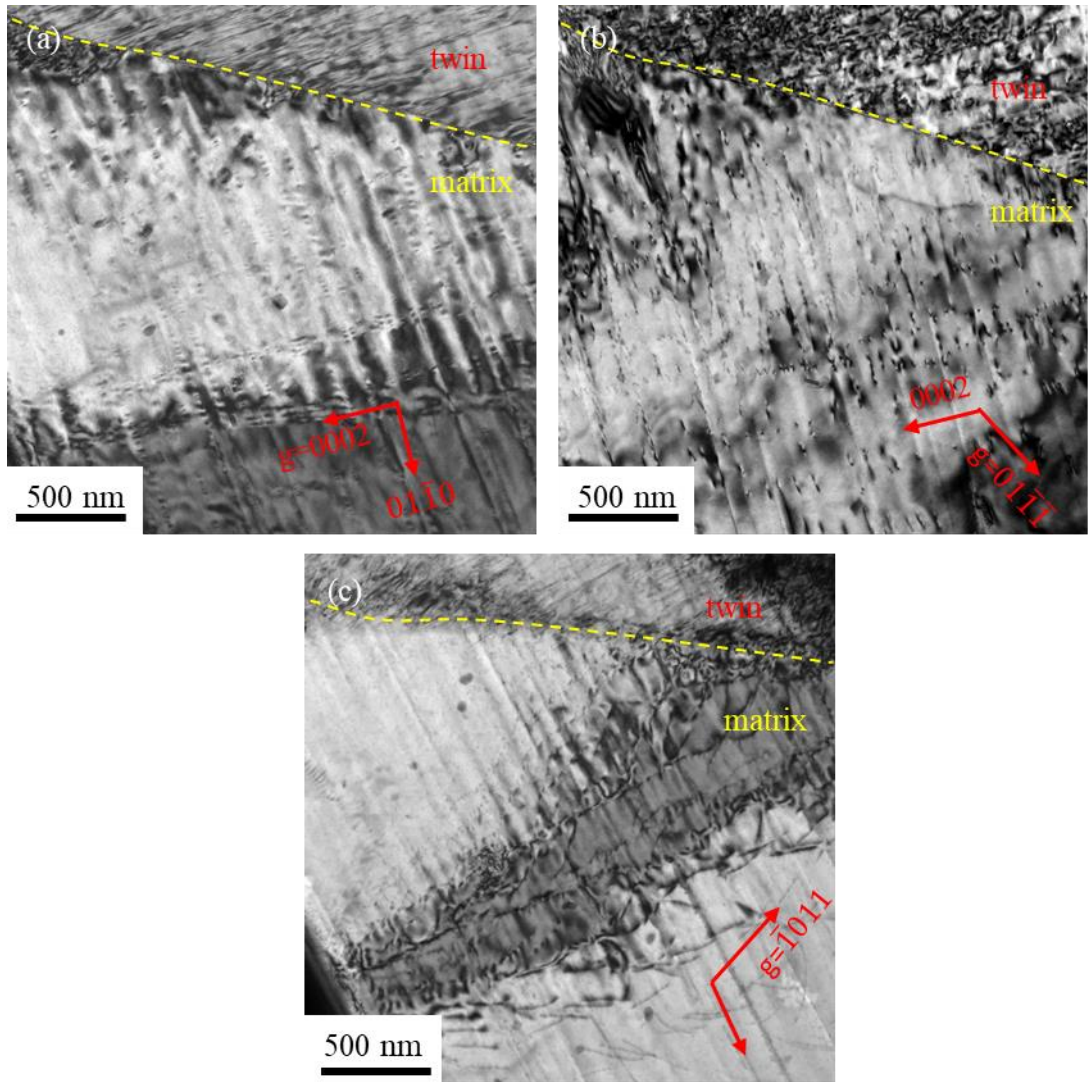


Figure 4.25 TEM bright-field images taken under various two-beam conditions showing the existence of basal $\langle a \rangle$ dislocations in the matrix region in the solution treated micro-pillar. (a) $g = 0002, BD \sim [2\bar{1}\bar{1}0]$, (b) $g = 01\bar{1}\bar{1}, BD \sim [2\bar{1}\bar{1}0]$ and (c) $g = \bar{1}011, BD \sim [2\bar{1}\bar{1}3]$.

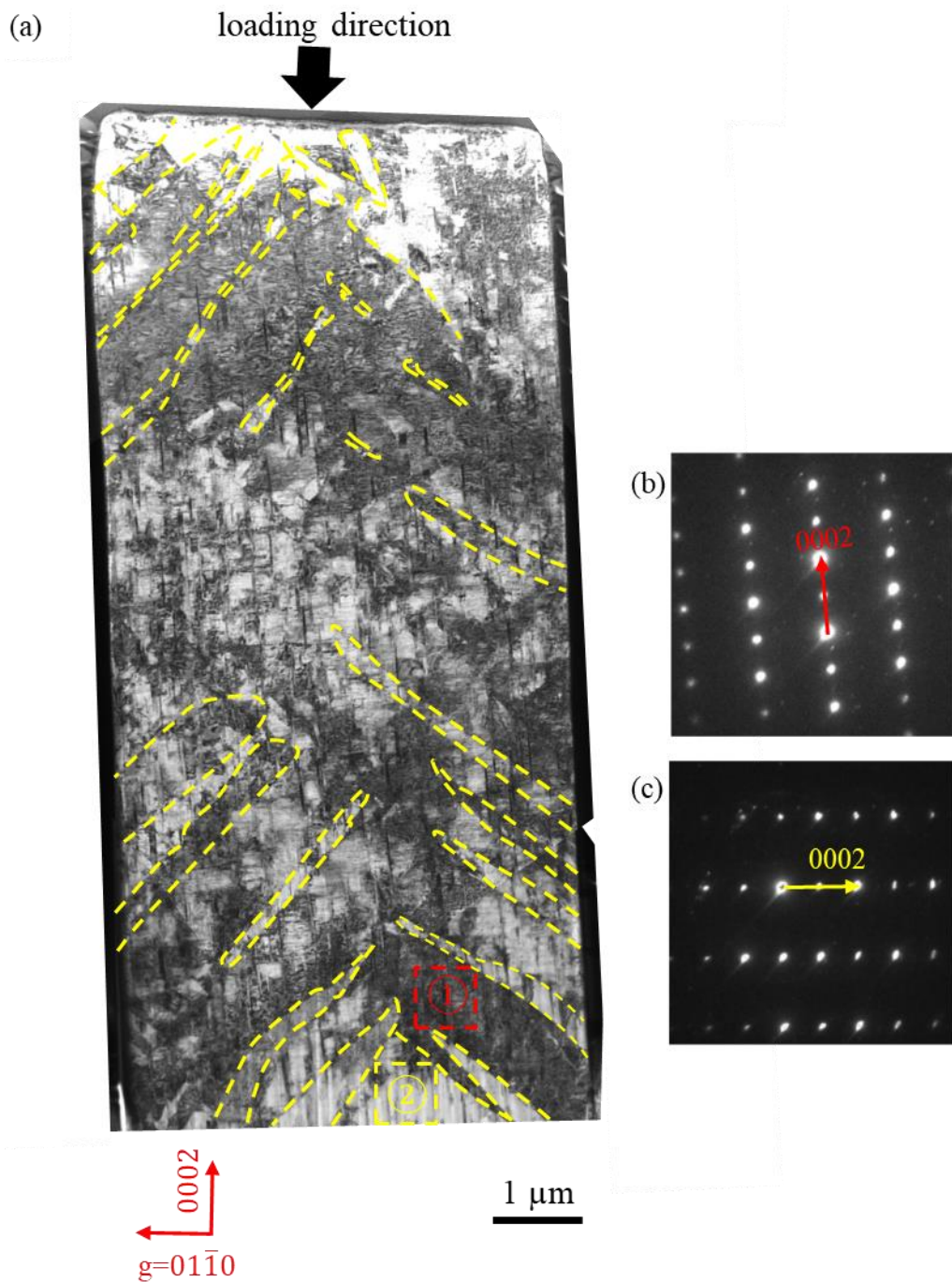


Figure 4.26 (a) A bright field image showing a TEM foil extracted along the loading axis from a 5% strain aged micro-pillar. $g = 01\bar{1}0$, $BD \sim [\bar{2}110]$ in the twin. Some twin boundaries are highlighted by yellow dashed lines. (b) $[\bar{2}110]$ diffraction pattern from the twinned area ① of (a). (c) $[\bar{2}110]$ diffraction pattern from the matrix area ② of (a).

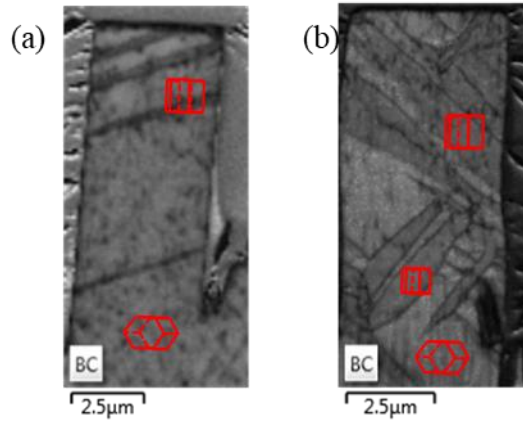


Figure 4.27 (a) Band contrast map in TKD of the aged micro-pillar after 2% strain. (b) Band contrast map in TKD of the aged micro-pillar after 5% strain.

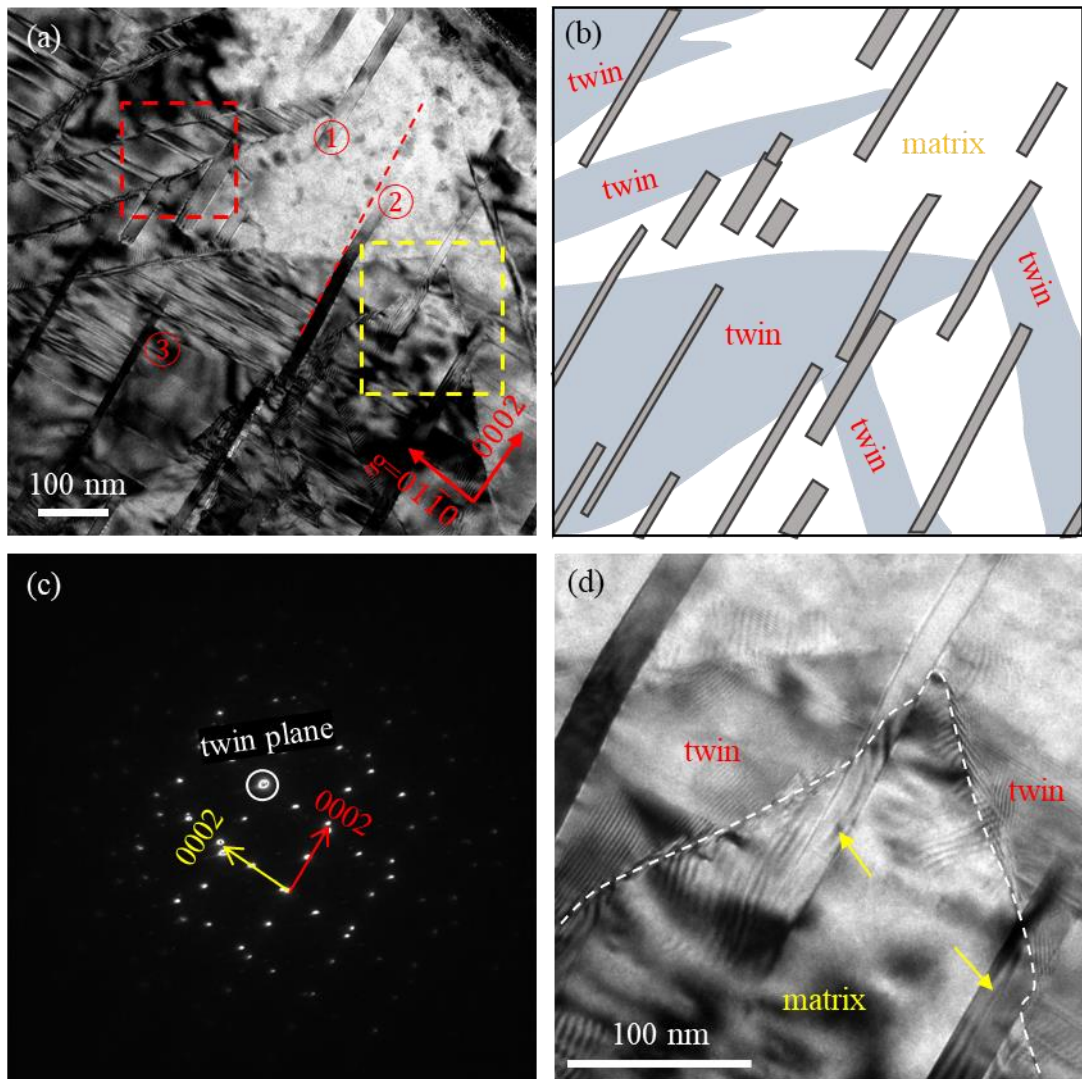


Figure 4.28 (a) A TEM bright field image of the aged micro-pillar after 5% strain, showing twins, matrix and precipitates with $g = 01\bar{1}0$ and $BD \sim [2\bar{1}\bar{1}0]$ in the twins. Precipitates ①, ② and ③ are labelled showing the interaction between precipitate and twin. (b) is a schematic diagram corresponding to (a). Twins are indicated by blue areas, precipitates are indicated by grey rectangles and the remaining white areas indicate the matrix. The selected diffraction pattern from the red-box area in (a) is shown in (c), confirming $[01\bar{1}1](0\bar{1}12)$ twin. (d) is the enlarged yellow-box area in (a), showing the precipitate induced curved twin boundary (highlighted by the white dashed lines). Moire fringes appear in the twin, matrix and precipitates in Figure 4.28(d).

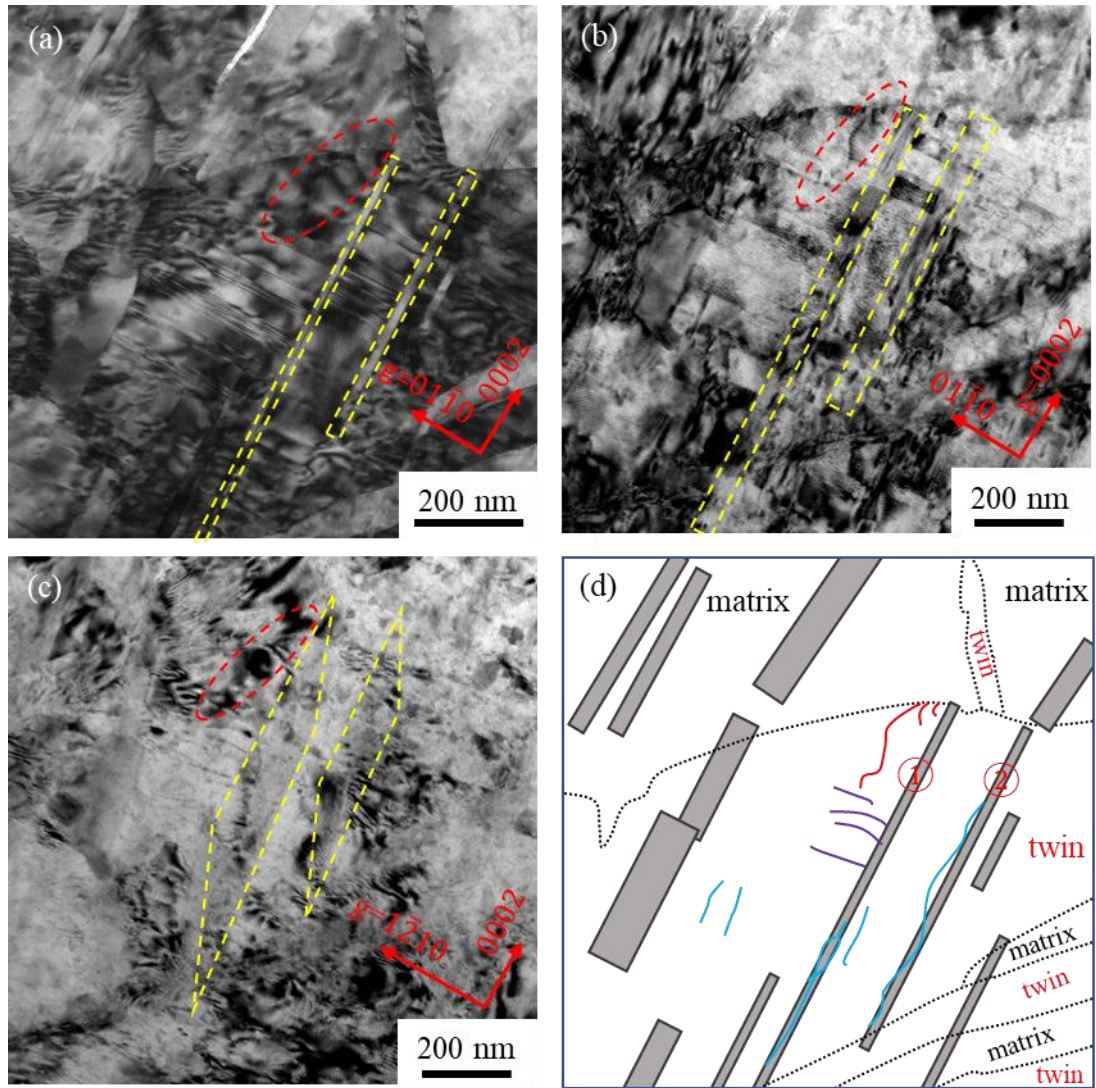


Figure 4.29 (a-c) TEM bright-field images taken under various two-beam condition showing dislocations in the twin. (a) $g = 01\bar{1}0$ and $BD \sim [2\bar{1}\bar{1}0]$. (b) $g = 0002$ and $BD \sim [2\bar{1}\bar{1}0]$. (c) $g = 1\bar{2}10$ and $BD \sim [10\bar{1}0]$. (d) is a schematic diagram and colour coding of the dislocations traced from Figure 4.29(a-c). The twin boundaries are indicated by black dotted lines. The precipitates are indicated by grey rectangles. The twin boundaries and precipitates are traced from Figure 4.29(a). Precipitates ① and ② are outlined by yellow dashed quadrangles in Figure 4.29(a-c). The red dislocations in Figure 4.29(d) are all visible for $g = 0002$, $g = 01\bar{1}0$ and $g = 1\bar{2}10$, and they are thus

identified as $\langle c + a \rangle$ dislocations. These $\langle c + a \rangle$ dislocations are also outlined by the red dashed ellipse in Figure 4.29(a-c). The cyan dislocations in Figure 4.29(d) are visible for $g = 0002$ and invisible for $g = 1\bar{2}10$, and they are therefore identified as $\langle c \rangle$ dislocations. The purple dislocations in Figure 4.29(d) are invisible for $g = 0002$ and visible for $g = 1\bar{2}10$, and they are identified as basal $\langle a \rangle$ dislocations.

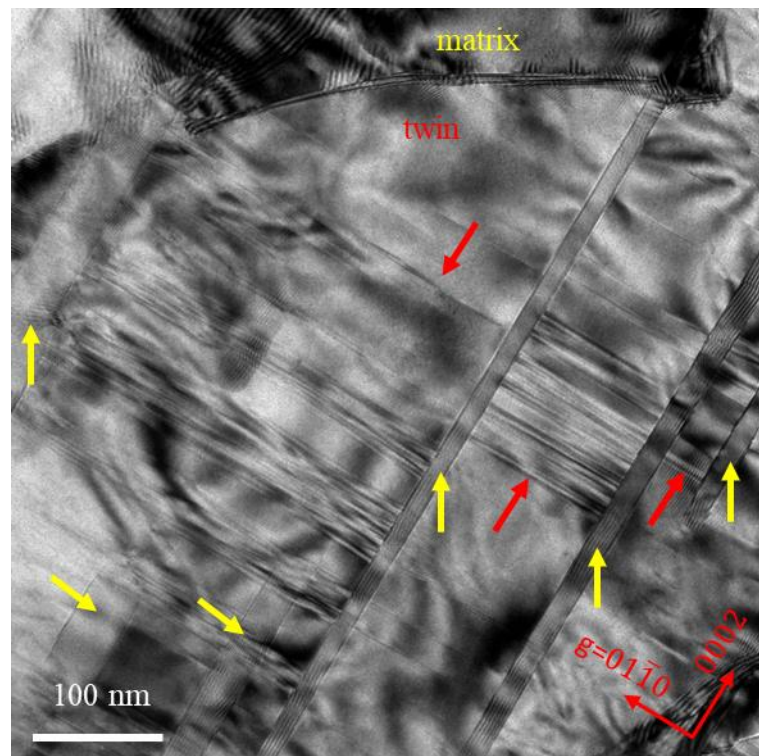


Figure 4.30 TEM bright-field image showing stacking faults in the twinned region in an aged specimen. The precipitates are indicated by yellow arrows and the stacking faults are indicated by red arrows.

4.3.4 Summary

The precipitate interaction with tension twins has been analyzed by micro-pillar compression along $[01\bar{1}0]$. The deformation behaviour is revealed by the stress-strain curves, SEM, TKD and TEM characterization.

The stress-strain curves show that both the solution treated and peak-aged micro-pillars are characterized by strain bursts and these strain bursts are attributed to tension twinning. There are more and smaller strain bursts in the aged micro-pillar than that in the solution treated micro-pillar which is characterised by less and larger strain bursts. The mean yield strengths (0.2% proof stresses) were determined to be 176.8 ± 21.2 MPa and 237.1 ± 23.7 MPa for the solution treated specimen and the aged specimen, respectively. The 0.2% proof stress was increased by about 60 MPa with the precipitation.

SEM images of the deformed micro-pillars under $[01\bar{1}0]$ loading show a slight buckling shape and show twin bands in weak contrast. More and smaller twin bands are observed on the aged micro-pillar surface than that on the solution treated micro-pillar surface.

TEM observations show that the tension twin has been activated in both the solution treated and aged specimens. Basal $\langle a \rangle$, $\langle c + a \rangle$ and $\langle c \rangle$ dislocations exist in the twinned region in both the solution treated and aged specimens. Stacking faults lying on (0001) have been observed in the twin in both the solution treated and aged specimens. The precipitate affects the tension twinning in the following ways:

(1) More and smaller twins are obtained in the specimen with precipitates than that in the specimen without precipitates.

(2) The stacking faults in the solution treated specimen are attached to either the twin boundaries or the micro-pillar surface. The stacking faults in the aged specimen are located between precipitates, apart from those attached to the twin boundaries and the specimen surface. Furthermore, the stacking faults in the aged sample are shorter than those in the solution treated sample due to their location between precipitates. A higher density of stacking faults is generated in the aged than in the solution-treated samples.

(3) The precipitate can be partly or completely engulfed by the twin and the precipitate itself is not twinned during deformation. The precipitate shows a small rotation of about 4° when it is partly engulfed by the twin. Also precipitate would lead to the curved twin boundary when the twin boundary passes through the precipitate.

4.4 In-situ TEM Compression of submicron-pillars oriented for $\{01\bar{1}2\}$ twinning

The precipitates introduce more and smaller twins than those in the precipitate free specimens. However, whether the precipitates increase the stress for twin nucleation or inhibit their growth cannot be ascertained by micro-pillar testing. Thus, in-situ TEM compression of the solution treated and the aged submicron-pillars was performed along $[01\bar{1}0]$ to record the real-time mechanical response of the $\{01\bar{1}2\}$ twinning along with TEM observations to answer these questions.

4.4.1 Mechanical behaviour

In-situ TEM compression of the solution treated and aged submicron-pillars was performed to different strains. 4 solution treated pillars and 4 aged pillars were fabricated and compressed. Figure 4.32 shows the true stress-strain curves for the solution treated and the aged pillars. The stress-strain curves are reasonably consistent for the solution treated and aged specimens.

The yield point is where the specimen starts to deform plastically. The yield stress is taken to be the stress required to produce 0.2% permanent strain because it is often hard to point out the exact stress where the plastic deformation starts. The in-situ TEM shows that twin

nucleation occurs either before or after the 0.2% strain. It is not accurate to describe the stress for twin nucleation by the 0.2% strain offset rule. In the present work, the stress for the first twin nucleation is obtained by correlating the in-situ TEM movies which record the twin deformation and the mechanical data. The example of first apparent twin nucleation stress confirmation for the submicron-pillars is given below in Figure 4.31. The first twin nucleation stresses for all the submicron-pillars are listed in Table 4.2. The apparent first twin nucleation stress for solution treated and aged submicron-pillars are 325.7 ± 65.4 MPa and 332.8 ± 94.4 MPa, respectively.

For all specimens, the flow stresses of the submicron-pillars far exceed the micro-pillar strengths. This can be explained by the ‘smaller is stronger’ trend. Both the solution treated and the aged submicron-pillars show obvious strain bursts which are attributed to extension twinning, similar to the strain bursts in the micro-pillar compression.

The hardening rate Θ is calculated based on the true stress-strain curves in Figure 4.32.

The hardening rate is given by:

$$\Theta = \frac{\Delta\sigma_{stress}}{\Delta\varepsilon_{strain}} \quad \text{Equation 4.1}$$

where σ_{stress} is the true stress and ε_{strain} is the true strain. If the maximum strain is higher than 0.1, $\Delta\varepsilon_{strain}$ is determined by a strain range of 0.02 to 0.1. If the maximum strain is lower than 0.1, $\Delta\varepsilon_{strain}$ is determined by a strain range of 0.02 to the maximum strain reached [124-126].

Figure 4.33 shows the hardening rates (Θ) of the solution treated pillars and the aged pillars. The submicron-scale aged pillars show a higher hardening rate than the solution treated ones.

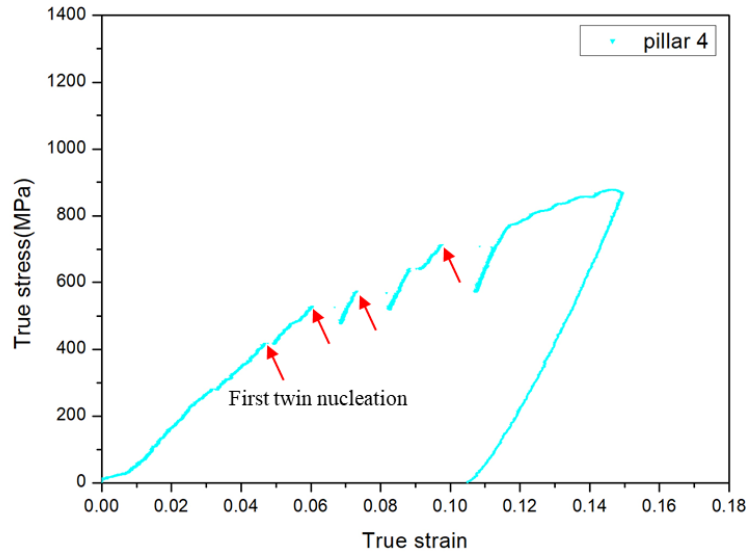


Figure 4.31 The example of overall twin nucleation stress. The red arrows indicate where the twin nucleation occurs correlating with the in-situ video. The stress at the first red arrow is taken as the first overall twin nucleation stress.

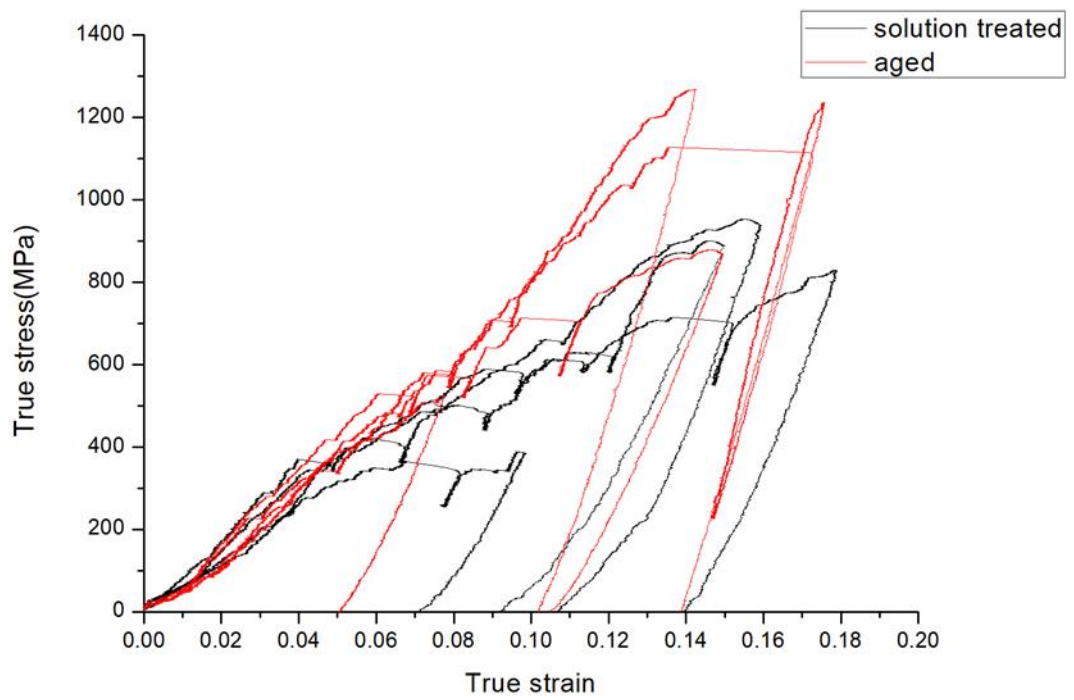


Figure 4.32 The true stress-strain curves for the solution treated and the aged submicron-pillars.

Table 4.2 First twin nucleation stress for each submicron-pillars

	Solution treated submicron-pillars/MPa	Aged submicron-pillars/MPa
Pillar 1	367.5	231.2
Pillar 2	365.0	349.5
Pillar 3	229.2	*
Pillar 4	341.1	417.9
Averaged stress	325.7 ± 65.4	332.8 ± 94.4

*: not used in the averaged stress calculation due to the different loading strategy.

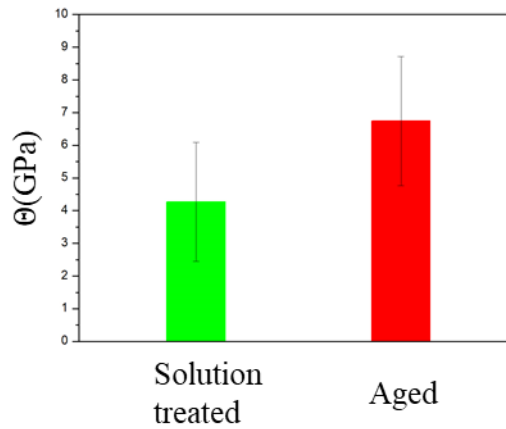


Figure 4.33 The hardening rate (θ) determined from true stress-strain curves in Figure 4.32.

4.4.2 Solution treated submicron-pillars

The crystal orientation of the foil to fabricate the pillars is shown in Figure 4.34 together with the SEM image. The loading direction was approximately parallel to $[01\bar{1}0]$. The

foil normal was near $[\bar{2}110]$ for a good view of real-time twin nucleation and growth due to the edge-on condition of the twinning plane.

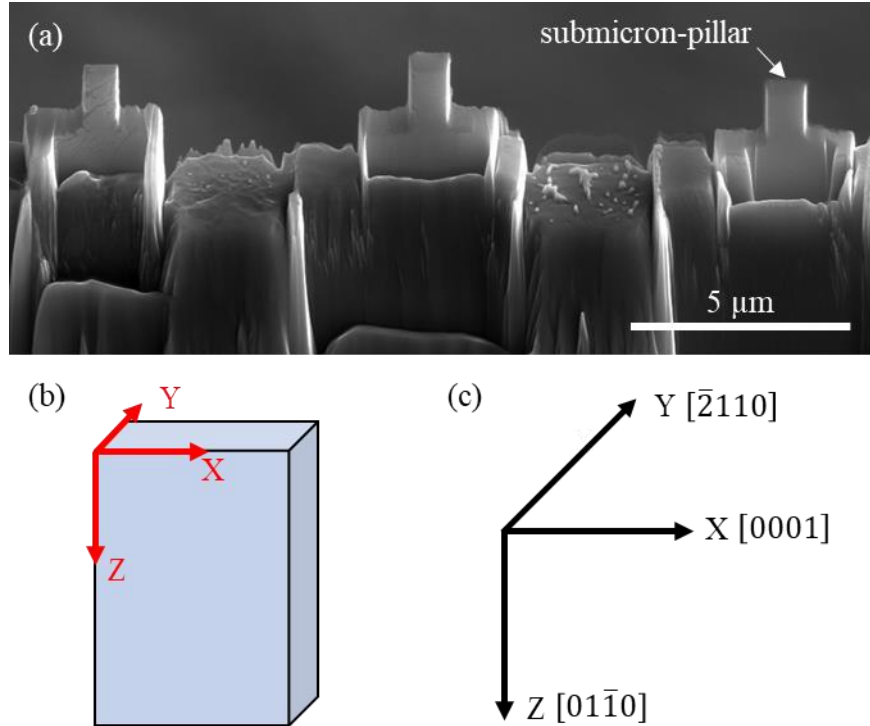


Figure 4.34 (a) SEM image showing the submicron-pillars. The image was taken at a tilt angle of 52° . (b) Schematic diagram showing the submicron-pillar shape. The front surface is the XZ plane as defined in Figure 4.34(c). (c) Crystal orientations measured by EBSD.

(1) Pillar 1

Figure 4.35 shows TEM bright field images of solution treated pillar 1 before in-situ TEM compression. Figure 4.35(a) shows no $\langle c + a \rangle$ or $\langle c \rangle$ dislocations in this pillar before compression using the 0002 reflection. Figure 4.35(b) shows the pre-existing basal $\langle a \rangle$ dislocations using the $01\bar{1}1$ reflection. The $[\bar{2}110]$ diffraction pattern in Figure 4.35(c)

confirms the loading direction to be $[01\bar{1}0]$. The loading direction is indicated by the yellow arrow in Figure 4.35.

Pillar 1 was compressed to around 6% strain. The real-time mechanical data and the corresponding microstructure were both recorded. Some frames extracted from the in-situ video are shown in Figure 4.36 in chronological order and the corresponding mechanical data are shown in Figure 4.37. The video was obtained using the $01\bar{1}1$ reflection. The deformation process is described as follows:

Figure 4.36(a) shows some of the pre-existing basal $\langle a \rangle$ dislocations in pillar 1 before compression. The pre-existing $\langle a \rangle$ dislocations were out of contrast and the elastic stress concentration region at the contact surface between the diamond tip and the pillar is shown clearly in Figure 4.36(b) and (c). This contact surface is called the top surface of the pillar in this thesis. The pillar was compressed continuously and reached an overall stress of approximately 367 MPa, when a twin nucleated from the top surface. The roughness of the diamond tip leads to a high local stress and this high local stress is favourable for twin nucleation. From the shape of this and later presented twins, the initial shear along the twinning direction is faster than subsequent shear, as shown in Figure 4.36(d). The first twin nucleation and immediate expansion correlate with the strain burst between points C and D in Figure 4.37. The twin grew laterally at a relatively slow speed as compared with the speed of twin nucleation and initial expansion. This twin grew as the stress increased from 367 MPa (Point C in Figure 4.37) to 636 MPa (Point I in Figure 4.37). The first twin propagated to the bottom of the pillar (the top area in the images). The propagation process is traced via the yellow dashed lines in Figure 4.36(e-i) and correlates with the E-I part in the stress-strain curve in Figure 4.37. The corner area

indicated by the red arrow in Figure 4.36(i) is where the second twin nucleates. A small second twin nucleated and propagated under the continuous compression (Figure 4.36(j)). The stacking faults and dislocations in the first twin are in contrast, which are outlined by the red dashed polygons in Figure 4.36(i-k).

Post-mortem TEM observations of pillar 1 are shown in Figure 4.38. The first twin is large and occupies almost the whole pillar. The dislocations in the twin are in contrast using the diffraction vector $g = 0002$ and they are thus identified as $\langle c + a \rangle$ or $\langle c \rangle$. The $[\bar{2}110]$ diffraction pattern in Figure 4.38(b) is taken from the matrix and the $[\bar{2}110]$ diffraction pattern in Figure 4.38(c) is from the twinned region. They confirm the $[0\bar{1}11](01\bar{1}2)$ twin. The fringes from the stacking fault in the twin are shown in Figure 4.38(d) when the specimen is tilted along $01\bar{1}0$. The stacking faults are on (0001) , similar to the stacking faults in the micro-pillars. The small second twin is outlined by a red circle in Figure 4.38(e).

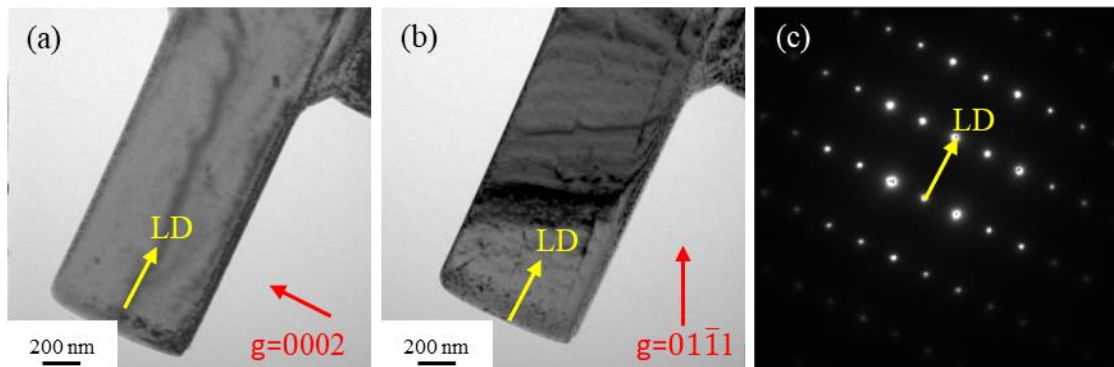


Figure 4.35 (a) TEM bright field image of pillar 1 before compression. The loading direction is indicated by the yellow arrow. $g=0002$ and $BD \sim [\bar{2}110]$. (b) Bright field image of pillar 1 before compression. $g=01\bar{1}1$ and $BD \sim [\bar{2}110]$. (c) $[\bar{2}110]$ diffraction pattern confirms the loading direction to be $[01\bar{1}0]$.

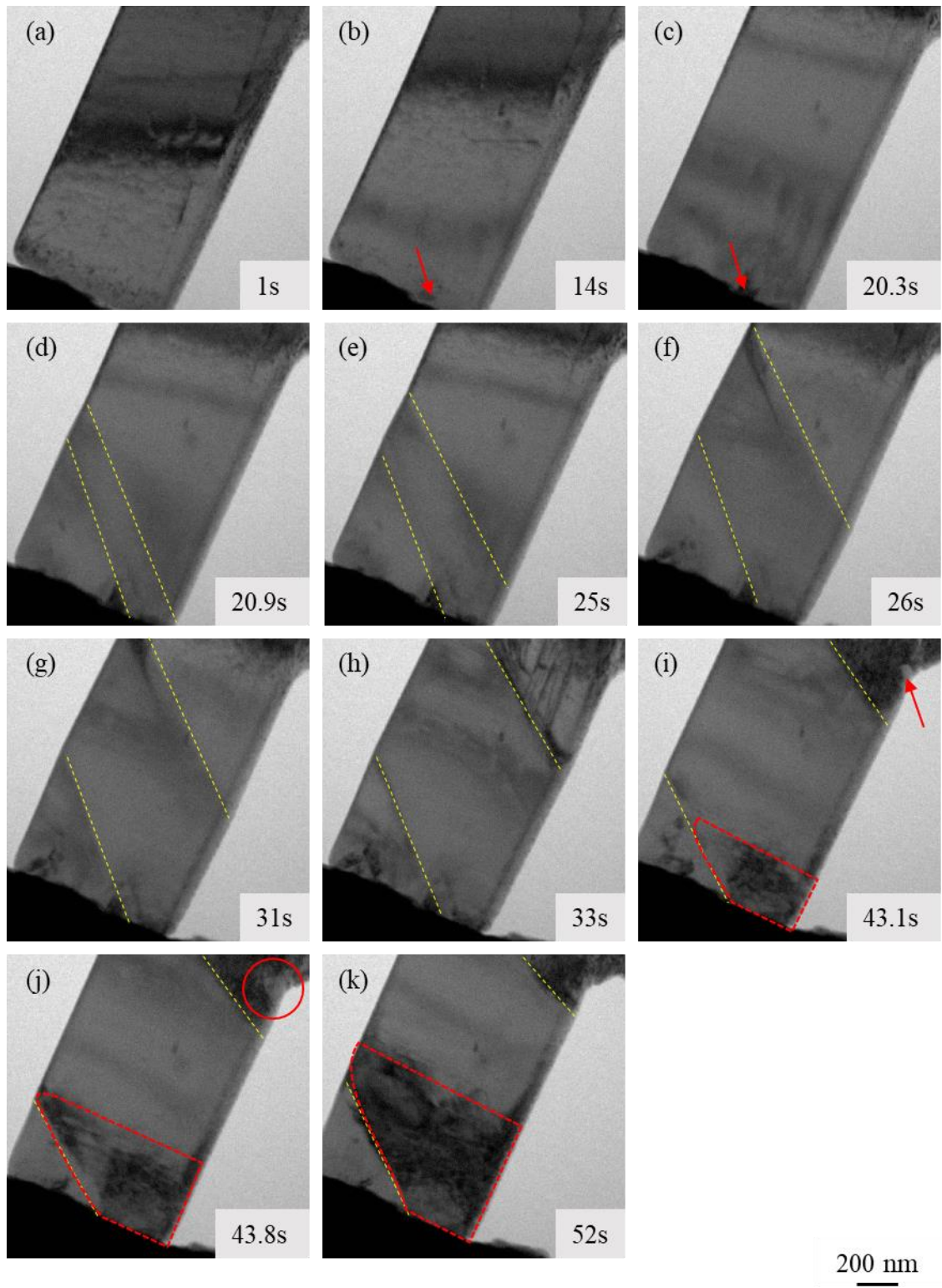


Figure 4.36 (a-k) are TEM bright field frames of solution treated submicron-pillar 1 from an in-situ video captured during compression. $g = 01\bar{1}1, BD \sim [\bar{2}110]$. The yellow

dashed lines indicate the twin boundary motion during compression. Images (a-k) correspond to points A-K in Figure 4.37. (a) shows the pre-existing basal $\langle a \rangle$ dislocations. (b) shows the elastic deformation process. (c) shows the stress concentration region before twin nucleation, indicated by a red arrow. The twin nucleation and initial twin propagation are shown in image (d). The twin continued growing with varying speeds from (d) to (i). (h) shows the activated basal $\langle a \rangle$ dislocations in the matrix. (i) shows a new stress concentration at the bottom corner of the pillar, highlighted by a red arrow. (j) shows a small second twin at the bottom corner of the pillar, outlined by a red circle. (k) shows contrast from the stacking faults on the basal planes and the dislocations in the twin. They are in the red-dashed polygons in images (i-k).

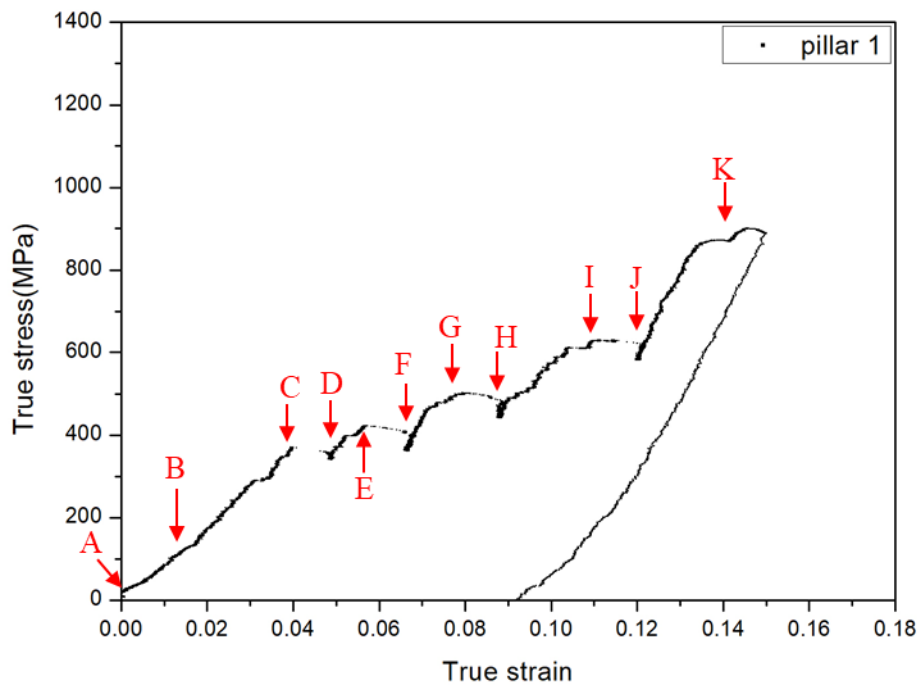


Figure 4.37 The true stress-strain curve for the solution treated submicron-pillar 1. Point A-K correspond to images (a-k) in Figure 4.36.

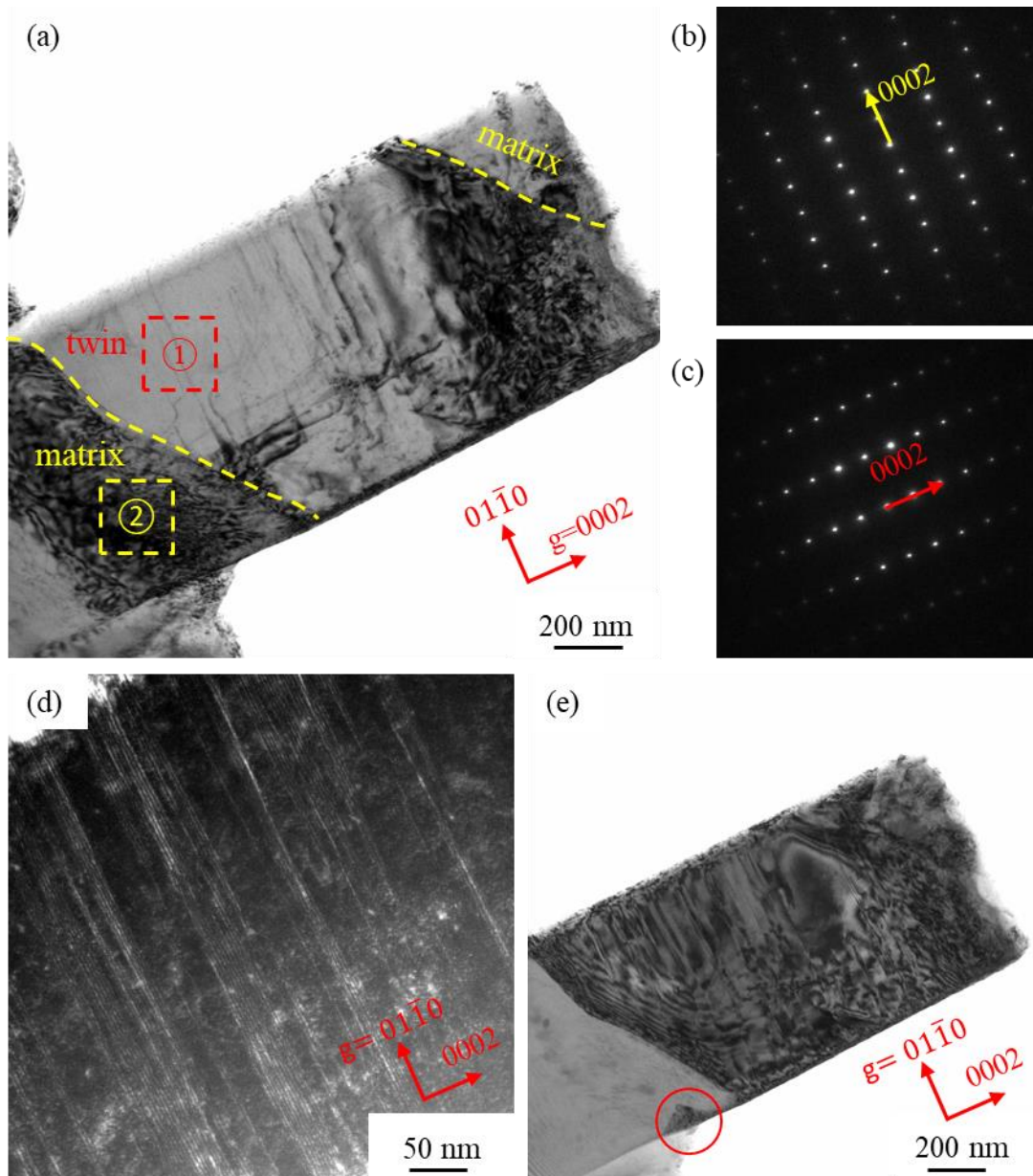


Figure 4.38 Post-mortem TEM observations of solution treated submicron-pillar 1. (a) Bright field image showing the twin boundaries and dislocations with Burgers vector $\langle c + a \rangle$ or $\langle c \rangle$. The twin boundaries are outlined by yellow dashed lines. $g = 0002$ and $BD \sim [\bar{2}110]$ in the twin. (b) Diffraction pattern from the matrix taken from area ② of Figure 4.38(a). (c) Diffraction pattern from the twin taken from area ① of Figure 4.38(a). (d) Weak beam dark field image showing the fringes of the stacking faults on (0001) in

the twin. $g = 01\bar{1}0$ and $BD \sim [\bar{2}110]$. (e) Bright field image shows the small second twin (Figure 4.36(j)) which is outlined by a red circle.

(2) Pillar 2

Figure 4.39 shows TEM bright field images of pillar 2 before in-situ TEM compression. The cyan arrowed dislocation in pillar 2 is visible for both $g = 0002$ and $g = 01\bar{1}1$, indicating that it is a $\langle c + a \rangle$ or $\langle c \rangle$ dislocation. Two basal $\langle a \rangle$ dislocations are located at the bottom of pillar 2 in Figure 4.39(b); they are visible for $g = 01\bar{1}1$ and invisible for $g = 0002$. The loading direction is $[01\bar{1}0]$.

Pillar 2 was compressed to 4.5% strain. Some frames extracted from the video and the true stress-strain curve are shown in Figure 4.40 and Figure 4.41, respectively. The deformation process was recorded using the $01\bar{1}1$ reflection. The deformation process is described as follows:

Some of the pre-existing dislocations are visible in pillar 2 before in-situ compression, as shown in Figure 4.40(a). The pre-existing dislocations were out of contrast under the elastic deformation (Figure 4.40(b)). Dislocations were generated before twinning, as shown in Figure 4.40 (c-e). When the overall stress reached approximately 365 MPa, a twin nucleated at the top surface of the pillar with the help of stress concentration, as shown in Figure 4.40(f). The first twin nucleation and initial expansion correlate with the strain burst between point E and point F in Figure 4.41. A second twin then nucleated at the first twin boundary, indicated by the red rectangle in Figure 4.40(g). The growth of two twins is shown in Figure 4.40(h) and (i). The twin boundaries between the first and

second twins are not shown clearly in the frames from the in-situ video. They are shown clearly in the TEM analysis after compression (Figure 4.42).

Figure 4.42 shows a post-mortem TEM bright field image of pillar 2. The first and second twins are shown and the twin boundaries are outlined by the yellow dashed lines. The $[\bar{2}110]$ diffraction patterns from the matrix and the twins confirm the $[01\bar{1}1](0\bar{1}12)$ twin.

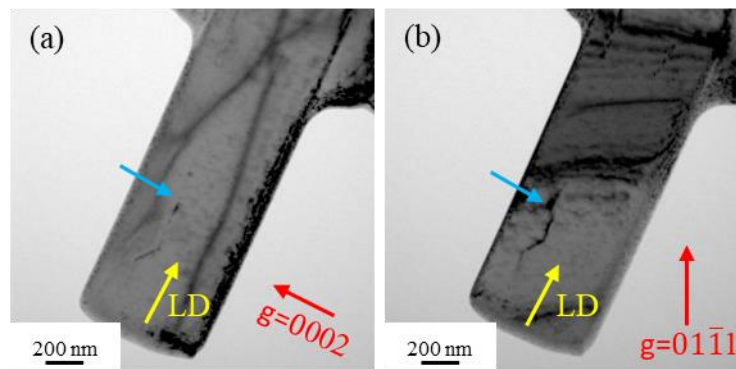


Figure 4.39 (a) Bright field image of pillar 2 before compression. $g=0002$ and $BD\sim[\bar{2}110]$. The loading direction $[01\bar{1}0]$ is indicated by the yellow arrow. The $\langle c \rangle$ or $\langle c + a \rangle$ dislocation is highlighted by the cyan arrow. (b) Bright field image of pillar 2 before compression. $g=01\bar{1}1$ and $BD\sim[\bar{2}110]$.

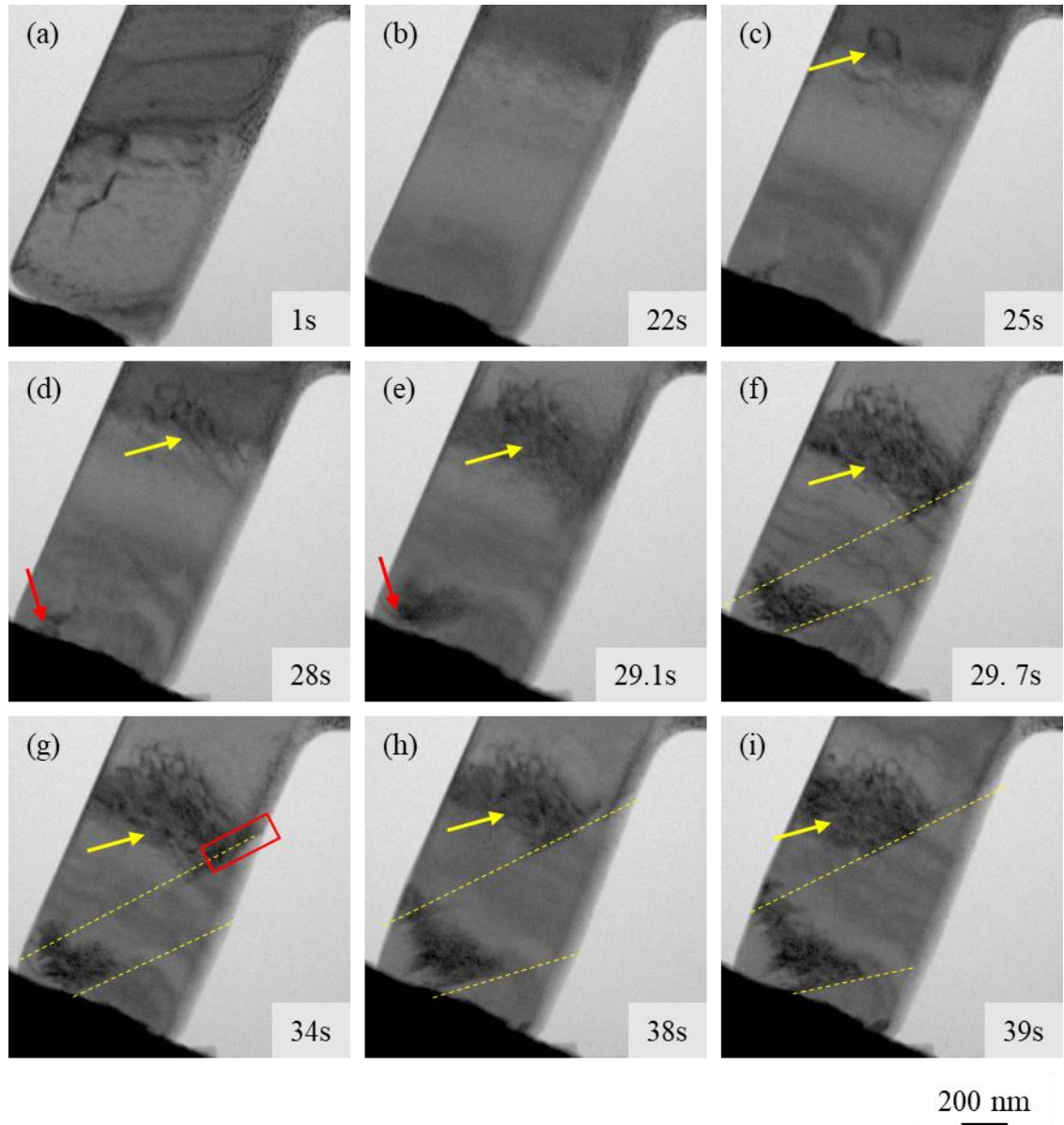


Figure 4.40 (a-i) are TEM bright field frames of pillar 2 from the in-situ video. $g = 01\bar{1}1$ and $BD \sim [\bar{2}110]$. The twin boundaries are indicated by the yellow dashed lines. The red arrow indicates the first twin nucleation region. The red box in (g) indicates the second twin nucleation region. Images (a-i) correspond to points A-I in Figure 4.41. (a) shows one of the pre-existing dislocations. (b) shows the elastic deformation process. The dislocations have left during compression. Images (c-e) show the dislocation generation before the twin nucleation. The first twin nucleated and grew quickly, as shown in image

(f). The time between image (e) and image (f) is less than 1 second, indicating the quick nucleation and initial growth. A second twin nucleated at the first twin boundary in (g). (h) and (i) show first and second twin growth.

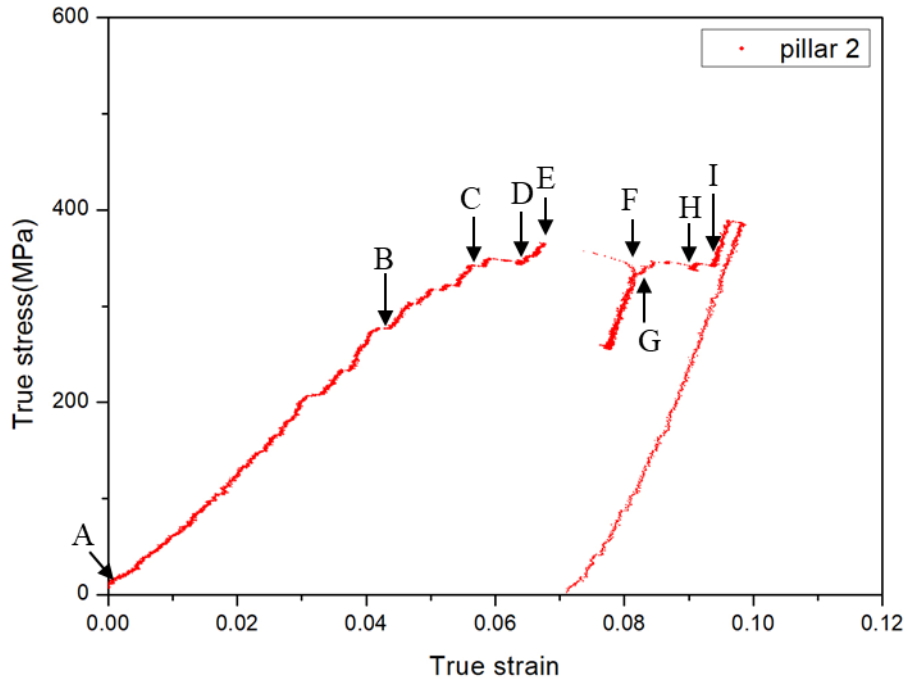


Figure 4.41 The true stress-strain curve for the solution treated pillar 2. Points A-I correspond to image (a-i) in Figure 4.40.

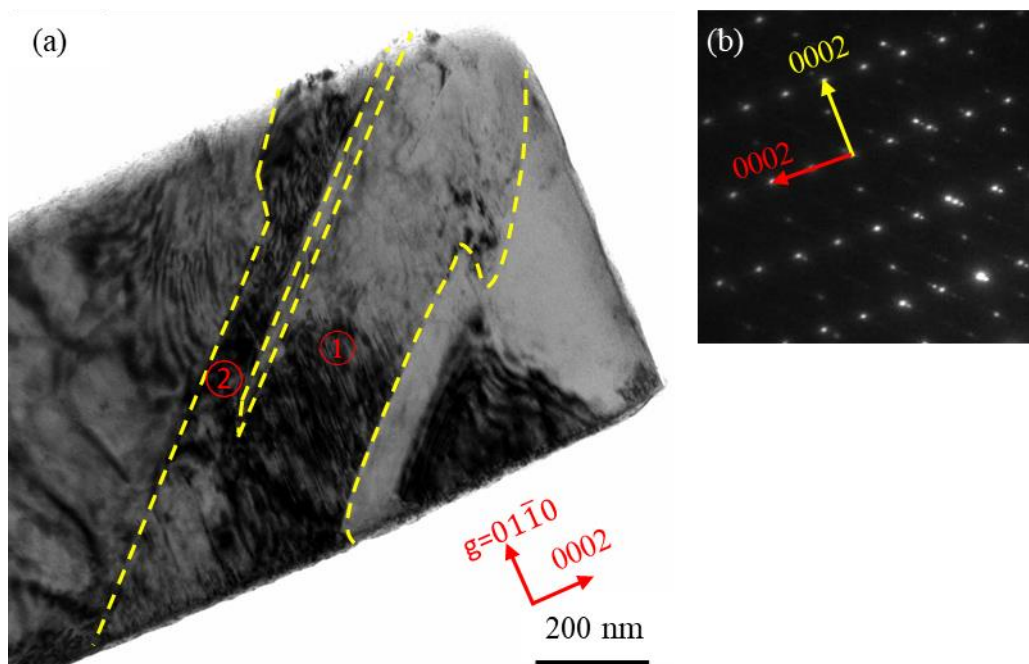


Figure 4.42 Post-mortem TEM observations of pillar 2. (a) The first and second twins are labelled ① and ②. The twin boundaries are outlined by yellow dashed lines. $g = 01\bar{1}0$ and $BD \sim [\bar{2}110]$ in the twin. (b) $[\bar{2}110]$ diffraction pattern from the matrix and the twins. The red arrow indicates the (0001) in the twin and the yellow arrow indicates the (0001) in the matrix.

(3) Pillar 3

Figure 4.43 shows no pre-existing dislocations in pillar 3. The black dots in the images are FIB introduced defects. The loading direction is $[01\bar{1}0]$.

Pillar 3 was compressed to 5.5% strain. Selected images picked out from the video and the mechanical data are shown in Figure 4.44 and Figure 4.45. The deformation process was captured using the $01\bar{1}1$ reflection.

Pillar 3 had no pre-existing dislocations, as shown in Figure 4.44(a). The local stress concentration before twin nucleation is shown in Figure 4.44(b). The first twin nucleated at the high local stress area when the apparent stress reached about 229 MPa as shown in Figure 4.44(b). A second twin nucleated at the first twin boundary as indicated by the red rectangle in Figure 4.44(g). Second twin growth is shown in Figure 4.44(f). There is a third twin according to the stress-strain curves after point F in Figure 4.45. The nucleation and growth are not visually recorded because the third twin was outside the viewing area. The third twin is observed in the post-mortem TEM observations shown in Figure 4.46.

Figure 4.46 shows the TEM images and corresponding diffraction patterns of pillar 3. Three twins were activated to accomplish the strain. The $[\bar{2}110]$ diffraction pattern from the matrix and the first twin (Figure 4.46(b)) confirm the twin type as $\{01\bar{1}2\}$ twin. The $[\bar{2}110]$ diffraction pattern from the matrix, the second twin and the third twin (Figure 4.46(c)) indicate that both twins are $[0\bar{1}11](01\bar{1}2)$ twin.

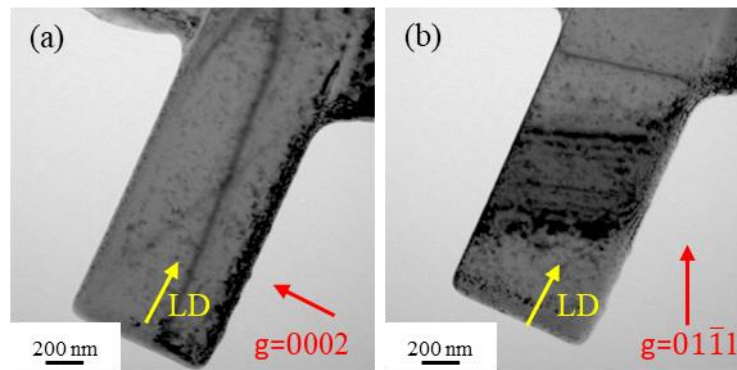


Figure 4.43 (a) Bright field image of pillar 3 before compression. $g=0002$ and $BD\sim[\bar{2}110]$. The loading direction $[0\bar{1}\bar{1}0]$ is indicated by the yellow arrow. (b) Bright field image of pillar 3 before compression. $g=01\bar{1}1$ and $BD\sim[\bar{2}110]$. No pre-existing dislocations were observed in the pillar.

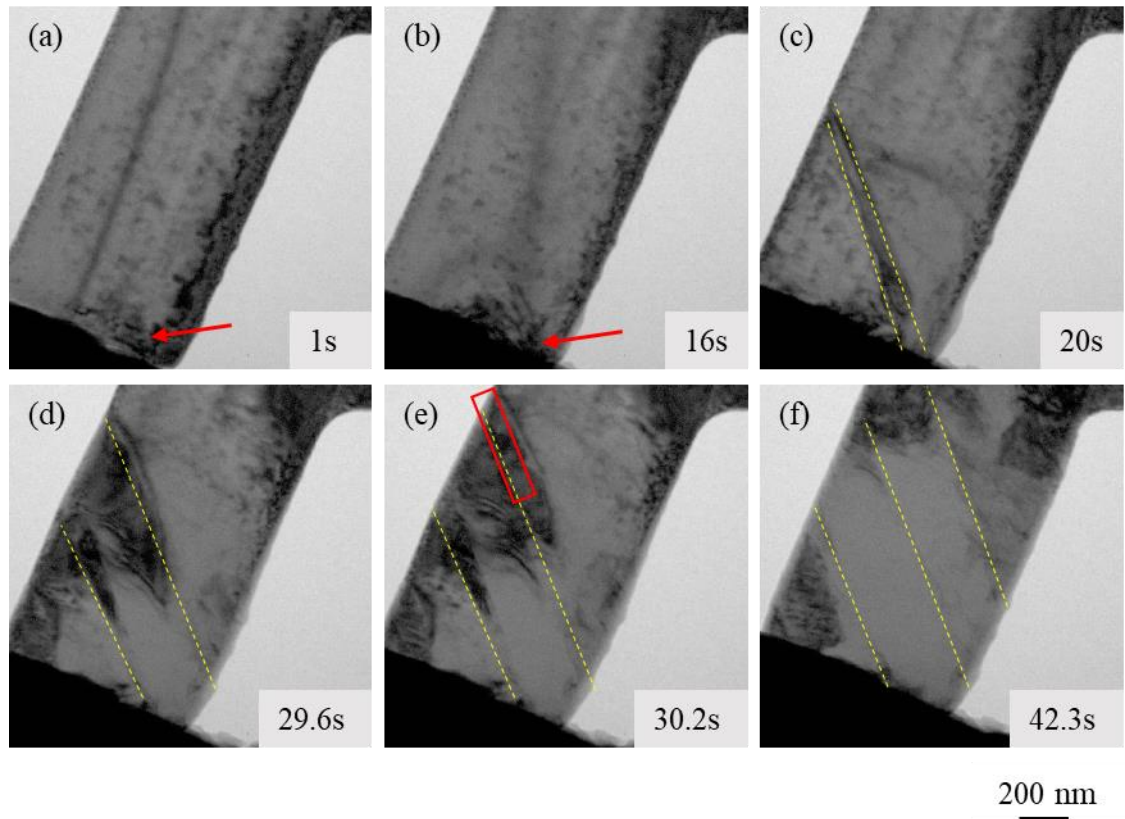


Figure 4.44 (a-f) are TEM bright field frames of pillar 3 from the in-situ video. $g = 01\bar{1}1$, $BD \sim [\bar{2}110]$. The yellow dashed lines indicate the twin boundaries. Images (a-f) correspond to points A-F in Figure 4.45. (a) and (b) shows the dislocation generation at the contact between the diamond tip and pillar top surface. The first twin nucleated at the place indicated by a red arrow in image (b). (c) and (d) show first twin growth. The red rectangle in (e) shows the second twin nucleation. (f) shows the second twin growth.

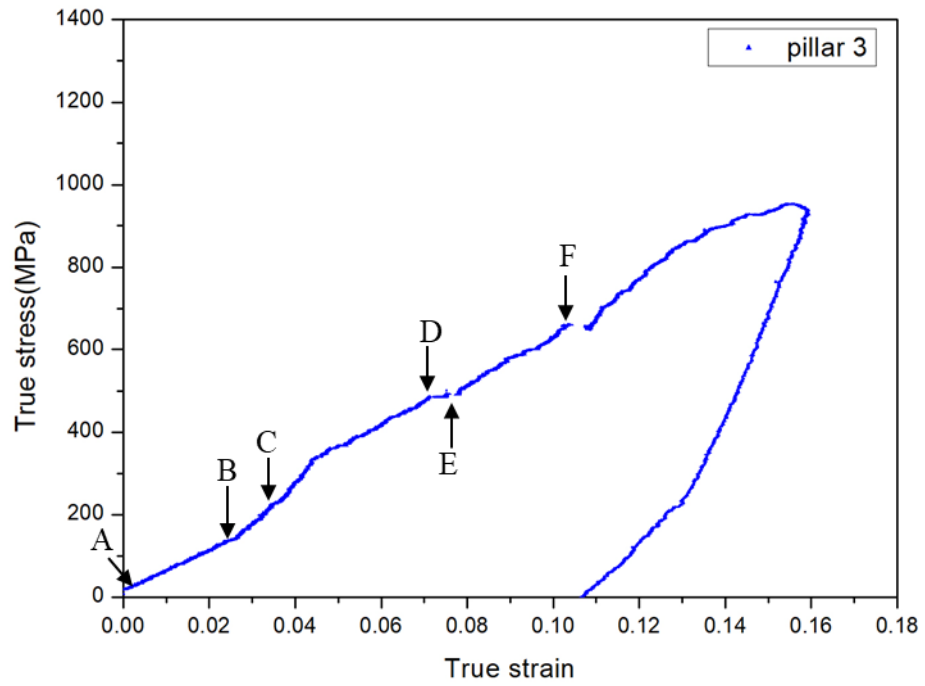


Figure 4.45 The true stress-strain curve for solution treated submicron-pillar 3. Points A-F correspond to Figure 4.44(a-f).

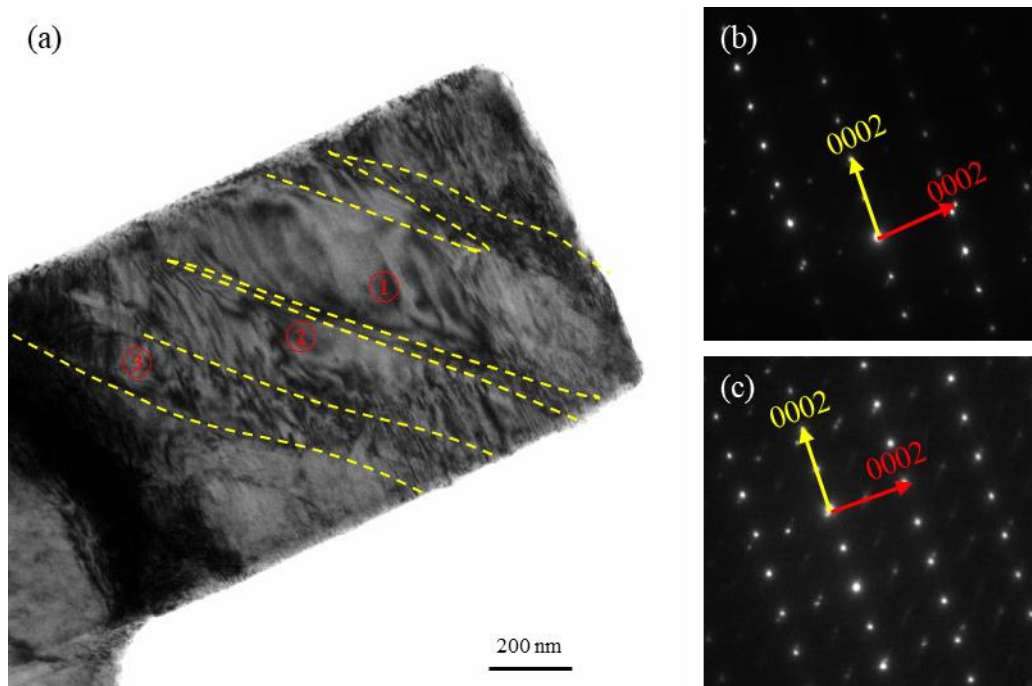


Figure 4.46 TEM analysis of deformed pillar 3: (a) bright field image, (b) dark field image. Three twins (labelled ①, ② and ③) were activated to accomplish the strain. The twin boundaries are outlined by yellow dashed lines. (b) The $[\bar{2}110]$ diffraction patterns are from matrix and twin ①. (c) The $[\bar{2}110]$ diffraction patterns are from matrix, twin ② and twin ③. The red arrows indicate the basal planes in the twin and the yellow arrows indicate the basal planes in the matrix.

(4) Pillar 4

Figure 4.47 shows the pre-existing dislocations in pillar 4. The cyan arrowed dislocation in the pillar is visible for both $g = 0002$ and $g = 01\bar{1}1$, indicating it has Burgers vector $\langle c + a \rangle$ or $\langle c \rangle$. The black dots in the bright field image are FIB introduced defects. The loading direction is $[01\bar{1}0]$.

Pillar 4 was compressed to around 7% strain. Some frames extracted from the video and the mechanical data are shown in Figure 4.48 and Figure 4.49. The video was obtained using the 0002 reflection dark field.

Figure 4.48(a) shows the $\langle c + a \rangle$ or $\langle c \rangle$ dislocation in pillar 4 before compression. The first twin nucleated at the high local stress area when the apparent stress reached approximately 341 MPa in Figure 4.48(b). Four twins have been activated in the compression process according to the corresponding stress-strain curves (four strain bursts). The nucleation and growth of the later twins are not visually recorded because the twins are outside the frame. These twins are confirmed to be $[0\bar{1}11](01\bar{1}2)$ twins by the TEM observation after compression in Figure 4.50.

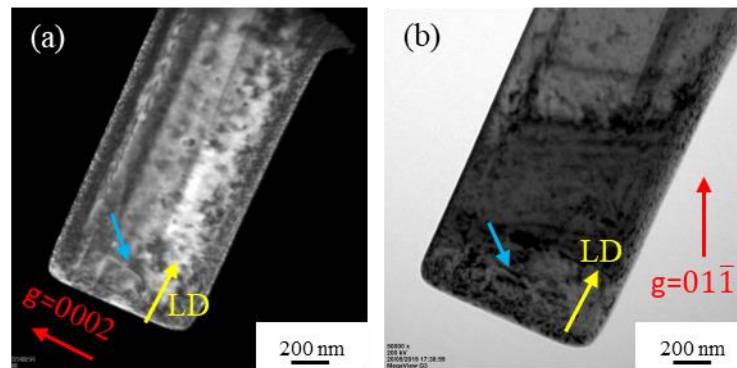


Figure 4.47 (a) Dark field image of pillar 4 before compression. $g = 0002$ and $BD \sim [\bar{2}110]$. The loading direction $[01\bar{1}0]$ is indicated by the yellow arrow. (b) Bright field image of pillar 4 before compression. $g = 01\bar{1}1$ and $BD \sim [\bar{2}110]$. No pre-existing dislocations were observed in pillar 4.

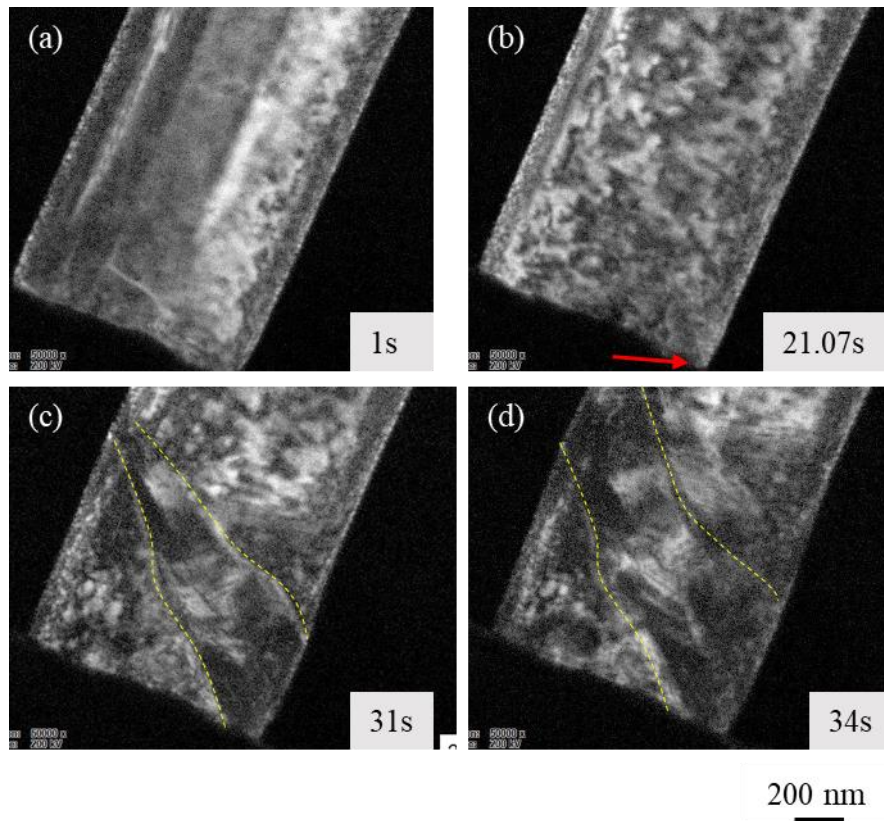


Figure 4.48 (a-d) are TEM dark field frames of pillar 4. $g = 0002$ and $BD \sim [\bar{2}110]$. The yellow dashed lines indicate the twin boundaries. Images (a-d) correspond to points A-D in Figure 4.49. (a) shows the $\langle c + a \rangle$ or $\langle c \rangle$ dislocation in the pillar before compression. (b) shows that the first twin nucleated at the place indicated by a red arrow. (c) shows first twin before a second twin nucleation. (d) shows the second twin. The boundaries between the first twin and second twin are difficult to separate from the in-situ movie.

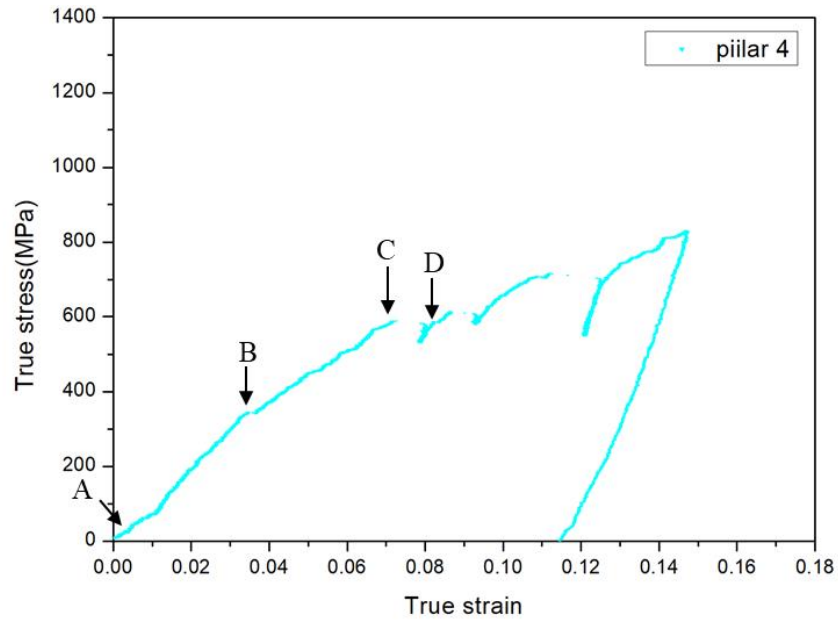


Figure 4.49 The true stress-strain curve for solution treated submicron-pillar 4.

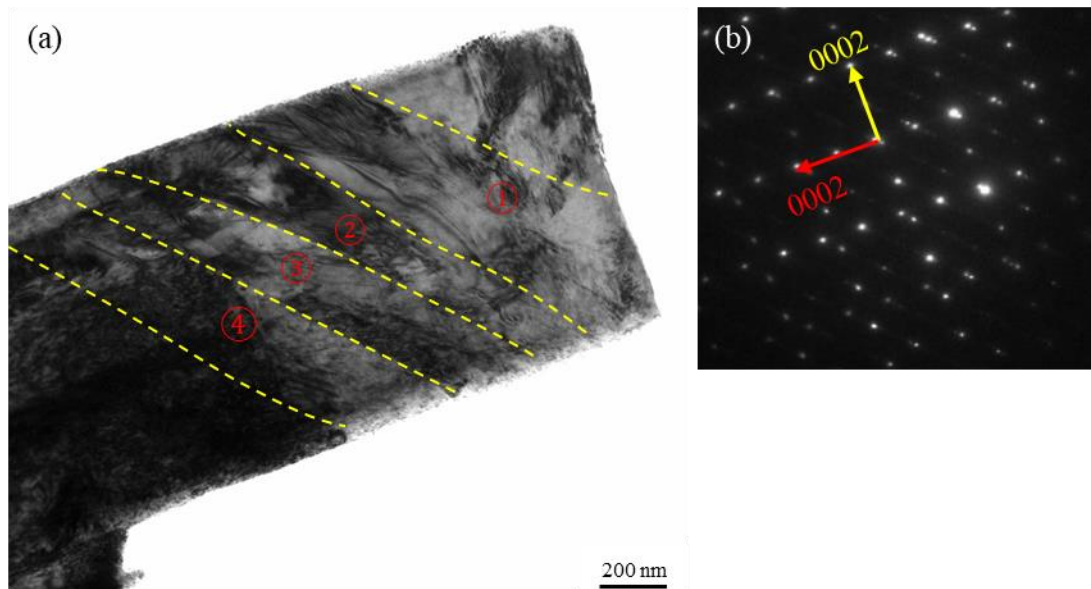


Figure 4.50 (a) A bright field image of deformed pillar 4. The twins are labelled ①, ②, ③ and ④. The twin boundaries are outlined by yellow dashed lines. (2) The $[\bar{2}110]$ diffraction pattern is taken for the whole pillar area. The red arrow indicates the basal planes in the twins and the yellow arrow indicate the basal planes in the matrix. The main twins in this pillar are confirmed to be $[0\bar{1}11](01\bar{1}2)$ twin.

4.4.3 Aged submicron-pillars

The crystal orientation of the foil to fabricate the aged pillars is the same as in Figure 4.34.

The foil normal was $[\bar{2}110]$.

(1) Pillar 1

Figure 4.51 shows TEM bright field images of pillar 1 before in-situ TEM compression.

Figure 4.51(a) shows the basal $\langle a \rangle$ dislocations in pillar 1 before compression using the $01\bar{1}1$ reflection and $BD \sim [\bar{2}110]$. The inset $[\bar{2}110]$ zone axis diffraction pattern confirms the loading direction to be $[01\bar{1}0]$. The loading direction is indicated by the yellow arrow. Figure 4.51(b) shows the relative position of basal precipitates under the 0002 reflection and $BD \sim [\bar{2}110]$. The precipitates are outlined by green boxes.

Pillar 1 was compressed to around 3.5% strain. Selected sequence of frames and the corresponding stress-strain curve are shown in Figure 4.52 and Figure 4.53. The video was obtained using the $01\bar{1}1$ reflection.

Figure 4.52(a) shows the basal $\langle a \rangle$ dislocations in pillar 1 before compression. The pillar was compressed continuously and reached a stress of approximately 231 MPa, where the first twin nucleated at the contact area between the diamond tip and the pillar top surface. The first twin nucleation and initial expansion correlate with the strain burst before point C in Figure 4.53. The first twin grew as the stress increased to 414 MPa. Two more twins nucleated and grew during the compression process. The second twin nucleation region is highlighted by the red box in Figure 4.52(e). A third twin is outside the viewing region and not visually recorded. These twins are confirmed by the post-mortem TEM

observations shown in Figure 4.54. There is no obvious interaction between the precipitates and twin in pillar 1.

Figure 4.54 shows the post-mortem TEM observations of pillar 1. Three twins (labelled ①, ② and ③ in Figure 4.54(a)) were activated to accomplish the strain. The inset diffraction pattern is taken at zone axis $\bar{2}110$. The crystal is rotated about 86° (comparing $[0001]$ of the twin and matrix), indicating a $[0\bar{1}11](01\bar{1}2)$ twin. The basal dislocations outside the twin are shown in Figure 4.54(b). Some of them are attached to the twin boundary. And the positions of precipitates and twins are shown in Figure 4.54(c).

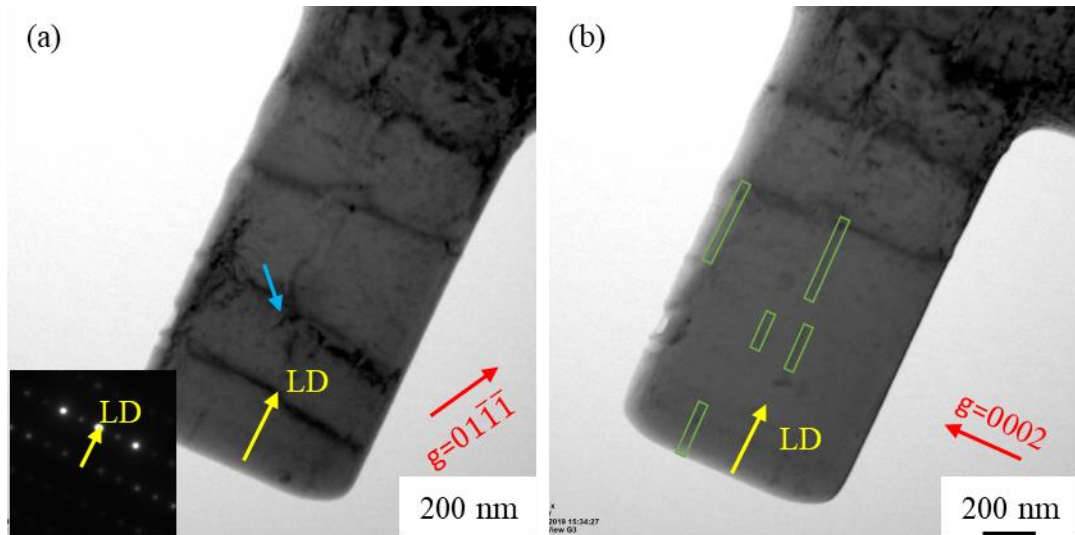


Figure 4.51 (a) Bright field image of pillar 1 before compression. $g = 01\bar{1}\bar{1}$ and $BD \sim [\bar{2}110]$. The loading direction is $[01\bar{1}0]$ and is indicated by the yellow arrow. The inset diffraction pattern is taken at $[\bar{2}110]$, confirming the loading direction to be $[01\bar{1}0]$. (b) Bright field image of pillar 1 before compression. $g = 0002$ and $BD \sim [\bar{2}110]$. The cyan arrowed pre-existing dislocation has Burgers vector of $\langle a \rangle$ type because it is visible for $g = 01\bar{1}\bar{1}$ and invisible for $g = 0002$. The precipitates are outlined by the green boxes in (b).

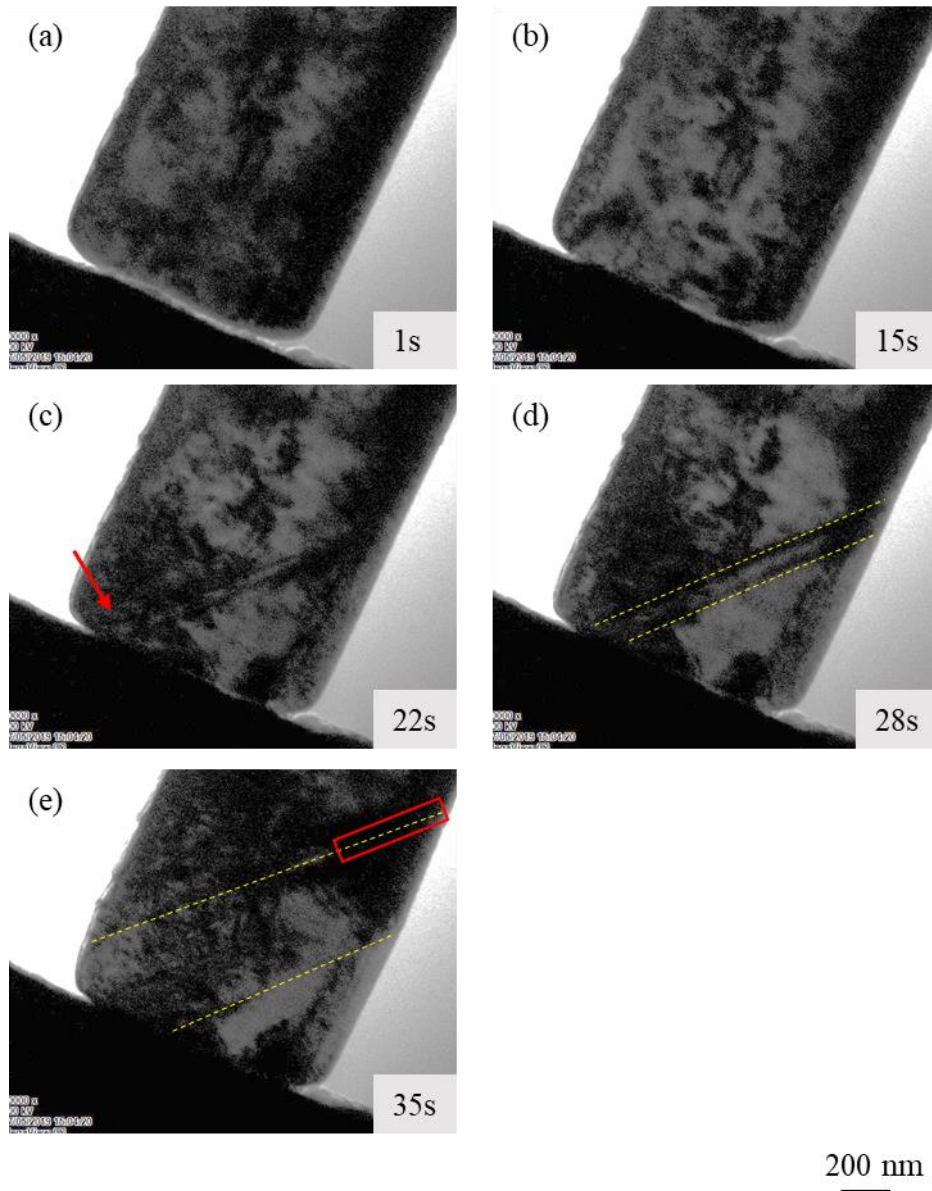


Figure 4.52 (a-e) are TEM bright field frames of pillar 1. $g = 0002$ and $BD \sim [\bar{2}110]$. The yellow dashed lines indicate the twin boundaries. Images (a-e) correspond to points A-E in Figure 4.53. (a) shows the $\langle a \rangle$ dislocation in the pillar before compression. (b) shows the elastic deformation. (c) shows the first twin nucleation at the position indicated by a red arrow. (d) and (e) show first twin growth. (e) also shows second twin nucleation at the position indicated by a red box.

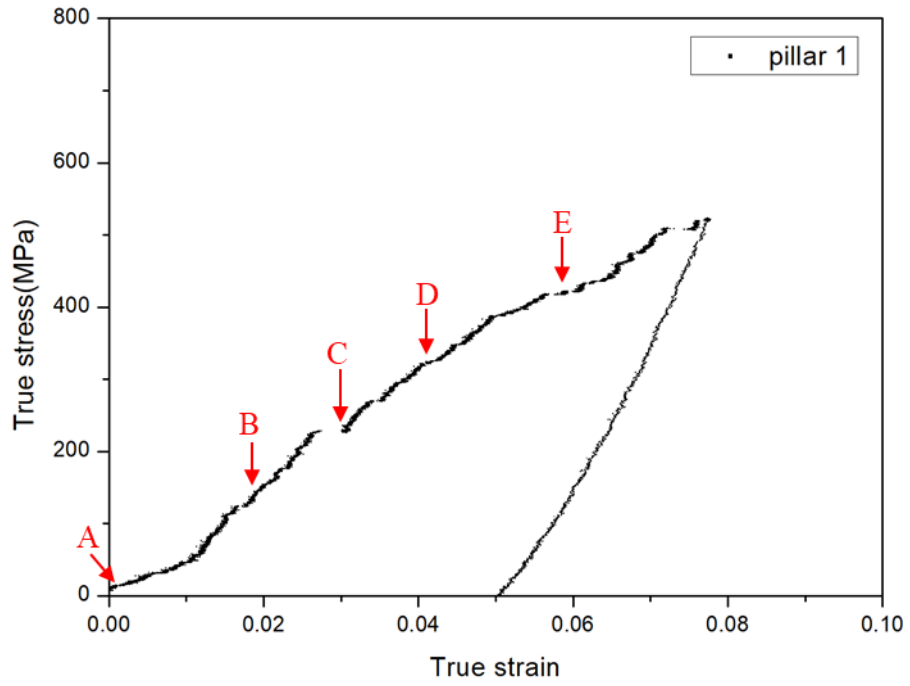


Figure 4.53 The true stress-strain curve for aged submicron-pillar 1. Points A-E correspond to Figure 4.52(a-e).

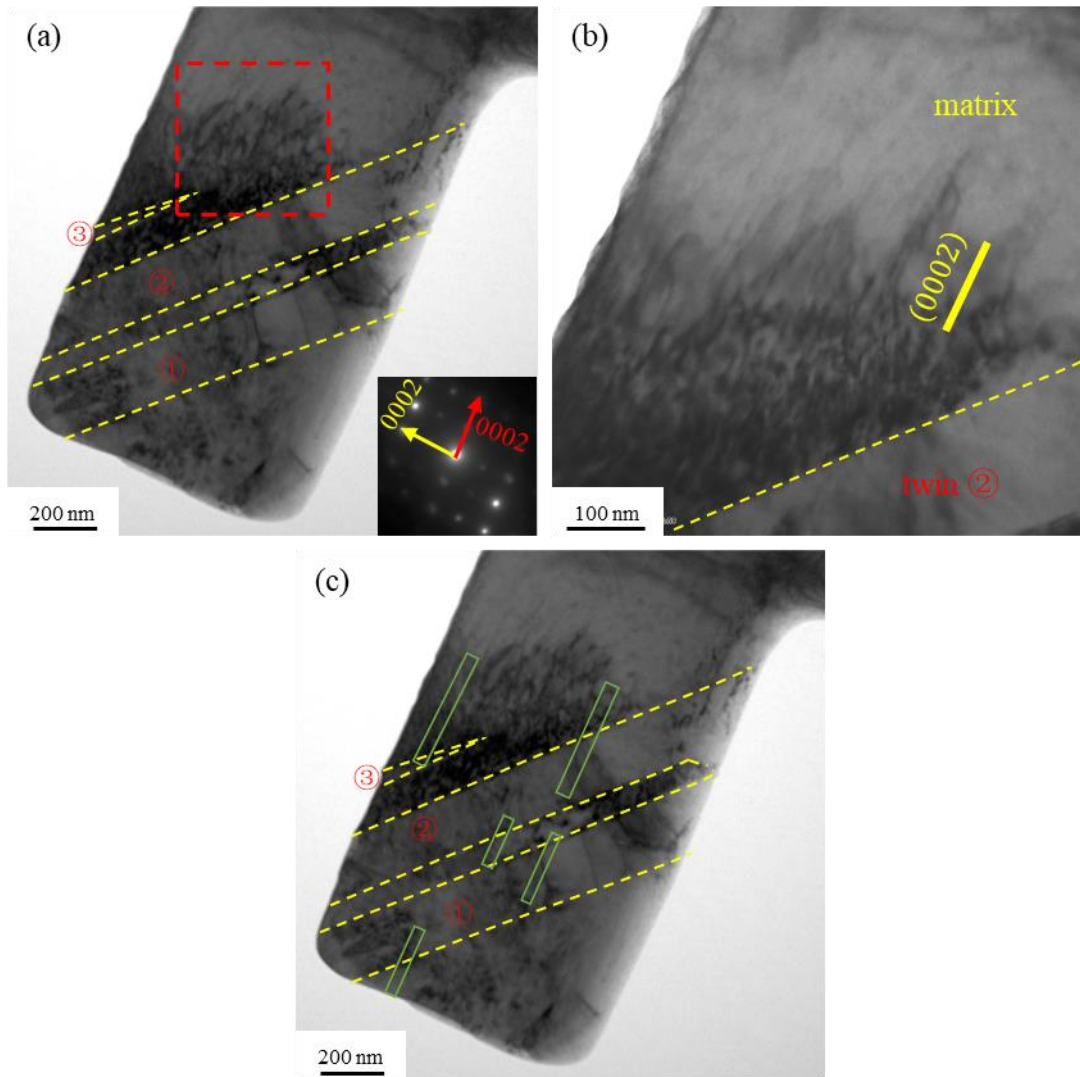


Figure 4.54 Post-mortem TEM observations of pillar 1. (a) A TEM bright field image shows the twins (labelled ①, ② and ③) which accomplished some of the strain. The twin boundaries are outlined by yellow dashed lines. The inset $[\bar{2}110]$ diffraction pattern confirms the $\{01\bar{1}2\}$ twin. (0002) in yellow indicates the basal plane in the matrix and (0002) in red indicates the basal planes in the twins. (b) An enlarged red-boxed area in Figure 4.54(a) shows basal dislocations outside the twin attached to the twin boundaries. (c) shows the positions of twins and precipitates (green boxes). The positions of the precipitates are extracted from Figure 4.51.

(2) Pillar 2

Figure 4.55(a) shows that using the $01\bar{1}\bar{1}$ reflection there are no visible dislocations in pillar 2 before in-situ TEM compression. The $[01\bar{1}0]$ loading direction is indicated by the yellow arrow. Figure 4.55(b) shows the positions of the precipitates before compression.

Pillar 2 was compressed to around 5% strain. Some frames extracted from the in-situ video and the mechanical data are shown in Figure 4.56 and Figure 4.57. The deformation process was recorded using the $01\bar{1}1$ reflection.

Figure 4.56(a) shows no pre-existing dislocations in pillar 2. (b) shows the progress of elastic deformation. (c) shows the nucleation of the first twin when the overall stress reaches 341MPa and then the initial twin growth. Images (d-i) show the nucleation and growth of the subsequent twins in pillar 2.

The compressed pillar was characterised by TEM bright field images and diffraction pattern, as shown in Figure 4.58. Five twins were activated to accomplish the strain. The twin nucleation occurs at the twin boundaries or at the contact area between the diamond tip and the pillar. The positions of the twins and basal precipitates are shown in Figure 4.58(c). This indicates that the twin nucleation position is not related to the precipitate positions in this pillar. Figure 4.58(b) shows the stacking faults in the twin. These stacking faults lie on (0001), the same as the stacking faults in the compressed solution treated submicron-pillars. The $[\bar{2}110]$ diffraction pattern in Figure 4.58(d) shows that the crystal is rotated about 86° (comparing $[0001]$ of the twin and the matrix), indicating that twin ④ and ⑤ are $[0\bar{1}11](01\bar{1}2)$ twins. Twin ① and ② show the similar twin planes with

twin ④ and ⑤ and thus they are identified as $[0\bar{1}11](01\bar{1}2)$ twins. Twin ③ shows different twin plane orientation and thus identified as $[01\bar{1}1](0\bar{1}12)$ twin.

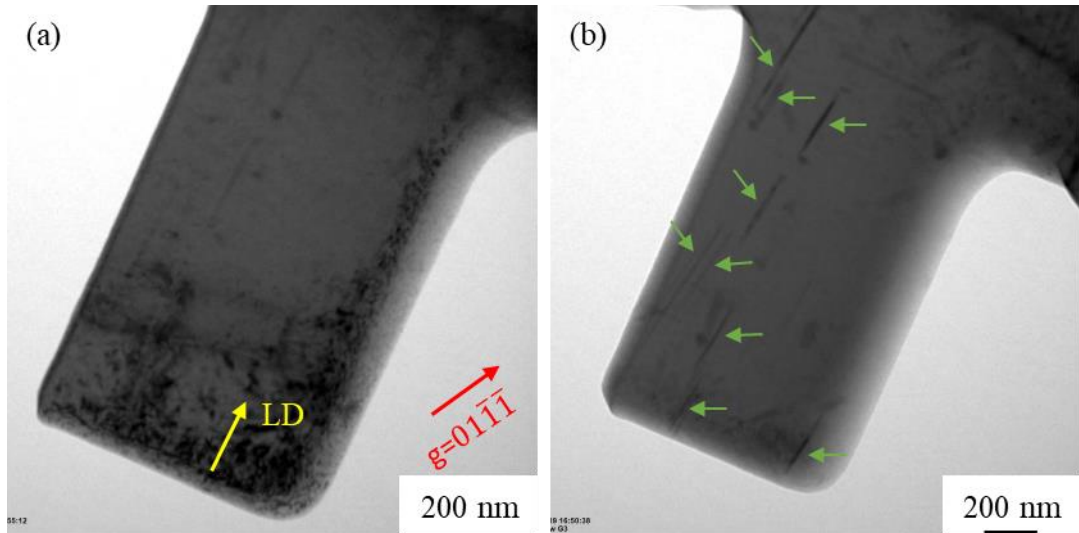


Figure 4.55 (a) Bright field image of pillar 2 before compression. $g = 01\bar{1}1$ and $BD \sim [\bar{2}110]$. The loading direction $[01\bar{1}0]$ is indicated by the yellow arrow. (b) Bright field image showing the positions of the precipitates (indicated by the green arrows).

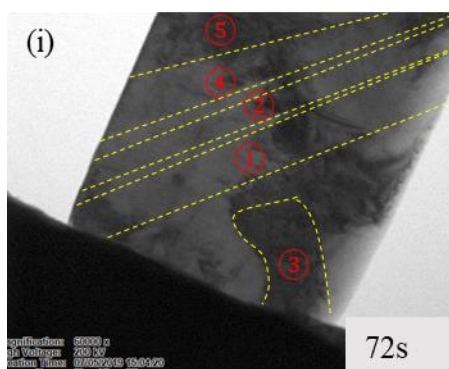
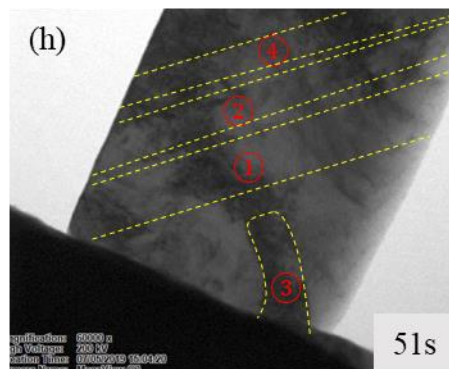
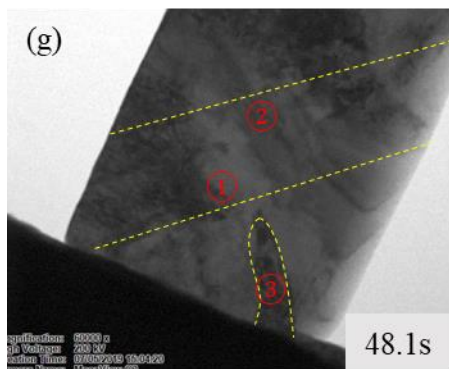
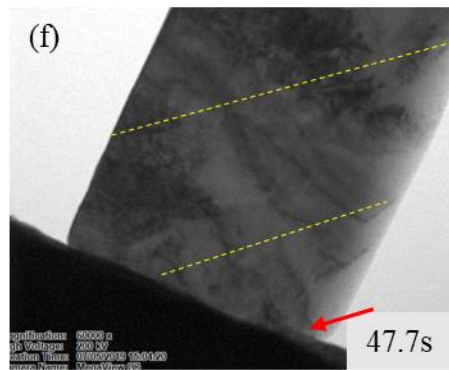
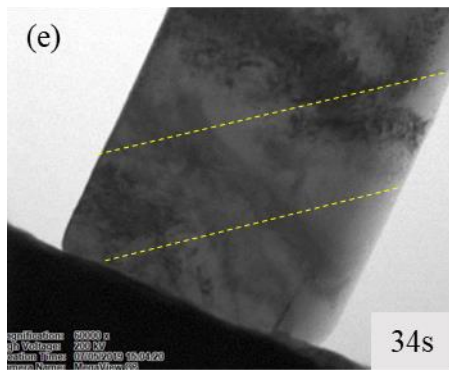
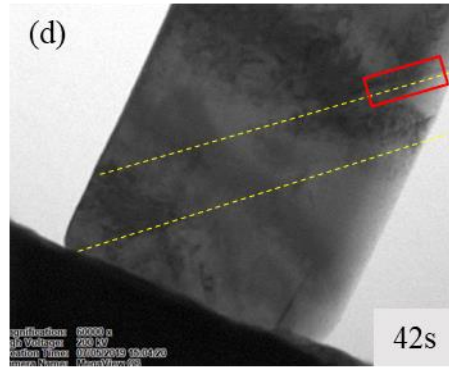
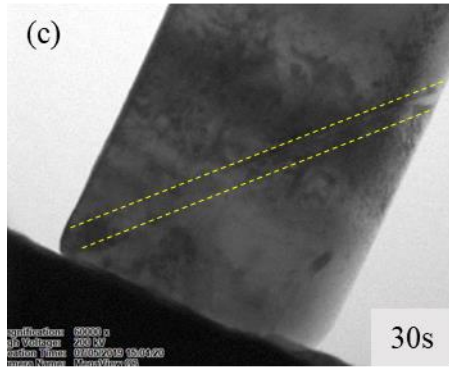
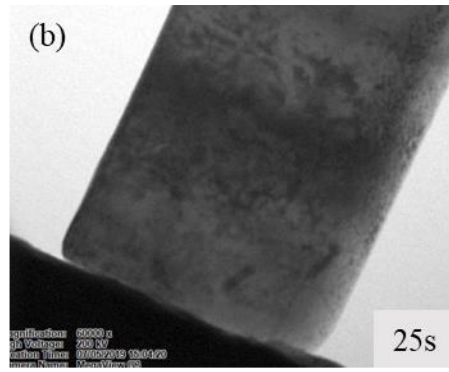
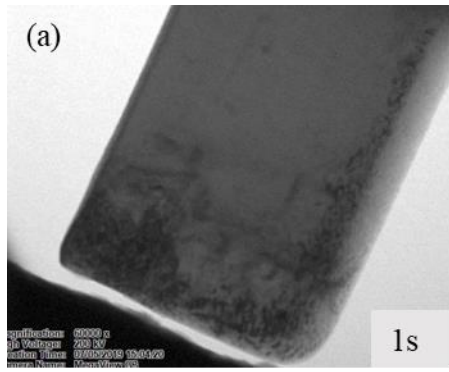


Figure 4.56 (a-i) are TEM bright field frames of pillar 2. $g = 01\bar{1}1$ and $BD \sim [\bar{2}110]$. The yellow dashed lines indicate the twin boundaries. Images (a-i) correspond to points A-I in Figure 4.57. (a) shows the pillar before compression. (b) shows the elastic deformation. (c) shows first twin nucleation and growth mainly along the twinning shear direction. (d) shows the subsequent growth of the first twin. The red rectangle indicates the place where a second twin nucleated. (e) The second twin nucleation and growth. The boundaries between the first twin and the second twin are not shown clearly in the video frames. Image (f) shows the place where the third twin nucleated indicated by a red arrow. (g) The third twin. (h) The fourth twin. (i) The fifth twin.

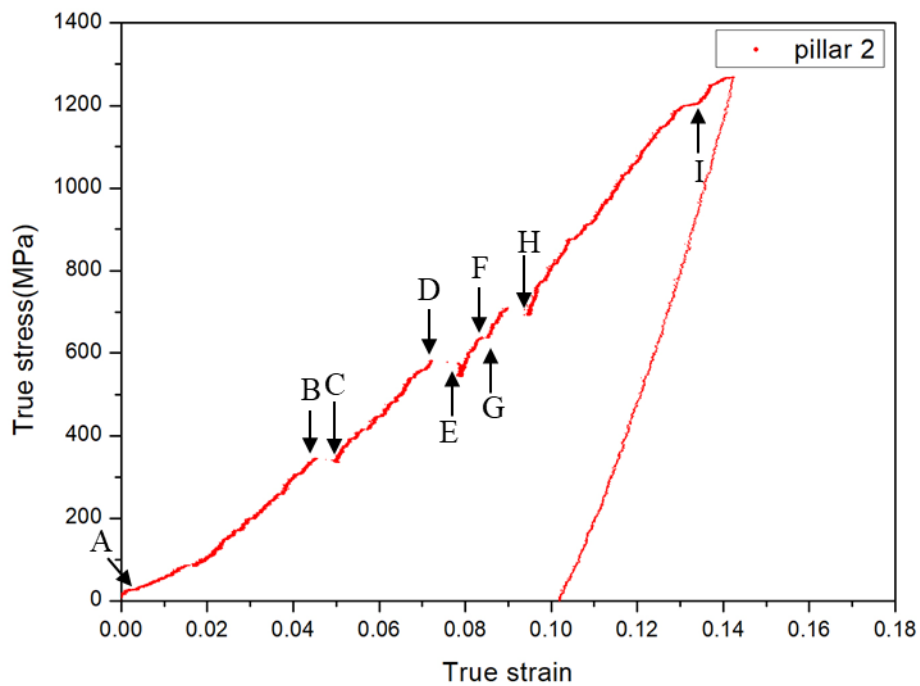


Figure 4.57 The true stress-strain curve for aged pillar 2.

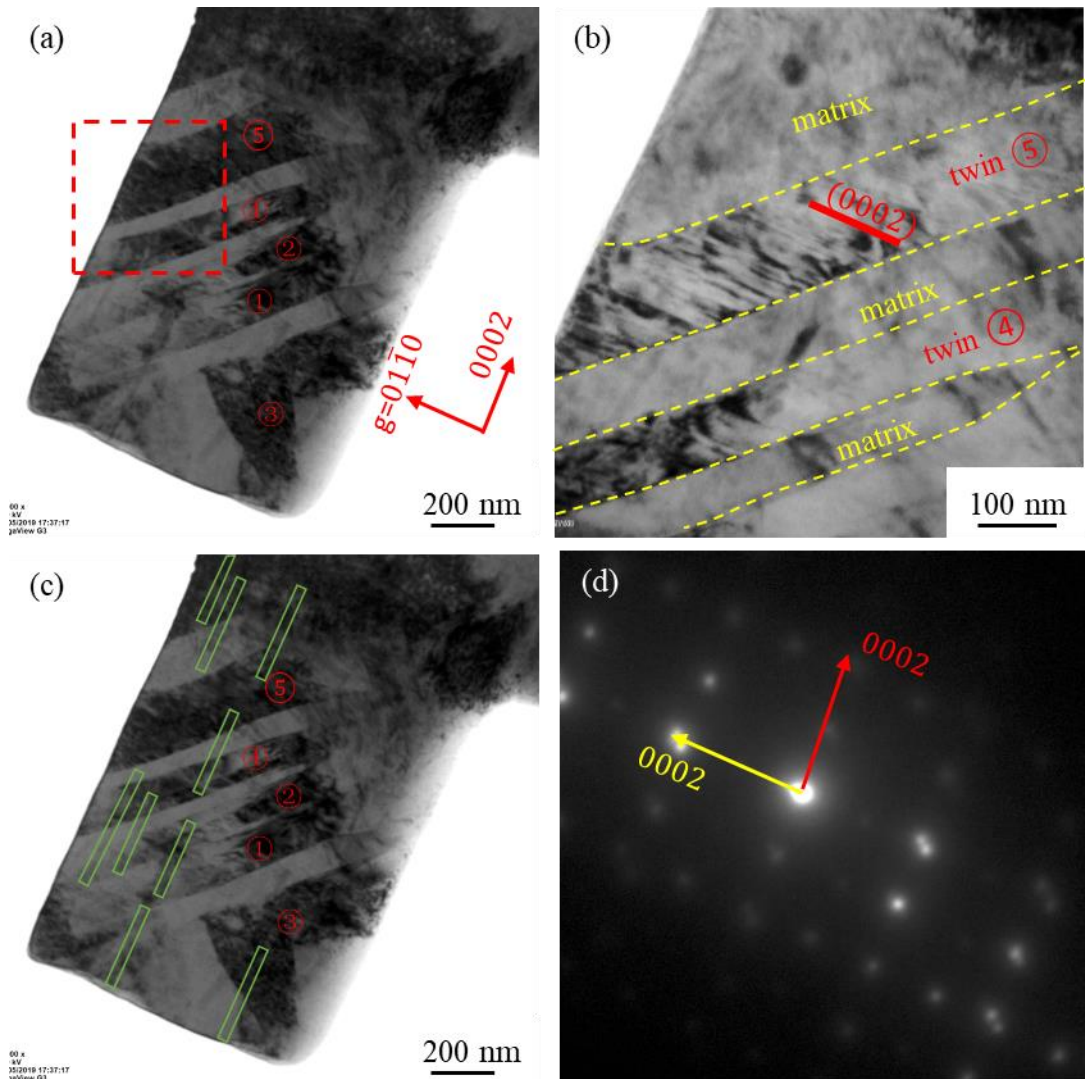


Figure 4.58 TEM characterizations of compressed pillar 2. (a) and (b) are bright field images using $g = 01\bar{1}0$ and $BD \sim [\bar{2}110]$ in the twin. (a) shows the positions of the five twins (labelled ①, ②, ③, ④ and ⑤) which accomplished the strain. (b) The enlarged red-boxed area in (a) shows the stacking faults in the twins. (c) shows the positions of twins and precipitates (green boxes). The positions of precipitates are extracted from Figure 4.55. (d) $[\bar{2}110]$ diffraction pattern of Figure 4.58(b). (0002) in yellow indicates the basal plane in the matrix and (0002) in red indicates the basal planes in the twins.

(3) Pillar 3

Figure 4.59(a) shows the pre-existing dislocations in pillar 3 before in-situ TEM compression. The $[01\bar{1}0]$ direction is indicated by the yellow arrow in the inset $[\bar{2}110]$ diffraction pattern. Figure 4.59(b) shows the positions of the precipitates. Figure 4.59(c) shows the loading point at the corner of the pillar, not exactly in the $[01\bar{1}0]$ direction. The pillar was tilted approximately 7° about $[01\bar{1}0]$ direction.

Pillar 3 was compressed to around 4% strain. Some frames extracted from the video and the corresponding stress-strain curve are shown in Figure 4.60 and Figure 4.61. The deformation process was recorded for $g = 01\bar{1}1$.

Figure 4.60 (a) shows the basal $\langle a \rangle$ dislocations in the pillar before in-situ TEM compression. (b) shows the diamond tip contacting the corner of pillar 3. The basal dislocations were generated at the region indicated by the red arrow. (c) shows the first twin nucleation indicated by the red arrow. Dislocations outside the twin are shown near the red arrowed area. The first twin grew more slowly as compared with all the other pillars, as shown in image (d). The second twin nucleated at the first twin boundary, indicated by the red arrow in image (d). The second twin grew with the increasing stress and was inhibited by the precipitate (indicated by the red dashed box) image (d). The second twin passed through the precipitate with increasing stress. Also, more twin nucleation and growth occur with increasing stress, as shown in images (d-h). Image (i) shows the small matrix region between twin ① and twin ② before unloading. Detwinning occurred during unloading of this pillar, as shown in image (j). The small matrix region in image (i) has become larger.

TEM characterization of the de-twinned region in deformed pillar 3 is shown in Figure 4.62. The twin boundaries are outlined by the yellow dashed lines. (a) shows twin ①, twin ② and the matrix between them. (b) shows the basal dislocations in the matrix after de-twinning. De-twinning in this pillar is achieved by the reverse motion of a twin boundary. De-twinning has been widely reported in Mg [27, 127-129].

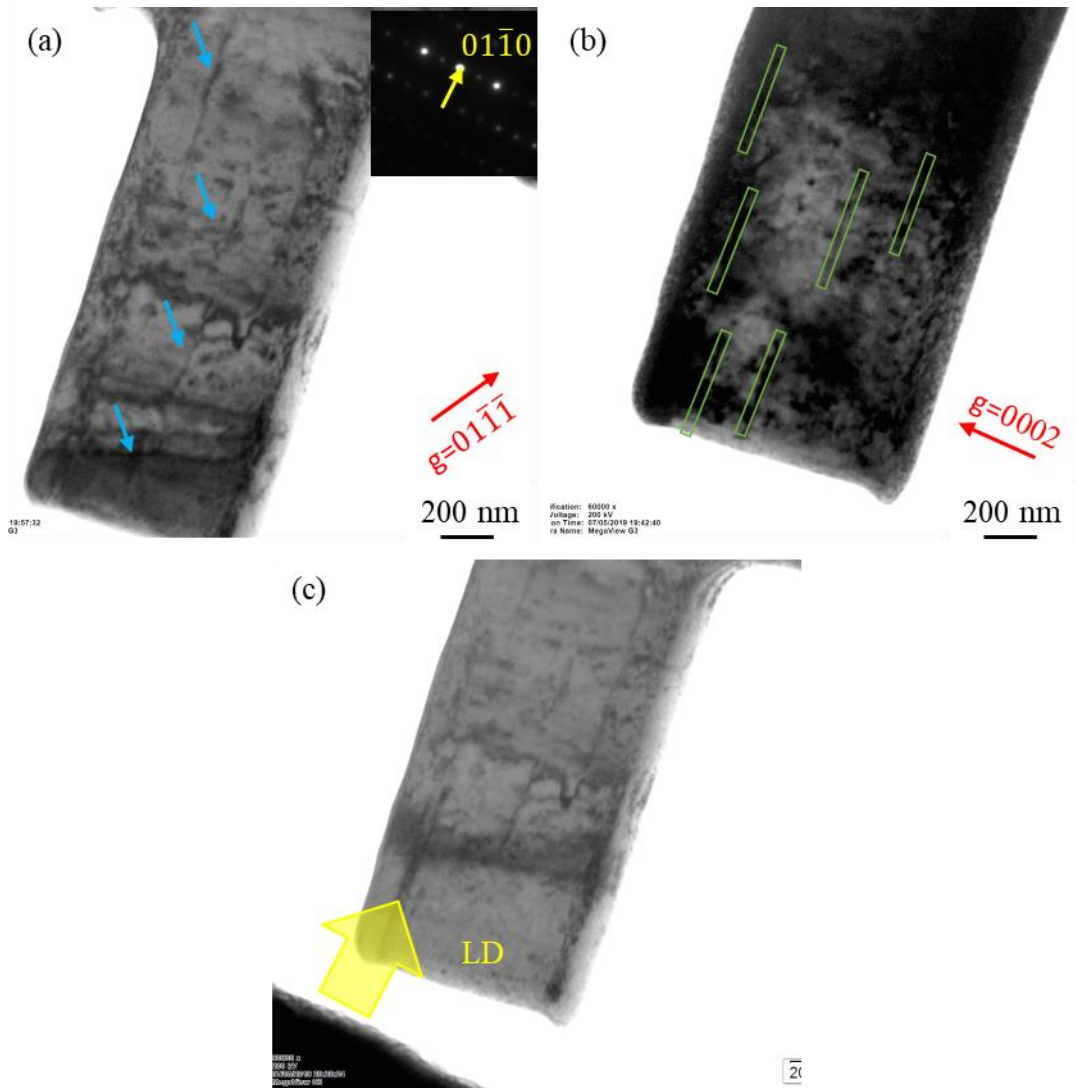
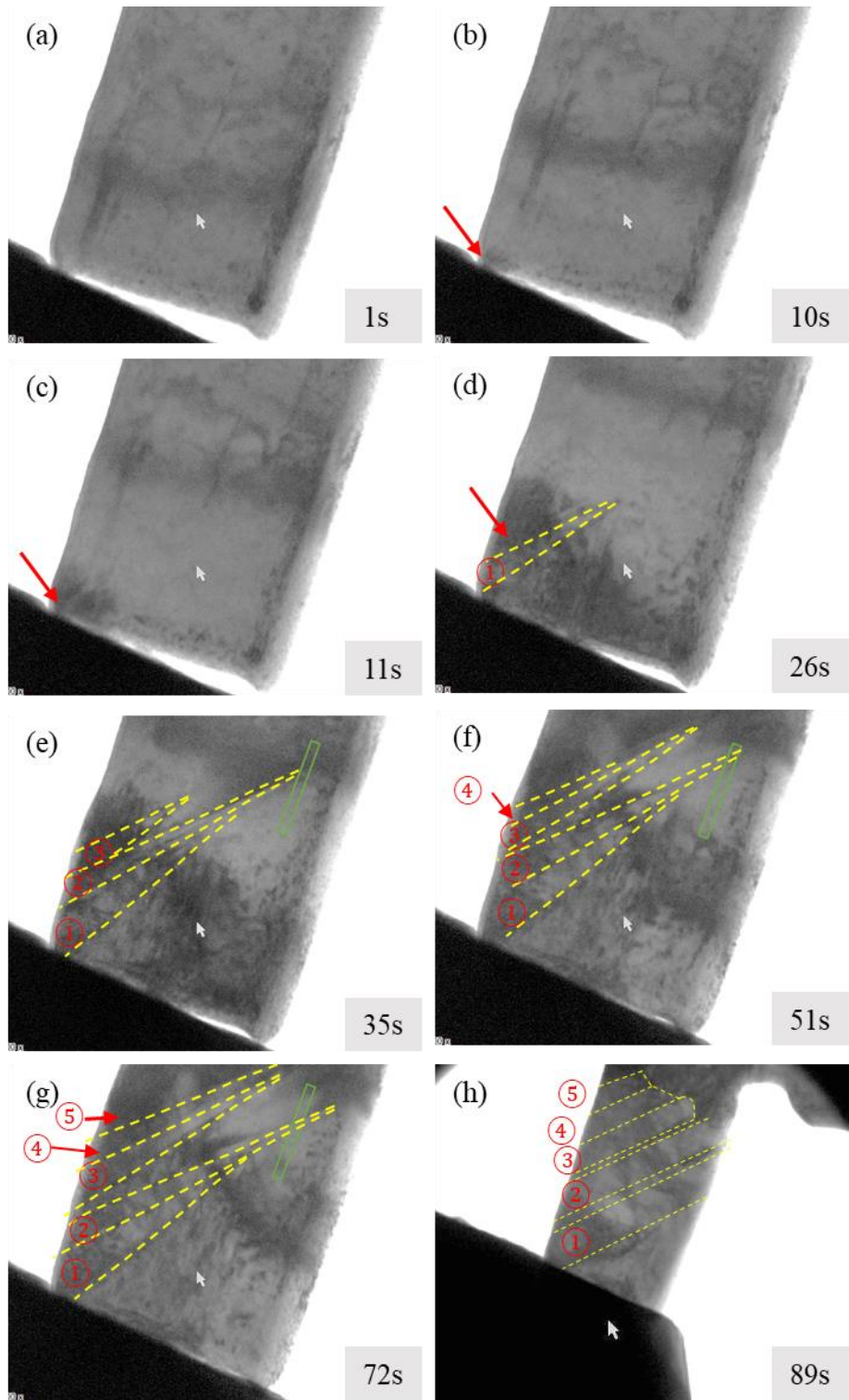


Figure 4.59 (a) Bright field image of pillar 3 before in situ TEM compression showing the pre-existing basal $\langle a \rangle$ dislocations in the pillar using $g = 01\bar{1}\bar{1}$ and $BD \sim [\bar{2}110]$. The dislocations are highlighted by the cyan arrows. The inset $[\bar{2}110]$ diffraction pattern is shown at the right top corner. The $[01\bar{1}0]$ direction is shown in the inset diffraction pattern. (b) Bright field image of pillar 3 showing the positions of the precipitates. $g = 01\bar{1}0$ and $BD \sim [\bar{2}110]$. The precipitates are outlined by green boxes. (c) shows the loading point is at the corner of the pillar, not exactly in the $[01\bar{1}0]$ direction.



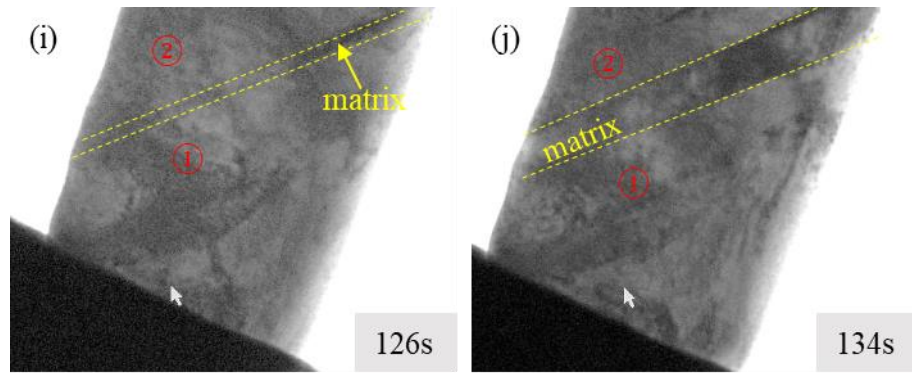


Figure 4.60 (a-j) are TEM bright field frames of pillar 3. $g = 01\bar{1}1$ and $BD \sim [\bar{2}110]$. The yellow dashed lines indicate the twin boundaries. The twin nucleation regions are indicated by red arrows. The position of one precipitate is outlined by a green box. Images (a-j) correspond to points A-J in Figure 4.61. (a) shows pre-existing dislocations and the loading from the corner of the pillar. (b) shows the local stress at the contacting region between the diamond tip and the pillar. (c-d) shows first twin nucleation and growth. A second twin nucleated and grew shown in image (d) and (e). The second twin growth was inhibited by the precipitate in image (e). Images (e-h) shows more twin nucleation and propagation. The twins are labelled ①, ②, ③, ④ and ⑤. (i) is the image before unloading. The matrix occupies a small area between twin ① and twin ②. (j) shows detwinning during unloading. The matrix region in image (j) is larger than that in image (i).

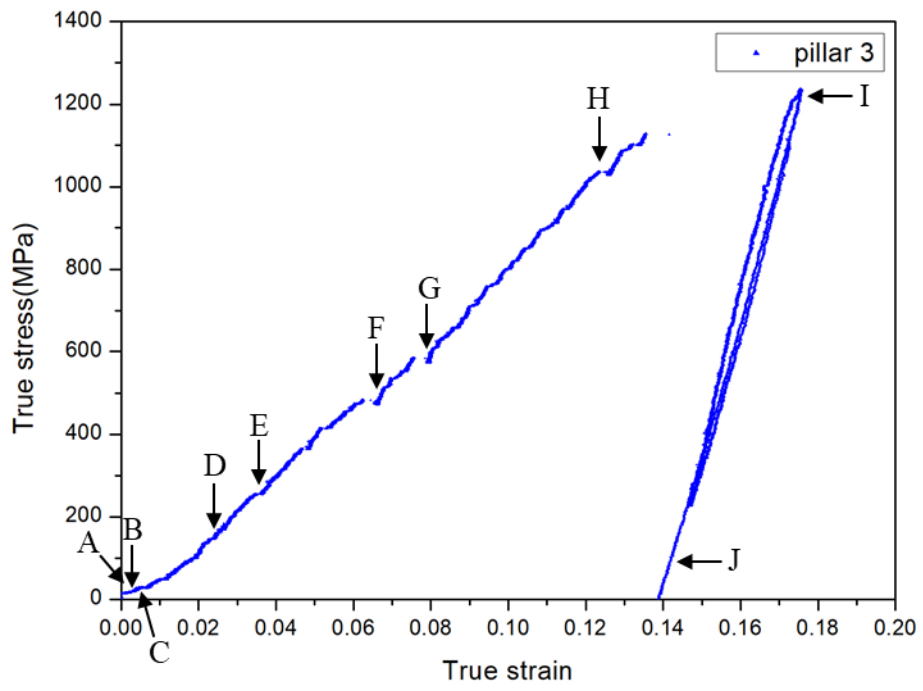


Figure 4.61 The true stress-strain curve for aged pillar 3.

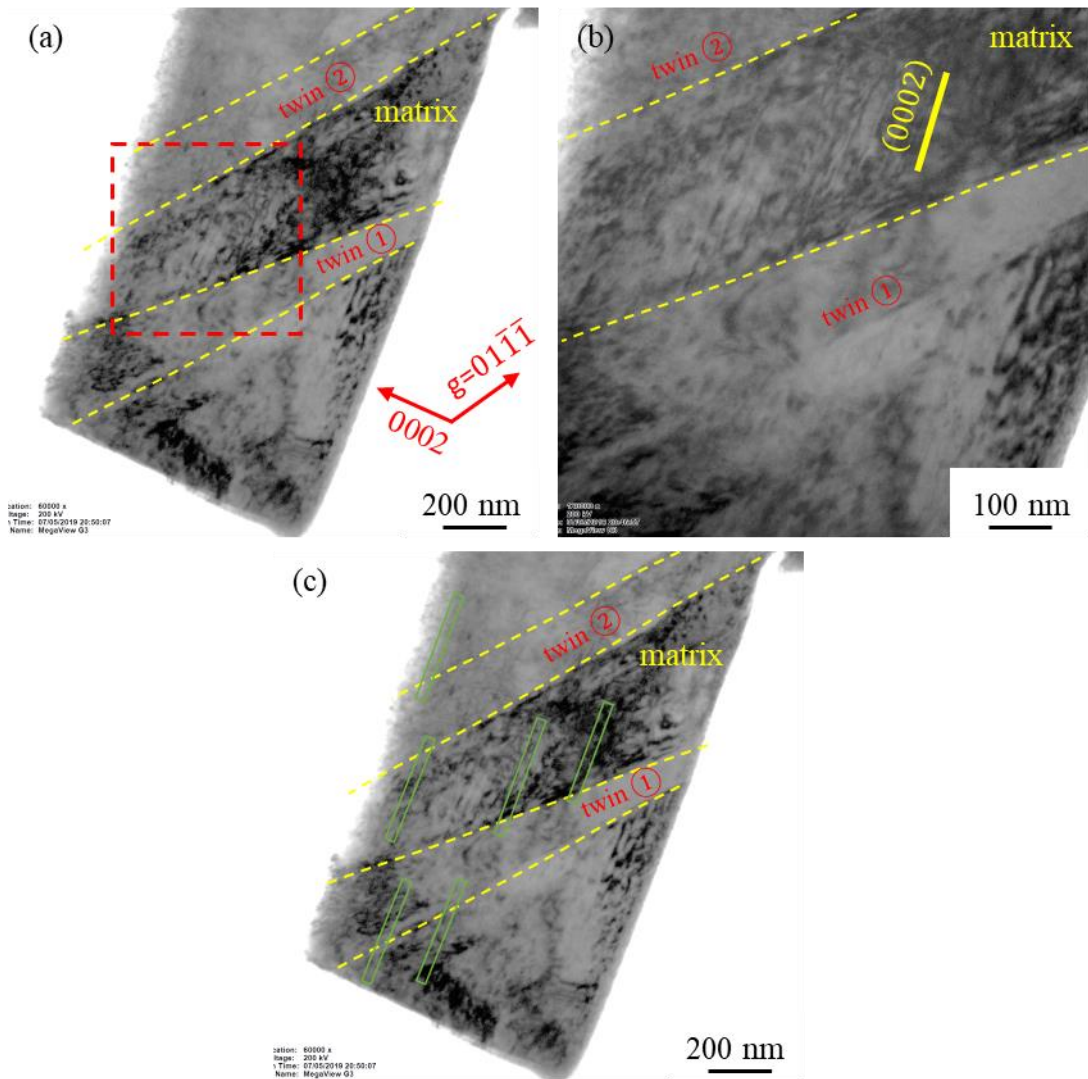


Figure 4.62 TEM bright field images of pillar 3 after compression for $g = 01\bar{1}1$ and $BD \sim [\bar{2}110]$ in the matrix. The twin boundaries are outlined by the yellow dashed lines. (a) shows two twins and the matrix induced by de-twinning. (b) The enlarged red-boxed area in (a) showing basal dislocations in the matrix after de-twinning. (c) shows the positions of twins and precipitates (green boxes).

(4) Pillar 4

Figure 4.63 shows the positions of the precipitates in pillar 4 before in-situ TEM testing. The loading direction is $[01\bar{1}0]$.

Pillar 4 was compressed to around 7% strain. The frames extracted from the video and the stress-strain curve are shown in Figure 4.64 and Figure 4.65. The deformation process was recorded using the 0002 reflection.

The first twin nucleation region is at the top surface of this pillar when the overall stress is approximately 417 MPa, as shown in Figure 4.64(b). The following images (c-e) shows more twins nucleation and growth under loading process. Twin nucleation occurs preferentially are at the contact surface between the diamond tip and the pillar and at twin boundaries in this pillar. The twin nucleation site is not influenced directly by the precipitates.

A bright field image of pillar 4 after compression is shown in Figure 4.66. The twins and the precipitates are outlined by the yellow dashed lines and the red boxes, respectively. The twin boundaries pass through the precipitates.

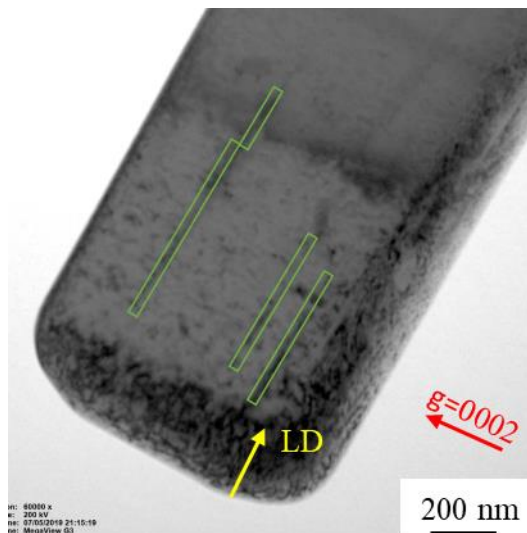


Figure 4.63 Bright field image of pillar 4 before compression, showing the positions of the precipitates. The precipitates are outlined by green boxes. $g = 0002$ and $BD \sim [\bar{2}110]$.

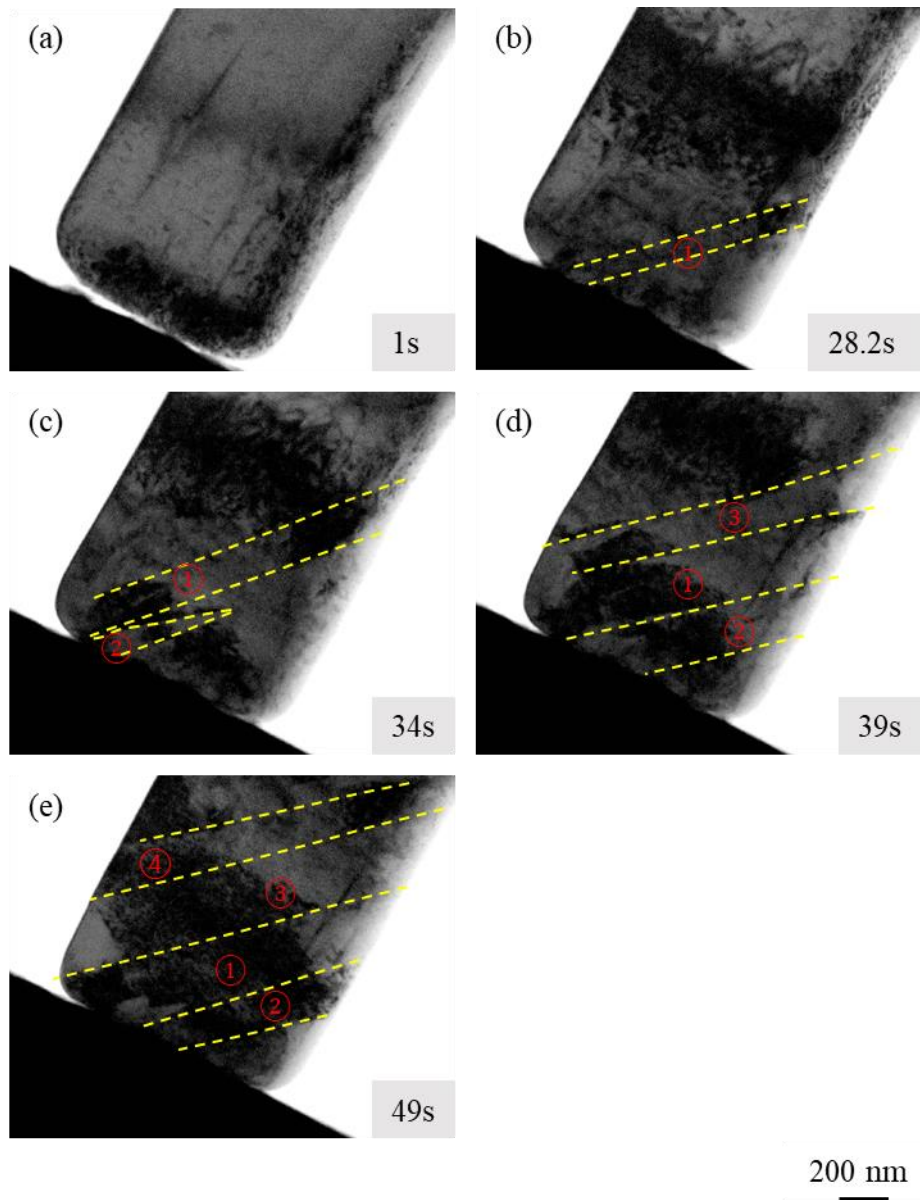


Figure 4.64 (a-e) are TEM bright field frames of pillar 4. Images (a-e) correspond to points A-E in image (f). (a) shows the pillar before compression. (b) shows the first twin. (c) The second twin. (d) The third twin. (e) The fourth twin.

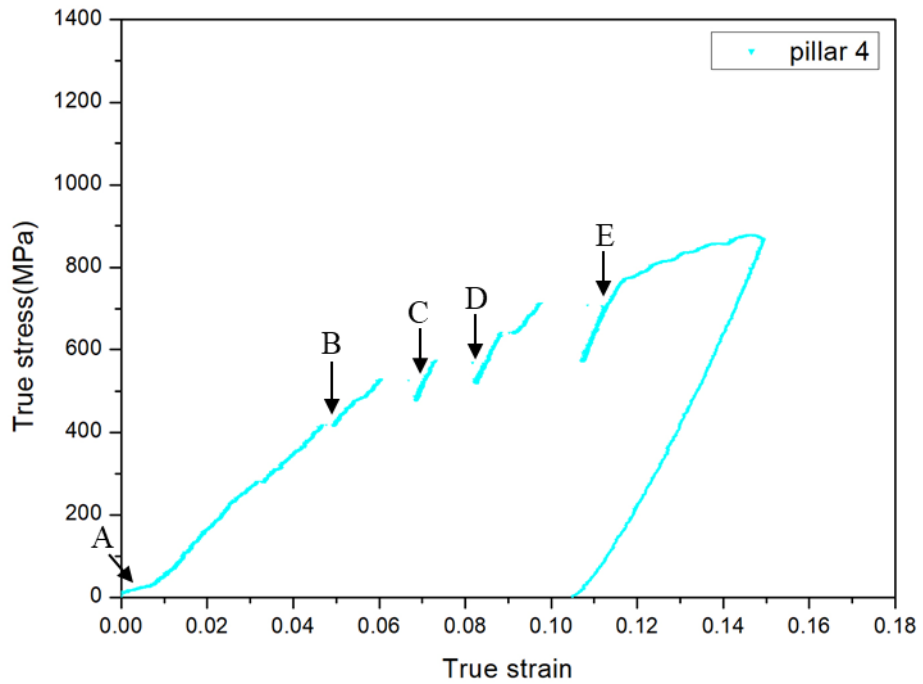


Figure 4.65 The true stress-strain curve for aged pillar 4.

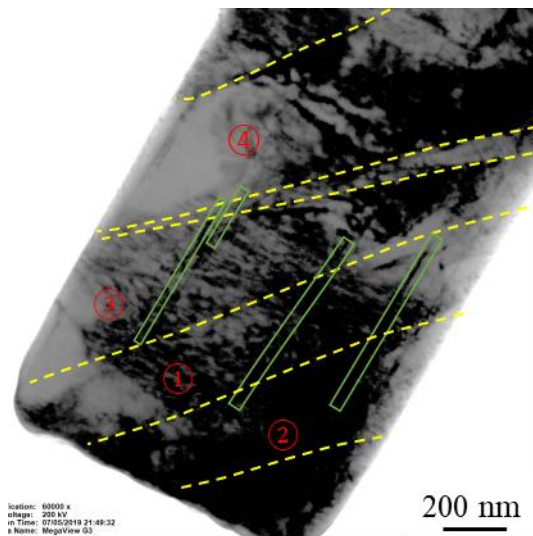


Figure 4.66 Post-mortem TEM observation of pillar 4. The bright field image is taken using $BD \sim [\bar{2}110]$. The twin boundaries are indicated by the yellow dashed lines. Three twins are labelled ①, ②, ③ and ④ in the image. The precipitate positions are indicated by the green boxes.

4.4.4 Summary

Tension twin has been activated when the solution treated and the under-aged submicron-pillars are compressed along $[01\bar{1}0]$. The apparent stress where the first twin nucleation occurs were determined to be 325.7 ± 65.4 MPa and 332.8 ± 94.4 MPa for the solution treated submicron-pillars and the aged submicron-pillars, respectively. There is no significant difference between them. The aged submicron-pillars show a higher hardening rate than the solution treated ones.

In situ TEM shows the high local stress region before $\{01\bar{1}2\}$ twin nucleation. The high local stress generally starts at the contact surface between the diamond tip and the pillar top surface. Twin nucleation occurs either at the high local stress region or at the twin boundaries for both the solution treated and the aged specimens, apart from twin ③ in aged pillar 1. The nucleation region of twin ③ in aged pillar 1 is not recorded by the video. It is probably helped by the high density of gliding basal $\langle a \rangle$ dislocations. Twin nucleation sites are not sensitive to the position of the precipitates.

For all the submicron-pillars except aged pillar 3, the axis of the diamond tip is parallel to the $[01\bar{1}0]$ direction of the pillars. The twin nucleation and initial growth are too quick to be captured. It is difficult to analyse the precipitate interactions with twins by the in-situ video. However, the aged pillar 3 exhibits a lower twin growth speed when the loading direction was around 7° about $[01\bar{1}0]$ direction and the diamond tip compressed the corner of the pillar at the beginning of deformation. The twin growth velocity can be controlled using this loading strategy for a not very well understood reason. The in-situ video of aged pillar 3 shows that the twin propagation is blocked by precipitates. And twin can overcome the precipitate with increasing applied stress.

5 Discussion

5.1 Age hardening behaviour of bulk AZ91

Chung [130] and Zeng [119] both measured the hardness evolution of solution treated AZ91 on aging at 200°C. A comparison of the age hardening curves of solution treated AZ91 is shown in Figure 5.1. The maximum Rockwell hardness of 84.8 HRE was obtained after 15 hours of aging at 200°C by Chung [130]. There are no mathematically exact equations for hardness conversion from HRE to HV for Mg. Different loads and different shape of indenters complicate the problem. 84.8 HRE is approximately equivalent to 95 ~ 97 HV0.1 using the online equivalent hardness scale conversion chart for soft metals. The peak hardness was obtained after 15 hours aging, slightly longer than the present work. This may be due to the slightly different alloy compositions.

The maximum Vickers hardness of 95 HV0.5 was obtained after 10 hours of aging at 200°C by Zeng [119]. The peak hardness of the present work is 95 ± 5 HV0.5 which was obtained after 10 hours of aging at 200°C. The peak hardness in the present work is consistent with the results of Chung [130] and Zeng [119].

The material, heat treatment process and peak hardness of aged specimen were the same as those in Chung's and Zeng's work. The strength derived from the hardness for the bulk sample by Zeng [119] is therefore recalled and used to compare with the strength derived from the micro-pillar compression in the subsequent section 5.2.

The hardness of Mg₁₇Al₁₂ has been measured to be 4 ~ 5 GPa while the Mg matrix has been measured to be around 1 GPa by Chung [130].

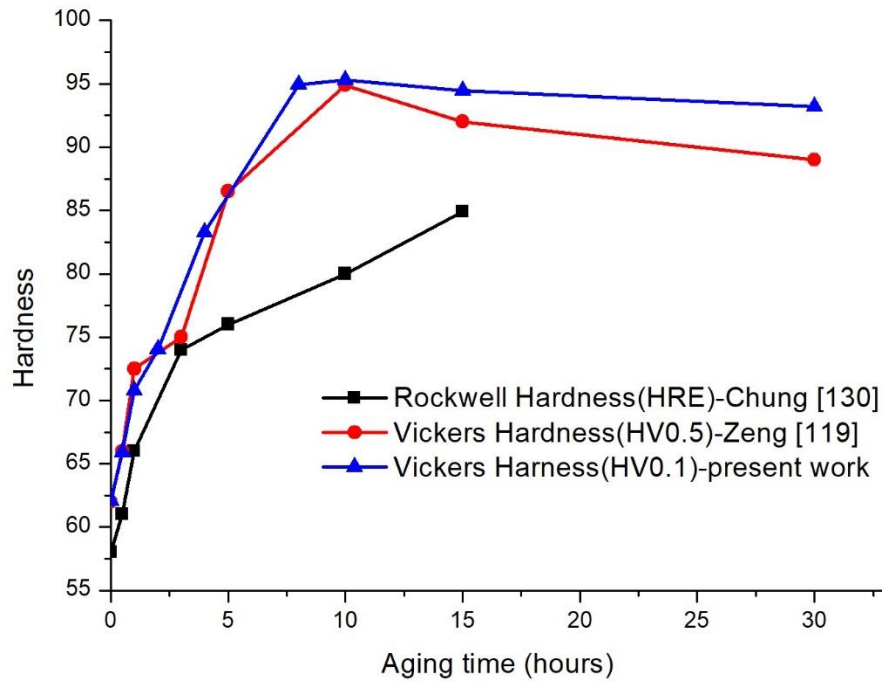


Figure 5.1 Comparison of the age hardening curves of solution treated AZ91 [119, 130].

The aging was carried out on AZ91, aging at 200°C.

5.2 Micro-compression tests

The subsequent section involves the testing of micro-specimens. They are all inheritably single crystal i.e. without considering the effect of grain boundaries and neighbouring grains which are relevant to polycrystalline samples.

The specimens were machined using the FIB. This introduced surface damage which will affect the results to some degree [131, 132]. The amorphous layer introduced by ion beam was estimated as 5 nm for Mg-9 wt% Al alloy by Monte Carlo simulation [133] and our own observations (not shown here) shows the surface damage layer is less than 10 nm. The ingress of dislocation from the surface damage layer and also the egress are expected to be similar for all the specimens in the current study.

5.3 Effects of precipitates on basal slip

The CRSS values of the basal $\langle a \rangle$ slip were derived from the stress-strain curves after the compression of micro-pillars along $[55 \bar{1}0 9]$. However, the results indicate only limited strengthening caused by the precipitates in AZ91. Based on the results obtained from a heavily textured AZ91, using the average Schmid factor, the peak-aged precipitation hardening (aging 30 h at 200°C) for basal slip (i.e. Δ CRSS) was found in earlier work to be about 5 MPa [88], which is close to the increase in CRSS (4 MPa) measured upon aging 10 h at 200°C in the current study.

The precipitation strength derived from the hardness of the bulk sample by Zeng [119] is 141 MPa using Taylor factor 4.5. The Orowan strengthening without Taylor factor is 31 MPa. This is a large increment as compared with the micro-pillar compression results in this thesis. The possible reason for the large discrepancy is as follows. The calculation of Orowan strengthening by Zeng [119] adopted the elliptical disc precipitate model described by Hutchinson [30]. This elliptical disc approximation is applied to basal plates with a length/width ratio of 4, a length/thickness ratio of 10 and a width/thickness ratio of 2.5. However, the dimensions measured by Zeng do not match the elliptical disc approximation well.

The Orowan equation used in the current work has been extended to Mg alloys by Robson [52], who considered a square array of circular disc shaped precipitates parallel to the basal plane. The Orowan equation used in this work [52] is described as (from Table 2.5)

$$\sigma_{Orowan} = \left(\frac{Gb}{2\pi\sqrt{1-\nu}} \right) \left(\frac{1}{\lambda} \right) \ln \left(\frac{d_p}{r_0} \right) \quad \text{Equation 5.1}$$

$$\lambda = \left(\frac{0.886}{\sqrt{f}} - 1 \right) d_t$$

Equation 5.2

where ν is the Poisson's ratio of the Mg matrix ($\nu = 0.35$), G is the shear modulus of the Mg matrix ($G = 17GPa$), b is the magnitude of the Burgers vector of basal $\langle a \rangle$ dislocations ($b = 0.32 nm$). d_p is taken equal to the mean planar diameter of the particles on the (0001) slip plane. d_p is equal to the uniform diameter d_t . To simplify the analysis, the uniform diameter d_t is set equal to the length (l) of the precipitate ($d_t = l = 550 nm$). r_0 is taken equal to the basal $\langle a \rangle$ dislocation core radius ($r_0 = 0.32nm$). The volume fraction of precipitates is estimated as 11.4% when the specimen is aged at 200°C [42]. The effective interparticle spacing on basal plane (λ) is 893 nm. And the calculated Orowan stress (σ_{Orowan}) resulting from the interaction between basal $\langle a \rangle$ dislocations and basal precipitates is 9 MPa. This increment is larger than the experimental results. The possible reasons are as follows.

A higher solute concentration is expected in the solution treated specimens (i.e. ~ 9 wt.% Al) than that in the matrix of the aged specimens (i.e. ~3 wt.% Al). Study of Mg-Al dilute alloys indicates that Al solutes increase the critical resolved shear stress for basal slip by an amount that is proportional to $c^{1/2}$, where c is the solute atomic concentration [48]. However, considering the difference in the solute atom concentration between the solution treated sample and the aged sample in the present work, this yields an equivalent CRSS difference of 3 ~ 4 MPa extracted from the Mg-Al micro-pillars compression [134], in line with the CRSS difference between the experimental result (4 MPa) and the calculated result (9 MPa). This explains the results presented here and elsewhere [88]. In other words, the measured CRSS values change with the peak aging is a result of the strengthening effect of the precipitates and weakening effect of the diluted matrix.

The TEM observations also showed no sign of precipitates blocking basal $\langle a \rangle$ dislocation motion. Attempts have been made using TEM to identify unambiguously the origin of the increase in CRSS associated with precipitates on the basal plane. Despite careful examination no Orowan loops have been observed when examining deformed aged samples over a range of electron beam directions. Mg-Mg₁₇Al₁₂ interphase shows local distortions at the interface boundaries using high-resolution TEM analysis [30, 135], indicating the interface is not totally coherent. Recent simulation work suggests that dislocations collapse into the Mg-Mg₁₇Al₁₂ interphase boundary [136], leaving no visible Orowan loops.

Images taken using precipitate reflections were used when examining deformed samples in a $\langle \bar{2}110 \rangle$ direction, which should make shearing of precipitates visible, but no evidence for this was found. This is perhaps not surprising since the large hardness discrepancy between Mg₁₇Al₁₂ and matrix [130]: these precipitates are expected to have very high strength and so would not be sheared during the small strain deformation of the micro-pillars.

5.4 Effect of precipitates on $\{01\bar{1}2\}$ twinning at the micro-scale

5.4.1 Precipitate rotation w.r.t. the matrix upon twinning

Twinning shape change is regarded as a simple shear process. Shearing of particles upon twinning has not been observed in the present work. Only twinning engulfed precipitates have been observed.

The engulfed precipitate undergoes a rigid body rotation and pure transformation strain to accommodate the twinning shear [137]. The tensor (e_{ij}^T) describing the shape change associated with twinning is

$$e_{ij}^T = \varepsilon_{ij}^T + \omega_{ij}^T \quad \text{Equation 5.3}$$

$$\varepsilon_{ij}^T = \begin{bmatrix} 0.5\gamma & -0.03\gamma & 0 \\ -0.03\gamma & -0.5\gamma & 0 \\ 0 & 0 & 0 \end{bmatrix}, \omega_{ij}^T = \begin{bmatrix} 0 & 0.5\gamma & 0 \\ -0.5\gamma & 0 & 0 \\ 0 & 0 & 0 \end{bmatrix} \quad \text{Equation 5.4}$$

where ε_{ij}^T is the pure strain component and ω_{ij}^T is the rotation component. The tension twinning shear (γ) in Mg is 0.129, as shown in Table 2.3.

The rigid body rotation is 3.7° about $[\bar{2}110]$, accounting for the small 4° rotation of the basal precipitate when the precipitate is engulfed by the twin [137].

5.4.2 Back stress caused by the non-shearable precipitates

When the twinned region contains shear resistant precipitates, the transformation strain ε_{ij}^T leads to strain incompatibility around the precipitate in the twin. This strain incompatibility will introduce a back stress [138-140] around the precipitate in the twin. Elastic or plastic deformation must occur to accommodate this strain discontinuity. This has been applied to precipitate interaction with twinning in Mg by Robson [141] as follows:

The entirely elastic accommodation is described by Eshelby's solution [142-144] when a precipitate is fully embedded in a tension twin. It shows how the strain and stress field look away from the precipitate. In Eshelby's solution, the basal precipitate is regarded as an 'inhomogeneity'. The basal precipitate is approximated as an ellipsoid with

dimensions $b = c \neq a$, as shown in Figure 5.2(b). The basal precipitates in the peak-aged micro-pillars have an aspect ratio of 15:1 ($\frac{d_t}{t_t} = \frac{l}{t} = \frac{550}{36} \approx 15$). Thus $15a = b = c$ is used as an approximation for the basal precipitate dimension in Eshelby's solution. The precipitate and the matrix are assumed to be elastically isotropic. The transformation strain ε_{ij}^T will be imposed on the precipitate and lead to a stress on the precipitate. This stress will be relaxed by deforming the surrounding matrix. Some other parameters used in the calculation are: Young's modulus (E) which is taken as 45 GPa and Poisson's ratio (ν) which is taken as 0.35 for an Mg matrix [145]. Young's modulus (E) which is taken as 80 GPa and Poisson's ratio (ν) which is taken as 0.35 for the basal precipitate [145].

Healy [146] published the MATLAB code that allows to solve the 3-dimensional Eshelby problem. This code is able to predict the elastic misfit strains and stresses in the matrix and ellipsoid precipitate with dimensions $b = c \neq a$. Full details of the MATLAB code are given in Ref. [146].

Applying all the parameters in the MATLAB routine, the elastic strains and stresses outside a precipitate are computed and are shown in Figure 5.3.

Figure 5.3 shows the calculated strains and shear stresses in 2-dimensional diagrams. The x-y planes pass through the centre of the basal precipitate where are the maximum elastic strains and stresses. Figure 5.3(a) shows that the predicted maximum strain is around 8%. The maximum strain is only reached in a very small volume of the matrix, just ahead of the precipitate on its habit plane. This high local strain can generate an extremely high shear stress, more than 2 GPa, which is ahead of the precipitate tip. The maximum strain and stress drop quickly as the distance from the precipitate increases. The high stress greatly exceeds the shear stress required to activate the plastic deformation (e.g., basal

slip, prismatic slip and pyramidal slip), so plastic relaxation is expected. Basal slip and non-basal slip are likely to be activated to accommodate the misfit strain around the precipitate. This extremely high stress greatly exceeds the flow stress, and thus entirely elastic deformation is not physically reasonable. Although the fully elastic deformation model is not realistic, it shows that the back stress can contribute to the strengthening against twin growth.

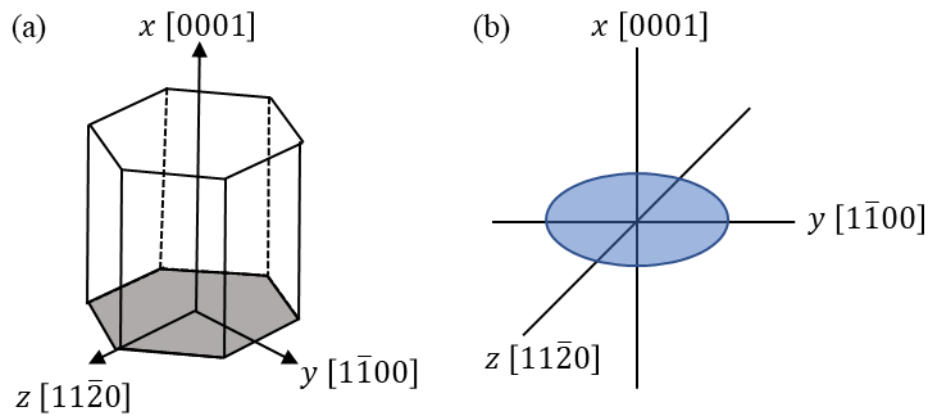


Figure 5.2 (a) x , y and z define a coordinate system in which the back stress is calculated. x axis is parallel to [0001] [137]. (b) The basal precipitate used in the present work. a , b and c are the semi-axis lengths of the basal precipitate. a , b and c are along the x , y and z axes, respectively. $15a = b = c$.

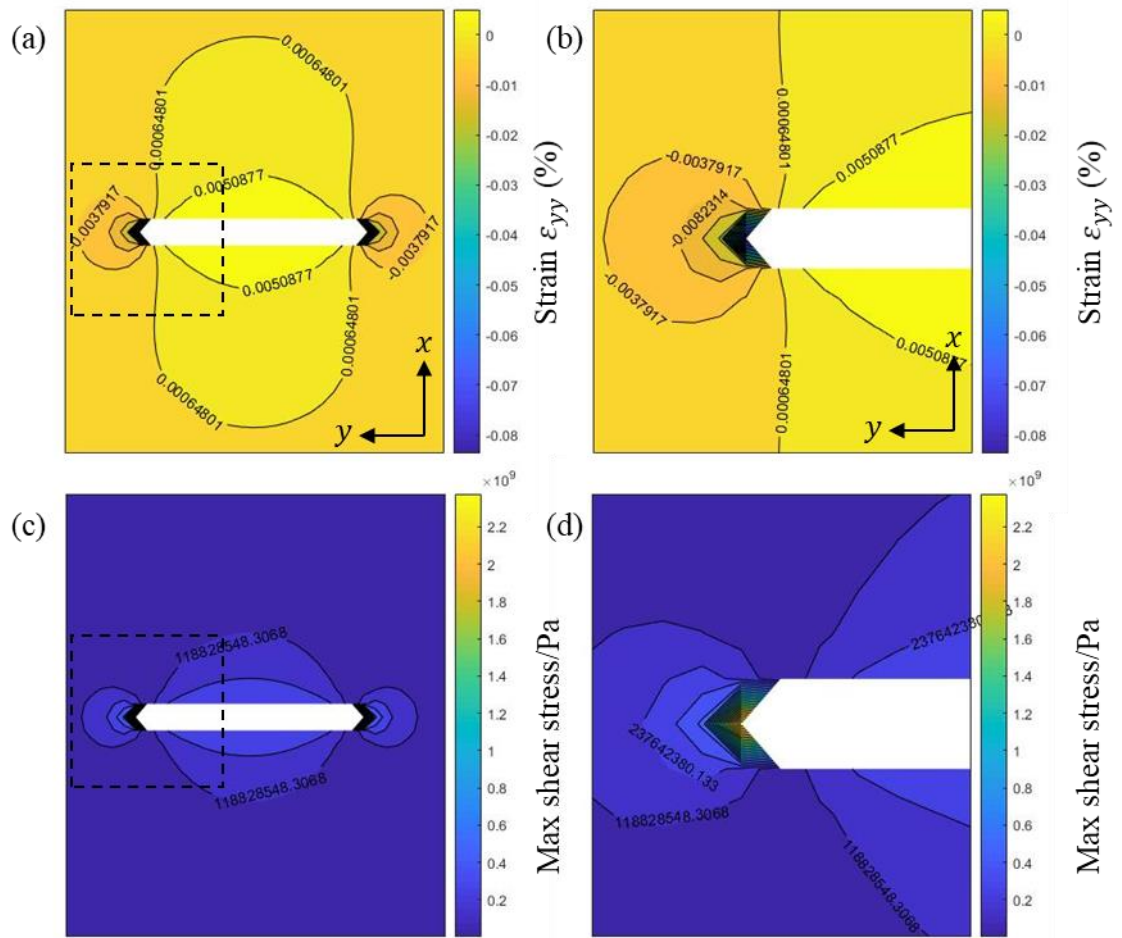


Figure 5.3 Elastic misfit strain and shear stress fields around a precipitate calculated by the Eshelby solution. The white area indicates the basal precipitate. (a) maximum normal strain in y direction for a precipitate. (b) an enlarged version of the dashed black box in figure(a). (c) maximum shear stress. (d) an enlarged version of the dashed black box in figure(c).

The purely elastic deformation approach is limited as regard to predicating the effect of precipitates on twin growth. Thus, a full-field crystal plasticity-phase field model (full-field CP-PF model) has been used by Liu et al. [147] to estimate the effect of precipitates on twin growth. Engineering stress-strain curves for the single crystal have been

simulated in the absence of basal plate precipitates and in the presence of basal plate precipitates, as shown in Figure 5.4(b). The critical applied stress for twin growth without precipitates is around 29 MPa. This stress increases to 67 MPa when the twin boundary approaches the precipitate and decreases speedily once the twin has overcome or engulfed the precipitate. However, the stress is 6 MPa higher than the stress in the absence of precipitates [147]. This might be attributed to the precipitate interaction with the plastic deformation in the twin (i.e., basal slip, pyramidal slip and stacking faults), which would introduce strengthening. Also the simulation shows that the stress state reaches a peak if the precipitate is partly engulfed in the twinned region (e.g., precipitate ② in Figure 4.28).

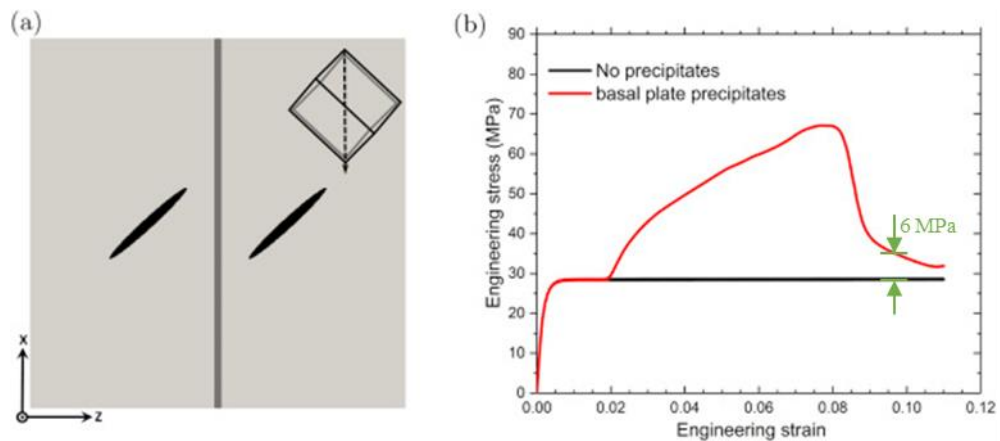


Figure 5.4 (a) A schematic illustration showing a single crystal containing two basal plate precipitates and a pre-existing twin. The basal precipitate is indicated by the black ellipse and the pre-existing twin is indicated by the long grey box in the centre of Figure 5.4(a). The dashed black arrow in the HCP unit cell indicates the twinning direction for a tension twin. (b) The simulated engineering stress-strain curves of the single crystal.[147]

5.4.3 Strain bursts in the stress-strain curves

For twinning, the true stress-strain curves obtained from the solution treated specimens show a large strain burst while those from the aged specimens show multiple small strain bursts. Subsequent TEM observations show a large single twinned region in each of the solution treated specimens and multiple smaller twins in each of the aged specimens. Although the deformation process is not clearly observed, it is not unreasonable to assume that the large strain burst observed from the solution treated specimen was caused by the nucleation and rapid growth of the twin later observed in the TEM image. Along the same line, one can assume that the small strain bursts recorded during the compression of the aged specimen correspond to the nucleation and growth of the small twins observed in the TEM image. Although we cannot attribute every individual strain burst to the nucleation of a twin in the current work, it is probably not unreasonable to assume that most of the strain bursts are associated with twin nucleation, especially the first strain burst. The first strain burst corresponds to the first twin which lies mainly along the $[01\bar{1}0]$ loading direction.

Each dot in Figure 5.5 represents one strain burst in the stress-strain curves in Figure 4.17. The stress for each strain burst is extracted. The apparent stress for the first twin nucleation of all the micron-pillars are shown in Figure 5.5, outlined by the black ellipses. The apparent first twin nucleation stresses for the solution treated and the aged micro-pillars scatter heavily which is related to the heterogeneous twinning nucleation mechanism. The averaged twin nucleation stresses for the solution treated and aged micron-pillars are 171.8 ± 46.5 MPa and 207.1 ± 62.1 MPa, respectively. This is mainly attributed to the high local stress concentration at the contact surface between the

diamond tip and the micro-pillar top surface in micro-scale compression. The true stress for the first twin nucleation is unpredictable in this micro-pillar compression.

More dots in the aged pillar show higher twin numbers in the aged micro-pillars than in the solution treated micro-pillars. 6 solution micro-pillars out of 10 show one large strain burst under $[01\bar{1}0]$ loading, showing no work hardening. 4 solution micro-pillars out of 10 show more than one large strain burst, probably due to the undissolved Al-Mn particles during solution treatment (outlined by the red dashed circle in Figure 4.5). All the aged micro-pillars show multiple strain bursts with increasing stress, indicating the moderate work hardening.

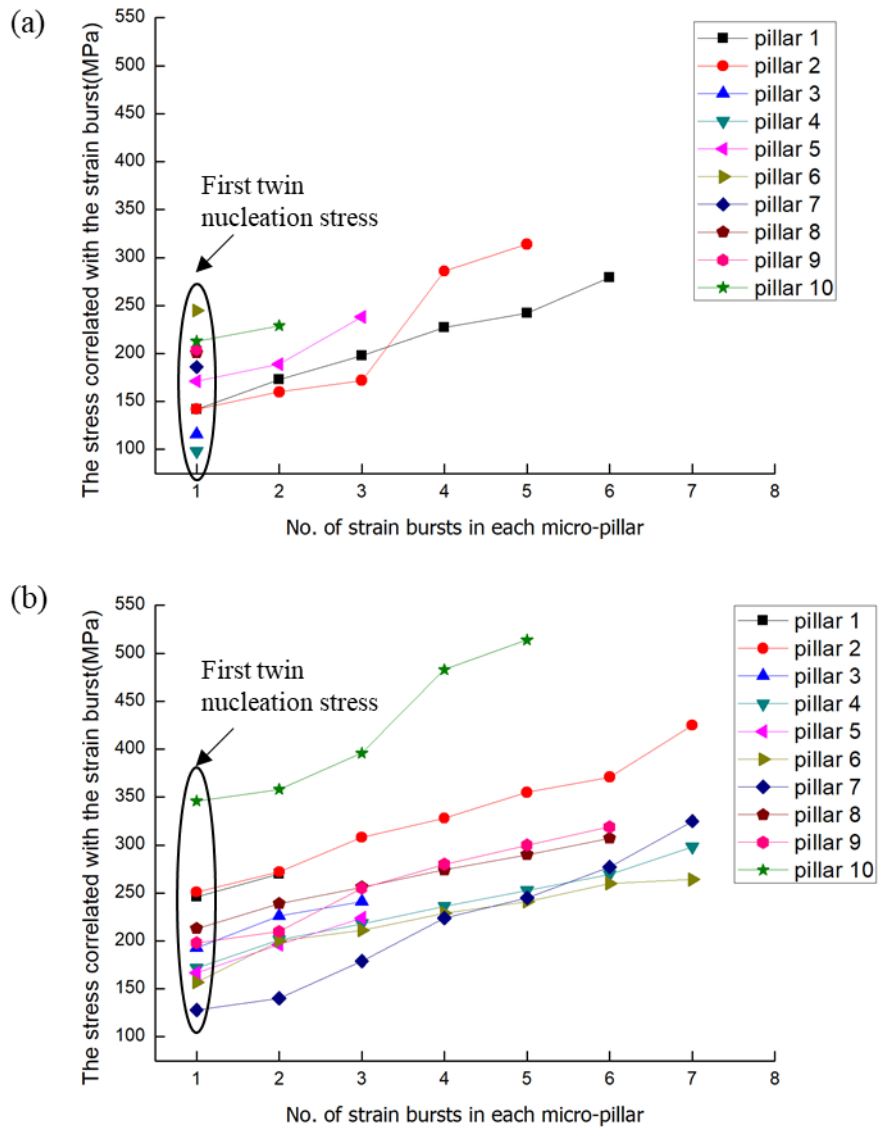


Figure 5.5 The apparent stresses at each strain burst recorded during all the compression tests on the solution treated (a) and the aged (b) micro-pillars, extracted from the stress-strain curves in Figure 4.17. The horizontal axis represents the sequence of the strain bursts in each micro-pillar. The vertical axis represents the stress where the strain burst occurs. The stresses for the first strain burst are outlined by the black ellipses. There is a large variation for the first strain burst stresses.

5.4.4 Apparent CRSS determined from mean yield strengths (0.2% strain offset rule)

The mean yield strengths (averaged 0.2% proof stresses) were determined to be 176.8 ± 21.2 MPa and 237.1 ± 23.7 MPa for the solution treated and aged micro-pillars. The mean yield stress of the solution treated micro-pillars is roughly the same as the first twin nucleation stress (171.8 ± 46.5 MPa) due to the large strain burst around 0.2% offset strain. The mean yield stress of the aged micro-pillars is higher than the first twin nucleation stress (207.1 ± 62.1 MPa), showing some of the first strain bursts occurring earlier than 0.2% strain.

Taken the 0.2% proof stress as the yield stress, the apparent CRSSs for tension twinning were determined to be 88.4 MPa and 118.6 MPa for the solution treated and aged micro-pillars in the current study. These two CRSS values are used to compare with the bulk samples results which generally regard the 0.2% strain point as the yield point.

Kada et al. [89] and Stanford et al. [88] both studied the precipitation strengthening effect on $\{01\bar{1}2\}$ twinning in bulk AZ91 specimens. The CRSS values reported by these authors for the solution treated AZ91 and aged AZ91 are shown in Table 5.1, exhibiting a large variation and quite different from the present work. This variation could be attributed to a difference in texture, grain size and a size effect of the micro-pillars. Despite the large variation in CRSS values in different specimens, the magnitudes of the hardening associated with precipitates are similar. It is reasonable to say that the CRSS increment determined from the bulk samples reflects the stress for twin growth.

The precipitation strengthening of $\{01\bar{1}2\}$ twinning studied by the micro-pillar compression tests is simplified and more straightforward to some extent without the influence of the other variables in the bulk sample experiments. And the effect of precipitates on twin nucleation and growth can be separated to some extent.

Table 5.1 Examples from the literature of the CRSS for twinning in AZ91.

	CRSS/MPa	Δ CRSS, $\Delta\tau$ /MPa	Ref.
Solution treated	~ 50	36	Kada et al. [89]
Aged	~ 86		
Solution treated	31~ 40	~ 22	Stanford et al. [88]
Aged	51~ 60		
Solution treated	88.4	30	Present work
Aged	118.6		

5.4.5 Stacking faults in the twin

The stacking fault morphology is a straight line for both the solution treated and aged micro-pillars when the specimens are viewed parallel to (0001) (e.g., $g = 0002, BD \sim [\bar{2}110]$), as shown in Figure 4.22(a) and Figure 4.29(b). The stacking faults show some fringes when the specimens are viewed oblique to (0001), e.g., Figure 4.22(b) using $g = 01\bar{1}1, BD \sim [\bar{2}110]$ and Figure 4.29(a) using $g = 01\bar{1}0, BD \sim [\bar{2}110]$. Therefore, the stacking faults in the solution treated and aged micro-pillars are lying on (0001).

From a purely geometrical point of view, the formation of stacking faults on (0001) is related to dislocation incorporation into twin boundaries. The dislocation is generally regarded as basal $\langle a \rangle$ dislocation due to the low CRSS of basal slip. The basal $\langle a \rangle$ dislocations with Burgers vectors parallel to the twin plane (denoted a_{0° type) enter the twin directly. The basal $\langle a \rangle$ dislocations with Burgers vectors 60° to the twin plane (denoted a_{60° and a_{120° type) may have dislocation reactions when entering into a twin [121, 148-150].

a_{0° type slip transfer:

$$\frac{1}{3}[\bar{1}2\bar{1}0]_m \rightarrow \frac{1}{3}[\bar{1}2\bar{1}0]_t \quad \text{Equation 5.5}$$

a_{60° type slip transfer:

$$2 \times \frac{1}{3}[\bar{1}1\bar{2}0]_m \rightarrow -2b_t + \frac{1}{3}[\bar{1}2\bar{1}3]_t \rightarrow -2b_t + \frac{1}{3}[\bar{1}\bar{1}00]_t + \frac{1}{3}[0\bar{1}\bar{1}0]_t + [0001]_t$$

Equation 5.6

where b_t is a zonal twinning dislocation. It has been left on the twin boundary after the reaction with a magnitude of $0.0643[\bar{1}011]$ [151, 152].

a_{120° type slip transfer:

$$2 \times \frac{1}{3}[\bar{2}\bar{1}\bar{1}0]_m \rightarrow -2b_t + \frac{1}{3}[\bar{1}2\bar{1}3]_t \rightarrow -2b_t + \frac{1}{3}[\bar{1}\bar{1}00]_t + \frac{1}{3}[0\bar{1}\bar{1}0]_t + [0001]_t$$

Equation 5.7

Equation 5.4 and 5.5 show the two steps of forming stacking faults on (0001) in the twin.

The two a_{60° and a_{120° type dislocations are incorporated into a twinning dislocation and

a perfect $\langle c + a \rangle$ dislocation. The latter one dissociates into a sessile $\langle c \rangle$ dislocation and two Shockley partial dislocations in the twin.

The interaction between the basal $\langle a \rangle$ slip and twin boundary indicates that the twin boundary acts as an effective emission source for partial dislocations [153] during twinning. Partial dislocations move along the twin growth direction. Analogous to grain boundaries, the $\text{Mg}_{17}\text{Al}_{12}$ precipitates in the twin act as strong barriers to partial dislocation motion. This is consistent with the observation of a large number of stacking faults being restricted by the precipitates in the twinned region in the aged specimens. Although it has not been explicitly reported, it is unreasonable to expect that the presence of stacking faults could act as (probably weak) barrier to dislocation motion during subsequent plastic deformation hence introducing the strengthening.

5.5 Effect of precipitates on $\{01\bar{1}2\}$ twinning at the submicron-scale

5.5.1 Twin nucleation

Twinning nucleation is sensitive to dislocations, grain boundaries, twin boundaries and dislocation pile-ups, cracks and slip bands. All the above microstructures are preferential sites for twin nucleation in bulk Mg [154-156]. In the present submicron-pillar compression experiment, there are no pre-existing grain boundaries, twin boundaries, cracks or slip bands before compression. And thus twin nucleation requires an alternative source. The in-situ TEM experiment shows directly that the localized high stress regions produced by the non-uniform contact between the pillar surface and diamond tip are preferential sites for twin nucleation, especially the first twin. The twin nucleation occurs

quickly within one video frame in most cases, resulting in the sudden appearance of a finite size of twinned region. The subsequent twins nucleate at the twin boundaries in most submicron-pillars. This is the case for both the solution treated and the aged submicron-pillars, indicating that the twin nucleation sites are nearly independent of the precipitate position.

The apparent first twin nucleation stress is determined to be 325.7 ± 65.4 MPa for the solution treated submicron-pillar and 332.8 ± 94.4 MPa for the under-aged submicron-pillar. It shows that the precipitate has little effect on the apparent first nucleation stress in the pillar compression test. The high local stress at contact surface, the source for twin nucleation, is higher than the apparent stress in the pillar compression test. Therefore the true twin nucleation stress cannot be estimated from the current study.

5.5.2 Twin growth

In bulk Mg, twins are mostly elliptical in shape and attached to the grain boundaries and twin boundaries. Kumar et al. [157] and Zhang et al. [158] reported that the stress level in elliptically shaped twins decreases drastically towards the twin tips. In the present study, the twin propagates along the shear direction and occupies the width of the pillar and then thickens perpendicular to the shear direction. The twin thickens upward to the top surface of the pillar and downward to the bottom of the pillar, dominantly along the downward direction. When the twin tip encounters a precipitate, the precipitate exerts an inhibiting effect on the twin front that exceeds the stress driving twin propagation and so stops the twin propagation. This is the case in Figure 4.60, in which of the propagation of the first twin is stopped by the precipitate (indicated by a red-dashed box) in aged submicron-pillar 3. With the increased applied stress, the twin tip is able to overcome the inhibiting

effect of the precipitate and pass through the precipitate. The in-situ TEM compression indicates the effective strengthening of the precipitate against twin growth

As discussed in Chapter 5.4.1, the twin nucleation is not influenced directly by the precipitates in the pillar compression tests. However, the twin number has increased in the aged pillars as compared with the solution treated ones, as shown in Table 5.2. It indicates more twin nucleation occurring in the aged specimen. The possible explanation is that the stress for subsequent twin nucleation on the existing twin boundaries is lower than the stress for a twin overcoming a precipitate, and thus resulted in more twin nucleation in the aged specimen.

Table 5.2 The number of basal precipitates and twins in each submicron pillar.

	Solution treated		Aged	
	precipitates	twins	precipitates	twins
Pillar 1		2	5	3
Pillar 2		2	9	5
Pillar 3	0	3	6	5
Pillar 4		4	4	4

5.6 General discussion of the effect of precipitates on twinning

The apparent CRSS increment for the basal plates in the current micro-pillar compression is 30 MPa. In-situ TEM compression shows that the samples containing precipitates show a higher work hardening. Micro-pillar compression of Mg-5%Zn shows a weak or zero strengthening effect of rod-shaped precipitates on twinning with the CRSS increasing

from 70 MPa to 71MPa [85]. The CRSS for twinning in WE43 (Mg-Y-Nd-Zr alloy) shows no increment between the solution treated (85 MPa) and peak aged condition (85 MPa) [87]. These apparent CRSS changes are the combined results of precipitate orientation, volume fraction, size and aspect ratio. Apart from the experimental work, some calculation and modelling has been carried out by Robson et al. [52, 141], Liu et al. [147] and Fan et al. [159, 160] in order to quantitatively estimate the precipitation strengthening effect on twinning.

(1) Precipitate orientation

Assuming precipitates with the same volume fraction, aspect ratio, size and with a random distribution, the influence of the precipitate orientation on twinning has been studied by molecular dynamics (MD) simulation [159, 160] and the full-field CP-PF model [147]. They both show that the precipitate shows the strongest hindering effect on twin growth when the habit plane of the precipitate is parallel to the twinning plane and the precipitate shows the weakest hindering effect on twin growth when the habit plane of the precipitate is perpendicular to the twinning plane. The area of the precipitate that the twin boundary has to overcome when the precipitate is engulfed by the twin reaches the maximum if the precipitate is parallel to the twinning plane. Liu et al. [147] also plotted the CRSS increment vs precipitate orientation, as shown in Figure 5.6.

The common habit plane in Mg is the basal plane (e.g. Mg-Al system) [29, 32, 35, 43] and prismatic plane (e.g. Mg-RE system) [59-61]. The angle between the habit plane of the precipitate and the tension twin $(10\bar{1}2)[\bar{1}011]$ is calculated and substituted in Figure 5.6 in order to estimate quantitatively the effect of the precipitate habit plane on twinning.

For the precipitates lying on basal plane, the angle between the basal plane and $(10\bar{1}2)$ twin plane is 43° . Substituting this 43° into Figure 5.6, the CRSS increment is about 48 MPa. The precipitates lying on prismatic planes are assumed to evenly distributed on $(1\bar{1}00)$, $(10\bar{1}0)$ and $(01\bar{1}0)$. A third of the precipitates lie on $(1\bar{1}00)$ and the angle between $(1\bar{1}00)$ and the $(10\bar{1}2)$ twin plane is 70° . A third of the precipitates lie on $(10\bar{1}0)$ and the angle between $(10\bar{1}0)$ and $(10\bar{1}2)$ is 47° . The last proportion of precipitates lie on $(01\bar{1}0)$ and the angle between $(01\bar{1}0)$ and $(10\bar{1}2)$ is again 70° . Substituting these angles into Figure 5.6, the strengthening effect on $(10\bar{1}2)[\bar{1}011]$ twinning from the precipitates lying on $(1\bar{1}00)$, $(10\bar{1}0)$ and $(01\bar{1}0)$ is 9.2 MPa, 14.6 MPa and 9.2 MPa, respectively. Therefore the overall CRSS increment from the prismatic precipitates is 33 MPa, so the precipitates lying on the basal plane show a higher strengthening effect on twinning than the precipitates lying on prismatic planes.

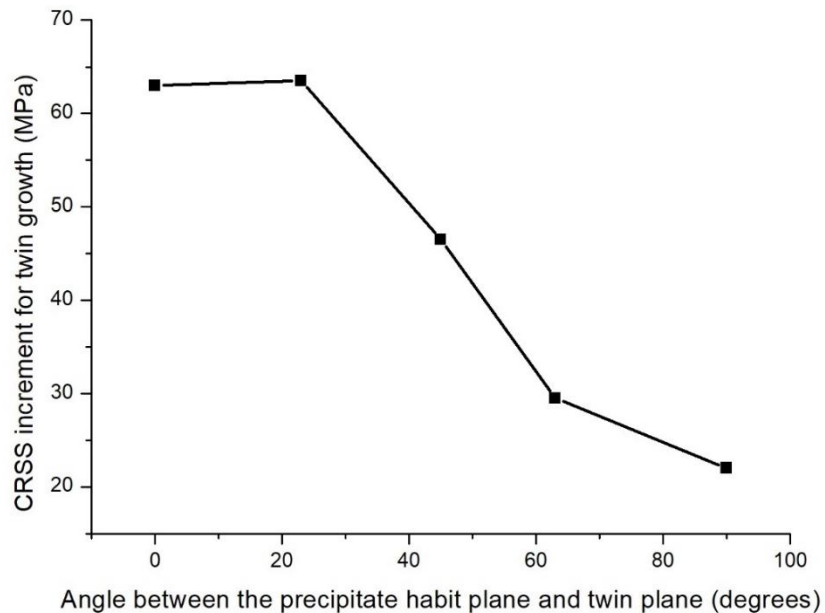


Figure 5.6 The CRSS increment is plotted as a function of angle between the precipitate habit plan and the twin plane [147].

(2) Volume fraction

The CRSS for twinning is positively correlated with volume fraction of the precipitates [52, 147, 160]. And the CRSS is almost linearly proportional to the volume fraction, as reported in Ref. [52, 147]. Increasing the volume fraction can increase the back stress against twin growth.

(3) Precipitate size

Liu et al.[147] simulated the CRSS dependence on precipitate size and shows the strengthening effect as ‘smaller is harder’. A critical precipitate size is reported. The simulated CRSS values show higher strengthening effect with decreasing precipitate size below the critical size while the simulated CRSS values are not sensitive to the precipitate size above the critical size.

(4) Aspect ratio

Applying different aspect ratios (from 1:1 to 20:1) in the MATLAB routine, the elastic stresses outside a plate are computed and are shown in Figure 5.7. The elastic stresses increase with increasing aspect ratio from 1:1 to 10:1 and reach the maximum when the aspect ratio is 10:1. The elastic stresses decrease with increasing aspect ratio from 10:1 to 20:1.

Plates with different aspect ratios have been simulated by Liu et al. [147] using the full-field CP-PF model, showing that the CRSS increment for twin growth and the back stress are both proportional to the aspect ratio from 1:1 to 16:1.

This discrepancy is probably due to the difference in the way of handling the back stress. The stresses calculated using the MATLAB code for the Eshelby's solution is fully elastic stress and no plastic relaxation is considered in the routine. The full-field CP-PF model simulated the plastic relaxation process directly [147]. The effect of aspect ratio on twinning requires further research to be ascertained.

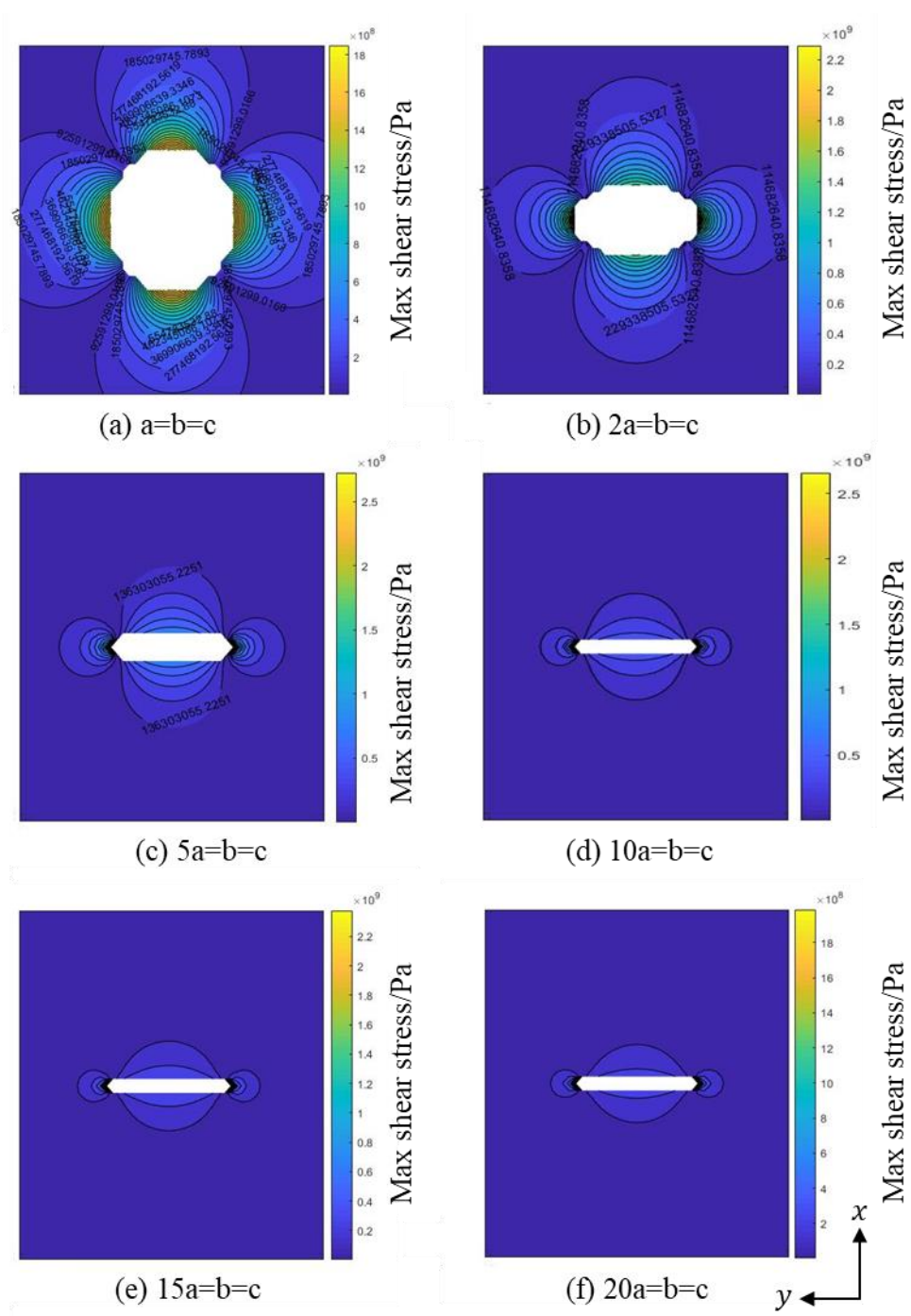


Figure 5.7 Evolution of elastic stresses around a precipitate with different aspect ratio.

The x-y planes pass through the centre of the basal precipitate.

In summary, the precipitate with habit plane parallel to the twinning plane, a high volume fraction and small size would together show the maximum hindering effect against twin growth.

6 Conclusions and future work

6.1 Conclusions

For micro-pillars of solution treated and peak-aged AZ91 alloy compressed along the $[55\bar{10}9]$ direction, $1/3[11\bar{2}0](0001)$ slip was activated. The following conclusions can be drawn:

- (i) The precipitates have limited strengthening effect on basal slip. The CRSS increment between the solution treated specimen and aged specimen is 4 MPa. The magnitude of precipitate hardening on the basal plane differs from that predicted using the analyses of Robson [52]. The Al concentration changes between the solution treated specimen and the aged specimen provide extra strengthening for the solution treated specimen and explain the discrepancy.
- (ii) No evidence for basal dislocations bowing around particles or shearing of precipitates has been obtained by TEM observation.

For micro-pillars of solution treated and peak-aged AZ91 compressed along the $[01\bar{1}0]$ direction, $\{01\bar{1}2\}$ twinning was activated. The following conclusions can be drawn:

- (iii) The apparent CRSSs (determined by the 0.2% strain offset rule) for tension twinning obtained from the solution treated AZ91 and aged AZ91 are very different from those reported for bulk AZ91, although the magnitude of the hardening associated with precipitates is similar. These differences arise from the use of textured polycrystals in the earlier work, where constraints from the surrounding grains will influence the effective local stress to varying extents.

- (iv) The precipitates introduced more and smaller twins to the aged micro-pillars than to the solution treated micro-pillars. The first twin nucleation occurs at a stress of 71.8 ± 46.5 MPa for the solution treated micro-pillars and 207.1 ± 62.1 MPa for the aged micro-pillars. The first twin nucleation stress is not sensitive to the presence and otherwise of the precipitates in micro-scale compression.
- (v) The precipitates themselves are neither sheared nor twinned during twinning deformation. The precipitates are only engulfed by the tension twin in the current work. A back stress around the precipitate is generated and provides the considerable contribution to hindering the twin growth.
- (vi) The samples with precipitates have a higher density of stacking faults than in the solution treated samples. The higher density of stacking faults may influence the transmission of dislocations and thus confer higher work hardening.

For submicron-pillars of solution treated and under-aged AZ91 compressed along the $[01\bar{1}0]$ direction, tension twinning was activated. The following conclusions can be drawn:

- (vii) The nucleation of the $\{01\bar{1}2\}$ twinning assessed by in-situ TEM shows that high local stress concentration is the source of the twin nucleation. The first twin nucleation occurs preferentially at the contact surface between the diamond tip and the pillar surface. Most subsequent twin nucleation occurs preferentially at the twin boundaries. The precipitates have no obvious influence on the twin nucleation in the in-situ TEM compression. The high local stress, the source of twin nucleation, is higher than the apparent stress. Therefore the true twin nucleation stress cannot be estimated from the current study.

- (viii) Twin growth is inhibited by the precipitates. Increasing the applied stress can help the twin to overcome the precipitates.

6.2 Suggestions for future work

- (i) The twin nucleation region has been captured in the in-situ TEM tests. However, the results are limited to ascertaining the true twin nucleation stress, the twin nucleus formation mechanism and the twin nucleus stable size. It is of interest to study the twin nucleation by simulation informed by the experimental results.
- (ii) Most in-situ TEM shows rapid twin nucleation and initial growth except under-aged submicron-pillar 3. This pillar gave a more controlled twin growth for not very well understood reasons. This should be investigated systematically in order to develop controlled twin growth strategy.
- (iii) For the in-situ TEM compression, the diamond tip is not perfectly flat and generates high local stress at the contact surface between the submicron-pillar and the diamond tip. This general shortcoming of the in-situ compression test can be overcome by the push-to-pull test. It is of importance to study the twinning mechanism without the influence of stress concentration. Therefore, it would be helpful to study in-situ deformation by tensile testing using a push-to-pull device.
- (iv) The basal precipitate interaction with easy $\langle a \rangle$ slip on basal planes and tension twinning has been studied in the current work. The precipitate interaction with $\langle a \rangle$ slip on prismatic planes and $\langle c + a \rangle$ slip on pyramidal planes is not fully understood. It would be interesting to study the precipitate interaction with non-basal slip by micromechanical testing. It would also help to understand the precipitate interaction with slip in the twin.

- (v) The effect of the precipitate aspect ratio on twin growth is not clear yet. More research on this subject is required for a better understanding of the precipitate interaction with twinning.

Appendix: Publish list

1. **S.S. Si**, J. Wu, I.P Jones, Y.L. Chiu. Role of precipitates on basal dislocation slip and $\{01\bar{1}2\}$ twinning in AZ91 micro-pillars. (submitted to Philosophical Magazine)
2. **S.S. Si**, J. Wu, I.P Jones, Y.L. Chiu. Study of precipitation hardening in AZ91 alloy using micro- pillar compression. Proceeding of the 11th international conference on Mg alloys and their application. 2018
3. J. Wu, **S.S. Si**, U. Ghari, Y.L. Chiu. Plastic deformation micro mechanisms in magnesium and its alloys. Advances in Engineering Materials, Structures and Systems: Innovations, Mechanics and Applications. 2019 :379 382.
4. J. Wu, **S. S. Si**, Kosuke Takagi, Tian Li, Yoji Mine, Kazuki Takashima, Y.L. Chiu. Study of basal $\langle a \rangle$ and pyramidal $\langle c + a \rangle$ slips in Mg-Y alloys using micro-pillar compression. (accepted by Philosophical Magazine)

References

- [1] G.W. Groves, A. Kelly, Independent slip systems in crystals, *Philosophical Magazine* 8(89) (1963) 877-887.
- [2] M.H. Yoo, Slip, twinning and fracture in hexagonal close-packed metals, *Metallurgical Transactions A* 12A (1981) 409-417.
- [3] P.G. Partridge, The crystallography and deformation modes of hexagonal close-packed metals, *Metallurgical Reviews* 12(1) (1967) 169-194.
- [4] D. Hull, D.J. Bacon, *Introduction to dislocations*, Butterworth-Heinemann (imprint of Elsevier) 2011.
- [5] A. Couret, D. Caillard, An in situ study of prismatic glide in magnesium-1. the rate controlling mechanism, *Acta Metall.* 33 (1985) 1447-1454.
- [6] A. Couret, D. Caillard, An in situ study of prismatic glide in magnesium-2 microscopic activation parameters, *Acta Materialia* 33 (1985) 1455-1462.
- [7] S.R. Agnew, Ö. Duygulu, Plastic anisotropy and the role of non-basal slip in magnesium alloy AZ31B, *International Journal of Plasticity* 21(6) (2005) 1161-1193.
- [8] H. Yoshinaga, R. Horiuchi, On the nonbasal slip in magnesium crystals, *Trans JIM* 5 (1963) 14-21.
- [9] W. Puschl, Models for dislocation cross-slip in close-packed crystal structures: a critical review, *Progress in Materials Science* 47 (2002) 415-461.

- [10] G.I. Taylor, Plastic strain in metals, *Journal of the Institute of Metals* 62 (1938) 207-342.
- [11] B.A. Bilby, A.G. Crocker, The theory of the crystallography of deformation twinning, *Proceedings of the Royal Society of London. Series A. Mathematical and Physical Sciences* 288 (1965) 240-255.
- [12] J.W. Christian, S. Mahajan, Deformation twinning, *Progress in Materials Science* 39(1-2) (1995) 1-157.
- [13] T.B. Britton, F.P.E. Dunne, A.J. Wilkinson, On the mechanistic basis of deformation at the microscale in hexagonal close-packed metals, *Proceedings of the Royal Society A: Mathematical, Physical and Engineering Science* 471(2178) (2015) 20140881.
- [14] B. Li, E. Ma, Atomic shuffling dominated mechanism for deformation twinning in magnesium, *Phys Rev Lett* 103(3) (2009) 035503.
- [15] B. Li, X.Y. Zhang, Global strain generated by shuffling-dominated $\{10\bar{1}2\}\langle 10\bar{1}1\rangle$ twinning, *Scripta Materialia* 71 (2014) 45-48.
- [16] E. Ma, Boundary motion coupled with tensile and compressive deformation: TEM observation of twinning-like lattice reorientation in Mg micropillars, *Nanomechanical Testing in Materials Research and Development V*, ECI Symposium Series, 2015.
- [17] P.B. Price, Nucleation and growth of twins in dislocation-free zinc crystals, *Proceedings of the Royal Society of London. Series A. Mathematical and Physical Sciences* (1960) 251-262.

- [18] R.L. Bell, R.W. Cahn, The nucleation problem in deformation twinning, *Acta Metallurgica* 1 (1953) 752-753.
- [19] R.L. Bell, R.W. Cahn, The dynamics of twinning and the interrelation of slip and twinning in zinc crystals, *Proceedings of the Royal Society of London. Series A. Mathematical and Physical Sciences* 239(1219) (1957).
- [20] R.E. Reed-Hill, J.P. Hirth, H.C.R. (Eds.), *Deformation twinning*, Gordon and Breach Science Publishers, New York, 1963.
- [21] S. Vaidia, Accommodation and formation of {11-21} twins in Co single crystals, *Acta Metallurgica* 28 (1980) 1123-1131.
- [22] A.H. Cottrell, B.A. Bilby, LX. A mechanism for the growth of deformation twins in crystals, *The London, Edinburgh, and Dublin Philosophical Magazine and Journal of Science* 42(329) (1951) 573-581.
- [23] N. Thompson, D.J. Millard, XXXVIII. Twin formation in cadmium, *The London, Edinburgh, and Dublin Philosophical Magazine and Journal of Science* 43(339) (1952) 422-440.
- [24] S. Mendelson, Dislocation Dissociations in hcp Metals, *Journal of Applied Physics* 41(5) (1970) 1893-1910.
- [25] Y. Li, Y. Cui, H. Bian, S. Sun, N. Tang, Y. Chen, B. Liu, Y. Koizumi, A. Chiba, Detwinning in Mg alloy with a high density of twin boundaries, *Sci Technol Adv Mater* 15(3) (2014) 035003.

- [26] Q. Yu, J. Zhang, Y. Jiang, Direct observation of twinning–detwinning–retwinning on magnesium single crystal subjected to strain-controlled cyclic tension–compression in [0 0 0 1] direction, *Philosophical Magazine Letters* 91(12) (2011) 757-765.
- [27] Y.N. Wang, J.C. Huang, The role of twinning and untwinning in yielding behavior in hot-extruded Mg–Al–Zn alloy, *Acta Materialia* 55(3) (2007) 897-905.
- [28] D. Duly, J.P. Simon, Y. Brechet, On the competition between continuous and discontinuous precipitations in binary Mg-Al alloys, *Acta metallurgica et Materialia* 43(1) (1995) 101-106.
- [29] K.N. Braszczynska-Malik, Discontinuous and continuous precipitation in magnesium–aluminium type alloys, *Journal of Alloys and Compounds* 477(1-2) (2009) 870-876.
- [30] C.R. Hutchinson, J.F. Nie, S. Gorsse, Modeling the Precipitation Processes and Strengthening Mechanisms in a Mg-Al-(Zn) AZ91 Alloy, *Metallurgical and Materials Transactions A* 36A (2005) 2093-2015.
- [31] M.X. Zhang, P.M. Kelly, Crystallography of Mg₁₇Al₁₂ precipitates in AZ91D alloy, *Scripta Materialia* 48 (2003) 647-652.
- [32] S. Celotto, TEM study of continuous precipitation in Mg-9%Al-1%Zn alloy, *Acta Materialia* 48 (2000) 1775-1787.
- [33] D. Duly, W.Z. Zhang, M. Audier, High-resolution electron microscopy observations of the interface structure of continuous precipitates in a Mg-Al alloy and interpretation with the O-lattice theory, *Philosophical Magazine A* 71(1) (1995) 187-204.

- [34] J.F. Nie, X.L. Xiao, C.P. Luo, B.C. Muddle, Characterisation of precipitate phases in magnesium alloys using electron microdiffraction, *Micron* 32 (2001) 857-863.
- [35] A.F. Crawley, K.S. Milliken, Precipitate morphology and orientation relationships in an aged Mg-9% Al-1%Zn-0.3% Mn alloy, *Acta Metallurgica* 22 (1974) 557-562.
- [36] Y. Wang, M. Xia, Z. Fan, X. Zhou, G.E. Thompson, The effect of Al₈Mn₅ intermetallic particles on grain size of as-cast Mg–Al–Zn AZ91D alloy, *Intermetallics* 18(8) (2010) 1683-1689.
- [37] G. Han, G. Ma, X. Liu, Effect of manganese on the microstructure of Mg–3Al alloy, *Journal of Alloys and Compounds* 486(1-2) (2009) 136-141.
- [38] S. Lun Sin, D. Dubé, R. Tremblay, Characterization of Al–Mn particles in AZ91D investment castings, *Materials Characterization* 58(10) (2007) 989-996.
- [39] T. Laser, M.R. Nürnberg, A. Janz, C. Hartig, D. Letzig, R. Schmid-Fetzer, R. Bormann, The influence of manganese on the microstructure and mechanical properties of AZ31 gravity die cast alloys, *Acta Materialia* 54(11) (2006) 3033-3041.
- [40] O. Zheng, J.P. Zhou, D.S. Zhao, J.B. Wang, R.H. Wang, J.N. Gui, D.X. Xiong, Z.F. Sun, The crystallography of continuous precipitates with a newly observed orientation relationship in an Mg-Al-based alloy, *Scripta Materialia* 60(9) (2009) 791-794.
- [41] J.B. Clark, Age hardening in a Mg- 9wt% Al alloys, *Acta Metallurgica* 16 (1968) 141-152.
- [42] J.F. Nie, Precipitation and Hardening in Magnesium Alloys, *Metallurgical and Materials Transactions A* 43(11) (2012) 3891-3939.

- [43] A.F. Crawley, B. Lagowski, Effect of two-step aging on the precipitate structure in magnesium alloy AZ91, *Metallurgical transactions A* 5 (1974) 949-951.
- [44] D. Duly, M.C. Cheynet, Y. Brechet, Morphology and chemical nanoanalysis of discontinuous precipitation in Mg-Al alloys-I. regular growth, *Acta metall. mater.* 42 (1994) 3843-3854.
- [45] R.L. Fleischer, Solution hardening, *Acta Metallurgica* 9(11) (1961) 996-1000.
- [46] R. Labusch, A Statistical Theory of Solid Solution Hardening, *Phys. Status Solidi* 41 (1970) 659-669.
- [47] C.H. Caceres, D.M. Rovera, Solid solution strengthening in concentrated Mg-Al alloys, *Journa of light metals* (2001) 151-156.
- [48] A. Akhtar, E. Teghtsoonian, Solid solution strengthening of magnesium single crystals—I alloying behaviour in basal slip, *Acta Materialia* 17 (1969) 1339-1349.
- [49] A. Akhtar, E. Teghtsoonian, Substitutional solution hardening of magnesium single crystals, *Philosophical Magazine* 25(4) (1972) 897-916.
- [50] L. Gao, R.S. Chen, E.H. Han, Effects of rare-earth elements Gd and Y on the solid solution strengthening of Mg alloys, *Journal of Alloys and Compounds* 481(1-2) (2009) 379-384.
- [51] J.F. Nie, Effects of precipitate shape and orientation on dispersion strengthening in magnesium alloys, *Scripta Materialia* 48(8) (2003) 1009-1015.

- [52] J.D. Robson, N. Stanford, M.R. Barnett, Effect of precipitate shape on slip and twinning in magnesium alloys, *Acta Materialia* 59(5) (2011) 1945-1956.
- [53] F. Wang, J.J. Bhattacharyya, S.R. Agnew, Effect of precipitate shape and orientation on Orowan strengthening of non-basal slip modes in hexagonal crystals, application to magnesium alloys, *Materials Science and Engineering: A* 666 (2016) 114-122.
- [54] W.B. Sun, C.M. Liu, Y.H. Gao, Z.Y. Chen, X.Z. Han, Research on the precipitation strengthening of particle with a new shape model in magnesium alloys, *Materials Science and Engineering: A* 642 (2015) 309-315.
- [55] J. Jain, P. Cizek, W.J. Poole, M.R. Barnett, Precipitate characteristics and their effect on the prismatic-slip-dominated deformation behaviour of an Mg–6 Zn alloy, *Acta Materialia* 61(11) (2013) 4091-4102.
- [56] X. Gao, J.F. Nie, Characterization of strengthening precipitate phases in a Mg–Zn alloy, *Scripta Materialia* 56(8) (2007) 645-648.
- [57] Y.S. Kim, T.K. Ha, Microstructure and mechanical properties of Mg-Zn alloys, *International Scholarly and Scientific Research & Innovation* 10 (2016) 177-180.
- [58] C. Bettles, Enhanced age-hardening behaviour in Mg-4 wt.% Zn micro-alloyed with Ca, *Scripta Materialia* 51(3) (2004) 193-197.
- [59] X. Gao, S.M. He, X.Q. Zeng, L.M. Peng, W.J. Ding, J.F. Nie, Microstructure evolution in a Mg–15Gd–0.5Zr (wt.%) alloy during isothermal aging at 250°C, *Materials Science and Engineering: A* 431(1-2) (2006) 322-327.

- [60] S.M. He, X.Q. Zeng, L.M. Peng, X. Gao, J.F. Nie, W.J. Ding, Precipitation in a Mg–10Gd–3Y–0.4Zr (wt.%) alloy during isothermal ageing at 250°C, *Journal of Alloys and Compounds* 421(1-2) (2006) 309-313.
- [61] J.F. Nie, B.C. Muddle, Characterisation of strengthening precipitate phase in a Mg–Y–Nd alloy, *Acta Materialia* 48(8) (2000) 1691-1703.
- [62] R.L. Fullman, Measurement of particle sizes in opaque bodies, *Journal of Metals* (1953) 447-452.
- [63] B. Bhattacharya, M. Niewczas, Work-hardening behaviour of Mg single crystals oriented for basal slip, *Philosophical Magazine* 91(17) (2011) 2227-2247.
- [64] H.Y. Wu, F.Z. Lin, Mechanical properties and strain-hardening behavior of Mg alloy AZ31B-H24 thin sheet, *Materials Science and Engineering: A* 527(4-5) (2010) 1194-1199.
- [65] C.C. Tasan, J.P.M. Hoefnagels, M.G.D. Geers, A Micropillar compression methodology for ductile damage quantification, *Metallurgical and Materials Transactions A* 43(3) (2011) 796-801.
- [66] W.B. Hutchinson, M.R. Barnett, Effective values of critical resolved shear stress for slip in polycrystalline magnesium and other hcp metals, *Scripta Materialia* 63(7) (2010) 737-740.
- [67] T. Obara, H. Yoshinga, S. Morozumi, {11-22} {-1-123} slip system in magnesium, *Acta Materialia* 21 (1973) 845-853.

- [68] G.S. KIM, Small Volume Investigation of slip and twinning in magnesium single crystals, Université de Grenoble, PhD thesis, 2011.
- [69] A. Akhtar, E. Teghtsoonian, Solid solution strengthening of magnesium single crystals-II the effect of solute on the ease of prismatic slip, *Acta Metallurgica* 17 (1969) 1351-1356.
- [70] H. Conrad, W.D. Robertson, Effect of temperature on the flow stress and strain-hardening coefficient of magnesium single crystals, *Transactions AIME* 9(4) (1957) 503-512.
- [71] R.E. Reed-Hill, W.D. Robertson, The crystallographic characteristics of fracture in magnesium single crystals, *Acta metallurgica* 5 (1957) 728-737.
- [72] A. Chapuis, J.H. Driver, Temperature dependency of slip and twinning in plane strain compressed magnesium single crystals, *Acta Materialia* 59(5) (2011) 1986-1994.
- [73] S.R. Agnew, C.N. Tomé, D.W. Brown, T.M. Holden, S.C. Vogel, Study of slip mechanisms in a magnesium alloy by neutron diffraction and modeling, *Scripta Materialia* 48(8) (2003) 1003-1008.
- [74] S.R. Agnew, Plastic Anisotropy of Magnesium Alloy AZ31B Sheet, TMS Annual Meeting, Magnesium Technology 2002, Seattle 2002.
- [75] B.C. Wonsiewicz, Plasticity of magnesium crystals, Massachusetts Institute of Technology. Dept. of Metallurgy, Massachusetts Institute of Technology, 1966.

- [76] A. Jain, S.R. Agnew, Modeling the temperature dependent effect of twinning on the behavior of magnesium alloy AZ31B sheet, *Materials Science and Engineering: A* 462(1-2) (2007) 29-36.
- [77] E.W. Kelley, W.F. Hosford, Plane-strain compression of magnesium and magnesium alloy crystals, *TRANS Met Soc AIME* 242 (1968) 5-13.
- [78] S. Kurukuri, M.J. Worswick, D. Ghaffari Tari, R.K. Mishra, J.T. Carter, Rate sensitivity and tension-compression asymmetry in AZ31B magnesium alloy sheet, *Philos Trans A Math Phys Eng Sci* 372(2015) (2014) 1-16.
- [79] I. Ulacia, N.V. Dudamell, F. Gálvez, S. Yi, M.T. Pérez-Prado, I. Hurtado, Mechanical behavior and microstructural evolution of a Mg AZ31 sheet at dynamic strain rates, *Acta Materialia* 58(8) (2010) 2988-2998.
- [80] M. Tucker, M. Horstemeyer, P. Gullett, H. Elkadiri, W. Whittington, Anisotropic effects on the strain rate dependence of a wrought magnesium alloy, *Scripta Materialia* 60(3) (2009) 182-185.
- [81] M. Ardeljan, I.J. Beyerlein, B.A. McWilliams, M. Knezevic, Strain rate and temperature sensitive multi-level crystal plasticity model for large plastic deformation behavior: Application to AZ31 magnesium alloy, *International Journal of Plasticity* 83 (2016) 90-109.
- [82] J.V.D. Planken, A. Deruyttere, Solution hardening of magnesium single crystals by tin at room temperature, *Acta Metallurgica* 17 (1969) 451-454.

- [83] N. Stanford, M.R. Barnett, Solute strengthening of prismatic slip, basal slip and twinning in Mg and Mg–Zn binary alloys, *International Journal of Plasticity* 47 (2013) 165-181.
- [84] N. Stanford, R.K.W. Marceau, M.R. Barnett, The effect of high yttrium solute concentration on the twinning behaviour of magnesium alloys, *Acta Materialia* 82 (2015) 447-456.
- [85] J. Wang, N. Stanford, Investigation of precipitate hardening of slip and twinning in Mg5%Zn by micropillar compression, *Acta Materialia* 100 (2015) 53-63.
- [86] P. Hidalgo-Manrique, J.D. Robson, M.T. Pérez-Prado, Precipitation strengthening and reversed yield stress asymmetry in Mg alloys containing rare-earth elements: A quantitative study, *Acta Materialia* 124 (2017) 456-467.
- [87] S.R. Agnew, R.P. Mulay, F.J. Polesak, C.A. Calhoun, J.J. Bhattacharyya, B. Clausen, In situ neutron diffraction and polycrystal plasticity modeling of a Mg–Y–Nd–Zr alloy: Effects of precipitation on individual deformation mechanisms, *Acta Materialia* 61(10) (2013) 3769-3780.
- [88] N. Stanford, J. Geng, Y.B. Chun, C.H.J. Davies, J.F. Nie, M.R. Barnett, Effect of plate-shaped particle distributions on the deformation behaviour of magnesium alloy AZ91 in tension and compression, *Acta Materialia* 60(1) (2012) 218-228.
- [89] S.R. Kada, P.A. Lynch, J.A. Kimpton, M.R. Barnett, In-situ X-ray diffraction studies of slip and twinning in the presence of precipitates in AZ91 alloy, *Acta Materialia* 119 (2016) 145-156.

- [90] N. Stanford, M.R. Barnett, Effect of particles on the formation of deformation twins in a magnesium-based alloy, *Materials Science and Engineering: A* 516(1-2) (2009) 226-234.
- [91] J.D. Robson, N. Stanford, M.R. Barnett, Effect of particles in promoting twin nucleation in a Mg–5wt.% Zn alloy, *Scripta Materialia* 63(8) (2010) 823-826.
- [92] M.D. Uchic, D.M. Dimiduk, J.N. Florando, W.D. Nix, Sample dimensions influence strength and crystal plasticity, *Science* 305(5686) (2004) 986-9.
- [93] H. Bei, S. Shim, E. George, M. Miller, E. Herbert, G. Pharr, Compressive strengths of molybdenum alloy micro-pillars prepared using a new technique, *Scripta Materialia* 57(5) (2007) 397-400.
- [94] J.R. Greer, W.D. Nix, Nanoscale gold pillars strengthened through dislocation starvation, *Physical Review B* 73(24) (2006).
- [95] O. Kraft, P.A. Gruber, R. Mönig, D. Weygand, Plasticity in Confined Dimensions, *Annual Review of Materials Research* 40(1) (2010) 293-317.
- [96] A. Dubach, R. Raghavan, J. Löffler, J. Michler, U. Ramamurty, Micropillar compression studies on a bulk metallic glass in different structural states, *Scripta Materialia* 60(7) (2009) 567-570.
- [97] C.A. Volkert, A. Donohue, F. Spaepen, Effect of sample size on deformation in amorphous metals, *Journal of Applied Physics* 103(8) (2008) 083539.
- [98] C.J. Lee, J.C. Huang, T.G. Nieh, Sample size effect and microcompression of Mg₆₅Cu₂₅Gd₁₀ metallic glass, *Applied Physics Letters* 91(16) (2007) 161913.

- [99] A. Bharathula, S.-W. Lee, W.J. Wright, K.M. Flores, Compression testing of metallic glass at small length scales: Effects on deformation mode and stability, *Acta Materialia* 58(17) (2010) 5789-5796.
- [100] E. Lilleodden, Microcompression study of Mg (0001) single crystal, *Scripta Materialia* 62(8) (2010) 532-535.
- [101] J. Ye, R.K. Mishra, A.K. Sachdev, A.M. Minor, In situ TEM compression testing of Mg and Mg–0.2wt.% Ce single crystals, *Scripta Materialia* 64(3) (2011) 292-295.
- [102] T.A. Parthasarathy, S.I. Rao, D.M. Dimiduk, M.D. Uchic, D.R. Trinkle, Contribution to size effect of yield strength from the stochastics of dislocation source lengths in finite samples, *Scripta Materialia* 56(4) (2007) 313-316.
- [103] H. Gao, Y. Huang, Geometrically necessary dislocation and size-dependent plasticity, *Scripta Materialia* 48 (2008) 113-118.
- [104] D.M. Norfleet, D.M. Dimiduk, S.J. Polasik, M.D. Uchic, M.J. Mills, Dislocation structures and their relationship to strength in deformed nickel microcrystals, *Acta Materialia* 56(13) (2008) 2988-3001.
- [105] A.M. Minor, S.A. Asif, Z. Shan, E.A. Stach, E. Cyrankowski, T.J. Wyrobek, O.L. Warren, A new view of the onset of plasticity during the nanoindentation of aluminium, *Nat Mater* 5(9) (2006) 697-702.
- [106] Z.W. Shan, R.K. Mishra, S.A. Syed Asif, O.L. Warren, A.M. Minor, Mechanical annealing and source-limited deformation in submicrometre-diameter Ni crystals, *Nat Mater* 7(2) (2008) 115-119.

- [107] Q. Yu, Z.W. Shan, J. Li, X. Huang, L. Xiao, J. Sun, E. Ma, Strong crystal size effect on deformation twinning, *Nature* 463(7279) (2010) 335-338.
- [108] P.M. Kelly, A. Jostsons, R.G. Blake, J.R. Napier, The determination of foil thickness by scanning transmission electron microscopy, *Phys. Status Solidi* 31 (1975) 771-780.
- [109] S.M. Allen, Foil thickness measurements from convergent-beam diffraction patterns, *Philosophical Magazine A* 43(2) (2006) 325-335.
- [110] P.R. Okamoto, G. Thomas, On the Four-Axis Hexagonal Reciprocal Lattice and its Use in the Indexing of Transmission Electron Diffraction Patterns, *phys. stat. sol.* 28 (1968) 81-91.
- [111] R.R. Keller, R.H. Geiss, Transmission EBSD from 10 nm domains in a scanning electron microscope, *Journal of Microscopy* 245(3) (2012) 245-251.
- [112] P.W. Trimby, Orientation mapping of nanostructured materials using transmission Kikuchi diffraction in the scanning electron microscope, *Ultramicroscopy* 120 (2012) 16-24.
- [113] X.Z. Liang, M.F. Dodge, J. Jiang, H.B. Dong, Using transmission Kikuchi diffraction in a scanning electron microscope to quantify geometrically necessary dislocation density at the nanoscale, *Ultramicroscopy* 197 (2019) 39-45.
- [114] J.M. Cairney, P.R. Munroe, Redeposition effects in transmission electron microscope specimens of FeAl–WC composites prepared using a focused ion beam, *Micron* 34(2) (2003) 97-107.

- [115] B.I. Prenitzer, C.A. Urbanik-Shannon, L.A. Giannuzzi, S.R. Brown, R.B. Irwin, T.L. Shofner, F.A. Stevie, The correlation between ion beam/material interactions and practical FIB specimen preparation, *Microsc Microanal* 9(3) (2003) 216-36.
- [116] K.A. Unocic, M.J. Mills, G.S. Daehn, Effect of gallium focused ion beam milling on preparation of aluminium thin foils, *J Microsc* 240(3) (2010) 227-38.
- [117] Y.M. Kim, C.D. Yim, B.S. You, Grain refining mechanism in Mg–Al base alloys with carbon addition, *Scripta Materialia* 57(8) (2007) 691-694.
- [118] Y. Tamura, J. Yagi, T. Haitani, T. Motegi, N. Kono, H. Tamehiro, H. Saito, Observation of Manganese-Bearing Particles in Molten AZ91 Magnesium Alloy by Rapid Solidification, *Materials Transactions* 44 (2003) 552-557.
- [119] R.L. Zeng, Precipitation hardening in AZ91 Magnesium alloy, University of Birmingham, PhD, 2013.
- [120] S.Q. Zhu, S.P. Ringer, On the role of twinning and stacking faults on the crystal plasticity and grain refinement in magnesium alloys, *Acta Materialia* 144 (2018) 365-375.
- [121] S. Morozumi, M. Kikuchi, H. Yoshinaga, Electron Microscope Observation in and around {1102} Twins in Magnesium, *Trans. JIM* 17 (1976) 158-164.
- [122] N. Stanford, A.S. Taylor, P. Cizek, F. Siska, M. Ramajayam, M.R. Barnett, Twinning in magnesium-based lamellar microstructures, *Scripta Materialia* 67(7-8) (2012) 704-707.

- [123] B. Li, P.F. Yan, M.L. Sui, E. Ma, Transmission electron microscopy study of stacking faults and their interaction with pyramidal dislocations in deformed Mg, *Acta Materialia* 58(1) (2010) 173-179.
- [124] C.P. Frick, B.G. Clark, S. Orso, A.S. Schneider, E. Arzt, Size effect on strength and strain hardening of small-scale [111] nickel compression pillars, *Materials Science and Engineering: A* 489(1-2) (2008) 319-329.
- [125] D. Kiener, P.J. Guruprasad, S.M. Keralavarma, G. Dehm, A.A. Benzerga, Work hardening in micropillar compression: In situ experiments and modeling, *Acta Materialia* 59(10) (2011) 3825-3840.
- [126] C.A. Volkert, E.T. Lilleodden, Size effects in the deformation of sub-micron Au columns, *Philosophical Magazine* 86(33-35) (2006) 5567-5579.
- [127] B.M. Morrow, R.J. McCabe, E.K. Cerreta, C.N. Tomé, In-Situ TEM Observation of Twinning and Detwinning During Cyclic Loading in Mg, *Metallurgical and Materials Transactions A* 45(1) (2013) 36-40.
- [128] C.H. Cáceres, T. Sumitomo, M. Veidt, Pseudoelastic behaviour of cast magnesium AZ91 alloy under cyclic loading–unloading, *Acta Materialia* 51(20) (2003) 6211-6218.
- [129] P.G. Partridge, Cyclic twinning in fatigued close-packed hexagonal metals, *The Philosophical Magazine: A Journal of Theoretical Experimental and Applied Physics* 12(119) (2006) 1043-1054.
- [130] C.W. Chung, Microstructure and mechanical properties of ECAP processed AZ91 and AZ80 magnesium alloys, PhD, The university of Auckland, 2010.

- [131] K.S. Ng, A.H.W. Ngan, Deformation of micron-sized aluminium bi-crystal pillars, *Philosophical Magazine* 89(33) (2009) 3013-3026.
- [132] R. Soler, J.M. Molina-Aldareguia, J. Segurado, J. Llorca, R.I. Merino, V.M. Orera, Micropillar compression of LiF [111] single crystals: Effect of size, ion irradiation and misorientation, *International Journal of Plasticity* 36 (2012) 50-63.
- [133] T. Kamino, Evaluation of TEM samples of an Mg-Al alloy prepared using FIB milling at the operating voltages of 10 kV and 40 kV, *Journal of Electron Microscopy* 53(5) (2004) 459-463.
- [134] J.Y. Wang, N. Li, R. Alizadeh, M.A. Monclús, Y.W. Cui, J.M. Molina-Aldareguía, J. Llorca, Effect of solute content and temperature on the deformation mechanisms and critical resolved shear stress in Mg-Al and Mg-Zn alloys, *Acta Materialia* 170 (2019) 155-165.
- [135] R.M. Wang, A. Eliezer, E. Gutman, Microstructures and dislocations in the stressed AZ91D magnesium alloys, *Materials Science and Engineering A* (2002) 279-287.
- [136] A. Vaid, J. Guérolé, A. Prakash, S. Korte-Kerzel, E. Bitzek, Atomistic simulations of basal dislocations in Mg interacting with Mg₁₇Al₁₂ precipitates, *Materialia* 7 (2019) 100355.
- [137] M.A. Gharghouri, G.C. Weatherly, J.D. Embury, The interaction of twins and precipitates in a Mg-7.7 at.% Al alloy, *Philosophical Magazine A* 78(5) (1998) 1137-1149.

- [138] P. Bate, W.T. Roberts, D.V. Wilson, The plastic anisotropy of two-phase aluminium alloys—I. Anisotropy in unidirectional deformation, *Acta Metallurgica* 29(11) (1981) 1797-1814.
- [139] L.M. Brown, W.M. Stobbs, The work-hardening of copper-silica: I. A Model Based on Internal Stresses, with no Plastic Relaxation, *Philosophical Magazine* 23(185) (1971) 1185-1199.
- [140] L.M. Brown, W.M. Stobbs, The work-hardening of copper-silica: II the role of plastic relaxation, *Philosophical Magazine* 23(185) (1971) 1201-1233.
- [141] J.D. Robson, The effect of internal stresses due to precipitates on twin growth in magnesium, *Acta Materialia* 121 (2016) 277-287.
- [142] J.D. Eshelby, The determination of the elastic field of an ellipsoidal inclusion, and related problems, *Proceedings of the Royal Society of London. Series A. Mathematical and Physical Sciences* 241(1226) (1957) 376-396.
- [143] J.D. Eshelby, The elastic field outside an ellipsoidal inclusion, *Proceedings of the Royal Society of London. Series A. Mathematical and Physical Sciences* 252(1271) (1959) 561-569.
- [144] J.D. Eshelby, Elastic Inclusions and Inhomogeneities, *Progress in Solid Mechanics* 2 (1961) 87-140.
- [145] M. Gharghouri, Study of the mechanical properties of magnesium-8.5wt% aluminum by in-situ neutron diffraction, McMaster University, 1996.

- [146] D. Healy, Elastic field in 3D due to a spheroidal inclusion—MATLAB™ code for Eshelby's solution, *Computers & Geosciences* 35(10) (2009) 2170-2173.
- [147] C. Liu, P. Shanthraj, J.D. Robson, M. Diehl, S. Dong, J. Dong, W. Ding, D. Raabe, On the interaction of precipitates and tensile twins in magnesium alloys, *Acta Materialia* 178 (2019) 146-162.
- [148] K.D. Molodov, T. Al-Samman, D.A. Molodov, Profuse slip transmission across twin boundaries in magnesium, *Acta Materialia* 124 (2017) 397-409.
- [149] A.W. Sleeswyk, C.A. Verbraak, Incorporation of slip dislocations in mechanical twins-1, *Acta Metallurgica* 9 (1961) 917-927.
- [150] M. Hyong Yoo, C.-T. Wei, Growth of deformation twins in zinc crystals, *Philosophical Magazine* 14(129) (1966) 573-587.
- [151] M.H. Yoo, B.T.M. Loh, Structural and elastic properties of zonal twin dislocations in anisotropic crystals, *Conference on fundamental aspects of dislocation theory; Gaithersburg, United States, 1970*, pp. 479-493.
- [152] M.H. Yoo, Reply to “zonal dislocations and dislocation reactions with twins in hexagonal-close-packed metals”, *Scripta Metallurgica* 4(1) (1970) 9-11.
- [153] X. Wu, Y.T. Zhu, M.W. Chen, E. Ma, Twinning and stacking fault formation during tensile deformation of nanocrystalline Ni, *Scripta Materialia* 54(9) (2006) 1685-1690.
- [154] J. Wang, S.K. Yadav, J.P. Hirth, C.N. Tomé, I.J. Beyerlein, Pure-Shuffle Nucleation of Deformation Twins in Hexagonal-Close-Packed Metals, *Materials Research Letters* 1(3) (2013) 126-132.

- [155] J. Wang, I.J. Beyerlein, C.N. Tomé, An atomic and probabilistic perspective on twin nucleation in Mg, *Scripta Materialia* 63(7) (2010) 741-746.
- [156] I.J. Beyerlein, L. Capolungo, P.E. Marshall, R.J. McCabe, C.N. Tomé, Statistical analyses of deformation twinning in magnesium, *Philosophical Magazine* 90(16) (2010) 2161-2190.
- [157] M. Arul Kumar, A.K. Kanjarla, S.R. Niezgoda, R.A. Lebensohn, C.N. Tomé, Numerical study of the stress state of a deformation twin in magnesium, *Acta Materialia* 84 (2015) 349-358.
- [158] R.Y. Zhang, M.R. Daymond, R.A. Holt, A finite element model of deformation twinning in zirconium, *Materials Science and Engineering: A* 473(1-2) (2008) 139-146.
- [159] H. Fan, Y. Zhu, Q. Wang, Effect of precipitate orientation on the twinning deformation in magnesium alloys, *Computational Materials Science* 155 (2018) 378-382.
- [160] H. Fan, Y. Zhu, J.A. El-Awady, D. Raabe, Precipitation hardening effects on extension twinning in magnesium alloys, *International Journal of Plasticity* 106 (2018) 186-202.